

**Pharmacological Characterization of
Phenanthroindolizidine Alkaloids and
Fungal-Derived Metabolites
as Novel Drug Candidates for the Treatment
of Triple-Negative Breast Cancer**

Inaugural-Dissertation

zur Erlangung des Doktorgrades
der Mathematisch-Naturwissenschaftlichen Fakultät
der Heinrich-Heine-Universität Düsseldorf

vorgelegt von

Irene Reimche
aus Kaliningrad

Düsseldorf, November 2022

aus dem Institut für Pharmakologische Biologie und Biotechnologie
der Heinrich-Heine-Universität Düsseldorf

durchgeführt an dem Institut für Gesundheitsforschung und Bildung,
in der Abteilung „Biomedizinische Grundlagen“
der Universität Osnabrück“
und
an der Fakultät für Angewandte Naturwissenschaften,
Arbeitsgruppe „Bio-Pharmazeutische Chemie & Molekulare Pharmakologie“
der Technischen Hochschule Köln

Gedruckt mit der Genehmigung der
Mathematisch-Naturwissenschaftlichen Fakultät der
Heinrich-Heine-Universität Düsseldorf

Berichtersteller:

1. Frau Prof. Dr Nicole Teusch

2. Herr Prof. Dr Matthias Kassack

Tag der mündlichen Prüfung:

24.03.2023

Table of content

INDEX OF FIGURES AND SUPPLEMENTARY FIGURES	VII
INDEX OF TABLES AND SUPPLEMENTARY TABLES.....	XI
INDEX OF EQUATIONS.....	XIII
INDEX OF SCHEMES	XIII
INDEX OF ABBREVIATIONS	XIII
1 ABSTRACT.....	XVI
1 ZUSAMMENFASSUNG.....	XVIII
1 INTRODUCTION.....	1
1.1 Triple Negative Breast Cancer (TNBC).....	1
1.1.1 Clinical prognosis	1
1.1.2 Molecular characteristics of TNBC.....	3
1.1.3 Drug resistance in TNBC	6
1.1.4 The tumour microenvironment (TME)	10
1.2 Screening for novel drug candidates in TNBC therapy.....	14
1.2.1 Natural sources for drug discovery	14
1.2.2 Current preclinical models for drug screening regarding therapy of solid tumours	18
1.3 Aims of the studies	21
2 MATERIALS AND METHODS	22
2.1 Commercial consumables.....	22
2.1.1 Disposable materials	23
2.1.2 Chemicals and Kits.....	25
2.1.3 Primer and siRNA.....	27
2.1.4 Antibodies.....	28
2.2 Compounds	29
2.2.1 Commercial compounds	29
2.2.2 Natural products isolated from the plant <i>Tylophora ovata</i>	31
2.2.3 Natural products isolated from fungi	32
2.2.4 Chemically synthesized compounds	34

2.2.5	Dilution of lyophilized compounds	35
2.2.6	Serial compound dilution	35
2.3	Electronic devices and software.....	37
2.4	Cell culture	39
2.4.1	Cell lines	41
2.4.2	Subculture	44
2.5	NF κ B-inhibition	45
2.5.1	NanoGlo assay, 2h	45
2.5.2	Luciferase assay, 24 h.....	46
2.6	Gene expression studies	46
2.6.1	Real-Time quantitative Polymerase-Chain Reaction (RT-qPCR) in a 2D co-culture of MB-231 and PBMC	46
2.6.2	Gene expression in MB-231	47
2.7	Cell viability studies	49
2.7.1	2D CellTiterGlo	49
2.7.2	2D PrestoBlue	50
2.7.3	3D CellTiterGlo	51
2.7.4	2D colony formation.....	51
2.8	Cell cycle studies.....	51
2.8.1	Cell cycle population in MB-231.....	51
2.8.2	Cell cycle population in MB-468-UnaG	52
2.8.3	Quantification of the cell cycle population	52
2.9	Migration Studies.....	53
2.9.1	2D wound healing.....	53
2.9.2	3D TNBC invasion	57
2.10	Immunofluorescence studies	59
2.10.1	2D immunostaining	59
2.10.2	3D immunostaining	60
2.11	3D TNBC co-culture establishment.....	61
2.11.1	Selecting the seeding cell number	61

2.11.2	Spheroid characterization to determine culture conditions	62
2.11.3	3D co-culture formation	62
2.12	TYLO-1 characterization in the 3D TNBC model.....	63
2.12.1	3D monoculture growth in matrigel®.....	64
2.12.2	3D co-culture growth in collagen type I	64
2.12.3	3D co-culture cell type distribution	64
2.13	Hypoxia studies	64
2.13.1	Hypoxia Inducible Factor (HIF)-1 α -inhibition	65
2.13.2	3D TNBC co-culture to study hypoxia	65
2.14	Western blot	67
2.14.1	I κ B α protein level in MB-231	67
2.14.2	I κ B α protein level in MB-468	67
2.14.3	SDS-PAGE and immunoblotting	68
2.15	Protein knockdown studies	70
2.15.1	Lipofectamine™-based siRNA transfection	71
2.15.2	P65 knockdown	72
2.15.3	YAP Knockdown.....	72
2.16	Statistical analysis	76
3	RESULTS	77
3.1	Anti-tumour characterization of phenanthroindolizidine alkaloids (P-alkaloids) isolated from the plant <i>Tylophora ovata</i> in TNBC	77
3.1.1	Pharmacological mode of action of P-alkaloids.....	77
3.1.2	3D TNBC monoculture studies	99
3.1.3	3D TNBC co-culture spheroid model establishment.....	103
3.1.4	3D co-culture studies	110
3.1.5	Pathway crosstalk: HIF and NF κ B	115
3.1.6	Pathway crosstalk: YAP and NF κ B	123
3.2	Anti-tumour characterization of fungus-derived metabolites in TNBC.....	126
3.2.1	Azaphilones isolated from the fungus <i>A. falconensis</i> suppress NF κ B-mediated gene transcription in TNBC	126

3.2.2	Polyketides isolated from the fungus <i>A. falconensis</i> suppress TNBC migration	128
3.2.3	Decahydrofluorenes isolated from the fungus <i>Didymella</i> sp. IEA-3B.1 inhibit NFκB-mediated gene expression in TNBC.....	130
3.3	Anti-tumour characterization of engineered and chemically prepared histone deacetylase inhibitors (HDACIs) in TNBC	131
4	DISCUSSION	134
4.1	Characterization of P-alkaloids in TNBC	134
4.1.1	Anti-tumour mechanism of P-alkaloids against TNBC.....	134
4.1.2	SAR of P-alkaloids concerning <i>in vitro</i> and <i>in vivo</i> activities.....	136
4.1.3	The anti-inflammatory potential of P-alkaloids is maintained under hypoxic conditions	139
4.1.4	P-alkaloids block proliferation in TNBC through arrest at the G0/G1-state, thereby, delaying cell cycle progression.....	141
4.1.5	P-alkaloids have multiple target sites in TNBC, including YAP.....	143
4.1.6	TYLO-1 interferes with the tumour-stroma crosstalk by mitigating cytokines production.....	145
4.1.7	3D cultures as preclinical drug screening models for TNBC.....	146
4.1.8	P-alkaloids maintain anti-tumour potential in a 3D TNBC co-culture model and block growth as well as invasion of 3D TNBC spheroids.....	150
4.1.9	TYLO-1/TYLO-1s exhibits superior anti-tumour potential compared to the chemotherapeutic agent paclitaxel.....	152
4.2	Fungus-derived metabolites possess anti-inflammatory and anti-migratory potential, suggesting a SAR in TNBC.....	153
4.3	SAR studies of synthetically engineered HDACIs	154
4.4	Chemical synthesis of natural products, including derivatives and novel analogues, to improve drug efficacy for clinical purposes	156
4.5	Current and future perspectives for TNBC therapy	158
4.6	Conclusions	162
5	REFERENCES	163
6	APPENDIX	195
6.1	Supplementary figures.....	195

6.2	Supplementary tables	218
6.3	Plasmid sequences for reporter gene assays	227
6.3.1	MB-231-NanoLuc	227
6.3.2	MB-231-Firefly	228
6.3.3	MB-468-UnaG	228
6.4	Macro script for batch processing using Fiji	231
6.4.1	Quantification of nuclear YAP in images with.....	231
6.4.2	Image saving of separate recorded channels.....	238
LIST OF PUBLICATIONS		CCXLI
CURRICULUM VITAE		CCXLIII
DANKSAGUNG		CCXLV
EIDESSTAATLICHE ERKLÄRUNG		CCXLVII

Index of figures and supplementary figures

FIGURE 1-1 GLOBAL BREAST CANCER (BC) INCIDENCE AND MORTALITY RATE IN 2020.	2
FIGURE 1-2 TRIPLE-NEGATIVE BREAST CANCER (TNBC) PATIENTS HAVE THE WORST PROGNOSIS.....	3
FIGURE 1-3 PROPORTION OF TNBC AND BASAL-LIKE SUBTYPES IN BC.....	5
FIGURE 1-4 STIMULATION AND REGULATION OF THE TRANSCRIPTION FACTOR NUCLEAR FACTOR KAPPA (K) B (NFkB) SIGNALLING.....	8
FIGURE 1-5 HYPOXIA-INDUCIBLE FACTOR (HIF) REGULATION BY THE CELLULAR OXYGEN LEVEL.....	10
FIGURE 1-6 CANCER-ASSOCIATED FIBROBLASTS (CAFs) CREATE A TUMOUR PROMOTING NICHE.	12
FIGURE 1-7 EXEMPLARY ILLUSTRATION OF THE PLANT FAMILY <i>TYLOPHORA</i> SPP.....	16
FIGURE 1-8 ANTI-TUMOUR POTENTIAL OF PHENANTHROINDOLIZIDINE ALKALOIDS (P- ALKALOIDS)	17
FIGURE 2-1 CHEMICAL STRUCTURE OF BAY 11-7085.	30
FIGURE 2-2 CHEMICAL STRUCTURE OF PACLITAXEL.	30
FIGURE 2-3 CHEMICAL STRUCTURE OF STAUROSPORINE.	30
FIGURE 2-4 CHEMICAL STRUCTURE OF P-ALKALOIDS ISOLATED FROM <i>TYLOPHORA OVATA</i>	31

FIGURE 2-5 CHEMICAL STRUCTURES OF POLYKETIDES ISOLATED FROM THE FUNGUS	
<i>ASPERGILLUS FALCONENSIS</i>	32
FIGURE 2-6 CHEMICAL STRUCTURES OF AZAPHILONES ISOLATED FROM THE FUNGUS	
<i>ASPERGILLUS FALCONENSIS</i>	33
FIGURE 2-7 CHEMICAL STRUCTURES OF DECAHYDROFLUORENES ISOLATED FROM THE FUNGUS	
<i>DIDYMELLA SP.</i>	33
FIGURE 2-8 CHEMICAL STRUCTURES OF THE HISTONE DEACETYLASE INHIBITORS (HDACIs)	35
FIGURE 2-9 QUANTIFICATION OF CELL CYCLE PHASE POPULATIONS	53
FIGURE 2-10 DETERMINING THE MDA-MB-231 (MB-231) CELL SEEDING DENSITY FOR THE 2D	
WOUND HEALING ASSAY	54
FIGURE 2-11 DETERMINING THE CAF CELL SEEDING DENSITY FOR INDIRECT CO-CULTURE	
STUDIES	55
FIGURE 2-12 MACHINE LEARNING IDENTIFICATION OF CELL COVERED AREAS AND CELL FREE	
AREAS	57
FIGURE 2-13 MEASUREMENT OF TNBC SPHEROID INVADED AREA	58
FIGURE 2-14 SPHEROID SIZE MEASUREMENT	62
FIGURE 2-15 QUANTIFICATION OF UNAG EXPRESSION IN MDA-MB-468-UNAG (MB-468-	
UNAG) CELLS	65
FIGURE 2-16 QUANTIFICATION OF THE NUCLEAR YES-ASSOCIATED PROTEIN (YAP) IN	
MONOLAYER CELLS	75
FIGURE 3-1 P-ALKALOIDS BLOCKED NFkB-MEDIATED GENE TRANSCRIPTION IN TNBC IN A	
DOSE-DEPENDENT MANNER	80
FIGURE 3-2 TIME- AND DOSE-DEPENDENT NFkB BLOCKADE BY P-ALKALOIDS IN TNBC	81
FIGURE 3-3 INITIAL STRUCTURE-ACTIVITY RELATIONSHIP (SAR) FOR P-ALKALOIDS IN TNBC	
.....	83
FIGURE 3-4 TYLO-1 SIGNIFICANTLY INHIBITED CYTOKINE EXPRESSION IN A 2D CO-CULTURE OF	
MB-231 AND PBMCs	84
FIGURE 3-5 TYLO-1 DECREASED INTERLEUKIN (IL)-8 SECRETION FROM MB-231	85
FIGURE 3-6 RELA/P65 KNOCKDOWN IN MB-231	86
FIGURE 3-7 TYLO-1 MEDIATED REDUCTION IN CELL VIABILITY IS P65-INDEPENDENT	86
FIGURE 3-8 TYLO-1s MODULATED CELL CYCLE POPULATIONS IN MB-231 WITHIN 48 H	89
FIGURE 3-9 TYLO-1s MODULATED CELL CYCLE POPULATIONS IN MB-231 WITHIN 72 H	90
FIGURE 3-10 TYLO-1s MODULATED CELL CYCLE POPULATIONS IN MB-468-UNAG WITHIN	
48 H	91
FIGURE 3-11 TYLO-1s MODULATED CELL CYCLE POPULATIONS IN MB-468-UNAG WITHIN	
72 H	93

FIGURE 3-12 PACLITAXEL ARRESTED CELL CYCLE PROGRESSION AT THE G2/M-STATE IN MB-231.	95
FIGURE 3-13 ANTI-MITOTIC PACLITAXEL ARRESTED CELL CYCLE TRANSITION AT THE G2/M-STATE IN MB-468-UNAG.	97
FIGURE 3-14 CoCl₂-SIMULATED HYPOXIA ARRESTED CELL CYCLE PROGRESSION AT THE G2/M PHASE.	98
FIGURE 3-15 CoCl₂-SIMULATED HYPOXIA AFFECTS CYTOTOXICITY OF PACLITAXEL BUT NOT TYLO-1s IN MB-468-UNAG.	99
FIGURE 3-16 TYLO-1s BLOCKED TNBC MONOCULTURE SPHEROID INVASION INTO A MATRIGEL®-BASED EXTRACELLULAR MATRIX (ECM).	101
FIGURE 3-17 TYLO-1 BLOCKED TNBC MONOCULTURE SPHEROID GROWTH IN A DOSE-DEPENDENT MANNER.	102
FIGURE 3-18 3D TNBC CO-CULTURE SPHEROID FORMATION AT VARIOUS SEEDING CONDITIONS.	106
FIGURE 3-19 Co-CULTURE SPHEROIDS SHOWED BEST REPRODUCIBILITY IN A LOW COLLAGEN CONCENTRATION.	108
FIGURE 3-20 CAFs ENCAPSULATE MB-231 CELLS WITHIN THE CO-CULTURE SPHEROIDS....	108
FIGURE 3-21 Co-CULTURE SPHEROID GROWTH IS COMPARABLE AFTER 72 H AND 96 H FORMATION.	109
FIGURE 3-22 Co-CULTURE SPHEROID GROWTH DEPENDS ON THE COLLAGEN-BASED MATRIX.	109
FIGURE 3-23 P-ALKALOIDS REDUCE CELL VIABILITY OF 3D CO-CULTURE SPHEROIDS.	111
FIGURE 3-24 REPRESENTATIVE DOSE-RESPONSE INHIBITION IN MB-231 MONOLAYER CELLS AND 3D CO-CULTURE SPHEROIDS FOR TYLO-1 AND PACLITAXEL.....	112
FIGURE 3-25 3D CO-CULTURE SPHEROID GROWTH IS SIGNIFICANTLY BLOCKED WITH TYLO-1 BUT NOT PACLITAXEL.....	114
FIGURE 3-26 CAF ENCAPSULATION IN CO-CULTURE SPHEROIDS IS MAINTAINED POST-TREATMENT WITH TYLO-1 AND PACLITAXEL.	114
FIGURE 3-27 CoCl₂ SIMULATED HYPOXIA BY ENHANCING HYPOXIA INDUCIBLE FACTOR (HIF) TRANSCRIPTIONAL ACTIVITY.....	116
FIGURE 3-28 DOSE-RESPONSE INHIBITION IN MB-468-UNAG FOR CoCl₂, TYLO-1s, BAY 11-7085 AND PACLITAXEL.	117
FIGURE 3-29 TYLO-1s DECREASED HIF-MEDIATED TRANSCRIPTION IN MB-468-UNAG.	120
FIGURE 3-30 TYLO-1s STABILIZES THE INHIBITOR KB A PROTEIN (IkBA) UNDER NORMOXIC AND HYPOXIC CONDITIONS.	122
FIGURE 3-31 TYLO-1 ENHANCES YAP EXPRESSION IN TNBC.	124
FIGURE 3-32 TYLO-1 INDUCED NFkB-INHIBITION IS YAP-INDEPENDENT.....	125

FIGURE 3-33 TYLO-1 MEDIATED REDUCTION IN CELL VIABILITY IS YAP-INDEPENDENT.....	125
FIGURE 3-34 AZAPHILONES SUPPRESSED NFkB-MEDIATED GENE TRANSCRIPTION IN A DOSE-DEPENDENT MANNER.	127
FIGURE 3-35 SULOCHRIN SUPPRESSED MIGRATION OF MB-231 CELLS.	129
FIGURE 3-36 REPRESENTATIVE DOSE-RESPONSE INHIBITION OF CELL VIABILITY FOR SULOCHRIN AND MONOCHLORSULOCHRIN IN MB-231.....	129
FIGURE 3-37 DOSE-RESPONSE INHIBITION OF NFkB-ACTIVITY AND CELL VIABILITY FOR DECAHYDROFLUORENES.	130
FIGURE 3-38 HDACIs DISPLAY DOSE-RESPONSE REDUCTION OF MB-231 CELL VIABILITY...	132
FIGURE 4-1 P-ALKALOIDS ARE NOVEL DRUG CANDIDATES TO TREAT INFLAMMATION AND HYPOXIA DRIVEN CANCER, INCLUDING TNBC.	136
FIGURE 4-2 PHARMACOPHORIC COMPARTMENTS OF HDACIs.	155
FIGURE 4-3 THERAPEUTIC OPTIONS FOR TNBC ACCORDING TO THE INTRINSIC SUBTYPES...	159
FIGURE 4-4 NF-KB AS THE MAIN NODE OF RESISTANCE TO RECEPTOR TYROSINE KINASE INHIBITORS IN TNBC	160
FIGURE S 1 BC STAGING.	195
FIGURE S 2 OPTIMIZING THE BALANCE OF THE NFkB-AGONIST AND ANTAGONIST IN MB-231.	196
FIGURE S 3 TYLO-1s MODERATELY STABILIZED IκBα IN MB-231.	197
FIGURE S 4 TYLO-1 AND PACLITAXEL SUPPRESSED COLONY FORMATION OF MURINE D2A1 CELLS.....	198
FIGURE S 5 TYLO-1 REDUCED TNFα-INDUCED EXPRESSION OF IL-6 BUT NOT IL-8.....	199
FIGURE S 6 TYLO-1s DID NOT MODULATE THE CELL CYCLE STATE IN MB-231 WITHIN 24 H.	200
FIGURE S 7 DMSO DID NOT MODULATE THE CELL CYCLE STATE.	201
FIGURE S 8 PACLITAXEL AND TYLO-1s INCREASED DNA FRAGMENTATION IN MB-468-UNAG.	202
FIGURE S 9 TYLO-1 BLOCKED TNFα-INDUCED MIGRATION OF MB-231.	203
FIGURE S 10 CAF-CONDITIONED MEDIUM DECREASES TNBC MIGRATION.....	204
FIGURE S 11 LOW CONCENTRATION OF TYLO-1s DID NOT IMPACT TNBC MONOCULTURE SPHEROID INVASION.	205
FIGURE S 12 DOSE-DEPENDENT MONOCULTURE SPHEROID GROWTH BLOCKADE BY TYLO-1.	205
FIGURE S 13 CELL TYPE IDENTIFICATION IN TNBC CO-CULTURE SPHEROIDS.	206
FIGURE S 14 CAFs ENCOMPASS THE CORE OF TUMOUR CELLS WITHIN THE SPHEROIDS.	206
FIGURE S 15 DECREASED CELL VIABILITY OF CO-CULTURE SPHEROIDS BY TYLO-1 TREATMENT CORRELATES WITH BIOACTIVITY IN MB-231.....	207

FIGURE S 16 DOSE-DEPENDENT CO-CULTURE SPHEROID GROWTH BLOCKADE BY TYLO-1.	208
FIGURE S 17 CO-CULTURE SPHEROIDS (MB-468-UNAG:CAF) AT VARIOUS CULTURE CONDITIONS.	209
FIGURE S 18 CO-CULTURE SPHEROID GROWTH (MB-468-UNAG:CAF) IN 0.05 MG/ML COLLAGEN TYPE I.	210
FIGURE S 19 CO-CULTURE SPHEROID GROWTH (MB-468-UNAG:CAF) WAS ATTENUATED UNDER COCL₂-SIMULATED HYPOXIA.	211
FIGURE S 20 COCL₂ INDUCED NFκB VIA DEGRADATION OF IκBA.	212
FIGURE S 21 LIPOFECTAMINETM-BASED siRNA TRANSFECTION DOES NOT AFFECT YAP ACTIVITY.	212
FIGURE S 22 LIPOFECTAMINETM-BASED siRNA TRANSFECTION DOES NOT AFFECT YAP EXPRESSION.	213
FIGURE S 23 NUCLEAR YAP IS UPREGULATED IN TUMOUR CELLS.	213
FIGURE S 24 TYLO-1 DECREASES YAP ACTIVITY IN TNBC.	214
FIGURE S 25 TYLO-1 DOES NOT REDUCE YAP ACTIVITY ADDITIONALLY TO YAP KNOCKDOWN.	215
FIGURE S 26 YAP KNOCKDOWN REDUCES YAP ACTIVITY IN MB-231 AND MCF10A.	216
FIGURE S 27 TYLO-1 DECREASES YAP ACTIVITY IN MB-231 BUT NOT IN MCF10A.	217
FIGURE S 28 PLASMID COMPARTMENTS FOR NFκB NANO LUC-LUCIFERASE REPORTER.	227
FIGURE S 29 PLASMID COMPOSITION FOR NFκB FIREFLY-LUCIFERASE REPORTER.	228
FIGURE S 30 PLASMID COMPARTMENTS FOR HIF-REPORTER GENE STUDIES.	229

Index of tables and supplementary tables

TABLE 1-1 IMMUNOHISTOCHEMISTRY-BASED CLASSIFICATION OF BREAST CANCER WITH THE CORRESPONDING CLINICAL PROGNOSIS	2
TABLE 1-2 THERAPY OPTIONS FOR TNBC ACCORDING TO THE TRANSCRIPTOME-BASED SUBTYPES	4
TABLE 1-3 GENETIC AND EPIGENETIC PROFILE OF BASAL-LIKE TNBC	5
TABLE 1-4 CLASSES OF HDAC ISOFORMS AND THEIR FUNCTION	6
TABLE 1-5 MODE OF ACTION OF P-ALKALOID DERIVATIVES IN CANCER	15
TABLE 1-6 FEATURES OF PRECLINICAL MODELS FOR DRUG SCREENING	20
TABLE 2-1 VENDORS AND THEIR LOCATIONS	22
TABLE 2-2 DISPOSABLE CONSUMABLES	23
TABLE 2-3 DISPOSABLE PLATES USED FOR CELL SEEDING, COMPOUND DILUTION AND qPCR	24
TABLE 2-4 RE-USED MATERIALS	24
TABLE 2-5 LIST OF CHEMICAL AGENTS, CYTOKINES, AND ENZYMES	25

TABLE 2-6 LIST OF KITS AND REAGENTS	26
TABLE 2-7 FORWARD AND REVERSE PRIMER SEQUENCE	27
TABLE 2-8 SIRNA AND THEIR TARGETS.....	28
TABLE 2-9 LIST OF ANTIBODIES USED IN WESTERN BLOT STUDIES.....	28
TABLE 2-10 LIST OF PRIMARY ANTIBODIES USED FOR IMMUNOFLUORESCENCE STUDIES.....	28
TABLE 2-11 LIST OF SECONDARY ANTIBODIES AND DNA STAINING DYE USED FOR IMMUNOFLUORESCENCE STUDIES	29
TABLE 2-12 COMMERCIAL COMPOUNDS	30
TABLE 2-13 PHENANTHROINDOLIZIDINE ALKALOIDS (P-ALKALOIDS) WITH THEIR INTERNAL CODE AND MOLECULAR WEIGHT	31
TABLE 2-14 MOLECULAR WEIGHT AND TARGET PROTEINS OF HISTONE DEACETYLASE INHIBITORS (HDACIs)	34
TABLE 2-15 COMPOUND CONCENTRATION APPLIED IN DOSE-RESPONSE INHIBITION STUDIES .	36
TABLE 2-16 ELECTRONIC DEVICES	37
TABLE 2-17 SOFTWARE FOR DATA ILLUSTRATION AND DATA ANALYSIS	38
TABLE 2-18 LIST OF CELL LINES WITH ORIGIN AND VENDOR	39
TABLE 2-19 CELL CULTURE MEDIUM, ANTIBIOTICS, AND AGENTS	40
TABLE 2-20 CELL SEEDING DENSITY FOR DOSE-RESPONSE INHIBITION STUDIES.....	49
TABLE 2-21 IMMUNOSTAINING SOLUTION FOR TWO DIMENSIONAL (2D) MONOLAYER CELLS AND 3D SPHEROID STAINING	59
TABLE 2-22 ANTIBODY COMBINATION USED FOR EXAMINING THE CELL TYPE DISTRIBUTION WITHIN CO-CULTURE SPHEROIDS	61
TABLE 2-23 LIST OF MANUALLY PREPARED SOLUTIONS FOR WESTERN BLOT STUDIES.....	69
TABLE 2-24 CELL SEEDING DENSITY FOR KNOCKDOWN STUDIES.....	71
TABLE 2-25 SIRNA MIXTURE TRANSFECTION AGENTS AND COMBINATION	71
TABLE 3-1 IC₅₀-VALUES DETERMINED FOR P-ALKALOIDS IN NFκB-INHIBITION AND REDUCTION OF CELL VIABILITY IN TNBC	79
TABLE 3-2 IC₅₀-VALUES DETERMINED FOR REDUCTION OF CELL VIABILITY IN CO-CULTURE SPHEROIDS	111
TABLE 3-3 IC₅₀-VALUES DETERMINED FOR REDUCTION OF CELL VIABILITY IN PRIMARY MURINE CANCER-ASSOCIATED FIBROBLASTS (CAFs)	112
TABLE 3-4 IC₅₀-VALUES FOR AZAPHILONES IN NFκB-INHIBITION AND REDUCTION OF CELL VIABILITY	127
TABLE 3-5 IC₅₀-VALUES FOR DECAHYDROFLUORENES IN NFκB-INHIBITION AND REDUCTION OF CELL VIABILITY	131
TABLE 3-6 IC₅₀-VALUES OF HDACIs FOR REDUCTION OF CELL VIABILITY IN MB-231	133

TABLE S 1 MOLECULAR SUBTYPES OF TNBC	218
TABLE S 2 NATURAL SOURCES OF P-ALKALOIDS	219
TABLE S 3 BIOACTIVITIES OF P-ALKALOIDS AND THEIR ANALOGUES	219
TABLE S 4 MODE OF ACTION OF P-ALKALOIDS AND THEIR ANALOGUES <i>IN SILICO</i> , <i>IN VITRO</i> AND <i>IN VIVO</i>	220
TABLE S 5 IC ₅₀ -VALUES DETERMINED FOR P-ALKALOIDS IN REDUCTION OF CELL VIABILITY IN MB-231.....	224
TABLE S 6 DOSE-RESPONSE INHIBITION FOR BAY-117085 IN MB-231	225
TABLE S 7 DOSE-RESPONSE OF TYLO-1 AND PACLITAXEL IN CAFs	225
TABLE S 8 DOSE-RESPONSE IN DIFFERENT CELL LINES FOR DIFFERENT TREATMENT DURATION	225
TABLE S 9 DRUG-DOSE RESPONSE IN MB-468-UNAG	226
TABLE S 10 DRUG-DOSE REDUCTION IN REDUCTION OF CELL VIABILITY OF 3D CO-CULTURE SPHEROIDS	226
TABLE S 11 DRUG-DOSE RESPONSE FOR TYLO-1 AND PACLITAXEL IN 3D CO-CULTURE SPHEROIDS	226

Index of equations

EQUATION 1 CALCULATION OF THE LIVE CELL NUMBER USING THE HAEMOCYTOMETER.	45
EQUATION 2 CALCULATION OF THE RELATIVE IκBα PROTEIN LEVEL IN WESTERN BLOT STUDIES.....	69

Index of schemes

SCHEME 1 TREATMENT COURSE FOR THE 3D TNBC SPHEROID STUDIES.	63
SCHEME 2 TREATMENT COURSE FOR KNOCKDOWN STUDIES.....	70

Index of abbreviations

×: FOLD CONCENTRATED 26	ATCC: AMERICAN TYPE CULTURE COLLECTION	BP: BANDPASS FILTER, [NM] 53
°C: DEGREE CELSIUS 40	23	BSA: BOVINE SERUM ALBUMIN 26
μM: MICROMOLAR 29	BA: BENZYL ALCOHOL 26	CAF: CANCER- ASSOCIATED
A. FALCONENSIS: ASPERGILLUS	BB: BENZYL BENZOATE 26	FIBROBLAST 11
FALCONENSIS 33	BC: BREAST CANCER 1	
AF: ALEXA FLUOR® 30		

CAFs: CANCER- ASSOCIATED FIBROBLASTS 113	EMT: EPITHELIAL-TO- MESENCHYMAL TRANSITION 4	IKK: IKB KINASE 8
CAS: CHEMICAL ABSTRACTS SERVICE REGISTRY NUMBER 31	EMA: WAVELENGTH OF EMISSION 51	IL: INTERLEUKIN 6
CDNA: COMPLEMENTARY DNA 47	ENZYME-LINKED IMMUNOSORBENT ASSAY: ELISA 47	INTDENS: INTEGRATED DENSITY 75
CLSM: CONFOCAL LASER SCANNING MICROSCOPE 39	ER: ESTROGEN RECEPTOR 1	IKBA: INHIBITOR KB A 8
CM: CONDITIONED MEDIUM 55	EXλ: WAVELENGTH OF EXCITATION 30	LPS: LIPOPOLYSACCHARIDE 26
CoCl ₂ : COBALT (II) CHLORIDE 26	FCS: FETAL CALF SERUM 42	MB-231: MDA-MB-231 16
CSC: CANCER STEM CELLS 6	FDA: FOOD AND DRUG ADMINISTRATION 155	MCF10A: MICHIGAN CANCER FOUNDATION- 10A 41
CT: CYCLE THRESHOLD 49	FW: FORWARD 28	MDA-MB: M.D. ANDERSON - METASTATIC BREAST 41
D: DIMENSIONAL 19	GI ₅₀ : HALF MAXIMAL GROWTH INHIBITION 102	MIN: MINUTE 40
DAPI: 4',6 DIAMIDINO-2- PHENYLINDOLE DIHYDROCHLORIDE 30	H: HOUR 40	ML: MILLILITER 45
DDH ₂ O: DOUBLE DISTILLED WATER 70	HDAC: HISTONE DEACTETYLASE 4	MW: MOLECULAR WEIGHT 31
DMEM: DULBECCO'S MODIFIED EAGLE'S MEDIUM 41	HDACI: INHIBITOR OF HDAC 4	NFKB: NUCLEAR FACTOR KAPPA B 6, 80
DMSO: DIMETHYL SULFOXIDE 26	HER2: HUMAN EPIDERMAL GROWTH FACTOR RECEPTOR-2 1	nM: NANOMOLAR 37
ECM: EXTRACELLULAR MATRIX 11, 14	HKP: HOUSEKEEPING PROTEIN 69	OS: OVERALL SURVIVAL 2
EDTA: ETHYLENEDIAMINE TETRAACETIC 26	HMEC: HUMAN MAMMARY EPITHELIAL CELLS 41	OVERANALYSES OF VARIANCE 77
EGF: EPIDERMAL GROWTH FACTOR 42	HTS: HIGH THROUGHPUT SCREENING 19	P-ALKALOID: PHENANTHROINDOLIZIDI NE ALKALOID 15
	IC ₅₀ : HALF MAXIMAL INHIBITORY CONCENTRATION 46	PBMC: PERIPHERAL BLOOD MONONUCLEAR CELL 41
		PFA: PARAFORMALDEHYDE 26

PH: POTENTIAL OF HYDROGEN 60	SD: STANDARD DEVIATION 77	TYLO-3: TYLOPHORIDICINE E 16
PI: PROPIUM IODIDE 26	SDS: SODIUM DODECYL SULFATE 27	TYLO-4: 2- DEMETHOXYTYLOPHORI NE 16
PR: PROGESTERONE RECEPTOR 1	SDS-PAGE: SDS POLYACRYLAMIDE GEL ELECTROPHORESIS 68	TYLO-5: TYLOPHORIDICINE D 16
PTB: PHENANTHRENE- BASED COMPOUND 138	SEC: SECOND 47	TYLO-6: ANHYDRODEHYDROTYL OPHORINIDINE 16
PVP: POLYVINYLPIRROLIDON E 26	SEM: STANDARD ERROR OF THE MEAN 77	V/V: VOLUME PER VOLUME 60
REV: REVERSE 28	SIRNAS: SMALL INTERFERING RNAs 28	VEGFR: VASCULAR ENDOTHELIAL GROWTH FACTOR RECEPTOR 142
RFU: RELATIVE FLUORESCENCE UNITS 51	<i>T. OVATA: TYLOPHORA</i> <i>OVATA</i> 32	W/V: WEIGHT PER VOLUME 52
RLU: RELATIVE LIGHT UNITS 46	TAM: TUMOUR- ASSOCIATED- MACROPHAGE 12	YAP: YES-ASSOCIATED PROTEIN 7
RPMI: ROSWELL PARK MEMORIAL INSTITUTE 42	TME: TUMOUR MICROENVIRONMENT 3	ZBG: ZINC BINDING GROUP 155
RT: ROOM TEMPERATURE 47	TNBC: TRIPLE NEGATIVE BREAST CANCER 1	A: ALPHA, GREEK LETTER 8, 27
RTK: RECEPTOR TYROSINE KINASE 6	TNFA: TUMOUR NECROSE FACTOR ALPHA 27	ASMA: A SMOOTH MUSCLE ACTIN 12
RTKI: RTK INHIBITOR 160	TYLO-1: O- METHYLTYLOPHORINIDI NE 16	K: KAPPA, GREEK LETTER 6
RT-QPCR: REAL-TIME QUANTITATIVE POLYMERASE-CHAIN REACTION 47	TYLO-2: TYLOPHORINIDINE 16	

1 Abstract

Triple-negative breast cancer (TNBC), representing the most aggressive form of breast cancer (BC) with currently no targeted therapy available, is characterized by an inflammatory and hypoxic tumour microenvironment (TME). Natural sources provide a broad spectrum of metabolites that are currently utilized as standard chemotherapeutics in TNBC therapy, including paclitaxel, or being investigated as novel drug candidates due to their anti-tumour effects in preclinical studies. Structure–activity relationship (SAR) is important to identify crucial chemical groups that determine compound activity. Furthermore, drug design enables improved activities of naturally occurring metabolites, or generation of novel compounds with selective molecular targets. To identify novel potential agents to combat TNBC, natural products isolated from plants and fungi, as well as synthetically engineered inhibitors of histone deacetylases (HDACs) were investigated to characterize their pharmacological mechanism of action.

To date, a broad spectrum of anti-tumour activities has been reported for phenanthroindolizidine alkaloids (P-alkaloids), however, their mode of action in TNBC remains elusive. Thus, six naturally occurring P-alkaloids isolated from the plant *Tylophora ovata* were investigated: O-Methyltylophorinidine (TYLO-1) and its five derivatives tylophorinidine (TYLO-2), tylophoridine E (TYLO-3), 2-demethoxytylophorine (TYLO-4), tylophoridine D (TYLO-5), and anhydrodehydrotylophorinidine (TYLO-6). In comparison to the natural TYLO-1 and for more in-depth studies, we also utilized a sample of a chemically prepared O-methyltylophorinidine molecule (TYLO-1s). Our results indicate a remarkably effective blockade of nuclear factor kappa B (NFκB) within 2 h for TYLO-1 and TYLO-1s ($IC_{50} = 17.1 \pm 2.0$ nM and 3.3 ± 0.2 nM) that is different from its effect on cell viability within 24 h ($IC_{50} = 13.6 \pm 0.4$ nM and 4.2 ± 1 nM). Furthermore, NFκB inhibition data for the additional five derivatives suggest a SAR. Mechanistically, NFκB is significantly blocked through the stabilization of its inhibitor protein kappa B alpha (IκBα) under normoxic as well as hypoxic conditions. In addition to the transcriptional factors (NFκB and HIF), the transcriptional coactivator yes-associated protein (YAP) was identified as a novel target of TYLO-1 by blocking its nuclear translocation. Knockdown studies targeting NFκB/p65 or YAP expression further support the hypothesis, that the underlying mechanism of P-alkaloids relies on multiple target sites. The TME plays a substantial role in tumour progression and drug resistance, mainly relying on the bidirectional crosstalk of tumour and stromal cells mediated via their secretome, including interleukin (IL)-6 and IL-8. In a direct 2D co-culture of the human TNBC cell line MDA-MB-231 (MB-231) and primary human peripheral blood mononuclear cells (PBMCs), TYLO-1 sufficiently blocked the crosstalk based on the cytokines, presumably by inhibiting NFκB-regulated expression.

To better mimic the TNBC TME *in vitro*, a 3D co-culture was established by combining the human MB-231 with primary murine cancer-associated fibroblasts (CAFs) and type I collagen. TYLO-1 demonstrates superiority against the therapeutic gold standard paclitaxel by diminishing spheroid growth by 40% at 100 nM. The anti-proliferative effect of TYLO-1s is distinct from paclitaxel in that it arrests the cell cycle at the G0/G1 state, thereby mediating a time-dependent delay in cell cycle progression. Furthermore, TYLO-1s inhibited invasion of TNBC monoculture spheroids into a matrigel®-based environment at 10 nM. In conclusion, P-alkaloids serve as promising agents with presumably multiple target sites to combat inflammatory and hypoxia-driven cancer, such as TNBC, with a different mode of action than the currently applied chemotherapeutic drugs. Moreover, P-alkaloids are capable modulators to suppress tumour-promoting features of the TME.

Despite various anti-tumour activities, fungus-derived metabolites are not yet approved for cancer therapy. Notably, culture conditions influence the gene expression profile, and thereby, accumulation of fungal metabolites. Hence, compounds were isolated after alteration of cultivation conditions. Regarding metabolites derived from *Aspergillus falconensis*, NFκB-mediated gene transcription was suppressed in TNBC within 24 h by all nine azaphilones, namely falconensin A, H, I, M, N, O, Q, R, S, that hint to a SAR. Falconensin Q displayed the strongest anti-inflammatory agent ($IC_{50} = 11.9 \pm 2.1 \mu M$) with no cytotoxicity detected. Amongst polyketides, isolated from *Aspergillus falconensis*, sulochrin demonstrated significant suppression of TNBC migration at 70 μM , while monochlorsulochrin showed no effects. Both substances were non-toxic against TNBC. The decahydrofluorenes isolated from *Didymella* sp. IEA-3B.1, suppressed NFκB-mediated gene transcription within 2 h in TNBC. Didymellanosine ($IC_{50} = 15.5 \pm 1.1 \mu M$) was the most potent agent compared to phomapyrrolidone A and ascomylactam C. However, reduced cell viability by ascomylactam C displayed a strong dependency on its anti-inflammatory effects, while phomapyrrolidone A and didymellanosine showed no cytotoxicity. In summary, fungal metabolites possess anti-cancer potential in TNBC at two-digit micromolar concentrations, with hint to a SAR. However, their efficacy is low compared to currently applied chemotherapeutic regimens.

Approved targeted therapy options are limited to TNBC patients experiencing metastasis and tumour relapse, which is the main cause of cancer death. Currently novel targeted strategies are explored, including the epigenetic modification by histone deacetylases. In this study, eight chemically prepared HDACIs were examined: LAK41, LAK107, LAK110, LAK121, LAK-ZnFD, KSK64, KSK75 and MPK265, that hint to a SAR. Cell viability was reduced by compounds, that simultaneously target HDAC1 and HDAC6, which are LAK41, KSK64 and MPK265 with an IC_{50} value of $4.5 \pm 1.7 \mu M$, $10.2 \pm 4.9 \mu M$ and $38.7 \pm 1.8 \mu M$, respectively.

1 Zusammenfassung

Der Triple-negative Brustkrebs (TNBC), welcher die aggressivste Form von Brustkrebs (BC) darstellt und derzeit keine gezielte Therapiemöglichkeit hat, ist durch ein inflammatorisches und hypoxisches Tumor Mikromilieu (TME) charakterisiert. Natürliche Ressourcen bieten ein breites Spektrum an Metaboliten, die derzeit als Standard Chemotherapeutika in der TNBC Therapie angewandt werden, miteingeschlossen Paclitaxel, oder welche aufgrund ihrer Anti-Tumor Effekte als neue Arzneimittelpotentialkandidaten in präklinischen Studien untersucht werden. Struktur-Aktivitäts Beziehungen (SAR) sind wichtig, um chemische Gruppen zu identifizieren, die entscheidend für die Substanzaktivität sind. Des Weiteren, ermöglicht ein Wirkstoffdesign verbesserte Aktivitäten von natürlich vorkommenden Metaboliten, oder ermöglicht die Herstellung von neuen Wirkstoffen für selektive molekulare Zielstrukturen. Um potenzielle Substanzen zu identifizieren, die den TNBC bekämpfen, wurden Naturprodukte, welche von Pflanzen und Pilzen isoliert wurden, so wie synthetisch entwickelte Histondeacetylase Inhibitoren (HDACIs) hinsichtlich ihrer pharmakologischen Wirkmechanismen untersucht.

Bis heute wurden vielfältige Anti-Tumor Wirkungen für die Phenanthroindolizidine Alkaloide (P-alkaloids) berichtet, wobei ihr Wirkmechanismus nach wie vor nicht in TNBC aufgeklärt ist. Deshalb wurden sechs natürlich vorkommende P-alkaloids, die von der Pflanze *Tylophora ovata* isoliert wurden, untersucht: O-Methyltylophorinidine (TYLO-1) und dessen fünf Derivate Tylophorinidine (TYLO-2), Tylophoridicine E (TYLO-3), 2-Demethoxytylophorine (TYLO-4), Tylophoridicine D (TYLO-5) und Anhydrodehydrotylophorinidine (TYLO-6). Im Vergleich zum natürlich vorkommenden TYLO-1 und für ausführlichere Studien wurde das chemisch hergestellte O-Methyltylophorinidine (TYLO-1s) verwendet. Unsere Ergebnisse weisen auf eine bemerkenswerte effektive Blockade vom Nuclear Factor Kappa B (NFκB) innerhalb von 2 h hin, wobei sich die Wirkung von TYLO-1 und TYLO-1s ($IC_{50} = 17.1 \pm 2.0$ nM und 3.3 ± 0.2 nM) von der reduzierten Zellviabilität innerhalb von 24 h unterscheidet ($IC_{50} = 13.6 \pm 0.4$ nM und 4.2 ± 1 nM). Außerdem suggerieren die Daten der NFκB-inhibition eine SAR. Mechanistisch basiert die signifikante NFκB Blockade auf die Stabilisierung vom Inhibitor Protein Kappa B Alpha (IκBα) unter Normoxie so wie auch unter hypoxischen Bedingungen. Zusätzlich zur Inhibition von Transkriptionsfaktoren (NFκB und HIF), wurde der Transkriptions-Koaktivator Yes-assoziiertes Protein (YAP) als neues Zielprotein von TYLO-1 entdeckt, welches die YAP Translokation in den Nucleus unterbindet. Die Protein Knockdown Studien mit NFκB/p65 oder YAP unterstützen die Hypothese, dass die Anti-Tumor Wirkung von P-alkaloids auf multiple molekulare Inhibitionen beruhen. Das TME spielt eine wesentliche Rolle bei der Tumorprogression und Wirkstoffresistenz. Dabei basiert die bidirektionale Interaktion von Tumor und Stroma Zellen auf deren Sekretom,

miteingeschlossen Interleukin (IL)-6 und IL-8. In einer direkten 2D Ko-Kultur von der humanen TNBC Zelllinie MDA-MB-231 (MB-231) und primären, periphere mononukleäre Blutzellen (PBMCs) unterdrückte TYLO-1 die Interaktion, welche auf den Zytokinen beruht, wahrscheinlich durch die Blockade der NFκB-regulierten Expression.

Für eine bessere *in vitro* Nachahmung des TNBC TME, wurde eine 3D Ko-Kultur aus humanen MB-231, so wie primären, murinen Krebs-assoziierten Fibroblasten (CAFs) und Typ I Kollagen hergestellt. TYLO-1 demonstriert eine Überlegenheit gegenüber dem therapeutischen Goldstandard Paclitaxel durch eine Verringerung des Sphäroidwachstums um 40% bei 100 nM. Die anti-proliferativen Effekte von TYLO-1s unterscheiden sich zu Paclitaxel, indem die den Zellzyklus in der G0/G1 Phase anhalten, wodurch eine zeitabhängige Verzögerung der Zellzyklus Progression vermittelt wird. Darüber hinaus, inhibiert TYLO-1s mit 10 nM die Invasion von TNBC Monokultur Sphäroiden in ein Matrigel®-basiertes Milieu. Zusammengefasst sind P-alkaloids vielversprechende Wirkstoffe mit wahrscheinlich multiplen Zielstrukturen, um Inflammation- und Hypoxie-angetriebene Krebsarten, inklusive TNBC, zu besiegen. Dabei haben die P-alkaloids eine andere Wirkweise als die derzeit angewandten Chemotherapeutika. Ebenfalls sind die P-alkaloids wirksame Modulatoren, um das Tumor-fördernde TME zu unterdrücken.

Trotz einer Breite von Anti-Tumor Effekten, sind Pilzmetabolite bisher nicht für eine Krebstherapie zugelassen. Grundsätzlich beeinflusst die Kultivierung das Genexpressions Profil und damit die Akkumulation von Pilzmetaboliten. Daher, wurden Pilzsubstanzen nach Veränderung der Kulturbedingungen isoliert. Mit Hinblick auf Metabolite, die aus dem *Aspergillus falconensis* isoliert wurden, wurde die NFκB-vermittelte Genexpression in TNBC innerhalb von 24 h von allen neun Azaphilonen blockiert, was eine SAR suggeriert. Namentlich gehören dazu Falconensin A, H, I, M, N, O, Q, R und S. Falconensin Q ist die effektivste anti-inflammatorische Substanz ($IC_{50} = 11.9 \pm 2.1 \mu M$), die keine Zytotoxizität aufweist. Unter den Polyketiden, welche vom *Aspergillus falconensis* isoliert wurden, zeigte Sulochrin eine signifikante Unterdrückung der TNBC Migration mit 70 μM , wobei Monochlorsulochrin keine Effekte hatte. Beide Substanzen waren nicht toxisch gegen TNBC. Die Decahydrofluorene, die von *Didymella* sp. IEA-3B.1 isoliert wurden, inhibierten die NFκB-vermittelte Genexpression in TNBC innerhalb von 2 h. Didymellanosine ($IC_{50} = 15.5 \pm 1.1 \mu M$) war die stärkste Substanz im Vergleich zu Phomapyrrolidone A und Ascomylactam C. Allerdings, zeigte die reduzierte Zellviabilität durch Ascomylactam C eine stärkere Abhängigkeit von der anti-inflammatorischen Wirkung, während Phomapyrrolidone A und Didymellanosine nicht zytotoxisch wirkten. Zusammenfassend lässt sich sagen, dass Pilzmetabolite bei TNBC in zweistelligen mikromolaren Konzentrationen krebshemmend wirken, wobei eine SAR vorliegt. Allerdings ist die Substanzwirkung sehr gering im Vergleich zu derzeit angewandten Chemotherapeutika.

Die Möglichkeiten zur gezielten Therapie sind nur für TNBC Patienten genehmigt, die bereits Metastasierung oder ein Tumor Rezidiv erfahren haben, was zur Haupt-Todesursache zählt. Derzeit werden neue zielgerichtete Therapie Strategien erforscht, einschließlich die epigenetische Modifikation durch Histondeacetylasen. In dieser Studie wurden acht chemisch produzierte HDACIs untersucht: LAK41, LAK107, LAK110, LAK121, LAK-ZnFD, KSK64, KSK75 und MPK265, die auf eine SAR hindeuten. Die Zellviabilität wurde von Molekülen reduziert, welche simultan das HDAC1 und HDAC6 blockieren. Dazu zählen LAK41, KSK64 und MPK265 mit jeweils einem IC_{50} Wert von $4.5 \pm 1.7 \mu M$, $10.2 \pm 4.9 \mu M$ and $38.7 \pm 1.8 \mu M$.

1 Introduction

1.1 Triple Negative Breast Cancer (TNBC)

1.1.1 Clinical prognosis

Among women, breast cancer (BC) is the predominant type of cancer and leading cause of cancer death (**Figure 1-1**). In 2022, there are an estimated 2.3 million new BC cases and 685,000 BC-related deaths [1]. Clinical-relevant subtypes are categorized based on expression of hormone receptors (estrogen receptor (ER) and progesterone receptor (PR)) or human epidermal growth factor receptor-2 (HER2/EGFR2/HER2neu) (**Table 1-1**). The triple-negative breast cancer (TNBC) lacks significant expression of these receptors (ER-/PR-/HER2-) and is more frequent among younger women [2,3] and regarding ethnic groups, among black women [4]. The clinical outcome depends on the BC subtype, hence, TNBC patients have the worst prognosis accounting for 10% of BC incidences and a disproportionate of 83% of BC-related deaths (**Table 1-1**) [5].

TNBC is characterized by a high rate of proliferation, high rate of metastasis and shorter overall survival due to recurrence after chemotherapy based on taxanes, e.g. paclitaxel, anthracyclines, e.g. doxorubicin, or platinum-based treatment regimens [6–9]. TNBC patients experience early metastasis, predominantly to the lung and brain [10]. Compared to non-TNBC diseases, TNBC patients display a higher cancer stage (**Figure S 1**) at the time of diagnosis [11], which is linked to the worse clinical outcomes (**Figure 1-2**). Metastasis drastically lowers the five-year survival rate of TNBC patients to 29% with distant spread compared to 86-99% with regional or local spread [12]. Dramatically, the median overall survival with a metastatic disease is about one year for TNBC patients, that is extremely low compared to non-TNBC types with four-five years [13]. The main treatment option for TNBC is surgery, radiation and systemic chemotherapy, however metastasis and drug resistance are the main cause of death [11]. Lacking target therapy options for TNBC emphasizes the urgent need to characterize the tumour disease and to identify novel treatment regimens.

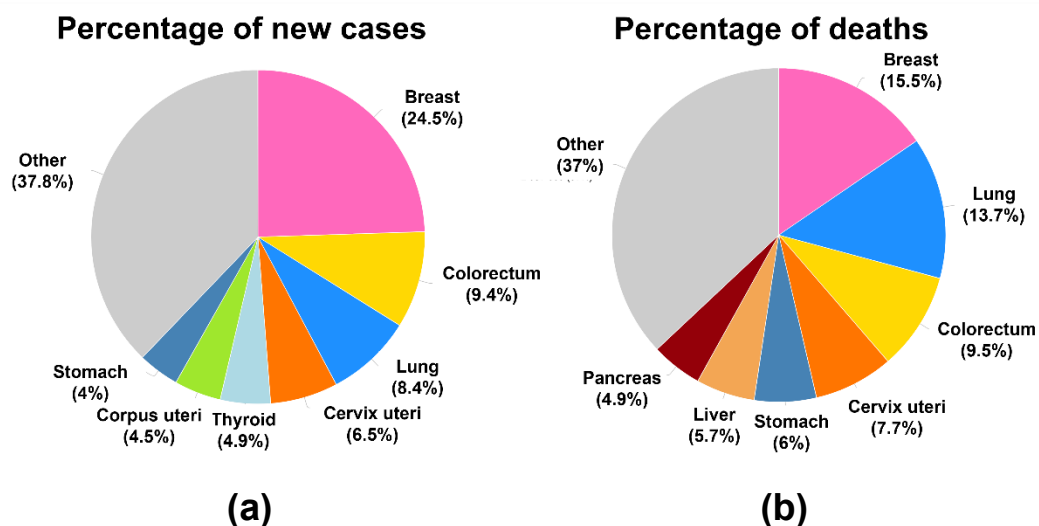


Figure 1-1 Global breast cancer (BC) incidence and mortality rate in 2020. Estimated number of (a) new BC cases and (b) BC-related deaths among females in 2020. Among women, BC has the highest incidence rate (24.55% of a total of 9,227,484) and mortality rate (15.5% of a total of 4,429,323). Illustration with minor modifications from Globocan (2020) [14].

Table 1-1 Immunohistochemistry-based classification of breast cancer with the corresponding clinical prognosis

BC subtype	IHC ¹ and molecular characteristics ²	Frequency (incidence)	Therapy and prognosis (Five-year overall survival (OS))
Luminal A	HER2- with (ER+/PR-), (ER+/PR+), (ER-/PR+), (ER-/PR-) and low Ki67	≥50%	Endocrine and chemotherapy (OS: 92%)
Luminal B	HER2+ with (ER+/PR-), (ER+/PR+), (ER-/PR+), (ER-/PR-) and high Ki67	20-30%	Endocrine and chemotherapy (OS: 89%)
HER2 enriched	HER2+ with ER-/PR-	15-20%	Endocrine + HER2 targeting antibodies (OS: 83%)
Triple-negative (basal-like)	ER-/PR-/HER2- and high Ki67	10-20%	Chemotherapy (OS: 77%)

Data were adapted from [12,15] ¹ IHC: Immunohistochemistry. Negative receptor expression is described with no significant expression of ER/PR/HER2 (<1% / < 20% / < 10%). ² Cut-off for Ki67 expression: high (> 30%), low (< 30%)

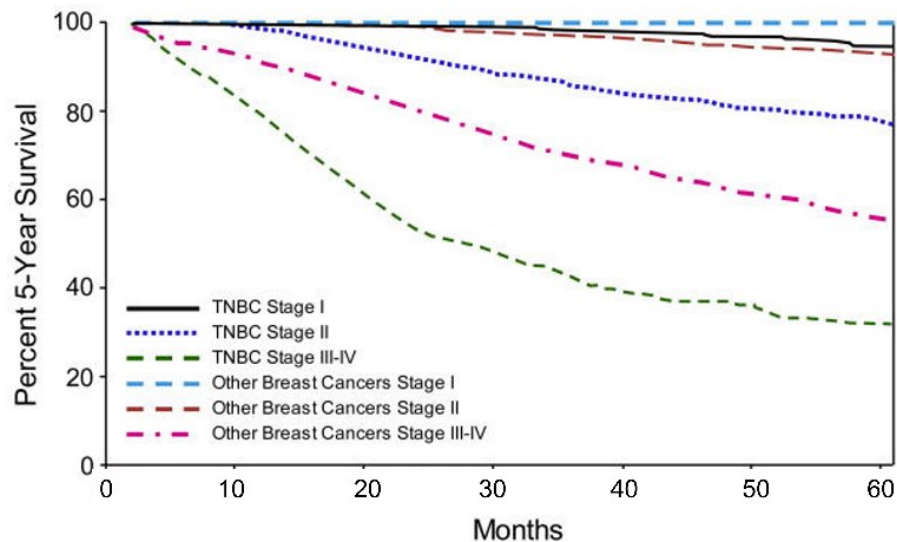


Figure 1-2 Triple-negative breast cancer (TNBC) patients have the worst prognosis.

Five-year survival rate according to the disease stage of BC with comparison of TNBC to non-TNBC subtypes [6]. At advanced stages with metastatic disease, median overall survival for non-TNBC spans four to five years, while it drastically decreases for TNBC patients to a maximum of 13 months [13]. Illustration with minor modifications from Pal, Childs and Pegram [6].

1.1.2 Molecular characteristics of TNBC

It became evident, that the intrinsic molecular subtyping has a higher predictive and prognostic value for the patient's outcome than the classical immunohistochemistry status [16]. Classification of molecular characteristics in TNBC was approached by various laboratories (compare **Table S 1**), highlighting the heterogenic character of this disease [17]. In addition to assessment of the genomic and transcriptomic landscape, there are novel approaches to include the landscape of proteomics, regulation of gene expression (e.g. epigenomics, alternative pre-mRNA splicing, long-non coding RNAs) and also assessment of immune cells within the tumour microenvironment (TME) [18] with regard to their subtype specific prognostic values, e.g. overall survival or disease-free survival [19]. It is not surprising, that the drug response varies depending on the TNBC subtype [20], thus therapy should be tailored according to the molecular features (**Table 1-2**) [21]. While non-basal-like BC can be treated with endocrine and HER2 targeted regimens, the therapy for basal-like tumours is limited to chemotherapeutics [22]. Basal-like tumours include a high percentage of TNBC (86%), and *vice versa*, TNBC includes a high percentage of basal-like tumours (78%) (**Figure 1-3**). To be considered, hyperactivated genes in TNBC correlate with tumour aggressiveness [3] and might present potential targets for therapy.

Molecular signalling is dysregulated in TNBC through mutation of tumour suppressor genes, e.g. predominantly in TP53 (80%), and gene amplification of oncogenes, e.g. PIK3CA,

KRAS (**Table 1-3**) [23]. In addition to genomic alterations, epigenetic modifications change cell features through methylation or acetylation. Regarding the methylation status of the promotor region, expression of genes is suppressed by hypermethylation, e.g. for BRCA1, while expression of genes that correlate with tumour aggressiveness are elevated by hypomethylation e.g. stem cell marker CD44 (**Table 1-3**) [24]. Of note, TNBC is characterized by enhanced hypomethylation [23] and has a lower methylation status in comparison to other BC classes [25]. In the course of gene transcription, chromatin relaxation is regulated by histone acetyltransferases through histone acetylation at lysine residues. The reversed process is accomplished by histone deacetylases (HDACs), thus resulting in chromatin condensation and gene repression [26]. HDACs are overexpressed in cancer and play a role in angiogenesis and metastasis of TNBC [26] through mediating epithelial-to-mesenchymal transition (EMT) [24]. HDAC inhibitors (HDACIs) selectively block HDAC isoforms, which are categorized into four classes (**Table 1-4**). While HDACIs, targeting class I HDACs, were able to induce ER expression in ER⁻ BC, HDACI, targeting class II, were reported to induce apoptosis [26], and moreover, to reverse drug resistance [27].

All in all, TNBC is a heterogenic disease. Targeting epigenetic modulation, e.g., acetylation, is a possible route to prevent tumour progression and to reverse drug resistance.

Table 1-2 Therapy options for TNBC according to the transcriptome-based subtypes

TNBC subtype ¹	Characteristics	Therapy option
Basal-like immune-suppressed (BLIS; 39%)	BRCA mutation	DNA damaging agents (cisplatin) + inhibition of DNA repair (PARP inhibitor)
Luminal androgen receptor (LAR; 23%)	Androgen receptor HER2 receptor	Antibodies against receptors; CDK4/6 inhibitors
Immunomodulatory (IM; 24%)	High infiltration of lymphocytes (TILs)	Targeting the tumour-stromal crosstalk in the TME (Immune checkpoint blockade by e.g., PD-L1 antibodies)
Mesenchymal-like (MES; 15%)	Features of stem cells JAK/STAT3 signalling	Inhibition of JAK/STAT3

¹ Subtypes were categorized based on their transcriptome [20].

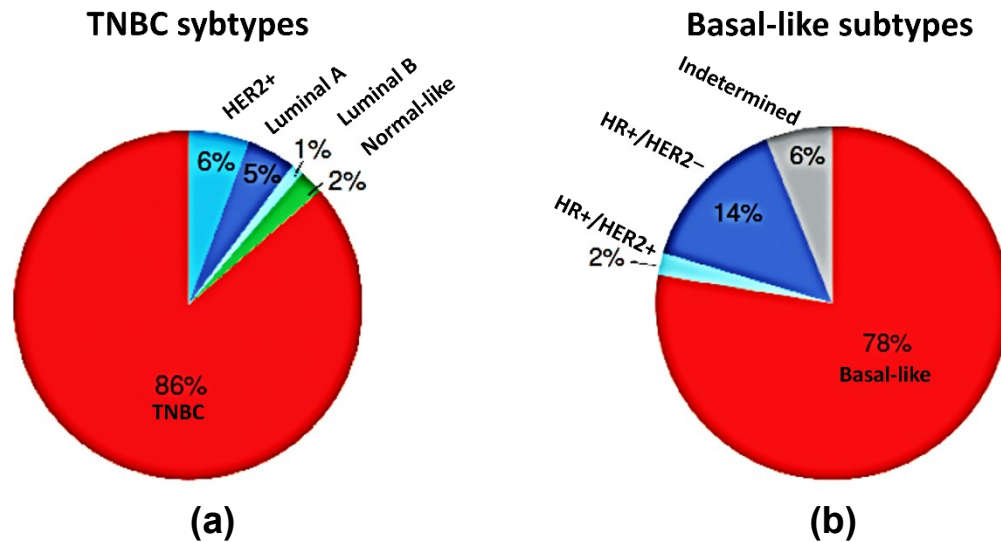


Figure 1-3 Proportion of TNBC and basal-like subtypes in BC. (a) Subtypes were defined in TNBC by Prediction Analysis of Microarray 50, short PAM50, analysis in the data base of The Cancer Genome Atlas, short TCGA. (b) Subtypes were classified in basal-like BC in the data base of TCGA. BC subtypes were defined according to the receptor status (ER, PR, HER2) determined with immunohistochemistry. (a,b) Proportion of cell types was similar and confirmed in another data base, namely METABRIC. Illustration with minor modifications from Garrido-Castro, Lin and Polyak (2019) [28].

Table 1-3 Genetic and epigenetic profile of basal-like TNBC

Molecular alteration	Modified gene expression
Gain of function mutation ¹	TP53 (80%); PIK3CA (7%)
Loss of function mutation ¹	Negative regulator of p53, namely MDM2 (14%); PTEN (35%); RB1 (20%); BRCA1 (30%); BRCA2 (6%); RB1(20%)
Hyperactivation (gene amplification) ¹	PIK3CA (49%); MYC (40%); KRAS (32%); BRAF (30%); EGFR (23%); cyclin E1 (9%)
Inactivation through gene deletion	TP53; PTEN; RB1
Inactivating hypermethylation ^{2,3}	RB; P73; BRCA1 (27%-37%) ⁵
Activating hypomethylation ^{1,2,4}	Cancer stem cell marker (CD44; CD133); EMT-marker (TWIST1); negative regulator of BRCA1 (ID4); Ras signalling (RAS3); tumour suppressor (FLJ43663);

¹ Reviewed in [23]. ² Reviewed in [24]. ³ Controversial findings for CDKN2B [29] and CD44 [30]. Methylation was described, although these genes are overexpressed in basal-like BC and correlate with poor prognosis. ⁴ Reported in [25]. ⁵ Hypermethylation of BRCA gene correlates with the features in BRCA1 mutated cells, which is referred to as "BRCAness" [24].

Table 1-4 Classes of HDAC isoforms and their function

HDAC class	HDAC isoforms	Cellular functions of HDAC
I	1, 2, 3	Nuclear lysine deacetylation
	8	Fatty acid deacetylation
IIa	4, 5, 7, 9	Acetyl-lysine recognition
IIb	6	Cytoplasmatic lysine deacetylation
	10	Polyamine deacetylation
IV	11	Fatty acid deacetylation

Summary was adjusted from Maccallini *et al.* (2022) [26].

1.1.3 Drug resistance in TNBC

The leading cause of death in TNBC is metastasis and tumour recurrence due to resistance after standard chemotherapy [31]. Failure of standard chemotherapy and worse clinical outcome [32,33] is managed by the so-called tumour initiating cells or cancer stem cells (CSC), which are enriched in TNBC [32,34] as well as in the TNBC cell line MB-231 (> 90%) [35]. CSCs are characterized as poorly differentiated cells that possess the capability for self-renewal, cell type differentiation and tumour initiation, defined by the potential of reconstituting an entire tumour upon engraftment *in vivo*. This heterogenic cell population causes metastasis, resistance to drugs as well as tumour relapse and displays a dynamic phenotype and proliferation state: rapidly proliferating epithelial-like cells or dormant mesenchymal-like cells [32], whereas CSC are described to co-express epithelial as well as mesenchymal markers in TNBC [36]. Although the gene expression profile is altered to sustain CSC features [37], CSCs can arise from non-CSCs without any genomic changes [32]. In particular EMT is linked to CSC maintenance [31], whereby EMT was discovered as a key process to convert non-CSCs to CSCs, and here, the transcription factor ZEB1 plays a crucial role to mediate EMT[32]. EMT may be induced through diverse pathways, which are also described as regulators for CSC features: nuclear factor kappa (κ) B (NF κ B)[38], TGF- β /SMAD, growth factors/receptor tyrosine kinase (RTK), Wnt/ β -catenin, Delta-like/Notch, hedgehog/SMO, cytokines/JAK, integrin/ILK or negative regulation by Hippo/LATs [32,39]. Growth factors trigger RTKs resulting in PI3K/AKT and ERK/MAPK signalling [39], while cytokines, e.g. interleukin (IL)-6 [40], mainly induce JAK/STAT3 [37] or NF κ B [38] signalling. In general, pro-inflammatory cytokines, IL-6 and IL-8, are enhanced in TNBC compared to other BC subtypes [38], and are linked to enrichment of CSC and poor prognosis [32]. Cytokines trigger NF κ B pathway in an autocrine and paracrine fashion [41,42]. In particular, NF κ B activity is enhanced in CSCs [38] and TNBC [43]. In TNBC, diverse soluble factors induce NF κ B activation, thus, targeting of e.g. RTK would be

compensated by another route resulting in downstream NFκB signalling, which is postulated as the main node to sustain drug resistance [44]. Indeed, NFκB was reported as one of the key mediators of cell plasticity and CSC features by producing pro-inflammatory cytokines [45]. Standard drugs in TNBC therapy, e.g. paclitaxel, change the gene expression profile [32] resulting in drug resistance by upregulating cytokines, like IL-6 and IL-8, and enrichment of CSCs [46]. In chemotherapy-enriched CSCs both, NFκB and Wnt pathway, are activated to produce cytokines and maintain a positive feedback loop of Wnt and NFκB signalling via JAK, STAT and AP-1 signalling [38]. NFκB and Wnt/β-catenin target genes, including cytokines, IL-6 and IL-8, are linked to a poor survival rate and shorter DFS [47]. NFκB [48] as well as Wnt [49] were reported to further transactivate the transcriptional co-activator yes-associated protein (YAP), which is linked to poor prognosis in basal-like BC [50] and shorter overall survival [51]. In TNBC, the transcriptional coactivator is also upregulated upon paclitaxel-based therapy [52] and the nuclear translocation of the transcriptional complex with TAZ (YAP/TAZ) is negatively regulated by phosphorylation mediated by the Hippo/LATS axis [53].

Also the TME has a tremendous effect on drug resistance by creating a niche to maintain CSC features and promoting drug resistance [54] [32]. The soluble factors in the TME, secreted by cancer as well as stromal cells, induce EMT [55]. EMT and the reversed state, mesenchymal-to-epithelial transition, are key processes to enable tumour metastasis, including invasion, as well as colonisation, respectively [56]. Furthermore, the low oxygen level (hypoxia) within the TME activates YAP [48], NFκB [57,58] and HIF signalling [59,60]. All three pathways, YAP [48], NFκB as well as HIF [31], mediate EMT, the key process of CSC, while blocking EMT reverses drug resistance [59,61–63].

In summary, TNBC has a limited sensitivity to standard chemotherapeutics, thus resulting in tumour relapse, which is mainly conducted by CSC. Targeting key pathways that sustain CSC features, namely YAP, NFκB or HIF, may improve clinical outcome.

1.1.3.1 Inflammation-associated nuclear factor kappa B (NFκB) pathway

Chronic inflammation is associated with oncogenesis [64] and the inflammatory TME in TNBC [65] is linked to a worse overall survival [66]. The transcription factor NFκB is a dominant regulator in inflammation and correlates with tumour aggressiveness in breast and other cancer types [67–72]. Compared to other BC subtypes, NFκB is highly activated in TNBC [43] and overexpression is linked to a poor clinical outcome [73]. In mammals, the NFκB family comprises five functionally conserved transcription factors: p50 (processed from p105), p52 (processed from p100), RelA (p65), RelB and c-Rel with p50/p65 representing the predominant dimer in ER– BC types [74]. P50/p65 is retained in the cytoplasm, when engaged to its inhibitor protein κB alpha (α) (IκBα). Various NFκB activating stimuli, e.g., tumour necrosis factor α (TNFα) or DNA damaging agents, such as

paclitaxel, trigger the complex of I κ B kinase (IKK) α /IKK β /IKK γ which phosphorylates the I κ B α /NF κ B complex. Subsequently, I κ B α is eliminated by proteasomal degradation and the p50/p65 dimer is released to translocate to the nucleus (**Figure 1-4**) [61,75]. Among over 150 target genes, the pro-inflammatory cytokines IL-6 and IL-8 maintain a positive feedback loop via NF κ B to orchestrate tumour growth, metastasis, and drug resistance in an autocrine manner [41,76]. In particular, migration, as a crucial step in metastasis, is regulated by NF κ B through activation of transcription factors involved in EMT [77]. Various pathways triggered by growth factors and cytokines are described to converge in NF κ B signalling, which emphasizes its role to maintain tumour progression and survival in an autocrine [78] and paracrine manner [65]. Resistance to drugs, such as paclitaxel, is mediated by NF κ B through enhanced expression of anti-apoptotic factors including Bcl-2 [61]. Targeting NF κ B signalling is sufficient to inhibit cancer cell migration as well as invasion [79] and reverses paclitaxel resistance [61]. Based on these findings, NF κ B represents a promising target to combat TNBC.

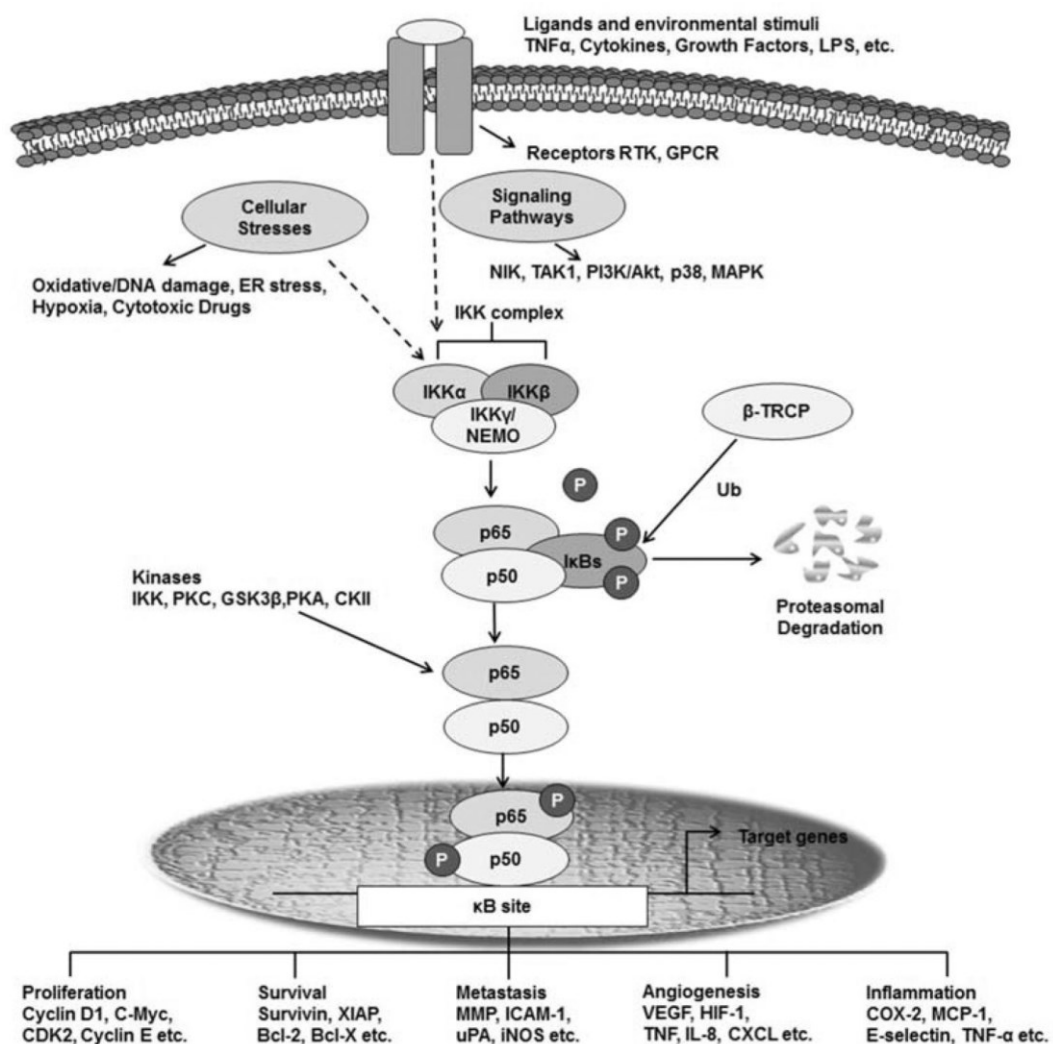


Figure 1-4 Stimulation and regulation of the transcription factor nuclear factor kappa (κ) B (NF κ B) signalling. The IKK complex is the main transducer of soluble as well as

cellular stimuli resulting in NF κ B (p65/p50) activity. Phosphorylation by the IKK complex releases p65/p50 for nuclear translocation and transcription of genes, which are linked to tumour progression and drug resistance. Illustration from Wang, Nag and Zhang (2015) [80].

1.1.3.2 Hypoxia-associated hypoxia-inducible factor (HIF) pathway

A disbalance of rapidly proliferating tumour cells and a poor vascularization causes hypoxia, that is characteristic for TNBC but not for non-TNBC diseases [62]. Low oxygen concentration at $< 0.1\%$ ($pO_2 < 0.7$ mmHg) increases genomic instability of cells and selection pressure of cells [81]. The spatially distinct oxygen level within the tissues creates a gradient with hypoxic conditions at vessel free areas and oxygen supply near blood vessels (normoxic conditions) [82]. Hypoxia can be detected in the core of microtumours or cells with a distance of $> 100 \mu m$ to blood vessels providing oxygen [83]. Due to the increasing relevance of hypoxia in the tumourigenesis and tumour progression, hypoxia induced alternative splicing is declared as the 11th hallmark of cancer [84], whereby the 10 hallmarks of cancer were earlier declared by Hanahan and Weinberg in 2011 [85]. In this context, poor clinical outcome due to hypoxia is linked to a high activity of the transcription factor hypoxia-inducible factor 1 α (HIF-1 α), which is stabilized under hypoxia and mediates cell survival [86,87]. In BC, HIF is overexpressed and highly activated [88]. In particular, the hypoxic TME in TNBC has a considerable impact in supporting tumour growth, invasiveness, and resistance to therapy [81].

The HIF transcription factor family comprises oxygen-sensing α -subunits (HIF-1 α , HIF-2 α , HIF-3 α) and oxygen-insensitive β -subunits (e.g., HIF-1 β), both dimerizing to form heterodimeric HIF-transcription complexes under hypoxic conditions, stabilizing HIF-driven gene expression. During normoxia, oxygen-sensing HIF-1 α is hydroxylated and degraded via the proteasome, whereby under hypoxic conditions, hydroxylation is impaired due to oxygen shortage, resulting in HIF-1 α stabilization and nuclear translocation. HIF regulates over 1500 target genes, that are related to drive angiogenesis, tumour growth, and multiple steps of metastasis (**Figure 1-5**) [88,89]. Hypoxia-induced vessel formation is characterized by a poor connection between pericytes and endothelial cells, thus causing vessel leakiness and facilitating metastasis [90]. Crosstalk with other pathways, such as NF κ B [89] or STAT3 [91], further drives tumour progression and mediates drug resistance. In cancer, hypoxia is described to induce NF κ B activity [92], while in turn, NF κ B transcriptionally regulates HIF [89] and both pathways correlate with worse clinical outcome [33]. Blockade of HIF-1 α expression reduced proliferation as well as induced apoptosis in TNBC [93], and further reversed CSC features, resulting in increased drug sensitivity [94].

In conclusion, hypoxia is a crucial driver of tumour aggressiveness, and blocking transcriptional activity of the key pathway HIF-1 α is a promising approach to combat TNBC.

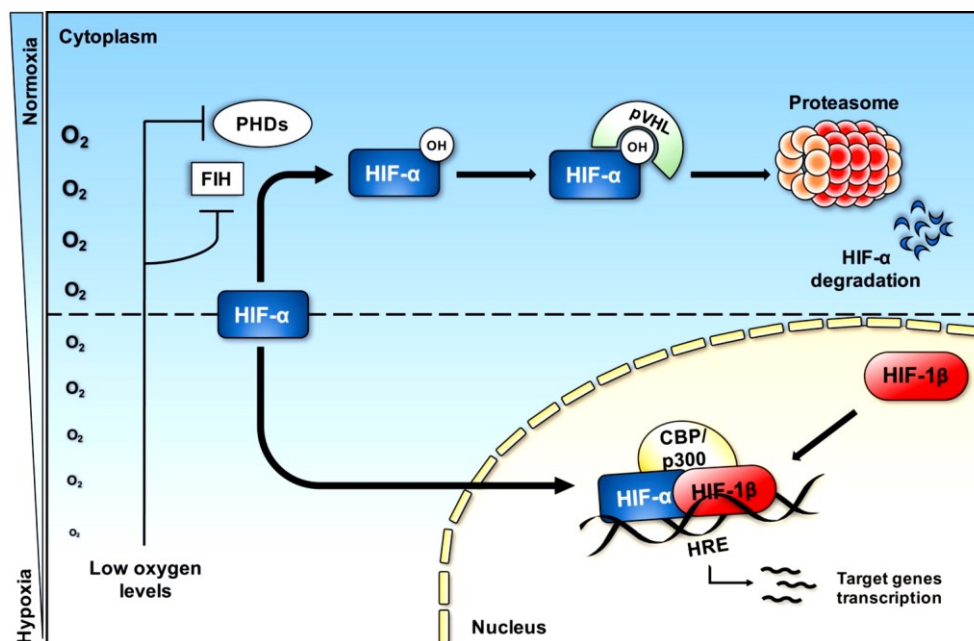


Figure 1-5 Hypoxia-inducible factor (HIF) regulation by the cellular oxygen level. In normoxia, HIF-1 α degradation is induced by prolyl hydroxylases (PHD) controlled hydroxylation, which is recognised by von-Hippel-Lindau (pVHL). Hypoxia inhibits factor inhibiting HIF (FIH) and PHD, thus, stabilizing HIF-1 α , which translocates to the nucleus and regulates gene transcription in a complex with nuclear HIF-1 β and CBP/p300. Illustration from D'Ignazio *et al.* (2017) [89].

1.1.4 The tumour microenvironment (TME)

The TNBC TME is a complex network of cellular components including cancer as well as stromal cells (endothelial cells, immune cells, adipocytes, fibroblasts), and non-cellular components including the extracellular matrix (ECM) as well as soluble factors released from all cell types [95–97]. The tumour's secretome recruits non-cancerous stromal cells, that are involved to create an inflammatory tumour-promoting environment [98], reducing drug sensitivity [99], and preparing a pre-metastatic niche at distant organs [100]. Stromal cells are enriched in the TNBC TME [101] and are associated with poor prognosis [101].

1.1.4.1 Predominant cell types

Tumour-derived cytokines, e.g. TGF- β [102], recruit and activate fibroblasts to so-called cancer-associated fibroblasts (CAFs), that represent the predominant stromal cell population [98] with a percentage of up to 70% of the total tumour mass [103]. CAFs sustain a niche with optimal conditions for colonisation of tumour cells, in particular CSC [32], and correlate with cancer relapse and poor prognosis [33]. Transcriptome-based subtyping of CAFs revealed heterogeneous origins, e.g. from resident fibroblasts or epithelial cells that underwent EMT, and heterogeneous contribution to tumour progression [104,105].

Although there are no specific CAFs marker, this cell type is identified based on e.g., α smooth muscle actin (α SMA), which is a characteristic marker for activated fibroblasts, the so-called myofibroblasts, that play a role regarding wound healing [106]. Myofibroblasts are the main regulator of wound repair in response to acute tissue damage and afterwards, the activation state of fibroblasts is reversed or cells are eliminated by apoptosis. Collaborating with immune cells, activated fibroblasts regulate inflammation, angiogenesis and ECM deposition as well as ECM remodelling [102]. However, under chronic inflammation, associated with tumourigenesis [107], fibroblasts conduct tissue fibrosis (desmoplasia) with maintenance of their activated state, also due to epigenetic changes. The tumour tissue is quite alike the desmoplastic tissue, because CAFs recruit immunosuppressive cells and excessively produce ECM components, such as collagen and fibronectin [102]. In TNBC patients, CAFs correlate with poor clinical outcome [105] by supporting tumour growth, metastasis and drug resistance [108]. The tumour promoting role is conducted through their secretome including growth factors, e.g. EGF, TGF- β and VEGF, and cytokines, e.g. IL-6, and IL-8 and ECM components, mainly collagen, and proteases for ECM degradation [99,109,110]. The secretome is a major contributor to TNBC progression by inducing NF κ B and HIF signalling [31,42]. In CAFs, NF κ B is highly activated and maintains pro-tumourigenic features, while targeting NF κ B reverses the CAF state [111]. All in all, targeting pathways, that maintain tumour-promoting features of CAFs, is promising to attenuate tumour aggressiveness.

CAFs are involved in immune evasion and protect tumour cell elimination by creating an immunosuppressive environment (**Figure 1-6**) [112,113]. Through paracrine signalling CAFs [112] as well as TNBC [110] recruit monocytes and polarize macrophage differentiation towards a tumour-promoting type [112], the so-called tumour-associated-macrophages (TAMs), which are the predominant immune cell population within the TME [112]. TAMs can make up to more than 50% of the tumour mass in BC [114] and correlate with poor prognosis in TNBC [110,114]. There are two phenotypes of macrophages, whereas M1-like cells are anti-tumourigenic and M2-like cells release cytokines, growth factors and proteases to support tumour growth, metastasis, angiogenesis as well as tumour cell survival [110]. Therefore, M2-like macrophages are linked to a shorter overall survival [114]. Tumour-promoting features in the inflammatory TME, including cytokine expression by TAMs, including IL-8, rely on NF κ B/p65 mediated transcription [115]. Blockade of NF κ B disrupts the crosstalk of TAMs and TNBC through suppressing cytokines expression, IL-6 and IL-8 [79,116], thereby resulting in suppression of tumour progression [70,111]. Thus, NF κ B is a promising target to decrease tumour-promoting features of TAMs. Both predominant cell types, CAFs and TAMs, promote immune evasion [113,114], TNBC growth, ECM remodelling, metastasis, angiogenesis and chemotherapy resistance

[112,117–119] based on the crosstalk via several growth factors, cytokines and chemokines, including VEGF, IL-6 and IL-8 [120]. These secreted factors are associated with enhanced NFκB signalling [47,121] and further associated with tumour proliferation, migration [120] and invasiveness [99]. Moreover, pathways triggered by growth factors and cytokines converge in NFκB signalling [65], that is a key pathway in mediating drug resistance [61]. NFκB/p65 is important for IL-8-induced Notch1 signalling, which initiates migration and invasion mediated through the bidirectional tumour-stroma crosstalk [115]. Moreover, pro-inflammatory cytokines, such as TNFα and IL-8 are enriched in basal-like BC [65], and blocking cytokine-induced signalling, e.g. IL-8, decreased tumour growth, metastasis [120] and angiogenesis [65].

In conclusion, interfering the bidirectional tumour-stroma communication by blocking cytokine-induced signalling or key pathways for tumour-promoting features of stromal cells, e.g., NFκB, might present a promising approach to combat TNBC.

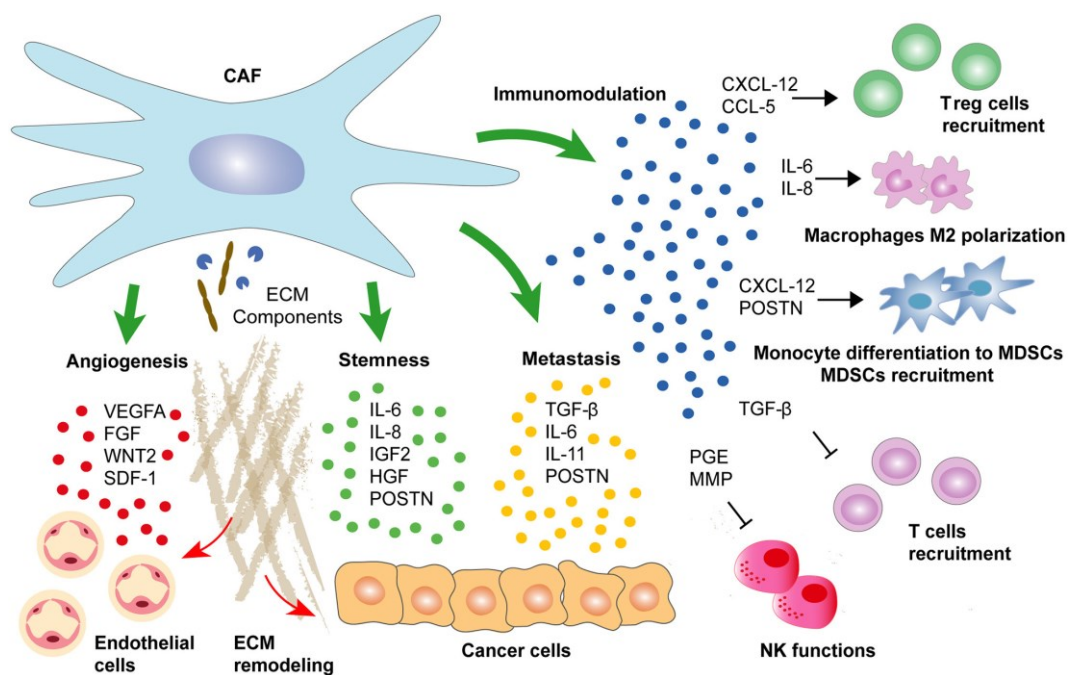


Figure 1-6 Cancer-associated fibroblasts (CAFs) create a tumour promoting niche.

CAF-secreted factors support tumour aggressiveness, including maintenance of the CSC state and initiation of angiogenesis. Through secretion of e.g., lysyl oxidases, collagen and hyaluronic acid, CAFs remodel the ECM, thereby additionally driving tumour progression. Via their secretome, CAFs recruits innate and adaptive immune cells to create an inflammatory and immunosuppressive milieu. In this process, monocytes are differentiated towards a pro-tumourigenic M2-like macrophage type. Among lymphocytes, CAFs enrich the immunosuppressive regulatory T-cells (T reg) and eliminate anti-tumourigenic cytotoxic

T-cells or decrease their activation, also by inhibiting antigen-presenting dendritic cells. Furthermore, anti-tumour potential of NK cells is decreased [113,122]. Illustration from Linares *et al.* (2020) [122].

1.1.4.2 The extracellular matrix (ECM)

Within the TME, CAFs are the main producer of the ECM [123], which is composed of fibrous collagens, glycoproteins, proteoglycans and polysaccharides [124]. Collagens, including the most abundant collagen type I, are the main structural proteins in the ECM of TNBC. CAFs modulate the ECM by production of collagen, altering collagen orientation and produce ECM degrading proteases such as MMP-9 and MMP-13 [99], which results in release of bound growth factors that enhance tumour progression and survival [124]. Especially, linear organisation of collagens provides a route for metastasis in BC, also for co-migration with macrophages, to support the tumour niche formation at distant organs [124]. Metastasis is also facilitated by CAFs-derived growth factor VEGFA, that initiates angiogenesis, but also results in leakiness of the vasculature, thus, enabling tumour cells to escape [99]. The high collagen type I level acts as a physical barrier for nutrient as well as drug exchange and correlates with reduced drug response [33,125]. Indeed, chemotherapy is hampered by the ECM through binding to the ECM itself and thus reducing the concentration of effective drugs. In general, excessive ECM generation increase tissue stiffness [124], and the TNBC tissue was found to be more stiff compared to luminal BC. Tissue stiffness relies on ECM thickening through cross-linking of ECM components, especially collagen by e.g., a lysyl oxidase. Rigidity associates with an invasive character and further enhances infiltration of immunosuppressive cells [126]. Of note, hypoxia within the TME enhances ECM deposition, correlates with tissue fibrosis as well as ECM stiffness and enhances collagen type I secretion from CAFs as well as tumour cells [124].

The mechanical cues in the TME, especially the stiffened ECM [127] and contractile forces, drive and maintain the CAF phenotype [122] as well as BC progression [128]. Further the ECM sustains the CSC character through collagen-induced EMT, which is mediated through NFkB, Wnt or NOTCH signalling [124]. Tissue rigidity is sensed through pathways involved in mechanotransduction, e.g. RhoA [53] and Hippo/LATS [129], which negatively regulates YAP/TAZ [124]. YAP is a transcriptional coactivator, which is linked to paclitaxel resistance [52]. In particular, the stiff tissue induces tumourigenesis in non-tumour cells via YAP [130]. Rigid tissues result in an altered cell morphology and activate gene transcription mediated by e.g. NFkB and YAP1 [131]. Both, NFkB and YAP, share upstream regulators, such as RhoA signalling [132] and are linked to enhanced cell survival [53] and cell migration [48]. In particular, RhoA is also transactivated by e.g. hypoxia (HIF1/2) [88] and inflammation (NFkB and IKKy/NEMO) [133]. In addition to that, hypoxia was also reported to stimulate YAP activity through decreasing Hippo pathway signalling by degradation of

downstream LATS [48]. Increasing relevance for YAP was found in the TME, because YAP/TAZ is highly activated in stromal cells [134], including tumour infiltrated cells [51], and correlates with tumour progression [122] and relapse [52]. YAP produces cytoskeletal regulators to remodel the ECM [135], whereas degradation of the ECM, e.g. the Hippo pathway ligand hyaluronan, further increases YAP activity [136]. Additionally, tissue stiffness triggers YAP signalling, thus establishing a feed-forward loop which maintains the CAF phenotype [49].

Targeting CAFs or key factors that are involved in modulation of the ECM and sensing tissue rigidity, such as NFκB and YAP, are potential targets to prevent drug resistance.

1.2 Screening for novel drug candidates in TNBC therapy

1.2.1 Natural sources for drug discovery

In the last decades natural products gained interest in the cancer research field due to their diverse bioactivities[137]. More than half of the currently used anticancer drugs are either natural products or natural product derivatives as well as synthetic analogues, and several important chemotherapeutic drugs are derived from plants, such as taxanes and their analogues, revealing out the important role of plant-derived natural products for anti-cancer drug discovery [138]. Novel therapy approaches seek for unique options to interfere with molecular processes that correlate with tumour progression. Hence, regarding to targeting inflammation, plant-derived [139] as well as fungus-derived [116] secondary metabolites displayed marked activity to inhibit BC progression by blocking inflammation associated NFκB signalling. The fact, that still some new species and new compounds are discovered [140,141], elevates chances to identify novel treatment regimens for cancer therapy.

1.2.1.1 Plant-derived phenanthroindolizidine alkaloids (P-alkaloids).

Among various natural sources (see **Table S 2**) [142], phenanthroindolizidine alkaloids (P-alkaloids) are derived from the plant *Tylophora* spp., belonging to the family *Apocynaceae*, which are endogenous to (sub-)tropical Africa, Asia and Australia [143,144]. This plant has been used for diverse medicinal purposes and its vernacular names vary within each region. *Tylophora* spp. Is known to be rich with alkaloids, flavonoids and saponins, in addition to steroids, lipids, carbohydrates and other proteins [145]. Among plant-derived secondary metabolites, P-alkaloids were found to possess a broad bioactivity, including anti-tumour potential (**Table S 3**) [146]. These class of compounds are isolated from roots and leaves of *Tylophora* spp. [146], and derivatives isolated since 2000 were previously reported [142]. The morphological characteristics of *Tylophora* spp. are exemplarily shown for *Tylophora lui* (**Figure 1-7**) and detailed description is summarized elsewhere [145,147].

P-alkaloids exhibit anti-cancer potential by blocking proliferation [148], migration [149], inflammation [150,151] as well as angiogenesis [152], and inducing apoptosis [153,154], or reversing drug resistance [154] (**Table S 4**). Regarding BC, tylophorine acts as an anti-proliferative agent in the TNBC cell line MDA-MB-231 (MB-231) and the luminal BC cell line MCF7 as well as T47D [148,155,156], whereas in T47D tylophorine was sufficient to enhance drug sensitivity to doxorubicin [154]. To date, no studies assessed the pharmacological mode of action in TNBC, and hence, we aimed to study the potential of P-alkaloids as novel drug candidates. In this study, six naturally occurring derivatives isolated from the plant *Tylophora ovata* were examined: O-methyltylophorinidine (TYLO-1), tylophorinidine (TYLO-2), tylophoridicine E (TYLO 3), 2-demethoxytylophorine (TYLO-4), tylophoridicine D (TYLO-5) and anhydrodehydrotylophorinidine (TYLO-6). Described bioactivities of these derivatives are summarized in **Table 1-5** and **Figure 1-8** **Table 1-5**. The anti-tumour mechanism of these compounds depends on blocking cell signalling, e.g. NFκB in HepG2 [150] or HIF in T47D [157], and on suppressing DNA replication and protein synthesis [158,159]. To date, their mode of action remains elusive in TNBC. Thus, these derivatives were characterized in TNBC with investigating their mode of action regarding cytotoxicity and blockade of proliferation as well as invasion. To study their pharmacological targets, we investigated the NFκB, HIF and YAP pathway. Additionally, we utilized O-methyltylophorinidine from chemical synthesis (TYLO-1s) for comparison to TYLO-1 and for more in-depth studies.

Table 1-5 Mode of action of P-alkaloid derivatives in cancer

Mode of action or molecular target	Cell type (cell line) and P-alkaloids ¹
Anti-tumour cytotoxicity ²	Prostate [160], hepatocellular (HepG2) [150] and pancreatic cancer (PANC-1) [150,161] by TYLO-1 .
	Rectum adenocarcinoma (HCT-8) [162], hepatocellular (HepG2), pancreatic (PANC-1) [150] and nasopharyngeal (KB) cancer by TYLO-2 .
	Nasopharyngeal (KB), lung (A549) and colorectal (HT-29) [163] cancer by TYLO-3 .
	Lung (A549), colorectal (HT-29) and colon (HCT-116) cancer by synthetically prepared TYLO-3 and TYLO-4 [164].
Blockade of transcriptional activity of AP-1 ³ , CRE ⁴ and NFκB ⁵	Hepatocellular cancer (HepG2) by TYLO-2 [150].
Blockade of transcriptional activity of HIF ^{6,7}	BC (T47D) by TYLO-1 , TYLO-2 , TYLO-3 [157].

Blockade of telomerase activity	Binding to human telomeric DNA and G-quadruplex DNA formation by TYLO-5 and TYLO-6 [165].
Blockade of DNA synthesis	Inhibition of thymidylate synthase in leukaemia (primary leukocytes) by TYLO-2 [166].
Blockade of tumour growth (in vitro)	Growth blockade of 3D co-culture spheroids (PANC-1 and pancreatic CAFs) by TYLO-1 [161].
Blockade of tumour growth (in vivo)	Growth blockade of hepatocellular cancer (HepG2, xenograft model) by TYLO-2 [150]. Growth blockade of murine sarcoma (Meth A) by TYLO-3 [163].

¹ Derivatives are highlighted in bold font. ² TYLO-5 was tested, but showed no cytotoxicity in nasopharyngeal cancer (KB) and rectum adenocarcinoma (HCT-8) [162].

³ Transcriptional activity was induced with forskolin. ⁴ Transcriptional activity was induced with 12-O-tetradecanoylphorbol 13-acetate. ⁵ Transcriptional activity was induced with TNF α . ⁶ Transcriptional activity was induced upon hypoxia (< 1% O₂).

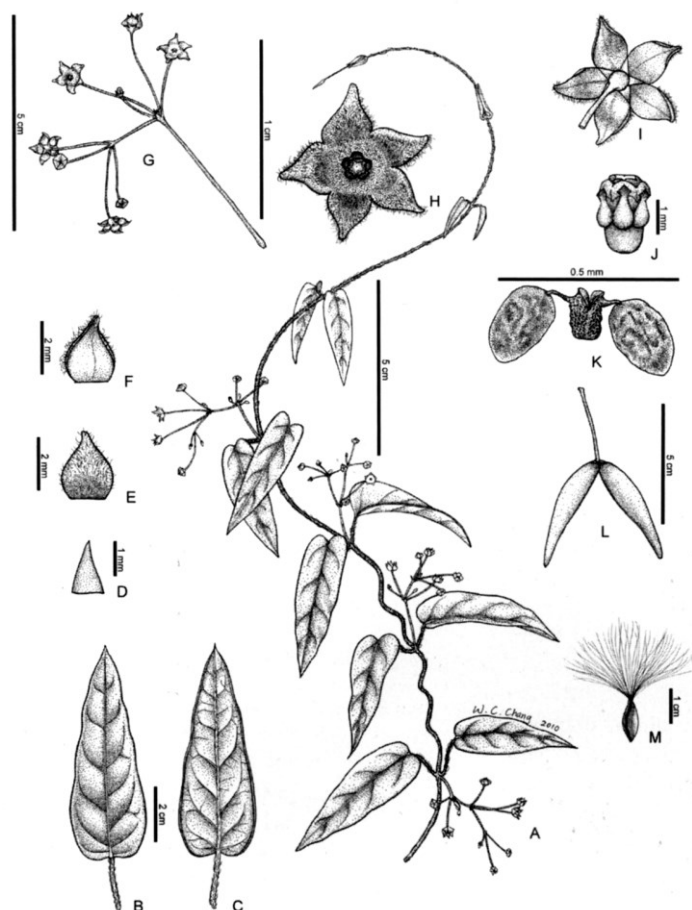


Figure 1-7 Exemplary illustration of the plant family *Tylophora* spp.. Depiction of the holotype of *Tylophora lui*, a new species found in Taiwan, in 2011. A Habit. B Leaf adaxial surface. C Leaf abaxial surface. D Sepal. E Petal inner surface. F Petal outer surface. G Inflorescence. H Flower upper surface. I Flower lower surface. J Gynostegium. K Prollinium. L Fruit. M Seed. Illustration from Tseng and Chao (2011) [140].

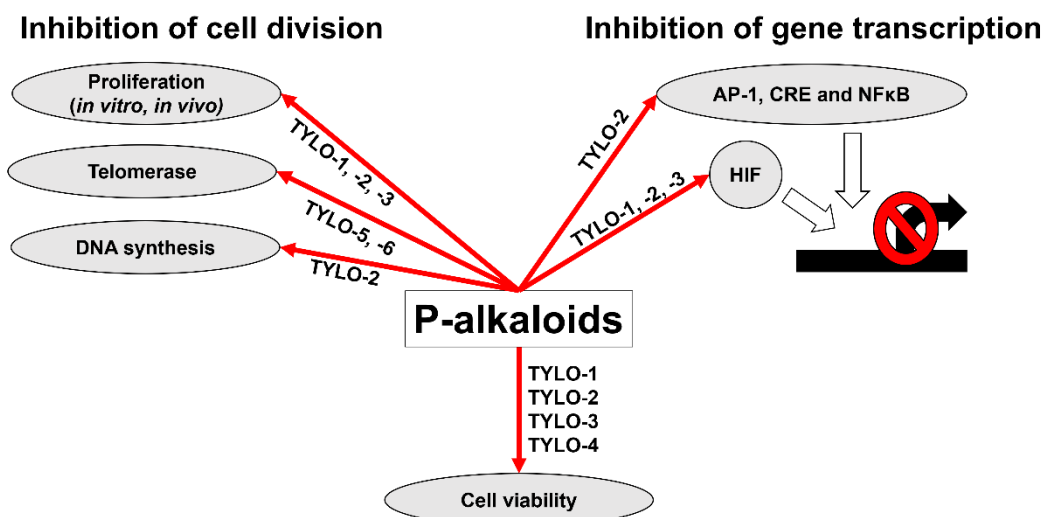


Figure 1-8 Anti-tumour potential of Phenanthroindolizidine alkaloids (P-alkaloids)

P-alkaloids TYLO-1 to TYLO-6 exhibit anti-tumour features through negative regulation (red arrow) of cellular processes [150,157,161–166].

1.2.1.2 Fungal-derived compounds

Kingdom fungi encompasses eucaryotic organisms with estimated 1.5 million species, with only a small number that is identified yet (< 10%). Fungi can be classified into lichenized fungi, macrofungi and microfungi that are found in the soil, sea, and as symbiotic endophytes in plants [167]. Fungal-derived secondary metabolites have various activities, including anti-viral, anti-bacterial [168], and anti-cancer potential, whereas in TNBC fungal metabolites were associated with cytotoxic, anti-inflammatory and anti-migratory features [169,170]. Regarding fungal metabolites, it is known, that transcription of specific gene clusters is usually silenced in fungi, whereby the change in culture conditions promotes accumulation of known or novel compounds [171]. Thus, in this study, we examined fungal substances that were isolated after fermentation on solid rice medium with changing cultivation conditions to alter their metabolites profile. In this study, we investigated azaphilones and polyketides which were isolated from the marine-derived fungus *Aspergillus falconensis*, in addition to studying decahydrofluorenes which were extracted from *Didymella* sp. IEA-3B.1, an endophyte of *Terminalia catappa*.

Hence, after cultivation of *A. falconensis* in sodium chloride-based medium, azaphilone derivatives were isolated including four known azaphilones (falconensins A, M, N, H) and one novel compound (falconensin O). When replacing sodium chloride with sodium bromide, resulted in isolation of falconensin I alongside with three novel azaphilones (falconensin Q, R, S). Meanwhile, when exchanging sodium chloride with ammonium sulfate, this resulted in isolation of two known polyketides, namely, sulochrin and monochlorsulochrin. Both compounds were not naturally accumulated in sodium chloride-

based culture. Azaphilones were described as anti-inflammatory compounds with blocking NF κ B-inhibition and migration in TNBC [170]. Thus, we characterized nine azaphilones in TNBC with evaluating their anti-inflammatory potential. Polyketides are described as anti-cancer agents in various cancer types including the anti-proliferative properties in TNBC [172]. Docking studies for sulochrin and monochlorsulochrin revealed blockade of matrix metalloproteases (MMP)-13, which are associated with an invasive behaviour [141]. Thus, we characterized these two polyketides regarding their anti-migratory potential in TNBC. In addition, when *Didymella* sp. IEA-3B.1 was cultivated in sodium chloride-based medium, compounds of the class decahydrofluorene were isolated including two known metabolites, ascomylactam C and phomapyrrolidone A, and one novel metabolite, didymellanosine. Anti-tumour potential was reported for ascomylactam C and phomapyrrolidone A in various cancer types including TNBC [169]. Thus, decahydrofluorenes were characterized in TNBC with regard to their anti-inflammatory capacity.

1.2.2 Current preclinical models for drug screening regarding therapy of solid tumours

Only 10% of drugs that were tested in preclinical studies were also successful in clinical trials with showing no cytotoxicity [173]. Drug failure relies on the limited predictability of preclinical models that do not or in a limited manner reflect *in vivo* conditions of cancer diseases [27]. Current preclinical models present partially controversial limitations and benefits (**Table 1-6**) [83,174,175].

For initial drug screening, an adherent monolayer of cells, also referred to as two-dimensional (D) culture, presents a convenient model for high-throughput screening (HTS) due to its reproducibility and low cost [83]. However, drugs tested in 2D cultures are mostly overestimated regarding their anti-cancer potential and fail *in vivo* due to excessive toxicity and their side effect profile [173]. A major drawback of 2D cultures is the accumulation of genetic and epigenetic changes during subculture, so that the tumour cells used for examinations differ from the original state of the primary tumour [27], especially regarding CSC features and drug resistance [174]. Because 2D cultures lack *in vivo* conditions [83], such as the vasculature [176] and TME [109], animal models are beneficial to estimate drug efficacy regarding tumour growth, metastasis and drug resistance [174].

Due to ethical reasons, mice models are more accepted in research than companion animals, despite higher genetic similarity to humans. Syngeneic mice are advantageous due to a competent immune system, however, spontaneous tumourigenesis caused by genetic modification or carcinogen exposure may extend the period of establishing the model and also impacts the time for drug studies [175].

Besides the impact of the TME [113], heterogeneity displayed within the distinct molecular TNBC subtypes [20,22], including various proportion of CSC [36], is a major factor that determines drug response. To individually test drugs, patient-derived xenograft mouse models serve as a suitable model to mimic the complex tumour TME with maintaining the tumour's original chemosensitivity, epigenetic, and molecular changes and is engrafted including the ECM at its original architecture [27]. Giving the fact, that TNBC has a higher rate of metastasis, it is important to screen drugs, that may be investigated in a complete organism and an intact blood brain barrier [21]. However, immune cells, that regulate tumour progression [109] are compromised and thus, this model is not meeting all conditions that impact chemosensitivity [135]. Mice are not suitable as a model for HTS [177] and the main disadvantages for *in vivo* drug screening are high costs and the long duration until receiving the experimental results [83]. Notably, the injection of tumour cells into the animal model displays a decisive variable to impact tumour engraftment and growth [178]. Although xenograft models meet most physiological conditions of a cancer patient, differences in species (mouse vs. human) may influence drug efficacy [83] and may further explain that some patient-derived tumour cells will not engraft in mice models [174]. Remarkably, 85% of all drugs loose efficacy in translation from animal models to clinical trials [177]. Most unfortunate, anti-cancer potential of drugs may even be underestimated in mice models due to a modest drug response *in vitro* [179], thus, some agents may not be considered for *in vivo* examinations and overlooked as a therapeutic option. To sum it up, due to all these limitations, mice models do not fully predict efficacy in clinical trials.

Preclinical models, that may overcome some limitations of 2D cultures or animal models, are 3D *in vitro* models. In particular, spheroids resemble solid tumours with gradients in nutrients and oxygen that impact the metabolism, induce proliferation, and drug resistance. They are advantageous in HTS by including the heterogenic cell and ECM compositions, that reconstitute spatial interactions of cell-cell as well as cell-ECM and further drive tumour aggressiveness [83]. In TNBC, spheroids mimicking microtumour characteristics have higher migratory as well as invasive behaviour, and exhibit enhanced resistance to chemotherapeutics, e.g. doxorubicin, when compared to 2D monolayer cells [180]. It is well-known, that the drug efficacy differs in a monolayer of cells compared to the respective 3D biology [100,101], and drug response in 3D can be studied within less than 7 days regarding tumour growth or invasiveness [79,161,181].

In conclusion, 3D spheroids serve as a predictable model for HTS to identify novel drug candidates in cancer therapy. The advantages of this model include mimicking the cellular organisation of tumours and mimicking the characteristic interactions within the TME.

Table 1-6 Features of preclinical models for drug screening



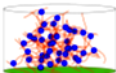
Preclinical model	Advantages	Disadvantages
<p>2D models</p> 	<ul style="list-style-type: none"> • Quick and simple model for examinations • Relatively cost-effective 	<ul style="list-style-type: none"> • Unable to recapitulate complex TME interactions, including tumour cell-ECM, angiogenesis • Cell cycle, growth rate and gene expression profile differ from <i>in vivo</i> tumours
<p>Animal models</p> 	<ul style="list-style-type: none"> • Physiologically intact model <ul style="list-style-type: none"> ○ Partially, intact immune system ○ Similar mammary environment ○ Realistic nutrient delivery and waste removal systems 	<ul style="list-style-type: none"> • Ethical questionable • High costs • Low biochemical control • Does not mimic the human organism
<p>3D models</p> 	<ul style="list-style-type: none"> • Physiologically intact model <ul style="list-style-type: none"> ○ Morphology ○ Intratumoural gradients of nutrients and drugs ○ Growth rate • Cost-effective compared to animal models • Easily and highly tailorable 	<ul style="list-style-type: none"> • No standardised established methods for 3D model generation and data interpretation • Compared to 2D models <ul style="list-style-type: none"> ○ Lower reproducibility ○ Slower throughput

Table content was adapted with minor modifications from Clegg *et al.* (2020) [182], including additional information from [173,183].

1.3 Aims of the studies

To characterize the anti-tumour potential of P-alkaloids in TNBC

1. To identify a SAR for P-alkaloids, including TYLO-1 to TYLO-6, regarding their anti-inflammatory effects and cytotoxicity in 2D cultures as well as 3D models
2. To verify the biological activity of the chemically prepared TYLO-1s regarding NFκB-inhibition and reduced cell viability in 2D cultures as well as 3D models
3. To investigate the anti-inflammatory potential of TYLO-1s under hypoxia and to determine the molecular target for NFκB inhibition as well as to evaluate effects on HIF-mediated transcription
4. To examine the effects of TYLO-1 on the mechanosensing pathway YAP
5. To explore the crosstalk between NFκB and HIF as well as NFκB and YAP for the bioactivity of TYLO-1 or TYLO-1s
6. To assess the mechanism of action for anti-proliferative effects of TYLO-1s under normoxic as well as hypoxia-simulated conditions
7. To elucidate the effect of TYLO-1 on the bidirectional communication between TNBC and PBMCs via NFκB-regulated cytokines, explored in a direct 2D co-culture
8. To establish a simplified preclinical *in vitro* 3D model encompassing TNBC cancer cells, ECM (type I collagen), and primary murine CAFs to mimic the human TNBC TME suitable for HTS assays
9. To examine TYLO-1/TYLO-1s regarding tumour progression, including growth or invasion, in a 3D TNBC monoculture model, grown in matrigel®, and 3D TNBC co-culture model, grown in collagen type I

To characterize the anti-tumour potential of fungus-derived metabolites in TNBC

1. To evaluate anti-inflammatory potential of azaphilones isolated from the marine-derived fungus *Aspergillus falconensis*.
2. To assess anti-migratory effects of polyketides isolated from the marine-derived fungus *Aspergillus falconensis*.
3. To investigate anti-inflammatory features of decahydrofluorenes isolated from the endophytic fungus *Didymella* sp. IEA-3B.1.

To characterize the anti-tumour potential of synthetically engineered HDACIs in TNBC

1. To examine TNBC cell viability in response to chemically synthesized HDACIs

2 Materials and methods

2.1 Commercial consumables

Name and location of vendors providing commercial materials are listed in **Table 2-1**.

Table 2-1 Vendors and their locations

Vendor	City/state	Country
Alfa Aesar	Kandel	Germany
Analytik Jena	Jena	Germany
ATCC, American Type Culture Collection	Virginia	USA
Beckmann Coulter	Krefeld	Germany
BioCat	Heidelberg	Germany
Bio-Rad	Düsseldorf	Germany
Roth	Karlsruhe	Germany
Cell Signalling	Leiden	Netherlands
Cenibra	Bramsche	Germany
Corning	Taufkirchen	Germany
ECACC, European Collection of Authenticated Cell Cultures	Salisbury	UK
Eurofins	Ebersberg	Germany
Fisher scientific	Schwerte	Germany
GSL Biotech LLC	San Diego/CA	USA
Greiner; greiner bio-one	Frickenhausen	Germany
GraphPad Software, Inc	California	USA
Hecht-Assistent	Sondheim vor der Rhön	Germany
Hitec Zang	Herzogenrath	Germany
Hycultec	Beutelsbach	Germany
Ibidi GmbH	Gräfelfing	Germany
Lonza	Cologne	Germany
Luminex	MV 's-Hertogenbosch	The Netherlands
Memmert	Büchenbach	Germany
Merck	Darmstadt	Germany
Neolab	Heidelberg	Germany
Olympus	Hamburg	Germany
Peprotech	Hamburg	Germany
PerkinElmer Informatics	Hamburg	Germany
Peqlab, Life Science	Hannover	Germany

Promega	Mannheim	Germany
Qiagen	Hilden	Germany
R&D Systems	Wiesbaden	Germany
Scbt, Santa-Cruz Biotechnology	Heidelberg	Germany
Selleckchem	München	Germany
Sigma; Sigma-Aldrich	Taufkirchen	Germany
Signosis	Santa Clara, CA	USA
STARLAB	Hamburg	Germany
STEMCELL Technologies	Köln	Germany
TECAN	Männedorf	Swiss
Teqler	Wecker	Luxembourg
Thermo Fisher Scientific	Darmstadt	Germany
Yokogawa	Wehr	Germany
VWR	Langenfeld	Germany
Vilber	Eberhardzell	Germany
Zeiss	Oberkochen	Germany

2.1.1 Disposable materials

Pipette tips, reaction tubes, serological pipettes and cell culture flasks were provided by STARLAB, Sarstedt or Greiner. Further disposable materials are listed in **Table 2-2**. Disposable cell plates are listed in **Table 2-3**. Re-used materials are listed in ¹ Plate is closed with microseal B PCR plate sealing film (Bio-Rad, #MSB-1001).

Table 2-4.

Table 2-2 Disposable consumables

Material	Vendor	Catalogue number (cat#)
Plastic pasteur pipette	VWR	612-1685
2-well insert	Ibidi	80209
Cell scraper	Sarstedt	83.1832
Cryo vials, Nalgene™ (1.5 ml)	Thermo Fisher Scientific	5000-1012
Counting slides for LUNA II™	BioCat -Logos Biosystems	L12001
Nitrocellulose membrane (0.45 µm)	Merck	GE10600002
	Roth	4675.1
Aseptic filter (0.2 µm)	VWR	514-0073
Precast 12% polyacrylamide gel	Bio-Rad	456-1044
Syringe, 2 ml	Teqler	T135707
Blot filter paper (extra thick)	Bio-Rad	1703968

Table 2-3 Disposable plates used for cell seeding, compound dilution and qPCR

Wells	Characteristics	Vendor	Cat#
6	Transparent	Sarstedt	83.3920.005
		Greiner	657160
24	Transparent	Sarstedt	6020811
		Falcon	353047
		Greiner	662160
24	Black	Ibidi	82426
96	Non-sterile	Thermo Fisher Scientific	(plate frame) 437591
			(well inserts) 469914
96	Transparent qPCR plates ¹	Bio-Rad	MLL 9601
96	Transparent, V-bottom	Greiner	651161
		Sarstedt	83.3926
96	Transparent	Corning	353072
		Greiner	655180
96	White	Greiner	655098
96	Black	Greiner	655090
96	Black, square wells	Ibidi	89626
96	U-bottom, cell repellent	Corning	4515
		Greiner	650970
		Cenibra	ULA-96U
		Thermo Fisher Scientific	174925
384	White, opaque bottom	Greiner	781080
384	White, µclear bottom	Greiner	781098

¹ Plate is closed with microseal B PCR plate sealing film (Bio-Rad, #MSB-1001).

Table 2-4 Re-used materials

Characteristics	Vendor	Cat#	Application/Experiment
Freezing container		CellCamper® Mini	Long-term cell storage
Hemocytometer	Hecht-Assistent	40441	Cell counting
Axygen™ high profile; 96 bottom troughs“	Fisher Scientific	11380275	Reservoir for cell suspension; cell seeding with the pipette robot CyBio® well vario
Axygen™ high profile; 4-well	Fisher Scientific	12537867	Reservoir for cell suspension; seeding with the multi-channel pipette
Axygen™ low profile; 8-well	Fisher Scientific	11350265	Reservoir for cell suspension; seeding with the multi-channel pipette

2-Well insert	Ibidi	80209	2D wound healing assay
---------------	-------	-------	------------------------

2.1.2 Chemicals and Kits

Chemical agents, enzymes and cytokines are listed in **Table 2-5**. Commercial kits are listed in **Table 2-6**.

Table 2-5 List of chemical agents, cytokines, and enzymes

Chemical	Vendor	Cat#
BSA, bovine serum albumin	Roth	8076.2
BA, Benzyl alcohol	Alfa Aesar	L03258
BB, Benzyl benzoate	Alfa Aesar	L03292
Bromphenol blue	Roth	A512.1
Crystal violet	Sigma-Aldrich	C0775-25G
CoCl ₂ , cobalt (II) chloride	Sigma-Aldrich	C8661
DMSO, dimethyl sulfoxide	Sigma-Aldrich	67-68-5
EDTA, ethylenediaminetetraacetic acid	Roth	3053.1
Endotoxin free water	Sigma-Aldrich	TMS-011-A
Glycerol	Roth	3783.5
Glycine	Roth	HN07.2
LPS, Lipopolysaccharide extracted from E.Coli O111:B4; finally dissolved in endotoxin free water	Sigma-Aldrich	L2630
2-Mercaptoethanol	Roth	4227.3
Methanol	Roth	8388.6
PFA, paraformaldehyde	Sigma-Aldrich	0335.2
PBS, sterile, one-fold concentrated (1×) Dulbecco's Phosphate - Buffered Saline	Pan Biotech	P04-36500
Propium iodide (PI)	Sigma-Aldrich	4864
Protease inhibitor; Pierce ®	Thermo Fisher Scientific	A32955
Protease inhibitor; PMSF, phenylmethanesulfonyl fluoride	Sigma-Aldrich	P7626
Protein ladder; Precision Plus Protein™ Dual Colour Standards	Bio-Rad	1610374
PVP, polyvinylpyrrolidone	Sigma-Aldrich	P0930

RNase A	Thermo Fisher Scientific	EN0531
Sodium chloride	Roth	3957.1
SDS, sodium dodecyl sulfate	Roth	CN30.1
Sodium-deoxycholate	Sigma-Aldrich	D6750
TNF α , tumour necrose factor alpha (α); dissolved in endotoxin free water	Peprotech	300-01A
Tris	Roth	A411.4
Tris-HCl	Roth	9090.2
Triton® X-100	Sigma-Aldrich	X-100
Tween® 20	Roth	9127.1
U0126	Selleckchem	S1102

Table 2-6 List of kits and reagents

Kit/reagent	Vendor	Cat#	Experiment
Bradford reagent; Coomassie protein assay	Thermo Fisher Scientific	1856209	Western blot
3D CellTiterGlo Assay	Promega	G9682	3D cell viability
CDNA Synthese Kit	Bio-Rad	1708891	RT-qPCR, cDNA synthesis
CellTiter-Glo®, Luminescent Cell Viability Assay	Promega	G7570	2D cell viability
Chemiluminescent-substrate; SuperSignal™ West Pico PLUS	Thermo Fisher Scientific	34577	Western blot
IQ™ SYBR® Green Supermix	Bio-Rad	1708880	Gene expression; 2D co-culture
ITaq™ SYBR® Green Supermix	Bio-Rad	1725121	Gene expression in MB-231
Nano-Glo® Luciferase Assay System	Promega	N1110	NF κ B-inhibition (2 h)
Lipofectamine™ 3000	Thermo Fisher Scientific	L3000008	Knockdown studies
Luciferase Assay System	Promega	E1500	NF κ B-inhibition (24 h)
Luminex MAGPIX calibration Kit	Merck	MPX-CAL-K25, MPX-PVER-K25	IL-8 secretion
MILLIPLEX MAP Human Cytokine/Chemokine Magnetic Bead Panel	Merck	Merck HCYTOMAG-60K	IL-8 secretion

PrestoBlue	A13262	A13262	2D cell viability
ReliaPrep™ RNA Miniprep	Promega	Z6011	RT-qPCR, RNA isolation
RNeasy® Mini Kit	Qiagen	74104	

2.1.3 Primer and siRNA

All primer used for qPCR studies were purchased from Eurofins. Forward (fw) as well reverse (rev) primer sequences are listed in **Table 2-7**. Small interfering RNAs (siRNAs) used for knockdown studies are listed in **Table 2-8**.

Table 2-7 Forward and reverse primer sequence

Target gene ¹	DNA sequence of the primer
GAPDH fw	5'-TGCACCACCAACTGCTTAGC-3'
GAPDH rev	5'-GGCATGGACTGTGGTCATGAG-3'
IL-6 fw	5'-GGCACTGGCAGAAAACAACC-3'
IL-6 rev	5'-GCAAGTCTCCTCATTGAATCC-3'
IL-8 fw	5'-ACTGAGAGTGATTGAGAGTGGAC-3'
IL-8 rev	5'-AACCTCTGCACCCAGTTTTTC-3'
P65 fw	5'-CCCACGAGCTTGTAGGAAAGG-3'
P65 rev	5'-GGATTCCCAGGTTCTGGAAAC-3'
YAP fw	5'-CCTTCTTCAAGCCGCGGAG-3'
YAP rev	5'-CAGTGTCCCAGGAGAAACAGC-3'

1 Fw: forward. Rev: reverse.

Table 2-8 SiRNA and their targets

SiRNA	Target mRNA	Vendor	Cat#	Stock concentration [micromolar, μM]	Final application
Silencer Select, Negative Control No. 2	Unspecific (NCsiRNA)	Thermo Fisher Scientific	4390846	10 μM (134 ng/ μl)	80 nM
Sip65	P65	Scbt	sc-29410	10 μM (30 ng/ μl) ¹	30 nM
SiYAP	YAP	Scbt	sc-38637	10 μM (130 ng/ μl) ¹	80 nM

¹ RNA concentration of the solutions was measured using the spectrophotometer NanoDrop™ Lite.

2.1.4 Antibodies

Primary and species secondary antibodies used for western blot studies are listed in **Table 2-9**. Primary and species-specific secondary antibodies used for 2D and 3D immunostaining are listed in **Table 2-10** and **Table 2-11**, respectively.

Table 2-9 List of antibodies used in western blot studies

Antigen	Origin	Isotype	Vendor, cat#	Conjugate	Application
I κ B α	Rabbit	IgG	Cell Signalling, #9242	/	1:1000
Vinculin	Rabbit	IgG	Cell Signalling, #13901	/	1:1000
Rabbit IgG (H+L)	Goat	IgG	Thermo Fisher Scientific, #31460	Horseradish peroxidase (HRP)	1:5000

Table 2-10 List of primary antibodies used for immunofluorescence studies

Antigen	Origin (Clone#)	Isotype	Vendor, cat#	Concentration	Application
Ki67	Rabbit, monoclonal (1297A)	IgG	R&D, MAB7617	0.5 mg/mL	1.6:100
P53	Goat, polyclonal	IgG	R&D, AF1355	0.2 mg/mL	4:100
α SMA	Mouse, monoclonal (1A4)	IgG2	Sigma-Aldrich, A5228	2 mg/mL	0.4:100
YAP	Mouse, monoclonal	IgG2	Scbt, Sc-101199	100 $\mu\text{g}/\text{ml}$	1:100

Table 2-11 List of secondary antibodies and DNA staining dye used for immunofluorescence studies

Antigen	Origin	Isotype	Vendor, cat#	Conjugate or excitation wavelength (exλ)	Application ¹
Mouse IgG (H+L)	Donkey, polyclonal	IgG	Thermo Fisher Scientific, #A31571	Alexa Fluor® (AF)647	1:200
Goat IgG (H+L)	Donkey, polyclonal	IgG	Thermo Fisher Scientific, #A-11055	AF488	1:200
Rabbit IgG (H+L)	Donkey, polyclonal	IgG	Thermo Fisher Scientific, #A10040	AF546	1:200
DAPI, 4',6 diamidino-2-phenylindole dihydrochloride	/	/	Sigma-Aldrich, #D9542	DAPI, exλ at 340 nm; DAPI-DNA complex, exλ at 364 nm	1:500

¹ Antibodies were dissolved in PBS. DAPI was dissolved in ddH₂O at 1 mg/ml.

2.2 Compounds

2.2.1 Commercial compounds

Commercial compounds are listed in **Table 2-12**.

The NFκB-inhibitor BAY 11-7085 prevents release of NFκB/RelA/p65 by stabilizing its inhibitor IκBα [184]. Consequentially, gene expression under NFκB is blocked, which may induce arrest during cell division at the G0/G1 phase or apoptosis [185]. Molecule structure is depicted in **Figure 2-1**.

The antimitotic agent paclitaxel (tradename: Taxol®) belongs the group of taxanes. It prevents depolymerization of microtubules at the G2/M phase during cell division by binding and stabilizing the β-tubulins, thereby, resulting in apoptosis [186]. Paclitaxel is applied in systemic chemotherapy for TNBC [7]. Molecule structure is depicted in **Figure 2-2**.

The cytotoxic agent staurosporine induces apoptosis through inhibition of phospholipid/calcium-dependent protein kinases. Molecule structure is depicted in **Figure 2-3**.

Table 2-12 Commercial compounds

Compound (CAS ¹, MW)	Vendor	Cat#	Experiment
BAY 11-7085 (196309-76-9, 249.33 g/mol)	Hycultec	HY-10257	Positive control for NFκB inhibition
Paclitaxel, Taxol® (33069-62-4, 853.9 g/mol)	Scbt	sc-201439	Positive control for cytostatic /anti- proliferative effects
Staurosporine (62996-74-1; 466.5 g/mol)	Sigma-Aldrich	569397	Positive control for cytostatic effects

¹ Chemical Abstracts Service Registry Number (CAS) . ² Molecular weight (MW) .

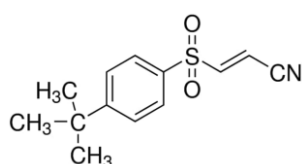


Figure 2-1 Chemical structure of BAY 11-7085. Illustration from Sigma-Aldrich (cat# B5681).

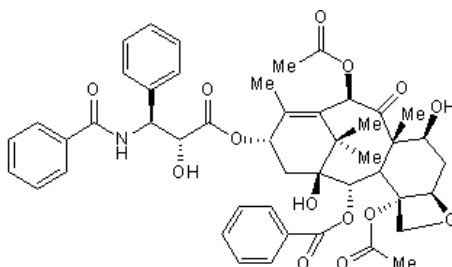


Figure 2-2 Chemical structure of paclitaxel. Illustration from R&D (cat#1097/10).

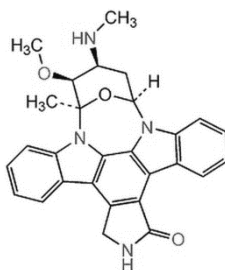


Figure 2-3 Chemical structure of staurosporine. Illustration from Sigma-Aldrich (cat#569397).

2.2.2 Natural products isolated from the plant *Tylophora ovata*

Plant-derived phenanthroindolizidine alkaloids (P-alkaloids) were kindly provided by Haiqian Yu (Institute of Pharmaceutical Biology and Biotechnology, Heinrich Heine University, 40225 Düsseldorf, Germany). The following derivatives were extracted from the plant *Tylophora ovata* (*T. ovata*): O-methyltylophorinidine (TYLO-1), tylophorinidine (TYLO-2), tylophoridicine E (TYLO 3), 2-demethoxytylophorine (TYLO-4), tylophoridicine D (TYLO-5) and anhydrodehydrotylophorinidine (TYLO-6). Compound isolation is described in our previous work [187]. The chemical structures of the compounds are depicted in **Figure 2-4** and their molecular weight is listed in **Table 2-13**.

Table 2-13 Phenanthroindolizidine alkaloids (P-alkaloids) with their internal code and molecular weight

Internal code	Compound	Molecular weight [g/mol]
TYLO-1	O-Methyltylophorinidine	379
TYLO-2	Tylophorinidine	365
TYLO-3	Tylophoridicine E	365
TYLO-4	2-Demethoxytylophorine	363
TYLO-5	Tylophoridicine D	360
TYLO-6	Anhydrodehydrotylophorinidine	346

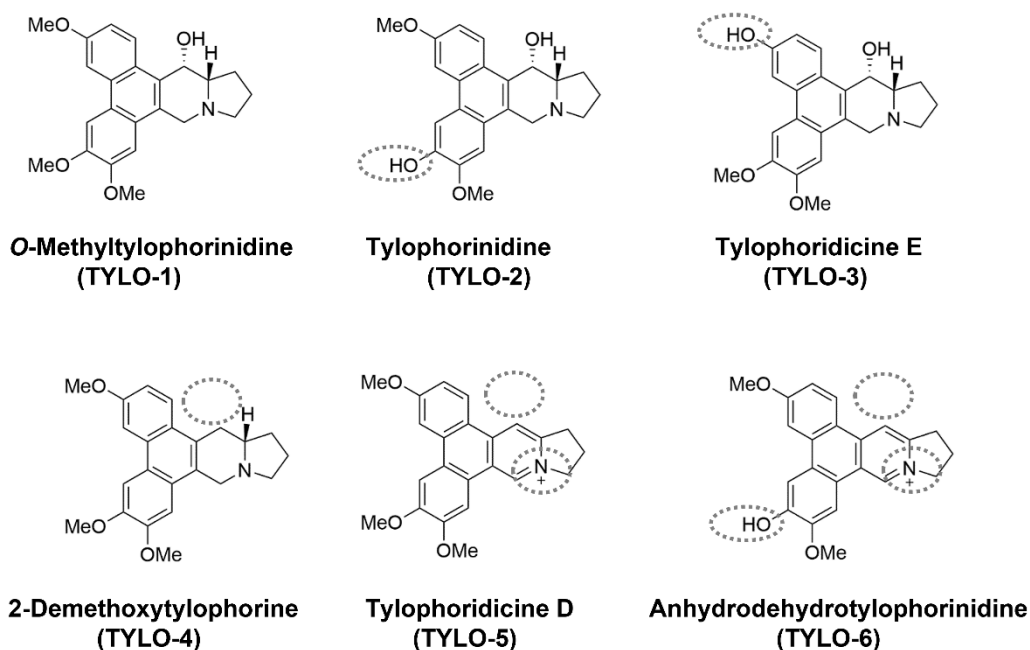


Figure 2-4 Chemical structure of P-alkaloids isolated from *Tylophora ovata*.

O-Methyltylophorinidine (TYLO-1) and its natural occurring derivatives, namely

tylophorinidine (TYLO-2), tylophoridicine E (TYLO-3), 2-demethoxytylophorine (TYLO-4), tylophoridicine D (TYLO-5), anhydrodehydrotylophorinidine (TYLO-6) are depicted with highlighting the distinct characteristics (grey dotted circles) compared to TYLO-1. Molecule structures were illustrated with ChemDraw.

2.2.3 Natural products isolated from fungi

Fungus-derived azaphilones and fungus-derived polyketides were kindly provided by Dina H. El-Kashef (Institute of Pharmaceutical Biology and Biotechnology, Heinrich-Heine-University Düsseldorf, 40225 Düsseldorf, Germany). Both, azaphilones [171] and polyketides [141], were isolated from the marine-derived fungus *Aspergillus falconensis* (*A. falconensis*) as described. Belonging to the polyketides, sulochrin and monochlorsulochrin were isolated. Chemical structures of polyketides are depicted in **Figure 2-5**. Amongst the azaphilones, falconensin A, H, I, M, N, O, Q, R and S were isolated. Chemical structures of the obtained azaphilones are depicted in **Figure 2-6**.

Fungus-derived decahydrofluorenes were kindly provided by Ni P. Ariantari (Institute of Pharmaceutical Biology and Biotechnology, Heinrich Heine University, Düsseldorf, 40225 Düsseldorf, Germany; Department of Pharmacy, Faculty of Mathematics and Natural Sciences, Udayana University, 80361 Bali, Indonesia). Decahydrofluorenes were extracted from the fungus *Didymella* sp. as described [168]. Within the decahydrofluorenes, didymellanosine, ascomylactam C and phomapyrrolidone A were isolated. Chemical structures are depicted in **Figure 2-7**.

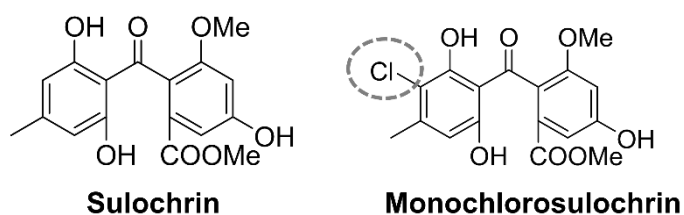


Figure 2-5 Chemical structures of polyketides isolated from the fungus *Aspergillus falconensis*. Sulochrin and Monochlorsulochrin are depicted with highlighting differences in structure (grey dotted circles). Illustration was adapted from El-Kashef *et al.* (2020) [141].

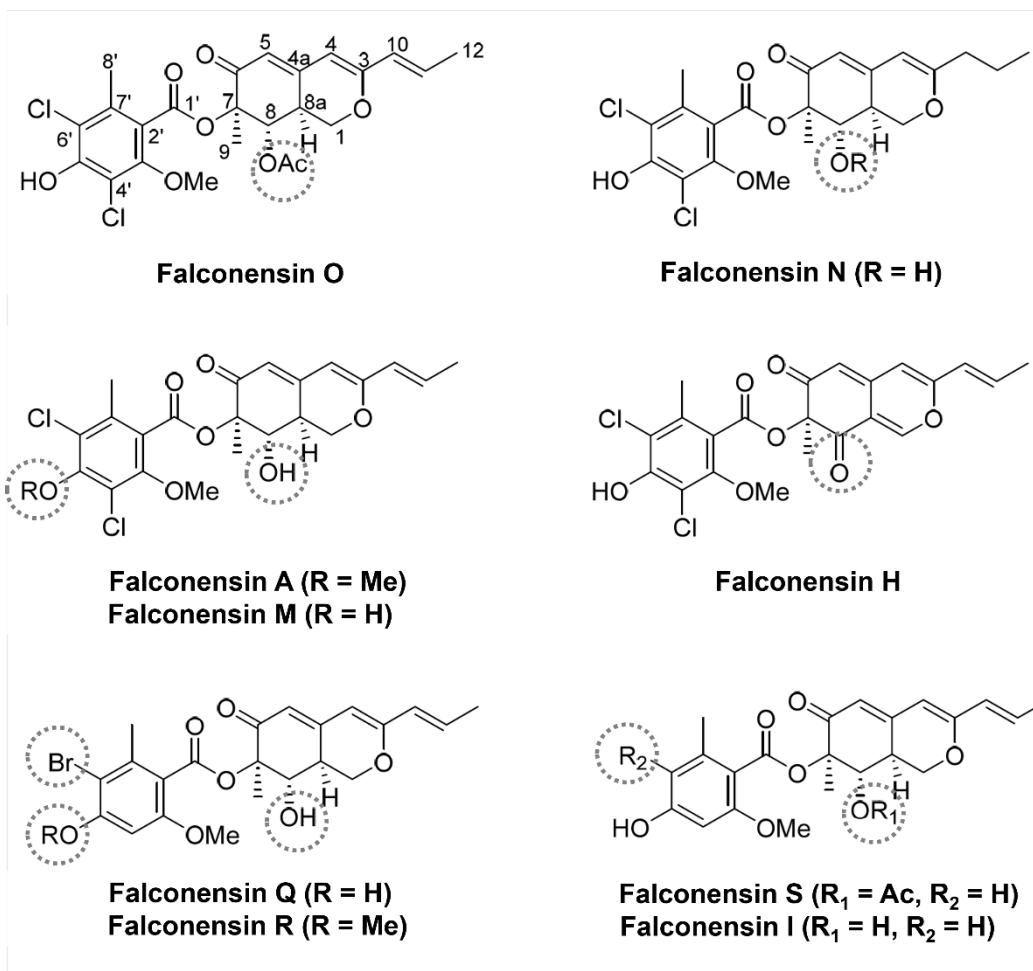


Figure 2-6 Chemical structures of azaphilones isolated from the fungus *Aspergillus falconensis*. Azaphilone derivatives are depicted with highlighting differences in structure (grey dotted circles): Falconensin A, H, I, M, N, O, Q, R and S. Adapted from El-Kashef *et al.* (2020) [171].

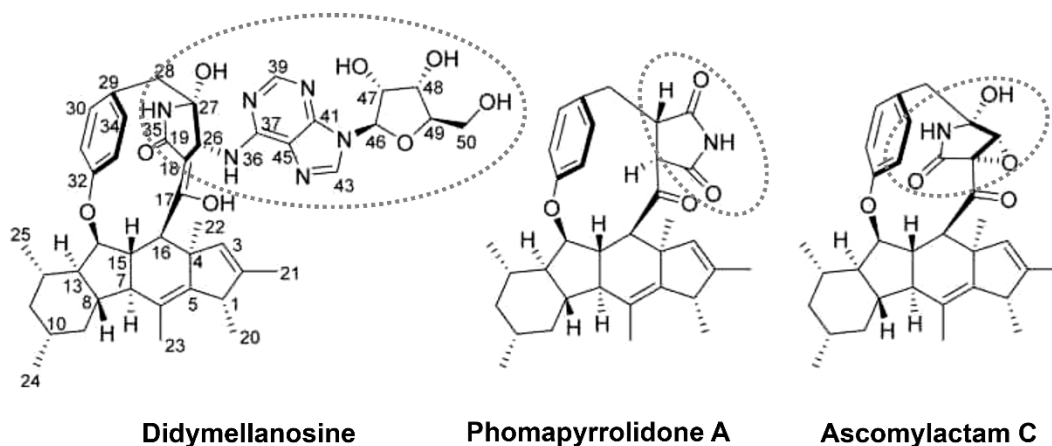


Figure 2-7 Chemical structures of decahydrofluorenes isolated from the fungus *Didymella sp.* Decahydrofluorene derivatives are depicted with highlighting differences in their structure (grey dotted circles): Illustration was adapted from Ariantari *et al.* (2020) [168].

2.2.4 Chemically synthesized compounds

Additionally, a chemically prepared O-methyltylophorinidine (TYLO-1s) was kindly provided by Kay Merkens (Department of Chemistry, University of Cologne, 50923 Cologne, Germany). Chemical synthesis is described in our previous work [187].

Synthetically prepared HDACIs were kindly provided by research group of Prof. Dr. Thomas Kurz (Institute of Pharmaceutical and Medicinal Heinrich Heine University, Düsseldorf, 40225 Düsseldorf, Germany): LAK41, LAK107, LAK110, LAK121, LAK-ZnFD, KSK64, KSK75 and MPK265. To date, solely the chemical preparation for LAK41 [188] and KSK64 [189] is published and both compounds were characterized as class I/IIb inhibitors. The molecular weight and pharmacologically proven targets for HDACI are listed in **Table 2-14**. Chemical structures of the HDACI are depicted in **Figure 2-8**.

Table 2-14 Molecular weight and target proteins of histone deacetylase inhibitors (HDACIs)

HDACI	Molecular weight [g/mol]	Proven targets of inhibition ¹ (Average IC ₅₀ ²)
LAK41	317.14	HDAC1 (37 nM), HDAC2 (92 nM), HDAC6 (173 nM), HDAC8 (9.8 µM); but not HDAC4 (>100 µM)
LAK107	449.07	HDAC3 (no concentration provided)
LAK110	544.09	HDAC1-2 (no concentration provided)
LAK121	431.02	HDAC1-3 (no concentration provided)
LAK- ZnFD	232.08	ZnFD from HDAC6 (2 µM)
KSK64	406.34	HDAC1 (43 nM), HDAC6 (3 nM), HDAC8 (1.5 µM); but not HDAC4 (>100 µM)
KSK75	354.02	HDAC6 (5 µM), HDAC8 (630 nM); but not HDAC1 (>100 µM)
MPK265	343.15	HDAC1 (742 nM), HDAC2 (1.4 µM), HDAC3 (900 nM), HDAC6 (20 nM)

¹ Data provided by Prof. Dr Matthias Kassack (Institute of Pharmaceutical and Medicinal Heinrich Heine University, Düsseldorf, 40225 Düsseldorf, Germany).

² IC₅₀: half maximal inhibitory concentration.

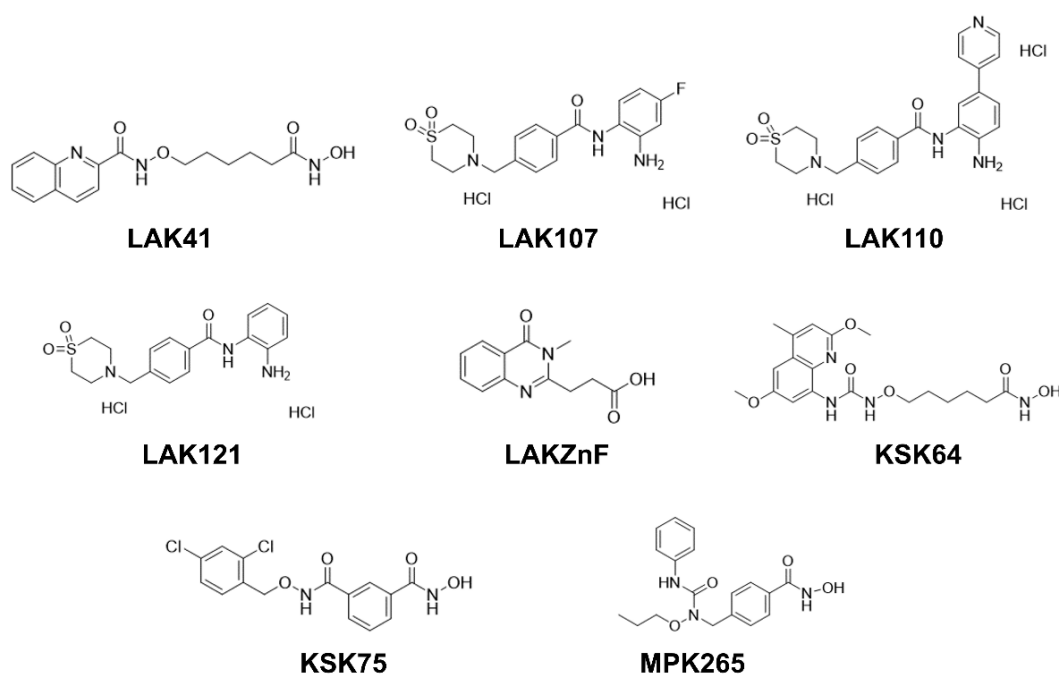


Figure 2-8 Chemical structures of the histone deacetylase inhibitors (HDACIs).
Molecule structures were illustrated with ChemDraw.

2.2.5 Dilution of lyophilized compounds

All compounds were dissolved at 10 mM using DMSO and stored at -20 °C. Further dilutions were conducted in the culture medium according to the method used. Untreated controls maintained the maximum DMSO amount which is equivalent to the DMSO concentration at the highest compound concentration in serial diluted compounds. In dose-response studies the highest compound concentration was 100 μ M (1% DMSO), with exception of azaphilones, where the highest compound concentration was 400 μ M (4% DMSO).

2.2.6 Serial compound dilution

For determining dose-response regarding NF κ B-inhibition (2.5), compounds were diluted in serum-reduced medium (2.2.6.1). For dose-response studies regarding cell viability (2.8), compounds were diluted in culture medium (2.2.6.1).

2.2.6.1 Dilution in serum reduced medium

Compounds were diluted at the final concentration using culture medium reduced to 1% FCS. The serial dilution for dose-response studies was prepared on a V-bottom 96-well plate using a multichannel pipette. The highest DMSO amount (maximum 1%) was maintained throughout every concentration. Each concentration was applied in triplicates. Final compound concentration range and dilution factor are listed in **Table 2-15**.

2.2.6.2 Dilution in cell culture medium

Compounds were diluted in culture medium to obtain a ten-fold concentrated (10×) compound. Serial compound dilution was prepared on a V-bottom 96-well plate using a multichannel pipette. The highest DMSO amount (maximal 1%) was maintained throughout every concentration. To obtain final 1× drug concentration, it was applied 2 µl on a 384-well plate (18 µl seeding volume), 10 µl on a 96-well plate (90 µl seeding volume), 11 µl on a 96-well plate (100 µl seeding volume). Each concentration was applied in triplicates. Final compound concentration range and dilution factor are listed in **Table 2-15**.

Table 2-15 Compound concentration applied in dose-response inhibition studies

Compound ¹	Dilution factor	Conc. range ² [nanomolar, nM]	Assay
BAY 11-7085	1:3	100,000 nM to 46 nM	NFκB-inhibition (2 h)
	1:2 or 1:3	50,000 nM to 390.6 nM or to 22.9 nM	NFκB-inhibition (24 h)
	1:2 or 1:3	100,000 nM to 781 nM or to 46 nM	2D CellTiterGlo (MB-231;96-well)
	1:3	50,000 nM to 22.9 nM	2D PrestoBlue (MB-231, low cell density; MB-468-UnaG)
	1:2	100,000 nM to 781 nM	3D CellTiterGlo
Decahydrofluorenes	1:2	100,000 nM to 781 nM	NFκB-inhibition (2 h), 2D CellTiterGlo (MB-231,384-well)
Falconensin A, H, I	1:2	400,000 nM to 781 nM	NFκB-inhibition (24 h), 2D CellTiterGlo (MB-231,384-well)
Falconensin I, M, N, O, Q, R, S	1:2	200,000 nM to 781 nM	NFκB-inhibition (24 h), 2D CellTiterGlo (MB-231,384-well)
HDACIs	1:2	100,000 nM to 781 nM	2D CellTiterGlo (MB-231, 384-well)
Paclitaxel	1:3	1000 nM to 0.5 nM	NFκB-inhibition (2 h, 24 h), 2D PrestoBlue (MB-231, 96-well, low and high cell density; MB-468-UnaG, 96-well), 3D CellTiterGlo
	1:2	1000 nM to 7.8 nM	2D PrestoBlue (MCF10A)
	1:2	100,000 nM to 781 nM	3D CellTiterGlo
	1:2	500 nM to 2.5 nM	2D CellTiterGlo (D2A1, 96-well)
	1:2	100,000 nM to 781 nM	NFκB-inhibition (24 h), 2D PrestoBlue (MB-231, 384-well)
Polyketides	1:4	1000 nM to 0.06 nM	NFκB-inhibition (2 h, 24 h)

TYLO-1, -2, -3, -4, -5, -6	3D CellTiterGlo		
	2D PrestoBlue (MB-231, low and high cell density)		
	2D CellTiterGlo (MB-231; 384-well, 96well)		
TYLO-4, -5	1:3	10000 nM to 4.6 nM	2D PrestoBlue (MB-231, low cell density)
TYLO-1	1 :4	1000 nM to 0.06 nM	2D CellTiterGlo (MB-231; PBMC), 2D PrestoBlue (MCF10A; MB-231, after p65 and YAP knockdown
TYLO-1	1:2	500 nM to 2.5 nM	2D CellTiterGlo (96-well in D2A1)
TYLO-1s	1:3	300 nM to 0.14 nM	3D CellTiterGlo,
	1:3	100 nM to 0.05 nM	2D PrestoBlue (KMB-231, low cell density; MB-468-UnaG) , 3D
			CellTiterGlo, NFkB-inhibition

¹ After compound injection, the plate was rotated for two min on a rocking platform before incubation for the duration of treatment. ² Concentration range (con-range).

2.3 Electronic devices and software

Electronic devices are listed in **Table 2-16**. Software programmes used for data acquisition or processing are listed in **Table 2-17**.

Table 2-16 Electronic devices

Device	Name	Vendor
Brightfield microscope	AE2000	Motif
Centrifuge (15 ml and 50 ml reaction tubes)	5810	Eppendorf
	Heraeus™	Thermo Fisher Scientific
	Megafuge 16R	
	Hettich® ROTOFIX 32 A (300 × g is equal to 1350 rpm)	Sigma-Aldrich
Imager	Fusion Pulse™	VILBER
Pipette robot	CyBio® Well vario	Analytik Jena
CO ₂ Incubator	Heracell™ 150i	Thermo Fisher Scientific
	Heracell™ VIOS 160i	Thermo Fisher Scientific
High-content imager	CQ1	Yokogawa
Flow cytometer	CytoFlex BA50446	Beckmann Coulter
Gas mixer	Gmix™	Hitec Zang
Automated cell counter	LUNA II™ (L40002-LG)	Logos Biosystems

Multimode microplate reader	Infinite M200 and	TECAN
	M1000 Pro	
	Spark®	TECAN
CLSM, confocal laser scanning microscope	LSM880 AxioObserver (20x lens M27)	Zeiss
	FluoView 3000 (10× lense UPLFLN; (60× lense PLAPON)	Olympus
Inverted brightfield and fluorescence microscope	Axio Vert.A1	Zeiss
Multiplexing system	MAGPIX®	Luminex
Micro centrifuge (1.5 ml reaction tube)	5418/5418R	Eppendorf (1.5 ml)
	Heraeus™ Fresco 21	Thermo Fisher Scientific
	Himac CT15RE	VWR
Micro centrifuge (0.5 ml reaction tubes)	-	SPROUT®
	-	ROTH
Multimode microplate reader	Infinite M200 and	TECAN
	M1000 Pro	
	Spark®	TECAN
	OPTIMA	BMG Labtech
Plate centrifuge	3-30KS (rotor; #11222)	Sigma-Aldrich
Plate shaker	PeqTWIST	Peqlab
Rocking platform	Rocker 3D Digital (#0004001000)	IKA®
	Mini Rocker Shaker MR-1	Kisker
Spectrophotometer	NanoDrop™ Lite (#ND-LITE)	Thermo Fisher Scientific
Thermal cycler	PeqStar (#732-2888DE)	PEQLAB
	CFX96 Touch Real-Timer PCR Detection System	Bio-Rad
Ultrasonic Bath	SONOREX DIGITEC	Bandelin
Vortexer	Genie 2	Scientific Industries
Water bath	-	Memmert

Table 2-17 Software for data illustration and data analysis

Software (Version)	Vendor	Device associated
CellPathfinder (3.04.02.02)	Yokogawa	CQ1
CFX Manager (3.1.1517.0823)	Bio-Rad	Thermal Cycler CFX96

ChemDraw (18.1.0.458).	PerkinElmer Informatics	None
CytExpert (2.4.0.28)	Beckmann Coulter	Flow cytometer CytoFlex
EvolutionCapt (unknown)	VILBER	
Fiji (1.52i)	Open source software [190]	-
GraphPad Prism (8.1.2)	GraphPad Software, Inc	-
MILLIPLEX® Analyst Software (unknown)	Merck	MAGPIX®
SnapGene (6.1.1.)	GSL Biotech LLC	-
OPTIMA, integrated software (2.10 R2)/ firmware (1.20)	BMG Labtech	OPTIMA

2.4 Cell culture

Cell lines and their origins are listed in **Table 2-18**. Culture medium for cell growth, cell clone selection, cell counting and materials for tumour spheroid generation are listed in **Table 2-19**. Cell culture experiments were performed under sterile conditions. All cell lines were grown or incubated in a humid atmosphere at constant 37 °C and 5% CO₂. If not stated otherwise, overnight incubation in experiments was conducted for 24 h and cell incubation steps were conducted at 37°C. Cell culture media, trypsin-EDTA and PBS were prewarmed at 37 °C using a water bath. For collecting cells, they were centrifuged for 3 to 5 min at 300 × g. Freshly thawed cells were cultured in 25 cm² flasks with up to 8 ml culture medium, subculture was proceeded in 75 cm² flasks with up to 15 ml culture medium. Cell culture seeding and compound treatment for drug dose-response studies regarding NFκB-inhibition and cell viability was partially done using the pipette robot.

Table 2-18 List of cell lines with origin and vendor

Cell line	Origin	Purchased from : vendor, cat# or collaborating research groups
Murine CAFs, Cancer-associated-fibroblasts	Primary CAFs were isolated from 4T1-bearing BALB/c mice [191].	Kindly gifted by Ass. Prof. Dr Ute Jungwirth ¹ .
Murine D2A1	Cell line was derived from the malignant neoplasms of the BALB/c mouse mammary gland.	Kindly gifted by Ass. Prof. Dr Ute Jungwirth ¹ . Origin of cells is stated in the previous work of Jungwirth <i>et al.</i> (2018) [192].

HMEC, (Human mammary epithelial cells)	Human mammary epithelial cells isolated from an adult female.	Lonza, cat#CC-2551
MCF10A, Michigan Cancer Foundation-10A	Human mammary gland epithelial cells are derived from a 36-year-old woman, who experienced fibrocystic changes.	Kindly gifted by Dr Julia Sero ¹ . Commercially available at ATCC® (cat#CRL-10317TM).
MDA-MB-231 ¹ , M.D. Anderson - Metastatic Breast-231 (MB-231)	Metastatic cells were derived from the pleural effusion of a 51-year-old Caucasian woman bearing a breast adenocarcinoma and experienced chemotherapy.	Commercially available at ECACC (cat#92020424) and ATCC (#HB-26). Kindly gifted by Kate Gridley ¹ .
NFκB-MDA-MB-231-Firefly (NFκB-MB-231-Firefly)	The TNBC cell line MB-231 was transfected with a plasmid containing a NFκB regulated luciferase (firefly) reporter gene.	Signosis, cat#SL-0043
NFκB-MDA-MB-231MB-231-NanoLuc (NFκB-MB-231-NanoLuc)	The TNBC cell line MB-231 was transfected with a plasmid containing a NFκB regulated luciferase (NanoLuc®) reporter gene.	Cell line was established by Julia Sperlich [116]
MDA-MB-468-UnaG (MB-468-UnaG)	MDA-MB-468 were stably transfected with the plasmid pHRE-UnaG [82]. The original cell line is derived from metastatic cells of the pleural effusion of a 51-year-old black woman bearing a breast adenocarcinoma.	Kindly gifted by Nadine Bauer ² and Prof. Dr Friedemann Kiefer ^{2,3} .
PBMCs, peripheral blood mononuclear cells	Primary cells were isolated from the peripheral blood of a healthy human.	STEMCELL Technologies, Cat#70025.3

¹ Department of Life Sciences, University of Bath, Bath, UK. ² European Institute of Molecular Imaging, University of Münster, Münster, Germany. ³ Max Planck Institute for Molecular Biomedicine in Münster, Germany.

Table 2-19 Cell culture medium, antibiotics, and agents

Reagent	Vendor	Cat#
Cholera toxin	Sigma-Aldrich	C8052
Collagen type I, origin: rat tail	Thermo Fisher Scientific	A1048301
	Ibidi	50201
DMEM, high glucose Dulbecco's Modified Eagle's Medium	Thermo Fisher Scientific	41966-029

	Thermo Fisher Scientific	11995065
DMEM/F12	Thermo Fisher Scientific	11330-032
EGF, epidermal growth factor	Peptrotech	AF-100-15
Erythrosin B	BioCat GmbH	L13002
FCS, fetal calf serum	Gibco	10270-106
Geneticin disulfate (G418 disulfate)	Roth	CP 11.2
Hygromycin B (50 mg/ml)	Thermo Fisher Scientific,	10687010
Horse serum	Thermo Fisher Scientific	16050130
Hydrocortisone; finally dissolved in 100% ethanol	Sigma-Aldrich	H0888-1G
Insulin	Sigma-Aldrich	I9278
Matrigel	VWR	7340268
	Corning	356432
MEGM™, Mammary Epithelial Cell Growth Medium BulletKit™ (Mammary Epithelial Cell Basal Medium and the SingleQuots™ supplements (BPE, hEGF, hydrocortisone, GA-1000, Insulin)	Lonza	CC-3150
Opti-MEM	Thermo Fisher Scientific	31985062
PenStrep, penicillin-streptomycin (10,000 U/ml)	Thermo Fisher Scientific	15140-122
ReagentPack™ containing Trypsin/EDTA, Trypsin Neutralizing Solution and HEPES Buffered Saline Solution	Lonza	CC-5034
RPMI, Roswell Park Memorial Institute 1640	Thermo Fisher Scientific	21875-091
Trypan blue	BioCAT	T13001-LG
0.05% Trypsin-ethylenediamine tetra acetic (EDTA)	Thermo Fisher Scientific	25300054
0.25% Trypsin-EDTA	Thermo Fisher Scientific	25200-056

2.4.1 Cell lines

2.4.1.1 Human breast epithelial cell lines

2.4.1.2 MCF10A

The mammary epithelial cell line MCF10A was grown according to the culture method of Keller *et al.* (2019) [193]. The DMEM/F12 medium was supplemented with the following agents: 1% Pen-Strep, 5% horse serum, 500 ng/ml hydrocortisone, 100 ng/ml cholera toxin, 10 µg/ml insulin and 20 ng/ml eGF. Before applying to the medium, supplementary agents were mixed and filtered aseptically using a syringe and a 0.2 µm filter. At a cell confluency of 60% to 80%, adherent MCF10A were detached for further subculture or experiments. For that, cells cultured in a 25 cm² (75 cm²) flask were washed thrice in 3 ml (5 ml) PBS. Trypsinization was performed for 10 to 15 min at 37°C after addition of at least 3 ml (5 ml) 0.05% trypsin-EDTA. Trypsin reaction was stopped by applying equal volume of serum-rich

medium (DMEM/F12 + 20% horse serum+ 1% Pen-Strep). Cells were pelletized for 5 to 10 min at $200 \times g$. Finally, cells were dissolved in 3 ml medium and counted using the hemocytometer (see chapter 2.4.2.3.1). Cells were frozen as described in chapter 2.4.2.4, except for reducing the DMSO amount to 7.5%. The MCF10A were used as a non-cancerous cell line in the cell viability assay (2.7.2, 2.15.3) and YAP knockdown studies (2.15.3.4.2).

2.4.1.3 Human mammary epithelial cell (HMEC)

The human mammary epithelial cell line HMEC was grown in MEGM medium containing BPE, hEGF, hydrocortisone, GA-100, insulin and 1% Pen-Strep. For subculture, the Reagent Pack™ was prewarmed at RT. Cells grown in a 25 cm² (75 cm²) flask were washed with 5 ml (10 ml) HEPES Buffered Saline Solution and detached for 2-6 min with 2 ml (4 ml) Trypsin/EDTA. Final, it was applied 4 ml (8 ml) Trypsin Neutralizing Solution and cells were centrifuged at $220 \times g$ for 5 min. Finally, cells were dissolved in 3 ml medium and counted using the hemocytometer (see chapter 2.4.2.3.1). Cells were frozen as described in chapter 2.4.2.4, except of reducing the DMSO amount to 7.5%. HMEC cells served as a non-cancerous cell line in YAP knockdown studies (2.15.3).

2.4.1.4 TNBC cancer cell lines

2.4.1.5 Murine D2A1

The D2A1 cells were grown in DMEM supplemented with 10% FCS and 1% Pen-Strep. At a cell confluency of 70% to 90% cells were detached by trypsinization as described in chapter 2.4.2.2. Cells were used for cell viability studies (2.7.1.3) and for the colony formation assay (2.7.4)

2.4.1.6 MDA-MB-231 (MB-231)

The MB-231 cells were grown in RPMI supplemented with 15% FCS and 1% Pen-Strep. At a cell confluency of 70% to 90% cells were detached by trypsinization as described in chapter 2.4.2.2. The MB-231 cell line was used as a TNBC cell model for investigating the biological activity of plant-derived P-alkaloids, fungus-derived azaphilones, decahydrofluorenes or polyketides and synthetically engineered HDACIs.

2.4.1.7 NFκB-MB-231-NanoLuc (NFκB-MB-231-NanoLuc)

The MB-231 cell line is stably transfected with a plasmid containing a NFκB response element (compare 6.3.1) to regulate transcription of a NanoLuc® luciferase (NFκB-MB-231-NanoLuc). Culture medium is composed of DMEM supplemented with 10% FCS, 1% Pen-Strep and for cell clone selection with 400 µg/ml hygromycin B. At a cell confluency of 70% to 90%, cells were detached by trypsinization as described in chapter 2.4.2.2. The NFκB-

MB-231-NanoLuc were used to examine NFκB-inhibition within 2 h (2.5.1) to exclude cytotoxic effects and modulation of NFκB expression.

2.4.1.8 NFκB-MB-231-Firefly (NFκB-MB-231-Firefly)

The MB-231 cell line possesses a plasmid containing a NFκB response element (compare 6.3.2) to regulate transcription of a firefly luciferase (NFκB-MB-231-Firefly). Culture medium is composed of DMEM supplemented with 10% FCS, 1% Pen-Strep. Cell clones are selected in 100 µg/mL hygromycin B. At a cell confluency of 70% to 90% cells were detached by trypsinization as described in chapter 2.4.2.2. The NFκB-MB-231-Firefly were used to examine NFκB-inhibition within 24 h (2.5.2) and YAP after knockdown studies (2.15.3).

2.4.1.9 MDA-MB-468-UnaG (MB-468-UnaG)

The MDA-MB-468 cell line was stably transfected with the plasmid pHRE-dUnaG containing a hypoxia (HIF-1α) response element (HRE) (compare 6.3.3) to regulate transcription of the fluorescent protein UnaG (MB-468-UnaG). Culture medium is composed of RPMI supplemented with 10% FCS, 1% Pen-Strep and for cell clone selection in 1 mg/ml geneticin disulfate. At a cell confluency of 70% to 90%, cells were detached by trypsinization as described in chapter 2.4.2.2. The MB-468-UnaG were used for cell viability assays (2.7.2), cell cycle studies (2.8), hypoxia studies (2.13) and to examine IκBα in western blot studies (2.14.2).

2.4.1.10 Primary cells

2.4.1.11 Murine CAFs

The immortalized primary murine CAFs were grown in high glucose DMEM supplemented with 10% FCS and 1% Pen-Strep. At a cell confluency of 60% to 80%, CAFs were detached by trypsinization as described in chapter 2.4.2.2. The primary murine CAFs express GFP under the human Ubiquitin C promoter. The GFP-signal of the CAFs gets lost with the BA/BB clearing step performed in the 3D immunostaining (2.10.2). The CAFs were used in 3D TNBC co-culture studies with evaluating cell viability (2.7.2, 2.7.3), spheroid growth under normoxic (2.12.2) and hypoxic conditions (2.13.2), and cellular distribution (2.12.3).

2.4.1.12 Peripheral blood mononuclear cells (PBMCs)

PBMCs were thawed in RPMI supplemented with 15% FCS and 1% Pen-Strep. Before utilization for experiments, cells were incubated for 1 h at 37 °C. PBMCs were examined for cell viability (2.7.2) and they were used in a 2D co-culture with MB-231 to investigate cytokine expression (2.6.1).

2.4.2 Subculture

2.4.2.1 Thawing cells

Nitrogen-stored cells were thawed in a water bath at 37 °C and dissolved in 10 ml pre-warmed cell culture medium. Cells were centrifuged for 5 min at 300 × g, dissolved in culture medium and grown in 5 to 7 ml in a 25 cm² cell culture flask. When reaching 90% confluency, cells were detached by trypsinization as described in chapter 2.4.2.2 and transferred for further subculture to a 75 cm² cell culture flask in a total of 12 ml culture medium for 48 h incubation and in a total of 15 ml for 72 h incubation.

2.4.2.2 Detachment of adherent cells

At a cell confluency of 60% to 90%, cells were washed with PBS and detached in 0.25% Trypsin-EDTA for maximal 5 min at 37 °C in a volume that is appropriate to the cell culture flask size (1 ml in 25 cm²; 1.5 ml in 75 cm²; 3 ml in 175 cm²). To deactivate trypsin activity, at least equal volume of cell culture medium was added. For cell subculture, cell specific fraction (1:15 to 1:2) was transferred to a cell culture flask (25 cm², 75 cm² or 175 cm²) with a total cell culture volume of 12 ml, 15 ml or 28 ml, respectively. If cells were used for experiments, they were pelleted (5 min at 300 × g) and dissolved in culture medium (2 ml, 3 ml or 6 ml) according to their cell culture flask size (25 cm², 75 cm² or 175 cm²).

2.4.2.3 Cell counting

After detaching adherent cells, count cells manually (2.4.2.3.1) or automatically (2.4.2.3.2). For that, mix 10 µl cell suspension with a dye for dead cell exclusion. Cell density for cell seeding was calculated using the cell number of viable cells.

2.4.2.3.1 Manual cell counting: haemocytometer

The hemocytometer was used for counting CAFs, HMECs, MCF10A and PBMCs. Cell suspension is mixed 1:1 with 0.4% trypan blue and it was applied 10 µl to the hemocytometer. Cells were counted using a brightfield microscope at 100× magnification. The hemocytometer is sectioned into four squares (à 1mm²), whereby each square is sectioned into sixteen smaller squares (à 0.0025 mm²). The absolute number of viable cells per ml of the cell suspension was calculated as indicated in **Equation 1**. In brief, the total number of counted viable cells was divided by the total number of squares (à 1mm²) that were used for cell counting. Then, the average viable cell number per square was multiplied with the dilution factor two, because the cell suspension was diluted 1:2 in trypan blue. To extrapolate the cell number to 1 ml, the corrected viable cell number per square in 10 µl was then multiplied with the factor 10⁴.

Equation 1 Calculation of the live cell number using the haemocytometer.

$$\text{viable cells per ml} = \frac{\text{number of viable cells}}{\text{number of squares (à 1mm}^2\text{)}} \times 2 \times 10^4$$

2.4.2.3.2 Automated cell counting: LUNA II™

MB-231, NFκB-MB-231-Firefly, NFκB-MB-231-NanoLuc and MB-468-UnaG were counted using the automated cell counter LUNA II™. Cell suspension is mixed 1:1 with erythrosin B 0.4% trypan blue and it was applied 10 µl to a counting slide. Cells were counted according to following settings: Dilution Factor (2), Noise Reduction (5), Live Cell Sensitivity (2), Roundness (40), Minimal Cell Size (3 µm), Maximal Cell Size (60 µm), Declustering Level (low).

2.4.2.4 Long-term cell storage

After cell trypsinization (2.4.2.2) and cell counting (), cells were pelletized (5 min at 300 × g) and dissolved in culture medium supplemented with 10% DMSO to obtain a density of 2 to 4 × 10⁶ cells/ml in the. It was frozen 1 ml per cryo vial at - 80 °C using a freezing container. For long term storage, frozen cells were transferred to liquid nitrogen.

2.5 NFκB-inhibition

Modulation of the inflammatory NFκB pathway is determined in MB-231 based on the NFκB regulated luciferase reporter gene. To investigate negative effects on the NFκB pathway, compounds were pre-incubated before application of NFκB stimulants. To stimulate NFκB for 2 h (2.5.1), LPS was applied, and for 24 h, TNFα was applied (2.5.2).

2.5.1 NanoGlo assay, 2h

On day one, 4 × 10⁴ NFκB-MB-231-NanoLuc cells were seeded in a total of 100 µl on a white 96-well plate. On day two, serial compound dilution was performed as described (2.2.6.1) and cells were incubated for 20 min in 100 µl containing the final compound concentration (compare **Table 2-15**) before cells were incubated for another 2 h in 1 µg/ml LPS. Non-stimulated and untreated cells served as control. Measurement of NFκB-dependent luciferase activity was performed according to the manufacturer's instruction of the "Nano-Glo® Luciferase Assay System". For that, equal volume of 1:50 diluted NanoGlo® reagent was applied and cells were incubated for 3 min at RT. Luciferase-dependent luminescence was recorded in relative light units (RLU) using the multimode microplate reader Spark® with setting the integration time at 500 ms and the time at 1 ms. The half maximal inhibitory concentration (IC₅₀) was assessed by calculating the dose-response inhibition in a non-linear regression using GraphPad (2.16).

2.5.2 Luciferase assay, 24 h

On day one, 3×10^4 NF κ B-MB-231-Firefly cells were seeded in a total of 100 μ l medium on a white 96-well plate. On day two, serial compound dilution was performed as described (2.2.6.1) and cells were incubated for 20 min in 100 μ l containing the final compound concentration (compare **Table 2-15**) before cells incubated for another 24 h in 20 ng/ml TNF α . Non-stimulated and untreated cells served as control. Measurement of NF κ B-dependent luciferase activity was performed according to the manufacturer's instruction of the "Luciferase Assay System". In brief, cells were lysed for 15 min at room temperature (RT) in 20 μ l 1 \times cell lysis buffer (dissolved in PBS). By use of the multimode microplate reader M200 infinite® or Spark® 100 μ l luciferase substrate mixture was injected with subsequently measuring the luciferase-dependent luminescence in RLU with setting "integration time" at 10 sec. The IC₅₀ was assessed by calculating the dose-response inhibition in a non-linear regression using GraphPad (2.16).

2.6 Gene expression studies

Expression of interleukin (IL)-6 and IL-8, regulated by NF κ B, was analysed based on the mRNA level in the co-culture of MB-231 and PBMCs by performing Real-Time quantitative Polymerase-Chain Reaction (RT-qPCR) (2.6.1). In MB-231 monolayer cells, RT-qPCR (2.6.2). was performed to assess expression of IL-6, IL-8 under TNF α -induced NF κ B signalling (2.6.2, 2.6.2.2), expression of p65 (2.15.2.1, 2.6.2.2) or YAP (2.15.3.1, 2.6.2.2) after siRNA-mediated protein knockdown. Secreted IL-8 from MB-231 was evaluated with a multiplex enzyme-linked immunosorbent assay (ELISA) (2.6.2.3).

2.6.1 Real-Time quantitative Polymerase-Chain Reaction (RT-qPCR) in a 2D co-culture of MB-231 and PBMC

On day one, 1×10^6 MB-231 cells were seeded in a total of 2 ml culture medium on a transparent 6-well plate. On day two, medium was replaced with fresh medium and cells were left untreated or pre-incubated for 20 min in 1 ml at 100 nM TYLO-1. Subsequently, 1 ml culture medium was added to the MB-231 monoculture. For co-culture, 1×10^6 of freshly thawed PBMC in a total of 1 ml were added. Cells incubated in a total of 2 ml for 24 h. On day three, cells were harvested using 1 ml 0.25% Trypsin-EDTA and trypsin activity was neutralized with 1 ml culture medium. The cells were collected using a micro centrifuge at $300 \times g$ for 5 min. Cell pellet could be stored at -80 °C. The total RNA was isolated from the cell pellets according to the manufacturer's instruction of the "RNeasy Mini Kit". The total RNA concentration was measured with the multimode microplate reader Infinite M200 or M1000 Pro. Reverse transcription of 1 μ g RNA to the mRNA equivalent, the complementary DNA (cDNA) was performed according to the manufacturer's instruction

of the “Reverse transcription system”. Quantification of the cDNA was done using the “QuantiFast SYBR® Green PCR Kit”. Gene expression of IL-6, IL-8 and the housekeeping gene GAPDH were assessed using 30 ng cDNA in duplicates. Primers are listed in **Table 2-7** and each primer, fw and rev, was applied at 1.5 μ M for each target gene. Templates without cDNA served as negative control. Real time quantification was performed with the following settings using the thermal cycler CFX96: Denaturation at 95 °C for 900 sec and template amplification over 45 cycles (one cycle: 95 °C for 15 sec, 55 °C for 25 sec and 72 °C for 10 sec). Fold change of the mRNA level was calculated according to the $2^{-\delta\delta CT}$ method [194]: In the first step, the Ct value assessed for the target genes was normalized to GAPDH (δCT) and in the second step, the δCT values within the target gene group was normalized to the untreated co-culture group ($\delta\delta CT$).

2.6.2 Gene expression in MB-231

2.6.2.1 Cytokine expression

On day one, 3×10^5 MB-231 cells were seeded in a total of 2 ml culture medium on a 6-well plate. Cells were allowed to attach for in total 72 h, equivalently to knockdown studies. On day four, the medium was replaced with 2 ml serum reduced medium (1% FCS) and cells were pre-incubated for 20 min with 7 nM TYLO-1. Subsequently, TNF α was applied at a final concentration of 20 ng/ml and cells incubated for another 24 h. Unstimulated and untreated cells served as control. On day five, cells were harvested using 1 ml 0.25% Trypsin-EDTA and trypsin activity was neutralized with 1 ml culture medium. Cells were pelleted using a micro centrifuge at $300 \times g$ for 5 min. Cell pellet could be stored at -80 °C before proceeding with the RT-qPCR (2.6.2.2).

2.6.2.2 RT-qPCR in MB-231

The total RNA was isolated from the cell pellets according to the manufacturer's instruction of the “ReliaPrep Kit”. For that, cells were lysed and total RNA was captured via chromatography. DNA digestion by the DNase I was prolonged to 30 min. Spin columns were washed and dried before elution in 15 μ l nuclease free water. The total RNA concentration was measured with the spectrophotometer NanoDrop™ Lite. Reverse transcription of 1 μ g RNA to the mRNA equivalent, the cDNA, was performed using the “cDNA Synthese Kit” with the following settings at the thermal cycler PeqStar: Primer annealing at 25°C for 5 min, elongation at 46 °C for 20 min, inactivation of the reverse transcriptase at 95°C for 1 min. Quantification of the cDNA was done using the according to the manual of the “iTaQ SYBR Green Supermix” kit. The gene expression of IL-6, IL-8 and the housekeeping gene GAPDH were assessed using 50 ng cDNA in triplicates. Primer are listed in **Table 2-7** and each primer, forward and reverse, was applied at 0.25 μ M for

each target gene. Templates without cDNA served as a negative control. Real time quantification was performed with the following settings using the thermal cycler CFX96: Nucleic acid denaturation at 95 °C for 30 sec, template amplification over 37 cycles (each cycle: at 95 °C for 5 sec and at 58 °C for 40 sec) and for the melting curve analysis it was done an gradual increase in temperature from 65 °C up to 95 °C in 0.5 °C steps every 0.05 sec. Fold change of the mRNA level was calculated according to the $2^{-\delta\delta CT}$ method [194]: In the first step, the cycle threshold (CT) value assessed for the target genes was normalized to GAPDH (δCT) and in the second step, the δCT values within the target gene group was normalized to the untreated control ($\delta\delta CT$).

2.6.2.3 IL-8 secretion

IL-8 secretion was determined in MB-231 using a multiplex magnetic-based ELISA. On day one, 4×10^4 cells were seeded in 100 μ l on a flat transparent 96-well plate. On day two, medium was replaced with serum reduced medium (1% FCS) containing 10 nM, 100 nM or 1000 nM TYLO-1 in triplicates. After pre-incubation for 20 min, cells were stimulated with LPS at a final concentration of 50 ng/ml to stimulate NF κ B for another 24 h. Unstimulated and untreated cells served as control. On day three, supernatant was collected. Samples could be stored at -20 °C until analysis. If samples were frozen, they were thawed on ice and centrifuged for 5 min at 14,000 rpm using a micro centrifuge to eliminate cell debris. Samples were three-fold or ten-fold diluted in serum-reduced medium and IL-8 secretion was quantified according to the manufacturer's instruction of the "Magnetic Bead-Based Multiplex Assay". For that, the kit was equilibrated to RT before usage. The following incubation steps were done at RT under constant rotation at 600 rpm. The provided plate was washed with 200 μ l washing buffer per well. For immunological binding of the cytokines to the magnetic beads, it was mixed 25 μ l of the prior diluted samples with 25 μ l of the magnetic bead solution per well and the plate incubated for 2 h in the dark. The magnetic beads were washed twice for 30 sec in washing buffer and incubated for 1 h after injection of 25 μ l of detection antibodies and another 30 min after addition of 25 μ l streptavidin-phycoerythrin. Final, beads with linked IL-8 proteins were washed twice in washing buffer and incubated for 10 min after addition of 150 μ l of the drive-fluid that was required for the measurement. For MagPix® instrument preparation, it was rinsed six-times in the following order: ddH₂O, 70% ethanol solution and 2% sodium hypochlorite. The probe was sonicated for 15 min in 0.5 M sodium hydroxide using the ultrasonic water bath SONOROEX DIGITEC and the probe was calibrated no more than 24 h before measurement using the calibration kits. Subsequently, the probe was rinsed again as described before. The IL-8-dependent fluorescence of phycoerythrin was recorded in pg/ml using the multiplexing system MAGPIX®. Data were assessed and evaluated with the integrated MILLIPLEX® Analyst Software.

2.7 Cell viability studies

Cell viability was determined in monolayer cells by performing the 2D CellTiterGlo (2.7.1) or 2D PrestoBlue (2.7.2), while cell viability in tumour spheroids was determined with the 3D CellTiterGlo (2.7.3). Cell viability in the CellTiterGlo is based on ATP-dependent luciferase activity and cell viability in the PrestoBlue™ is based on metabolic reduction of resazurin to the fluorescent resofurin. In each assay, background signal resulting from the culture medium was subtracted from the measured values. The IC₅₀ was assessed by calculating the dose-response inhibition in a non-linear regression using GraphPad (2.16). To assess colony formation, viable cells were determined according to the 2D colony formation assay (2.7.4). Cell seeding density for each assay and cell type is listed in **Table 2-20**.

Table 2-20 Cell seeding density for dose-response inhibition studies

Assay method	Cell line	Cell seeding density (volume per well)
2D CellTiterGlo (384-well)	MB-231	5×10^4 cells/ml (18 μ l)
2D CellTiterGlo (96-well), 2D PrestoBlue	CAFs	2.5×10^4 cells/ml (100 μ l)
	MB-231	1.5×10^5 cells/ml (100 μ l)
	PBMC	3.5×10^5 cells/ml (100 μ l)
	D2A1	1×10^4 cells/ml (100 μ l)
2D PrestoBlue (24 h)	CAFs	High density: 1.5×10^5 cells/ml (100 μ l) Low density: 2.5×10^4 cells/ml (100 μ l)
	MCF10A	1×10^5 cells/ml (100 μ l)
	MB-231	High density: 1.5×10^5 cells/ml (100 μ l) Low density: 7.5×10^4 cells/ml (90 μ l)
	MDA-MB-468	1.5×10^5 cells/ml (100 μ l)
2D PrestoBlue (48 h)	MB-231	6×10^4 cells/ml (100 μ l)
3D CellTiterGlo	Co-culture spheroids (MB-231:CAF, 1:2)	6×10^4 cells/ml (50 μ l)

2.7.1 2D CellTiterGlo

Measurement of cell viability was performed according to the manufacturer's instruction of the "2D CellTiterGlo" assay.

2.7.1.1 Cell viability of MB-231 (384-well)

The pipette robot CyBio® Well vario was utilized for cell seeding on day one and compound injection on day two. On day one, 18 μ l was seeded at a density of 2.8×10^5 MB-231 cells/ml. On day two, serial dilution of compounds was prepared in culture medium as

described (2.2.6.2). For treatment in quadruples, 2 µl of the 10× concentrated compound was applied and cells incubated for 24 h. Final compound concentration for dose-response studies is listed in **Table 2-15**. On day three, cell viability-dependent luminescence was recorded as described (2.7.1.4).

2.7.1.2 Cell viability of MB-231 (96-well)

On day one, 100 µl cell suspension was seeded on a white 96-well plate. Cell seeding density is listed in **Table 2-20**. On day two, serial dilution of compounds was prepared in culture medium as described (2.2.6.2). For treatment in triplicates, 11 µl of the 10× concentrated compound was applied and incubated for further 24 h. Final compound concentration for dose-response studies is listed in **Table 2-15**. On day three, cell viability-dependent luminescence was recorded as described (2.7.1.4).

2.7.1.3 Cell viability of D2A1 (96-well)

On day one, 100 µl of the cell suspension was seeded on a transparent 96-well plate. Cell seeding density is listed in **Table 2-20**. On day two, the serial dilution of compounds was prepared in culture medium as described (2.2.6.2). For treatment in triplicates, 100 µl of the 2× concentrated compound was applied and cells were incubated for 72 h. The final compound concentration for dose-response studies is listed in **Table 2-15**. On day five, cell viability-dependent luminescence was recorded as described (2.7.1.4).

2.7.1.4 Luminescence measurement

After compound treatment, equal volume of the CellTiterGlo reagent (384-well/20 µl; 96-well/100 µl) was applied before the plate was rotated on a rocking platform for 2 min and incubated for 10 min in the dark. Luciferase-dependent luminescence was recorded in RLU using the multimode microplate reader Spark® with setting the integration time at 1000 ms.

2.7.2 2D PrestoBlue

On day one, 100 µl of the cell suspension were seeded on a black 96-well plate. The cell seeding density is listed in **Table 2-20**. On day two, the serial dilution of compounds was prepared in a culture medium as described (2.2.6.2). For treatment in triplicates, 11 µl of the 10× concentrated compound was applied and cells were incubated for the individual duration of the treatment (24 h or 48 h). The final compound concentration for dose-response studies is listed in **Table 2-15**. Post-treatment, cell viability was measured according to the manufacturer's instruction of the PrestoBlue™ Assay. For that, 12 µl PrestoBlue™ reagent was injected before the plate was incubated for 10 min at 37 °C. Cell-viability dependent fluorescence was recorded in relative fluorescence units (RFU) using the multimode microplate reader Spark® with exλ/emission λ (exλ/emλ) at 535nm/590 nm

for measurement in CAFs, MB-231 (high cell seeding density), MCF10A or at 560nm/590 nm (exλ/emλ) when measured in MB-231 (low cell seeding density).

2.7.3 3D CellTiterGlo

On day four, after co-culture spheroid formation for 72 h (2.11.3), a serial dilution of compounds was prepared in culture medium without collagen as described (2.2.6.2). Eleven µl of the 10× concentrated compound was applied in triplicates. The final compound concentration for dose-response studies is listed in **Table 2-15**. On day seven, after 72 h spheroid treatment, 50 µl medium containing the spheroid were transferred to a white 96-well plate. The cell viability was determined according to the manufacturer's instruction of the "3D CellTiterGlo". For that, the plate was incubated for 30 min at RT, before 50 µl of the CellTiterGlo reagent were applied. Subsequently, the plate was vigorously shaken on the plate shaker for 5 min and was incubated for another 25 min at RT in the dark. The cell viability-dependent luminescence was recorded in RLUS using the multimode microplate reader Spark® with setting the integration time at 1000 ms.

2.7.4 2D colony formation

On day one, 150 D2A1 cells were seeded in a total of 2 ml culture medium on a flat-bottom 6-well plate. On day two, TYLO-1 or paclitaxel were applied at the final concentration in culture medium. Cells were grown for further ten days. On day twelve, cells were washed in PBS to remove detached cells and stained for 15 min at RT using the crystal violet staining solution (0.4% (w/v) crystal violet powder dissolved in 5% methanol). Cells were washed using tap water and air dried for several hours. The cell plate was imaged using a digital camera (there are no information given about the vendor of the device).

2.8 Cell cycle studies

To assess modulation of the cell cycle states during proliferation, the DNA content in MB-231 (2.8.1) and MB-468-UnaG (2.8.2) was measured after exposure to TYLO-1s and paclitaxel under normoxic or hypoxic conditions.

2.8.1 Cell cycle population in MB-231

On day one, 1 ml cell suspension was seeded on a 24-well plate. MB-231 cells were seeded at a density of 1×10^5 cells/ml for 24 h and 48 h treatment or at a density of 8×10^4 cells/ml for 72 h treatment. On day two, medium was replaced with fresh culture medium containing TYLO-1s or paclitaxel at the final concentration. Cells were treated for 24 h, 48 h or 72 h before analysis of the DNA amount as described (2.8.3).

2.8.2 Cell cycle population in MB-468-UnaG

On day one, 1 ml cell suspension was seeded on a 24-well plate. MB-468-UnaG cells were seeded at a density of 8×10^4 cells/ml for 48 h treatment or at a density of 6×10^4 cells/ml for 72 h treatment. On day two, MB-468-UnaG were pre-treated to induce hypoxia. Cells incubated for 24 h with culture medium (normoxia) or 100 μ M CoCl₂ (hypoxia) in a total of 2 ml. On day three, MB-468-UnaG medium was replaced with fresh culture medium containing TYLO-1s or paclitaxel at the final concentration. Cells were treated for 48 h or 72 h before analysis of the DNA amount as described (2.8.3).

2.8.3 Quantification of the cell cycle population

Post-treatment, all cells (detached and after trypsinization) were collected in a 1.5 ml reaction tubes and cells were pelleted for 5 min at $300 \times g$ using a micro centrifuge. Cells were dissolved in 200 μ l PBS and transferred to a transparent V-bottom 96-well plate provided by Sarstedt. Further centrifugation steps were performed using the plate centrifuge (3-5 min at $300 \times g$). PBS was removed and cells were fixed in 70% ethanol overnight at 4°C and washed again in PBS. for DNA staining and RNA removal, cells were incubated for 15 min at 37°C in the presence of 10 μ g/ml PI and 100 μ g/ml RNase A dissolved in 0.1% Triton® X-100. Finally, cells were washed in PBS and fluorescence signal resulting from the PI-DNA complex formation was recorded in the ECD-A channel (exλ/emλ 488nm/610nm/bandpass filter (BP, [nm]) 20 using the flow cytometer CytoFlex. The cell cycle phase population was determined based on the DNA content of a set of chromosomes (2n) of cells using the integrated software CytExpert: sub-G0/G1 (< 2n), G0/G1 (2n), S (>2n, < 4n), G2/M (4n) or hyperploid (> 4n) cells. Procedure for determination the cell cycle phase in single cells is described in **Figure 2-9**. For assessing cell cycle phase population, we gated for single cells and subsequently for cells that displayed the chromosomal set of a healthy cell (2n - 4n). For assessing cell cycle phase populations to estimate apoptosis induction upon compound treatment, all events gated in cells (compare **Figure 2-9a**) were evaluated for events that indicated DNA fragmentation (< 2n) or hyperploid DNA sets (> 4n).

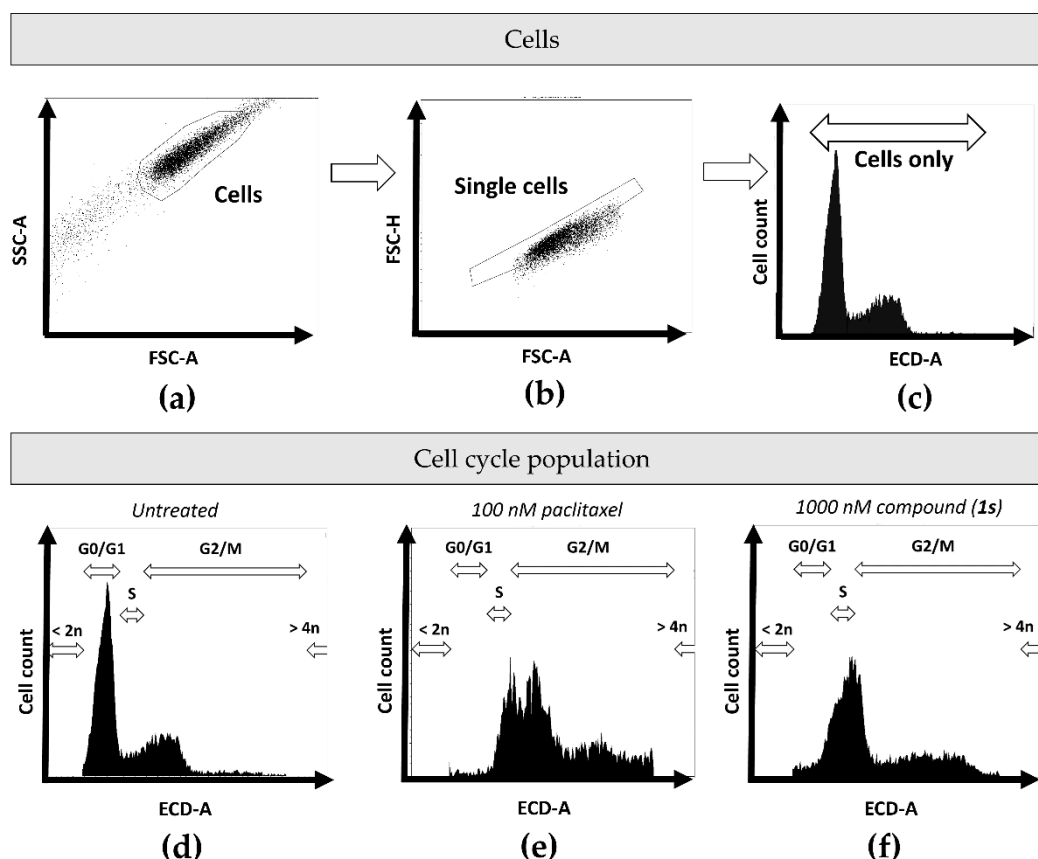


Figure 2-9 Quantification of cell cycle phase populations. Cells were exposed for a maximum of 72 h to paclitaxel or TYLO-1s (compound (1s)). Signal of the PI-DNA complex was recorded within the ECD-A channel using the flow cytometer CytoFlex. The cell population was gated for **(a)** cells and **(b)** single cells. **(c)** To evaluate cell cycle phases, the range of analysed cells was determined within the **(b)** single cells by excluding recorded events that extend the proportional distribution of the DNA chromosome set (n): $< 2n$; $> 4n$. **(d-f)** Gating for the cell cycle population sub-G0/G1 ($< 2n$), G0/G1 ($2n$), S, G2/M ($4n$) or hyperploid ($> 4n$) cells was done manually and maintained for each independent experiment and each individual time point of treatment. The cell cycle population G0/G1 was determined in relation to the **(c)** untreated group and G2/M was determined in relation to the highest concentration applied for **(d)** paclitaxel and **(e)** compound (1s). Histograms were illustrated using CytExpert. Illustration from Reimche *et al.* (2022) [187].

2.9 Migration Studies

2.9.1 2D wound healing

The anti-inflammatory TYLO-1 was also examined regarding its inhibitory potential in migration of MB-231 cells. In our experiment, the wound is defined as a cell free area, which was artificially introduced upon physical exclusion during cell growth (2.9.1.3). Initial optimal seeding density was determined for MB-231 to ensure observe migratory character

(2.9.1.1). We investigated the effect of TYLO-1 on TNBC migration with regard to the relevance of NF κ B signalling (2.9.1.4) and we investigated the impact of the tumour stroma on TNBC migration with performing indirect co-culture utilizing CAF conditioned medium (CAF-CM).

2.9.1.1 Cell seeding density for MB-231

To obtain a defined migration gap between two cell monolayers, a silicon-based 2-well insert was stuck to a 24-well plate before seeding. Per insert-well, 70 μ l were seeded containing 2×10^4 , 3×10^4 or 4×10^4 cells. After 24 h, inserts were removed, cells were washed in PBS and grown in 500 μ l serum-reduced medium (1% FCS). The migration gap between the cell monolayers was imaged after 8 h, 24 h and 48 h using the high-content imager CQ1 (**Figure 2-10**). Without any external stimuli, MB-231 cells show migratory behaviour and optimal cell confluency was observed when seeding of 4×10^4 cells per insert-well.

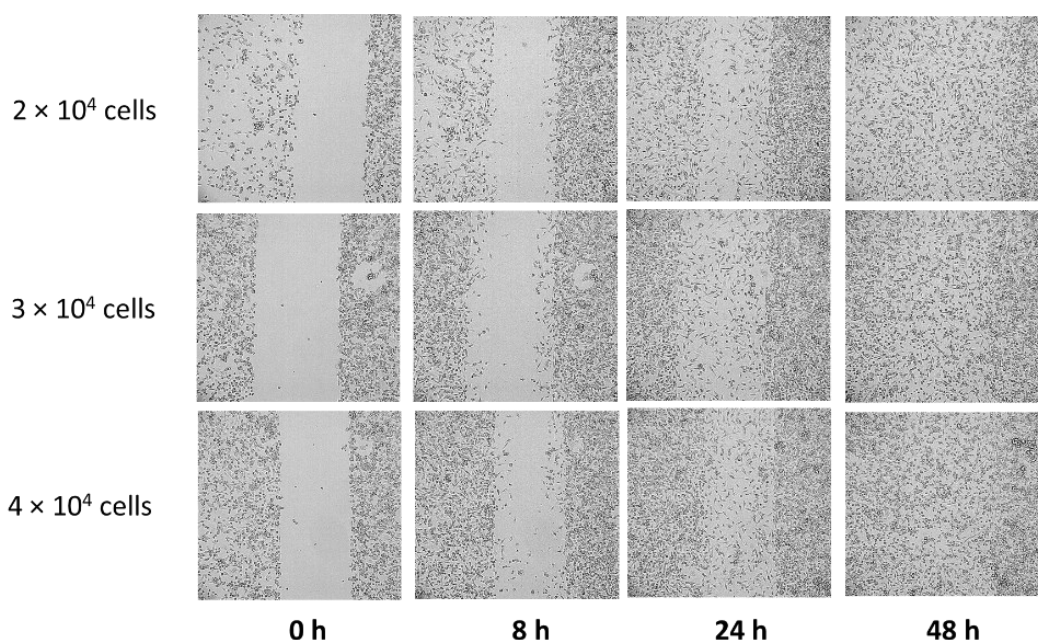


Figure 2-10 Determining the MDA-MB-231 (MB-231) cell seeding density for the 2D wound healing assay. Two cell monolayers of MB-231 cells were grown under physical exclusion. Per insert-well, 2×10^4 , 3×10^4 or 4×10^4 cells were seeded. After removing the inserts, cells were grown in serum-reduced medium. The migration gap between the cell monolayer was imaged after 8 h, 24 h and 48 h. Magnification: 100 \times .

2.9.1.2 Cell seeding density for CAFs

CAFs were seeded in 500 μ l culture medium (DMEM, 10% FCS) or serum-reduced medium (RPMI, 1% FCS) on a 24-well plate with a cell density of 1×10^4 to 1×10^5 cells per well (**Figure 2-11a**). Cell confluency was recorded 24 h post-seeding using the inverted brightfield microscope. Optimal cell confluency was observed with a seeding density of

5×10^4 cells per well showing a confluency of nearly 100% (**Figure 2-11b**), whereas some monolayer areas showed confluency of about 60% (not shown). Growth behaviour was independent on serum proportion (**Figure 2-11b**).

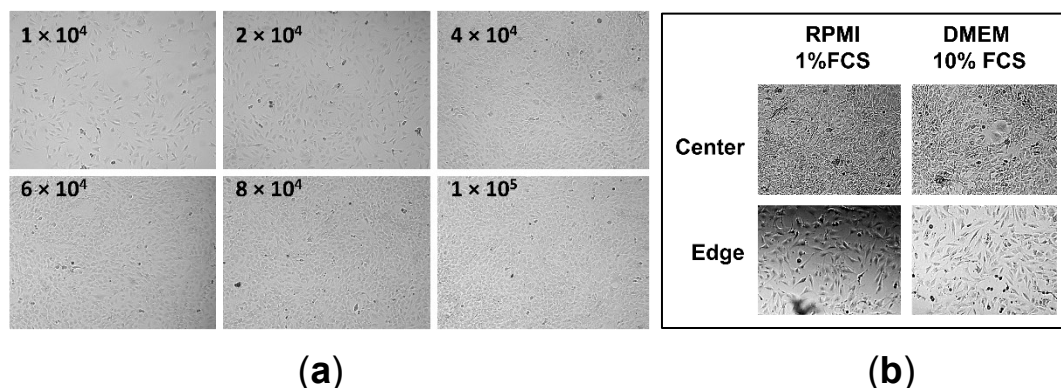


Figure 2-11 Determining the CAF cell seeding density for indirect co-culture studies.

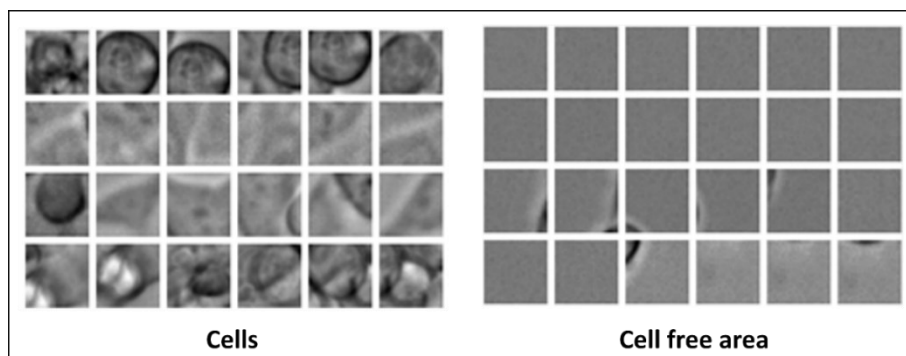
On a 24-well plate, 500 μ l was seeded in (a,b) serum-reduced medium (RPMI, 1% FCS) or (b) culture medium (DMEM, 10% FCS) containing CAFs at a cell density of (a) 1×10^4 , 2×10^4 , 4×10^4 , 6×10^4 , 8×10^4 , 1×10^5 or (b) 5×10^4 cells/well. (a,b) Brightfield images recorded 24 h post-seeding. Magnification: 100 \times .

2.9.1.3 MB-231 migration

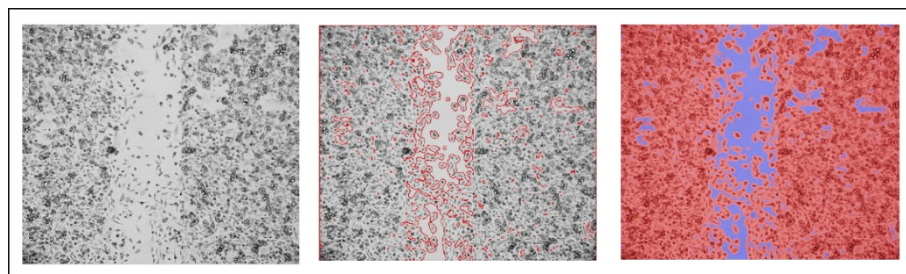
To obtain a defined migration gap between two cell monolayers, a silicon-based two-well insert was placed on a 24-well plate before seeding. On day one, 70 μ l containing a total of 4×10^4 MB-231 cells were seeded per well of a 2-well insert. After 24 h, on day two, inserts were removed and washed at least twice in 70% ethanol for reutilization. Cells were washed in pre-warmed PBS and serum-reduced medium (1% FCS). Treatment was conducted in serum-reduced medium as described in chapter 2.2.6.1. Within 24 h, the migration gap was recorded in the same area and at different time points using high-content imager CQ1. To record the maximal length of the migration gap, five fields per well were recorded. Each field was acquired in a z-stack comprising four images within the z-axis in a range of 15 μ m with setting “Brightfield Power” at 100% and “Exposure Time” at 50 ms. Automatic image recording with the CQ1 was ensured in a humid atmosphere at constant inflow (1 L/h) of a gas mixture containing 5% CO₂ and 95% air using the gas mixer Gmix™.

To quantify cell migration into the cell free migration gap, the cell free area at each time point of imaging was measured using the CQ1 integrated software CellPathfinder. The z-stacked images were projected to a 2D image to obtain a plane and maximal covered area by cells. Cell area identification was based on a machine learning algorithm after manually selecting characteristic areas that define a cell or a cell free area (**Figure 2-12a,b**). For each well, three different fields at the migration gap were analysed with the “X-

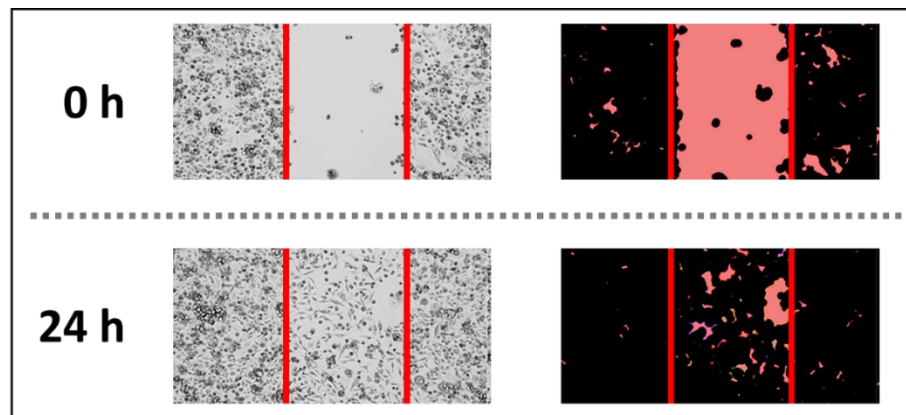
coordinate filter” set manually to determine the migration gap width (**Figure 2-12c**). However, a cell area outside the migration gap connected to cell areas within the defined gap, was also recognised as an area of migrated cells (**Figure 2-12b,c**). Thus, we determined the cell free area within the gap and defined migration as reduction in the cell free area. Because of the divergence in the migration gap width between the wells, the cell free area post-treatment (≤ 24 h) was normalized to the area pre-treatment (0 h; 100%). To calculate the area of migrated cells, the cell free area post-treatment (≤ 24 h) was subtracted from the maximum of cell free area pre-treatment (100%). For each independent experiment and time point, the area of migrated cells was normalized to the untreated control (100%).



(a)



(b)



(c)

Figure 2-12 Machine learning identification of cell covered areas and cell free areas.

(a) The machine learning identification in CellPathfinder is based on characterization of the cell area and the cell free area. Characterization is manually done by selecting areas for the object “Cells” or “Background”/cell free area. (b) The migration gap between two MB-231 cell monolayers was recorded 8 h after insert removal. Cells were identified based on the machine-learned algorithm using CellPathfinder. Red outlines indicate the border between the cell area and cell free area. Red areas indicate the area of cells. (c) The migration gap between two MB-231 cell monolayers was recorded directly at or 24 h after insert removal. Quantification of the cell free area within the migration gap was performed with the CellPathfinder after determining the border of the migration gap by setting “X--coordinate filter” (red lines). The cell free area (rose) and cell area (black) are visualized after CellPathfinder analysis.

2.9.1.4 Relevance of the NFκB pathway in TNBC migration

On day one cell seeding and imaging post-treatment was done as described in chapter 2.9.1. On day two, treatment was performed in duplicates. For that, cells were pre-incubated for 20 min in 450 µl serum-reduced medium (1% FCS) containing 5.5 µM BAY 11-7085 or 10 nM TYLO-1. To activate NFκB signalling, 50 µl of the ten-fold higher concentrated TNFα were applied to obtain a final concentration of 20 ng/ml. To maintain the final compound concentration, TNFα was pre-mixed in serum-reduced medium containing the final compound concentration. Cells were incubated for 8 h.

2.9.1.5 Indirect 2D co-culture with MB-231 and CAFs

To examine stromal cell regulation in TNBC migration, we performed indirect co-culture studies using conditioned medium of primary murine CAFs. MB-231 seeding on day one and imaging post-treatment was done as described in chapter 2.9.1.. On day two, MB-231 were washed and exposed to 500 µl of CAF-CM that was prepared as followed: First, we determined the optimal seeding density of CAFs (2.9.1.2), which is 500 µl serum-reduced medium (RPMI, 1% FCS, 1% PS) at a density of 1×10^5 cells/ml. CAFs was seeded on a 24-well plate. The supernatant, here referred to as CAF-CM, was collected 24 h post-seeding and centrifuged at $300 \times g$ for 5 min to remove cell debris. CAF-CM could be stored at -80°C until utilization. On day two, MB-231 were exposed to 500 µl CAF-CM and incubated for 24 h.

2.9.2 3D TNBC invasion

To study TNBC invasion into an ECM-like environment, spheroids of MB-231 cells were generated in the presence of matrigel® as described [79]. On a cell repellent U-bottom 96-well plate, 50 µl were seeded at a density of 6×10^4 cells/ml in 0.25% matrigel®. For cell aggregation, cells were centrifuged for 10 min at 1000 rpm ($136 \times g$) at constant 4°C before

grown for 72 h at 37°C. After injection of 50 μ l (100%) matrigel®, ECM formation was allowed for 1 h at 37°C. Subsequently, equal volume of the cell culture medium containing the invasion modulating agent TYLO-1s at a two-fold higher concentration was applied to give the following final concentration for a total of 100 μ l: 2 nM, 5 nM, 10 nM. Culture medium served as negative control. Invasion was allowed for another 72 h and at least three spheroids per treatment group were recorded using the inverted brightfield microscope Axio Vert.A1. The spheroid area was measured pre-treatment, and post-treatment using Fiji (**Figure 2-13**). The invaded area is calculated by normalizing the spheroid area post-treatment to the spheroid area pre-treatment (which was set to 1, fold-change).

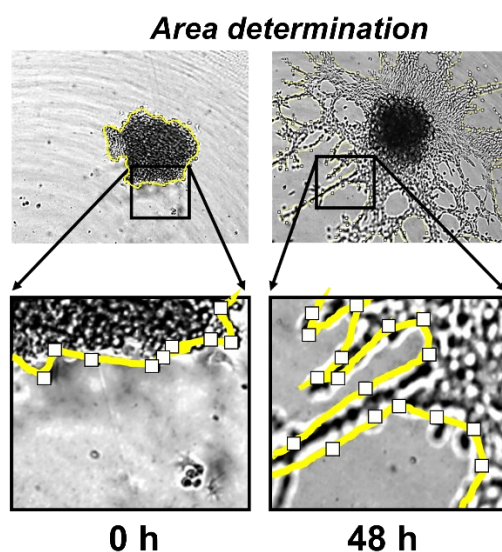


Figure 2-13 Measurement of TNBC spheroid invaded area. Monoculture spheroids were generated using MB-231 according to the 3D TNBC invasion assay. Spheroids were recorded before (0 h) and after (48 h) matrigel® application at 50x magnification using the Zeiss A.1 microscope. Area was measured using Fiji with manually picking positions (white squares) to determine the outline (yellow line) of the spheroid (0 h) and the invaded area (48 h). Adapted from Reimche *et al.* (2022) [187].

2.10 Immunofluorescence studies

Monolayer cells were analysed for YAP by 2D immunostaining (‘2.10.1) and spheroids were analysed for cell type distribution by 3D immunostaining (2.10.2). Composition of manually prepared solutions, used for the 2D and 3D immunostaining, are listed in **Table 2-21**.

Table 2-21 Immunostaining solution for two dimensional (2D) monolayer cells and 3D spheroid staining

Application	Solution	Components
Monolayer, spheroids	PFA/PBS	4% (w/v) PFA dissolved in PBS, pH 7.4
Monolayer	Blocking solution	5% (w/v) BSA and 0.3% Triton® X-100 dissolved in PBS
Monolayer	Washing solution	0.1% volume per volume (v/v) Tween® 20 dissolved in PBS
Monolayer	Antibody solution	1% (w/v) BSA, 0.3% (v/v) Triton® X-100 dissolved in PBS
Monolayer	DAPI-solution	1 µg/ml DAPI dissolved in washing solution (see below)
Spheroids	PVP/PBS	3 mg/ml PVP dissolved in PBS
Spheroids	Permeabilization solution	0.25% (v/v) Triton® X-100 dissolved in PBS
Spheroids	Blocking solution	0.1% (w/v) BSA and 0.01% (v/v) Tween® 20 dissolved in PBS
Spheroids	BA/BB (1:2)	Benzyl alcohol (BA) mixed with benzyl benzoate (BB) at a ratio of 1:2

2.10.1 2D immunostaining

The total volume used per each solution was 100 µl. All incubation steps were done on a rocking platform and all washing steps were repeated thrice à 5 min. Initially, cells were washed in PBS and fixed for 10 min at RT in PFA/PBS. After another washing step with PBS, cells were incubated with blocking solution for 15 min at RT. Cells were rinsed in washing solution and were incubated with the primary antibody (anti-YAP; 1:100 dissolved in antibody solution) for 19 h – 24 h at 4 °C. Further washing steps were performed with washing solution. Cells were washed prior to the incubation with the species-specific secondary antibody (donkey-anti-mouse; conjugated to AF647; 1:200 dissolved in antibody solution) for 1 h at RT in the dark. Subsequently, cells were washed and stained for the nucleus for 5 min at RT with DAPI-solution. Finally, cells were washed again and cells recorded with the cLSM FluoView3000 at 100× or 600× magnification with exλ/emλ at 405 nm/461 nm and 640 nm/671 nm.

2.10.2 3D immunostaining

The procedure is adapted from the method described in our previous work [161]. For examination of the cellular organisation within the spheroid, MB-231 are identified based on the proliferation marker Ki67 [15] or the highly activated p53 [23]: The primary murine CAFs are identified based on the marker for activated myofibroblast, that is alpha smooth muscle actin [195].

At least five round shaped spheroids per treatment group were combined in a 1.5 ml reaction tube using a cut 100 µl pipette tip. All the following incubation steps were performed on a rocking platform. To collect spheroids, they were centrifuged for 15 sec to 60 sec at a maximum of 2000 rpm ($\times g$) using a microcentrifuge. For structure preservation, the spheroids were fixed for 1 h in PFA/PBS. The spheroids were washed thrice in PVP/PBS and stores for no longer than fourteen days at 4 °C. For cell permeabilization, the spheroids were incubated for 1 h in the permeabilization solution and unspecific areas were blocked using the blocking solution for another 1 h at RT. Combination of primary and secondary antibodies to identify tumour cells and CAFs within the co-culture spheroids are listed in **Table 2-22**. Antibodies were diluted in blocking solution. Antibody labeling was performed overnight (19 – 24 h) at 4°C with 100 µl blocking solution containing the primary antibodies targeting Ki67, p53 or α SMA. Afterwards, spheroids were washed thrice for 15 min with blocking solution. The species-specific secondary antibody and DAPI were diluted in a total of 200 µl blocking solution, and antibody labelling was performed overnight (19 - 24 h) at 4°C. Spheroids were again washed thrice for 15 min with blocking solution and were subsequently dehydrated by applying ethanol at increasing concentration (diluted in ddH₂O). For that, the spheroids were incubated for 30 min at RT (without rotation) in each ethanol solution in the following order: 30%, 50%, 70%, 90%, 96% and twice in 100% ethanol. For clearing the cell structure, the spheroids were incubated for at least 1 h at RT (without rotation) in the BA:BB solution. Finally, spheroids were transferred to a black 96-well plate (square wells) using a cut 100 µl pipette tip. As little as possible of the BA:BB solution was transferred to avoid minimal movements of the spheroids during microscopic imaging. For transfer, spheroids could be made visible using the inverted fluorescence microscope with ex λ /em λ at 365/445 nm/BP50. Spheroids could be stored at 4°C up to 14 days until analysis. Spheroids were recorded using the cLSM LSM880 at 200 \times magnification with ex λ /em λ at 405 nm/442 nm, 488 nm/522 nm, 561nm /588 nm and 633 nm/ 703 nm.

Table 2-22 Antibody combination used for examining the cell type distribution within co-culture spheroids

Primary antibody	Secondary antibody	Conjugate
Mouse, anti- α SMA	Donkey anti-mouse	AF647
Rabbit, anti-Ki67	Donkey anti-rabbit	AF546
goat, anti-p53	Donkey anti-goat	AF488

2.11 3D TNBC co-culture establishment

To emulate the TNBC microenvironment for drug screening, spheroids were composed of MB-231 and primary murine CAFs in a collagen-based matrix. Co-culture medium is composed of a cell culture media mixture of DMEM:RPMI (1:1) supplemented with 12.5% FCS, 1% Pen-Strep and collagen type I. Optimal seeding conditions were determined with testing various cell seeding number, MB-231:CAF cell ratio, collagen concentration with evaluation of spheroid growth and cellular organisation to defined within the spheroids (2.11.1, 2.11.2, 2.11.3)

2.11.1 Selecting the seeding cell number

On day one, 50 μ l of the individual cell suspension was seeded on a cell repellent U-bottom 96-well plate. A total of 1500 cells were seeded, each with MB-231:CAFs at ratio of 2:1, 1:2 and 1:4, or a total of 3000 cells were seeded, each with MB-231:CAFs at a ratio of 2:1, 1:1, 1:2 and 1:4. Spheroids in each cellular composition was grown in co-culture medium supplemented with 0.05 mg/ml, 1 mg/ml or 0.3 mg/ml collagen type I. To evaluate the optimal spheroid formation, the cells were either directly incubated or exposed to mechanical forces with centrifugation for 10 min at $136 \times g$ using the plate centrifuge prior to incubation. On day two, 50 μ l of the individual culture medium containing the final concentration of collagen type I was added. Spheroids were grown for a total of 144 h and were imaged using the inverted brightfield microscope Axio Vert.A1 at 50 \times and 100 \times magnification. Spheroid shape was evaluated based on the brightfield images. Optimal co-culture conditions were selected to examine the cellular distribution of each cell type within the spheroid structure (chapter 2.11.2)

2.11.2 Spheroid characterization to determine culture conditions

For further spheroid characterization, co-culture conditions were chosen that showed reproducible round and compact spheroids. For that, on day one, 90 μ l of the co-culture cell suspension was seeded on a cell repellent U-bottom 96-well plate. A total of 3000 cells were seeded with a MB-231:CAFs ratio of 1:1 and 1:2. Spheroids in each cellular composition were grown in co-culture medium supplemented with 0.05 mg/ml, 0.1 mg/ml or 0.3 mg/ml collagen type I. On day four, 11 μ l medium without collagen was applied, which is equal to the volume for compound treatment. Spheroids were grown for a total of 144 h and were imaged using the inverted brightfield microscope. The spheroid size was measured in the brightfield images as described in **Figure 2-14**. On day seven, spheroids were collected for analysis of the cellular organisation within the spheroids according to the 3D immunostaining protocol (2.10.2).

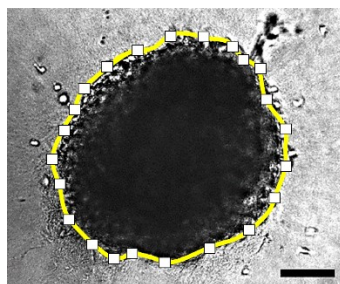


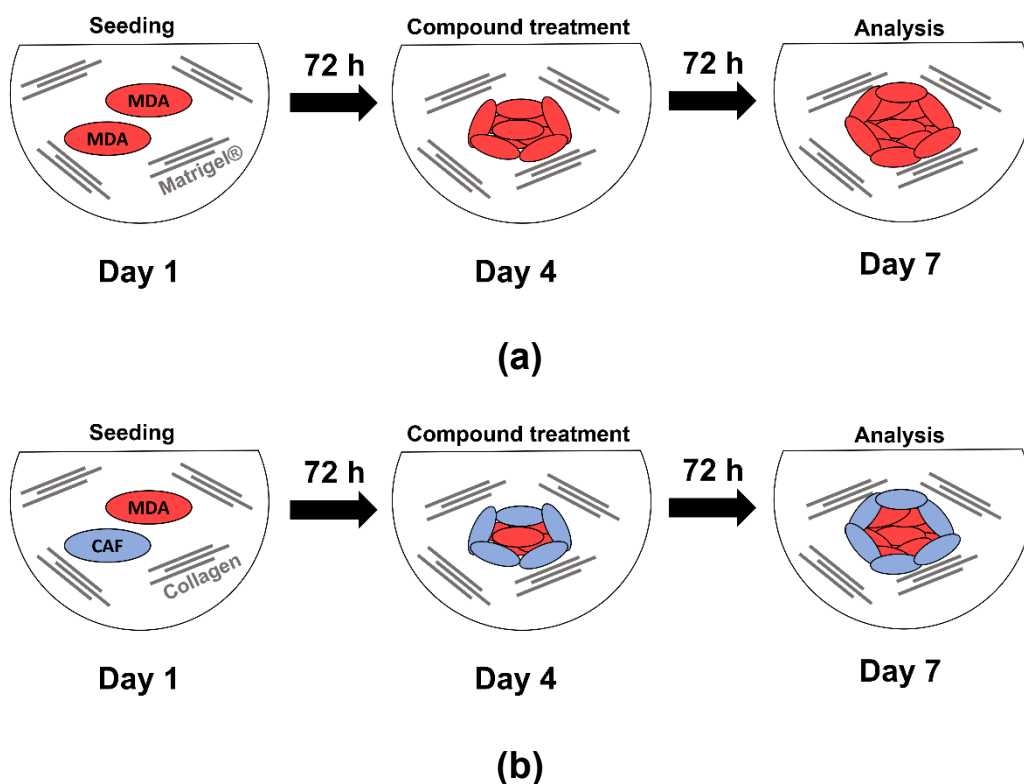
Figure 2-14 Spheroid size measurement. Representative brightfield image for spheroids. Here: Seeded with a total of 3000 cells (MB-231:CAF, 1:2) and grown for a total of 144 h in 0.05 mg/ml collagen type I. Spheroid size was quantified by determining the spheroid area in brightfield images using the open-source software Fiji. The outline of the spheroid (yellow line) is determined by manually picking positions (white squares). Scale bar: 200 μ m.

2.11.3 3D co-culture formation

To emulate the TNBC microenvironment, optimal conditions were selected (2.10) to generate spheroids comprising MB-231 and CAFs. On day one, 50 μ l cell suspension was seeded on a cell repellent U-bottom 96-well plate. The cell suspension contained MB-231 at a density of 2×10^4 cells/ml and CAFs at a density of 4×10^4 cells/ml. On day two, another 50 μ l co-culture medium containing the final collagen concentration was applied. On day four, spheroids were treated according to the method section of the cell viability testing (2.7.3), immunofluorescence studies (2.12.3) and growth studies (2.12.2). On day seven, after 72 h treatment, spheroids were analysed regarding their method.

2.12 TYLO-1 characterization in the 3D TNBC model

For mimicking the cellular organisation of TNBC tumours, monoculture spheroids were generated starting with a total of 3000 MB-231 cells, that were grown in an ECM supplemented with matrigel® (2.12.1). To include characteristic stromal cells from the TNBC TME, a co-culture was established that additionally comprises primary murine CAFs at a ratio of 1:2 (MB-231:CAF) (0, 2.11.3). Co-culture spheroids were grown in an ECM supplemented with type I collagen. The treatment course of monoculture or co-culture studies is depicted in **Scheme 1**. Spheroids were allowed to form for 72 h. Solid and round shaped spheroids were chosen for compound treatment for another 72 h and were subsequently analysed for growth (2.12.1, 2.12.2), cell viability (2.7.3) or cellular organisation of the cell types within the co-culture spheroids (2.12.3).



Scheme 1 Treatment course for the 3D TNBC spheroid studies. Components of the 3D TNBC spheroids are shown per well of a cell repellent U-bottom 96-well plate. Cells including ECM components were seeded on day one. After 72 h spheroid formation, the compound was conducted for another 72 h. On day seven, the spheroids were used for analysis. **(a)** Monoculture spheroids of MB-231 (MDA) were formed in a matrigel®-based matrix and **(b)** co-culture spheroids composed of MB-231 or MB-468-UnaG tumour cells (MDA) and primary murine CAFs (CAF) were formed in collagen-based matrix.

2.12.1 3D monoculture growth in matrigel®

To study TNBS spheroid growth in an extracellular matrix (ECM)-like environment, spheroids of MB-231 were generated in the presence of matrigel® [181]. On an ultra-low-attachment 96-well plate, 50 µl were seeded with a density of 6×10^4 cells/ml in 0.25% matrigel®. For cell aggregation, cells were centrifuged for 10 min at $136 \times g$ at constant 4°C before grown for 72 h at 37°C. On day four, 50 µl of double-concentrated substance was added to obtain following concentration of TYLO-1: 12.5 nM, 25 nM, 50 nM or 100 nM. Culture medium served as negative control and 10 µM of the MEK1/2 inhibitor, namely U0126, served as an anti-proliferative agent. Spheroid growth was allowed for another 72 h and at least two spheroids per treatment group were recorded pre-treatment (72 h after seeding) and post-treatment (144 h after seeding) using the inverted brightfield microscope. The spheroid size was measured in the brightfield images as described (**Figure 2-14**).

2.12.2 3D co-culture growth in collagen type I

After co-culture spheroid formation for 72 h, 5 to 6 spheroids for each treatment group were chosen. 11 µl of the ten-fold higher concentrated compound were applied to obtain 100 nM TYLO-1 or 100 nM paclitaxel. Co-culture medium served as the untreated control. Spheroids incubated for another 72 h. At least three spheroids were recorded per treatment group before and after treatment, on day four and day 7, using the inverted brightfield microscope Axio Vert.A1 at 100x magnification. The spheroid size was determined as described (**Figure 2-14**). In each independent experiment, spheroid size was normalized to the smallest area (which was set to 0%) and to the highest area (which was set to 100%).

2.12.3 3D co-culture cell type distribution

After co-culture spheroid formation for 72 h, 5 to 6 spheroids per treatment group were chosen. 11 µl of the ten-fold higher concentrated compound were applied to obtain 100 nM TYLO-1 or 100 nM paclitaxel. The spheroids were grown for another 72 h, before they were collected for 3D immunostaining (2.10.2).

2.13 Hypoxia studies

To investigate compounds under hypoxic conditions, we utilized the UnaG-reporter cell line MB-468-UnaG. To investigate HIF-1α activity in 2D monolayer cells, HIF-regulated UnaG expression was measured 24 h post-treatment under CoCl₂-simulated hypoxia (2.13.1). To further evaluate hypoxia in a 3D TNBC model, we established 3D co-culture spheroids comprising MB-468-UnaG and primary murine CAFs (2.13.2).

2.13.1 Hypoxia Inducible Factor (HIF)-1 α -inhibition

On day one, 100 μ l containing MB-468-UnaG cells at a density of 1.5×10^5 cells/ml was seeded on a black 96-well plate. On day two, the medium was replaced with 100 μ l culture medium containing TYLO-1s or BAY 11-7085 at the final concentration. Culture medium served as control. The cells were pre-treated for 1 h before grown for another 24 h in the absence (normoxia) or presence of the hypoxia-mimetic CoCl_2 (hypoxia). For hypoxia studies, 11 μ l of the ten-fold higher concentrated CoCl_2 were applied to obtain final 100 μM CoCl_2 . HIF-regulated UnaG expression was recorded in z-stacked images using the high-content imager CQ1 at 100 \times magnification. UnaG fluorescence intensity was determined in UnaG-expressing cell clones using the integrated CellPathfinder software as described in **Figure 2-15**.

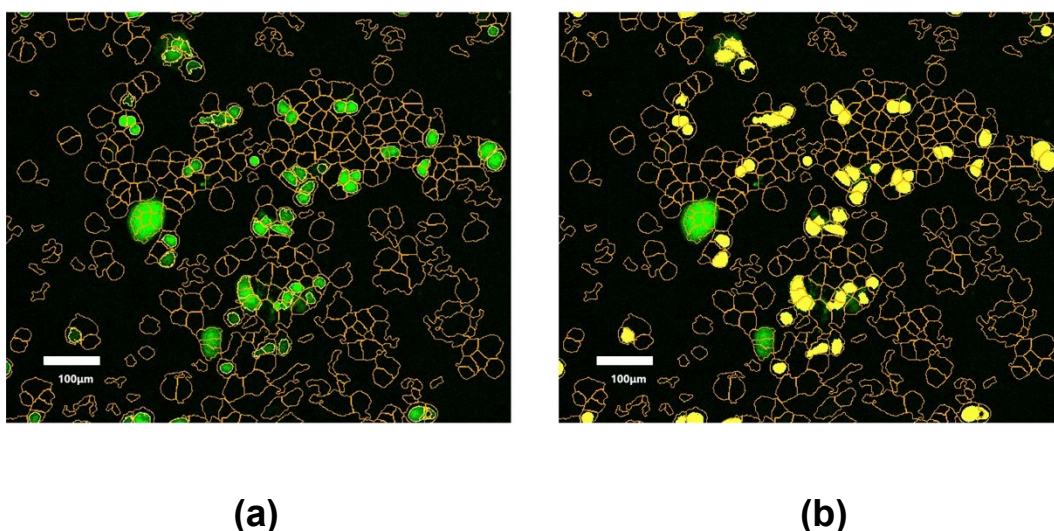


Figure 2-15 Quantification of UnaG expression in MDA-MB-468-UnaG (MB-468-UnaG) cells. Fluorescence images were recorded using the high-content imager CQ1 at 100 \times magnification. Cells, recorded using brightfield, were recognised by a machine learning algorithm (yellow outlines). **(a)** HIF-1 α -dependent UnaG expression (green area) was recorded in the 488 nm channel. Despite cell clone selection of HIF-mediated UnaG expressing cells, UnaG is not expressed in all cells. Thus, **(b)** UnaG expressing cells are recognised within a particular cell size (yellow area). Fluorescence intensity of UnaG was measured within the UnaG expressing cells. Scale bar: 100 μm .

2.13.2 3D TNBC co-culture to study hypoxia

To emulate the hypoxic TNBC microenvironment for drug screening, spheroids were composed of the hypoxia sensor TNBC cell line MB-468-UnaG and primary murine CAFs in a collagen-based matrix. Co-culture medium is composed of a cell culture media mixture of DMEM:RPMI (1:1) supplemented with 10% FCS, 1% Pen-Strep and collagen type I. First,

different conditions regarding the cell seeding number, ratio of cell type and collagen concentration were tested (2.13.2.1). Using optimal co-culture conditions to generate round shaped spheroids, we analysed cell type distribution and growth under CoCl₂-simulated hypoxia (2.13.2.2).

2.13.2.1 *Establishment of co-culture spheroids*

To establish the seeding cell number, co-culture spheroid with a total of 1500 cells or 3000 cells were seeded with a ratio MB-468-UnaG:CAFs ratio at 1:1, 1:2 and 1:4. Each cell mixture was grown in either 0.05 mg/ml or 1 mg/ml collagen type I. On day one, 50 µl of the cell mixture containing collagen was seeded on a cell repellent U-bottom 96-well plate. Cell-collagen mixture was pre-cooled on ice prior to seeding. On day two, 50 µl co-culture medium containing the final collagen concentration was added. On day four and day 7, spheroids were recorded using the inverted brightfield microscope Axio Vert.A1 at 100× magnification. The spheroid shape was evaluated based on microscopic images and the spheroid size was determined using Fiji as described in **Figure 2-14**. Optimal co-culture conditions were defined based on the spheroid shape and growth behaviour.

2.13.2.2 *Analysing the TNBC co-culture spheroids under hypoxia*

With evaluating different seeding conditions, the co-culture spheroid generation was similar to the 3D TNBC co-culture studies using MB-231 (2.11.3). Spheroids were generated starting with a total of 3000 cells and with MB-468:CAF at a ratio of 1:2 dissolved in co-culture medium that was supplemented with 0.05 mg/ml collagen type I. On day one, 50 µl cell suspension were seeded on a cell repellent U-bottom 96-well plate. The cell suspension contained MB-468-UnaG at a density of 2×10^4 cells/ml and CAFs at a density of 4×10^4 cells/ml in co-culture medium. On day two, another 50 µl co-culture medium were applied. On day four, at least five spheroids were treated with co-culture medium (untreated control) and to induce hypoxia with 100 µM or 200 µM CoCl₂. On day four and day seven, spheroids were recorded using the inverted brightfield microscope Axio Vert.A1 at 50× magnification and spheroid size was measured using Fiji as described in **Figure 2-14**. On day seven, five spheroids per treatment group were collected for analysing the cellular organisation within the spheroids as described in the method “3D immunostaining” (2.10.2). Because both, MB-468-UnaG and CAF express a fluorescence protein that is excited at 488 nm, we stained for cells using DAPI and for CAFs using an antibody against αSMA (origin mouse) and a species-specific antibody (goat-anti-mouse) that is conjugated with AF647. Z-stacked images of the spheroids were captured using the high-content imager CQ1 with exλ/emλ at 405 nm/447 nm/BP60, 488 nm/525 nm/BP50 and 640 nm/685 nm/BP40. For evaluation of HIF-1α mediated UnaG expression, fluorescence intensity of UnaG was analysed in UnaG

expressing cells within the z-stacked images of the spheroids using the CellPathfinder software as described in **Figure 2-15**.

2.14 Western blot

Modulation of NF κ B activity by TYLO-1s was evaluated based on the quantification of the protein level of the NF κ B inhibitor, namely I κ B α . For method establishment, the I κ B α protein level was analysed in MB-231 (compare 2.14.1) after exposure to BAY 11-7085 at a final concentration of 10 μ M or 20 μ M and exposure to TNF α at a final concentration of 10 ng/ml or 20 ng/ml. Based on immunoblotting, total I κ B α protein was quantified in MB-231 (2.14.1) and in MB-468-UnaG under normoxic (2.14.2.1) as well as under CoCl₂-simulated hypoxic (2.14.2.2) conditions.

2.14.1 I κ B α protein level in MB-231

On a flat-bottom 6-well plate 2.5 x10⁵ MB-231 cells were seeded in a total of 2 ml and cells were allowed to attach for 24 h. For treatment on the next day, medium was replaced with fresh culture medium containing the compounds at the final concentration in a total of 2 ml. Culture medium served as untreated control. Cells were pre-treated for 1 h at 37°C before stimulation with 5 ng/ml TNF α for 30 min to induce NF κ B signalling and thus I κ B α degradation. After treatment, I κ B α protein was analysed with SDS polyacrylamide gel electrophoresis (SDS-PAGE) and immunoblotting (2.14.3).

2.14.2 I κ B α protein level in MB-468

2.14.2.1 TYLO-1s treatment under normoxic conditions

On a flat-bottom 6-well plate 3.5 x10⁵ MB-468-UnaG cells were seeded in a total of 2 ml and the cells were allowed to attach for 48 h, which is equal to a treatment under hypoxic conditions (compare 2.14.2.2). For treatment, the medium was replaced with fresh culture medium containing TYLO-1s at the final concentration in a total of 2 ml. The culture medium served as untreated control. The cells were pre-treated for 1 h at 37°C before applying 10 ng/ml TNF α for 30 min to induce NF κ B signalling and thus I κ B α degradation. After the treatment, I κ B α protein was analysed with SDS-PAGE and immunoblotting (2.14.3).

2.14.2.2 TYLO-1s treatment under CoCl₂-induced hypoxic conditions

On day one, 3.5 x10⁵ MB-468-UnaG cells were seeded on a flat-bottom 6-well plate in a total of 2 ml and were allowed to attach for 24 h. On day two, to induce hypoxia, the medium was replaced with 100 μ M CoCl₂ in a total of 2 ml culture medium and the cells were incubated for further 24 h. On day three, the medium was replaced with fresh culture

medium containing TYLO-1s at the final concentration in a total of 2 ml with 100 μ M CoCl₂. The culture medium with and without CoCl₂ served as untreated control. Cells were pre-treated for 1 h at 37°C before application of 10 ng/ml TNF α for 30 min to induce NF κ B signalling and thus I κ B α degradation. After treatment, I κ B α protein was analysed with SDS-PAGE and immunoblotting (2.14.3).

2.14.3 SDS-PAGE and immunoblotting

All solutions that were manually prepared are listed in **Table 2-23**. After treatment, cells were pre-cooled on ice for harvesting and washed twice in ice-cold PBS before 30 min incubation in 100 μ l RIPA lysis buffer at 4 °C. Cells were detached by scratching using a commercial cell scraper or a manually bended 100 μ l pipette tip. Detached cells were collected and mixed vigorously by vortexing. To isolate proteins from cell debris, cells were centrifuged for 15 min at 14,000 \times g using the pre-cooled (4 °C) micro centrifuge micro centrifuge himac CT15RE. The supernatant containing the proteins could be stored at -20°C. To enable loading of the same protein amount, the protein concentration was determined in duplicated using the Bradford-Reagent according to the manufacturer's instruction. BSA was used as a standard protein control in a concentration range with increasing by 0.2 mg/ml: 0.2, 0.4, 0.6, 0.8 and 1.0 mg/ml. Prior to measurement, cell lysates were diluted ten-fold in sterile ddH₂O. Using a (white) flat bottom 96-well plate, 5 μ l of the protein or BSA samples were transferred per well. After injection of 250 μ l Bradford reagent, the cells incubated for 10 – 30 min at RT before the absorbance was measured at 590 nm using the multimode microplate reader OPTIMA. The final protein concentration in the cell lysates was automatically calculated with the integrated software. For protein denaturation, 25 μ l containing 20 μ g protein was dissolved in 1 \times SDS sample buffer or 1 \times laemmli buffer. The protein samples were boiled for 10 min at 95 °C, and, to remove cell debris, samples were centrifuged for 10 min at 14,8000 rpm using the micro centrifuge himac CT15RE. To ensure equal protein transfer, 24.5 μ l were loaded to a precast 12% polyacrylamide-gel. Proteins and a standard protein ladder were separated with performing an SDS-PAGE at a constant voltage of 120 V in 1 \times running buffer. Nitrocellulose membrane, gel and two blot filter papers were soaked for 15 min in blotting buffer. For protein transfer from the gel to the nitrocellulose membrane, semi-dry blotting was performed for 40 min at constant 20 V. All of the following incubation steps were performed on a rocking platform. The protein containing membrane was washed for 5 min in TBST buffer, blocked for at least 30 min in 5% BSA dissolved in TBST (BSA/TBST) and washed in TBST again. The membrane was probed overnight at 4 °C with the antibody against I κ B α (1:1000 diluted in 1% BSA/TBST) or against the housekeeping protein (HKP) vinculin (1:1000 diluted in 1% BSA/TBST). To remove residual antibodies, the membrane was washed four-times à 5 min in TBST, probed

with species-specific HRP-conjugated secondary antibodies (1:5000 diluted in 1% BSA/TBST) for at least 1 h at RT and washed four-times à 5 min in TBST. According to the manufacturer's instruction, the membrane incubated for 5 min at RT with the chemiluminescent-substrate. Chemiluminescence was recorded using the imager Fusion Pulse^{TS}. The protein level was quantified based on the protein volume within the protein lane using the provided software EvolutionCapt: the background was subtracted for each protein lane separately. The normalization of the target protein (IκBα) was done according to the "Housekeeping Protein Normalization Protocol" provided by Licor [196]. However, the calculation is summarized in **Equation 2**. In brief, lane normalization factor of the HKP was determined by dividing the chemiluminescence signal of the HKP lane by the signal of the HKP lane with the highest signal, here the untreated control. To normalize the target protein signal, the signal of the protein lane was divided by the lane normalization factor calculated for this lane.

Equation 2 Calculation of the relative IκBα protein level in western blot studies.

HKP normalization:	$\frac{\text{lane } x \text{ within the HKP}}{\text{lane with the highest signal}} = \text{lane normalization factor (LNF)}$
Target protein normalization:	$\frac{\text{lane } x \text{ within the target protein}}{\text{LNF calculated for lane } x} = \text{normalized protein}$
Relative target protein:	$\frac{\text{normalized protein for lane } x}{\text{normalized protein for TNFα treated cells}} = \text{relative protein}$

"Lane x" is defined as the lane of choice and describes the protein level that was recorded as the luminescence signal in the protein lane x.

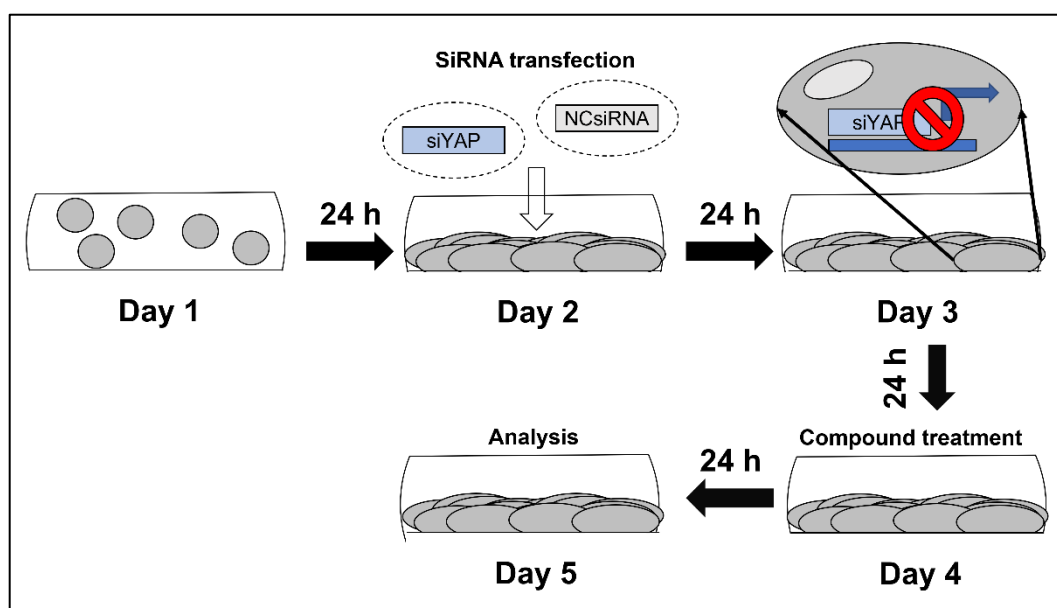
Table 2-23 List of manually prepared solutions for western blot studies

Solutions	Chemical agents
TBST; tris buffered	
saline with Tween® 20 (stored at 4 °C)	50 mM Tris-HCl; 150 mM NaCl (pH 7.4); 0.1% Tween® 20
RIPA lysis buffer (stored at -20°C)	50 mM Tris/HCl (pH 7.5); 1% Triton® X-100; 0,5% sodium-deoxycholate; 0.1% SDS; 150 mM NaCl; 1 mM EDTA; one pill protease-inhibitor Pierce ® per ml; 1mM PMFS (PMFS is diluted in ethanol and stored at -20°C, and due to instability, it is added directly when used)
BSA standard	BSA dissolved in double distilled water (ddH ₂ O) to a concentration in the range of 0.2 - 1 mg/ml
5× SDS sample buffer	15 ml (20%) SDS; 25 ml glycerol; 12.5 mg bromphenol blue; dissolved in 750 mM tris-HCl (pH 7.5)
4× Laemmli buffer	10% Glycerol; 62.5 mM tris-HCl; 1% LDS; 0.005% bromphenol blue; 355 mM 2-mercaptoethanol

10× Running buffer for SDS-gel electrophoresis	(10×) 0.25 M Tris; 1.92 M glycine; 1% SDS in ddH ₂ O (1×) 25 mM Tris, 192 mM glycine, 1% SDS in ddH ₂ O
2× Blotting buffer	20% Methanol; 192 mM glycine; 25 mM tris.

2.15 Protein knockdown studies

In HMEC, or MCF10A, MB-231 or NFκB-MB-231-Firefly cells protein translation of p65 and YAP was blocked based on siRNA interference induced by Lipofectamine™-based siRNA transfection (2.15.1). Time scheme for siRNA transfection, compound treatment and analysis is depicted in **Scheme 2**. To assess modulation of the targeted protein after siRNA transfection in 2D monolayer cells, mRNA level of p65 and YAP was quantified with RT-qPCR (2.15.2.1, 2.15.3.1). To investigate activities of TYLO-1, cell viability was determined after p65 (2.15.2.2) as well as YAP knockdown (2.15.3.3), NFκB-inhibition was determined after YAP knockdown (2.15.3.2) and YAP inhibition was quantified in non-cancerous as well as cancerous cell lines (2.15.3.4).



Scheme 2 Treatment course for knockdown studies. Representative treatment course for knockdown studies is depicted for YAP for one well. Cells were seeded on day one, and on day two, siRNA transfection was conducted using siRNA-containing liposomes (dotted circles). The medium was exchanged on day three to remove the residual transfection agent Lipofectamine™. Knockdown based on siRNA interference was allowed for a total of 48 h before compound treatment was conducted on day four. Cell analysis was conducted 24 h post-treatment on day five.

2.15.1 Lipofectamine™-based siRNA transfection

On day one, cells were seeded with at a total volume of 100 µl (black 96-well plate), 500 µl (transparent 24-well plate) or 2 ml (transparent 6-well plate). Cell seeding density for all cell lines is listed in **Table 2-24**. On day two, siRNA interference was induced according to the manufacturer's instruction of the "Lipofectamine™ 3000" kit. For this, cells were transfected with a scrambled siRNA (NCsiRNA) or siRNA consisting of a complementary gene sequence to the mRNA of YAP (siYAP) or p65 (sip65). OPTI-MEM mixture with Lipofectamine™ served as vehicle control, transfection with NCsiRNA served as untreated control. Combination of transfection agents are summarized in **Table 2-25**, whereas 100ng siRNA (30 nM sip65 or 80 nM siYAP) were transfected. OPTI-MEM-Lipofectamine™ solution was mixed 1:1 with the OPTI-MEM-siRNA solution. For stabilization of the lipid-siRNA-complex, solution was incubated for at least 15 min at RT and was not mixed afterwards to avoid destroying the lipid complex. Lipofectamine™-siRNA mixture was applied to the cells while gently shaking the plate for optimal distribution of the lipid-siRNA complex. On day three, medium was replaced with fresh culture medium. On day four, cells were treated according to the experimental protocol to assess cell viability (2.7.2), NFκB-inhibition (2.5.2), as well as target gene expression (2.15.3.1, 2.15.2.1) or target gene activity (2.15.3.4). On day five, after 24 h compound incubation, treatment groups were analysed according to the specific experimental protocol.

Table 2-24 Cell seeding density for knockdown studies

Experiment	Plate	Cell line	Seeding cell number
Quantification of mRNA level	6-well, transparent	MB-231	3 × 10 ⁵ cells/well
		NFκB-MB-231-Firefly	3 × 10 ⁵ cells/well
Quantification of nuclear YAP	24-well, transparent	HMEC	2 × 10 ⁵ cells/well
		MB-231	1 × 10 ⁵ cells/well
Quantification of nuclear YAP after knockdown/treatment	96-well, black	MCF10A	3 × 10 ³ cells/well
		MB-231	4 × 10 ³ cells/well
		NFκB-MB-231-Firefly	4 × 10 ³ cells/well
Cell viability after knockdown/treatment	96-well, black	MB-231	6 × 10 ⁴ cells/well
NFκB-inhibition after knockdown/treatment	96-well, black	NFκB-MB-231-Firefly	1 × 10 ⁴ cells/well

Table 2-25 SiRNA mixture transfection agents and combination

Plate	Total volume of the Lipofectamine™-siRNA	Final siRNA concentration ¹	Lipofectamine™ per well	P3000 per well
-------	---	---	----------------------------	-------------------

mixture in OPTI-MEM				
	[μl]			
6-well ¹	250 μl	30 nM sip65 80 nM siYAP	7.5 μl	5 μl
24 well	50 μl	80 nM siYAP	1.5 μl	1 μl
96-well ²	10 μl	30 nM sip65 80 nM siYAP	0.3 μl	0.2 μl

¹ In total 100 ng siRNA were transfected.

2.15.2 P65 knockdown

2.15.2.1 P65 expression after p65 knockdown

P65 expression in MB-231 was evaluated by assessing the p65 mRNA level. On day one, cells were seeded in a total of 2 ml on a 6-well plate. Cell density is listed in **Table 2-24**. P65 knockdown was induced with siRNA transfection as described (2.15.1) using NCsiRNA or sip65. On day four, 48 h after transfection, cells were treated for 24 h with 100 nM TYLO-1 in serum-reduced culture medium (1% FCS). Culture medium served as untreated control. On day five, 72 h after transfection, cells were harvested and p65 mRNA level was determined according to the RT-qPCR protocol (2.6.2.2).

2.15.2.2 Cell viability after p65 knockdown

To examine whether reduced cell viability by TYLO-1 depends on NFκB/p65, we measured cell viability with prior p65 knockdown. On day one, a total of 100 μl MB-231 cells were seeded on a black 96-well plate. Cell density is listed in **Table 2-24**. On day two, p65 knockdown was induced with siRNA transfection as described (2.15.1) using NCsiRNA or sip65. On day three, medium was exchanged. The following procedure was performed according to the 2D PrestoBlue (2.7.2). On day four, 48 h after transfection, serial dilution of compounds was prepared in culture medium as described (2.2.6.2). For treatment in triplicates, 11 μl of the 10× concentrated compound was applied and cells incubated for 24 h. Final compound concentration for TYLO-1 is listed in **Table 2-15**. Culture medium (0.01% DMSO) and 20 μM cytotoxic staurosporine served control. On day five, cell viability-dependent fluorescence was measured according to the 2D PrestoBlue assay (2.7.2).

2.15.3 YAP Knockdown

2.15.3.1 YAP expression after YAP knockdown

YAP expression in MB-231 and NFκB-MB-231-Frefly was evaluated by assessing YAP mRNA level. On day one, cells were seeded in a total of 2 ml on a 6-well plate. Cell density is listed in **Table 2-24**. YAP knockdown was induced with siRNA transfection as described (2.15.1) using NCsiRNA or siYAP. On day four, 48 h after transfection, cells were treated

for 24 h with 100 nM TYLO-1 in cell culture medium. Culture medium served as untreated control. On day five, 72 h after transfection, cells were harvested and YAP mRNA level was determined according to the RT-qPCR protocol (2.6.2.2).

2.15.3.2 *NFκB-inhibition after YAP knockdown*

To examine if YAP plays a role in the anti-inflammatory effect of TYLO-1, NFκB activity was measured after YAP knockdown. On day one, NFκB-MB-231-Firefly were seeded in a total of 100 µl on a black 96-well plate. Cell density is listed in **Table 2-24**. On day two, YAP knockdown was induced with siRNA transfection as described (2.15.1) using NCsiRNA or siYAP. On day three, medium was exchanged. The following procedure was performed as described for NFκB-inhibition studies (2.5.2). On day four, 48 h after transfection, serial dilution of TYLO-1 was prepared in culture medium as described (2.2.6.2). For treatment in triplicates, 11 µl of the 10× concentrated compound was applied and cells incubated for 24 h. Final compound concentration for TYLO-1 is listed in **Table 2-15**. On day five, NFκB-dependent luminescence was measured according to the NFκB-inhibition assay (2.5.2).

2.15.3.3 *Cell viability after YAP knockdown*

To examine if reduced cell viability by TYLO-1 depends on YAP, we measured cell viability with prior YAP knockdown. On day one, a total of 100 µl MB-231 cells were seeded on a black 96-well plate. Cell density is listed in **Table 2-24**. On day two, YAP knockdown was induced with siRNA transfection as described (2.15.1) using NCsiRNA or siYAP. On day three, medium was exchanged. The following procedure was performed according to the 2D PrestoBlue (2.7.2). On day four, 48 h after transfection, serial dilution of compounds was prepared in culture medium as described (2.2.6.2). For treatment in triplicates, 11 µl of the 10× concentrated compound was applied and cells incubated for 24 h. Final compound concentration for TYLO-1 is listed in **Table 2-15**. Culture medium (0.01% DMSO) and 20 µM cytotoxic staurosporine served control. On day five, cell viability-dependent fluorescence was measured according to the 2D PrestoBlue assay (2.7.2).

2.15.3.4 *YAP-inhibition*

Transcriptional activity of YAP is determined by the nuclear YAP protein level that was measured upon immunostaining. YAP activity was analysed in HMEC und MB-231 with no prior stimulation (2.15.3.4.1) and in MB-231 and NFκB- MB-231-Firefly after TYLO-1 treatment (2.15.3.4.2). To assess investigate effects of TYLO-1 on YAP, YAP was knockdown and investigated in MB-231 in comparison to NFκB-MB-231-Firefly or in MCF10A in comparison to MB-231 (2.15.3.5.1).

2.15.3.4.1 YAP activity in non-cancerous cell lines

MB-231 and HMEC were seeded in a total of 500 µl on a 24-well plate. Cell density is listed in **Table 2-24**. The next day, staining for YAP and the nucleic DNA as well as fluorescence imaging was performed according to the 2D immunostaining (2.10.1).

2.15.3.4.2 YAP activity after TYLO-1 treatment

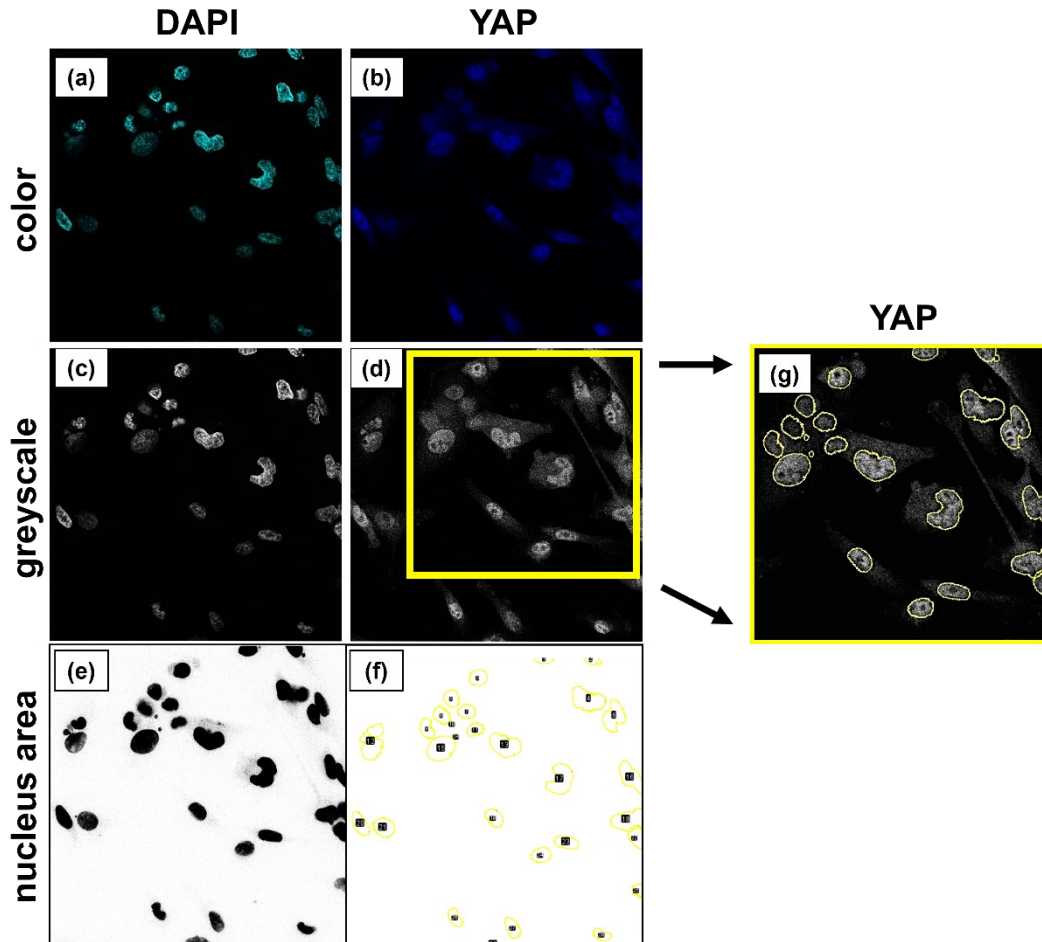
On day one, MB-231 and NFκB- MB-231-Firefly cells were seeded in a total of 100 µl on a black 96-well plate Cell density is listed in **Table 2-24**. On day two, cells were treated for 24 h with 100 nM TYLO-1. Culture medium served as untreated control. On day three, staining for YAP and the nucleic DNA as well as fluorescence imaging was performed according to the 2D immunostaining (2.10.1).

2.15.3.5 YAP activity after YAP knockdown and TYLO-1 treatment

On day one, MCF10A, MB-231 and NFκB-MB-231-Firefly cells were seeded in a total of 100 µl on a black 96-well plate Cell density is listed in **Table 2-24**. On day two, YAP knockdown was induced with siRNA transfection as described (2.15.1) using NCsiRNA or siYAP. On day three, medium was exchanged. On day four, 48 h after transfection, cells were treated for 24 h with 100 nM TYLO-1. Culture medium served as untreated control. On day five, staining for YAP and the nucleic DNA as well as fluorescence imaging was performed according to the 2D immunostaining (2.10.1).

2.15.3.5.1 Quantification of YAP activity

The nuclear YAP protein level in 2D monolayer cells was measured in at least two fluorescence images per treatment group using the open-source software Fiji as described (**Figure 2-16**) by performing batch analysis (6.4.1). For that, the nucleus area was determined based on the DAPI stained area. To determine nuclear YAP protein level, YAP was measured within the nucleus by quantification of the integrated density (IntDens) of fluorescence. The IntDens value is calculated by multiplication of the mean grey value and area (**Figure 2-16h**). For automatically saving colour or greyscale images of each recorded area (nucleus or YAP), batch processing was performed using Fiji (6.4.2).



(h) $IntDens(YAP) = mean\ grey\ value(YAP) \times area\ (combined\ ROIs\ for\ YAP)$

Figure 2-16 Quantification of the nuclear yes-associated protein (YAP) in monolayer cells. MB-231 cells were grown for a total of 96 h and stained for the nucleus (DAPI) and YAP according to the “2D immunostaining” protocol. Fluorescence images were analysed using Fiji with the following procedure: **(a, b)** Recorded fluorescence signal for the DAPI channel (cyan blue) and the YAP channel (blue) that were depicted as a coloured image were transformed to the **(c, d)** 8-bit image type (greyscale). **(e)** The area of the nucleus was determined in the DAPI channel by applying the colour auto threshold ‘Mean’. This nucleus area was transformed as a binary mask (the black area indicates the nucleus area). **(f)** The area of each nucleus was defined as the region of interest (ROI) for YAP (yellow outlines). **(g)** All ROIs were applied to the greyscale YAP channel and YAP fluorescence intensity was measured within all ROIs by assessing the integrated density (IntDens). **(h)** Equation to calculate the IntDens of the YAP protein within all ROIs (combined ROIs) and thus in all nuclei. The IntDens calculation was performed by Fiji as followed: The mean grey value for YAP is multiplied by the nucleus area that was determined in the greyscale YAP-channel.

2.16 Statistical analysis

The numeric results are depicted as mean \pm standard deviation (SD) or mean \pm standard error of the mean (SEM) derived from at least three independent biological replicates ($n = 3$). GraphPad Prism was utilized (I) for statistical analysis of data, (II) to calculate the half-maximal inhibitory concentration (IC_{50}) in drug dose–response studies and to illustrate (III) non-linear regression curves for drug dose–response studies, (IV) drug dose-response over time and (V) bars as well as stacked bars.

Statistical difference between two treatment groups was calculated with a two-tailed t -test. Statistical difference between more than two treatment groups was calculated with the one-way analysis of variance (ANOVA) or two-way-ANOVA with post analysis using Dunett's multiple comparison test for comparison of all groups with one another, or Tukey's multiple comparison test to compare all groups versus one control group. Statistical difference in 3D monoculture growth studies was calculated within all groups or vs. a control group using Šidáks multiple comparison test. Statistical significance is stated with a p value < 0.05 : ns = not significant, * $p < 0.05$; ** $p < 0.01$, *** $p < 0.001$).

3 Results

3.1 Anti-tumour characterization of phenanthroindolizidine alkaloids (P-alkaloids) isolated from the plant *Tylophora ovata* in TNBC

3.1.1 Pharmacological mode of action of P-alkaloids

3.1.1.1 *P-alkaloids block NFκB-mediated gene transcription through stabilization of the NFκB inhibitor IκBα*

To study anti-inflammatory potential of P-alkaloids (TYLO-1 to TYLO-6) in the TNBC, we utilized NFκB-dependent luciferase reporter cell lines and performed a western blot to assess modulation of the NFκB/p65 inhibitor IκBα. Additionally, we investigated a sample of the synthetically prepared O-methyltylophorinidine (TYLO-1s), the chemotherapeutic drug paclitaxel and the NFκB-inhibitor BAY 11-7085. To investigate suppression of tumour initiation, we evaluated TYLO-1 and paclitaxel in a colony formation assay.

Reduced NFκB-transcriptional activity is observed for TYLO-1 to TYLO-4 in a time- and dose-dependent manner. Among all compounds, TYLO-1 exhibits efficacious NFκB suppression within 2 h with an IC_{50} value of 17.1 ± 2 nM and within 24 h with a 5-fold decreased IC_{50} of 3.7 ± 1 nM (**Table 3-1, Figure 3-1**). Likewise, TYLO-2, TYLO-3 and TYLO-4 suppressed NFκB within 2 h with an IC_{50} of 211.8 ± 69.9 nM, 284.9 ± 60.4 nM, and 83.0 ± 14.7 nM, respectively. After 24 h, TYLO-2, TYLO-3 and TYLO-4 inhibited NFκB with a 5.5-fold ($IC_{50}=38.2 \pm 14.2$ nM), 2.5-fold ($IC_{50}=114.5 \pm 17.9$ nM) and 3-fold ($IC_{50}=28.3 \pm 5.6$ nM) decreased IC_{50} , respectively, indicating enhanced efficacy for P-alkaloids over time. NFκB-blockade after short time exposure to compounds indicates a modulation of NFκB, that is not dependent on NFκB transcription. To exclude cytotoxic effects as a cause of NFκB pathway suppression, we evaluated cell viability 24 h post-treatment (**Table 3-1, Figure 3-2, Table S 5**). Compared to NFκB blockade after 24 h, reduction of cell viability for TYLO-1 and TYLO-4 was observed at an around 4-fold higher concentration ($IC_{50} = 13.6 \pm 0.4$ nM and $IC_{50} = 127 \pm 21.4$ nM, respectively) and for TYLO-2 at a 2-fold higher concentration ($IC_{50} = 117.9 \pm 35$ nM). In contrast, TYLO-3 had a lower IC_{50} when comparing the IC_{50} for reduction in cell viability to NFκB-inhibition. Regarding cell viability that was analysed using another assay, namely 2D CellTiterGlo, effects of TYLO-3 were inconclusive, because this derivative was non-cytotoxic ($IC_{50} > 1000$ nM), while the active compounds (TYLO-1, TYLO-2, TYLO-4) maintained reduction of cell viability at a comparable concentration (**Table S 5**). Notably, compound TYLO-5 and TYLO-6 neither impaired NFκB activity ($IC_{50} > 1000$ nM), nor reduced cell viability ($IC_{50} > 1000$ nM). When

investigating the synthetic compound TYLO-1s we observed comparable effects to the plant-derived TYLO-1: NF κ B blockade within 2 h at an IC₅₀ of 3.3 ± 0.2 nM and reduction of cell viability within 24 h at an IC₅₀ of 4.2 ± 1 nM.

To investigate molecular targets upstream from NF κ B signalling, we evaluated the protein level of the NF κ B inhibitor I κ B α . At first, we optimized experimental conditions to investigate I κ B α stabilization upon NF κ B-blockade using BAY 11-7085 (**Figure S 2**). Initial testing of TYLO-1s revealed NF κ B-inhibition via stabilization of its inhibitor I κ B α (**Figure S 3**).

Time- and dose-dependent suppression of NF κ B-mediated gene transcription was also observed for BAY 11-7085 with an IC₅₀ of $5,500 \pm 2,000$ nM after 2 h treatment and an IC₅₀ of $12,623 \pm 1,542$ nM after 24 h treatment. Anti-inflammatory potential within 24 h correlates with reduction of cell viability at an IC₅₀ of $12,765 \pm 1,435$ nM (**Table S 6**), indicating a strong dependency on NF κ B-blockade for its cytotoxic effects. P-alkaloids display a high anti-tumour potential with displaying NF κ B-inhibition and cytotoxicity at a low nanomolar range, however, strong cytotoxicity was also observed for TYLO-1s in another TNBC cell line (MB-468-UnaG) with an IC₅₀ of around 4 nM and for TYLO-1 with an IC₅₀ of around 10 nM in non-cancerous cells, including primary murine CAFs, primary human PBMCs, and human breast epithelial cell line MCF10A (**Table S 7**, **Table S 8**).

Cytotoxicity of paclitaxel was observed at an IC₅₀ of 38.1 ± 9.3 nM. Notably, the commercially available paclitaxel is an anti-mitotic agent and therefore it is not surprising that we could not detect blockade of NF κ B within 2 h (IC₅₀ > 1000 nM), or after 24 h (IC₅₀ > 1000 nM) (**Table 3-1**). Interestingly, reduction of cell viability by TYLO-1 was stable over time with an IC₅₀ of around 10 nM after 24 h, 48h as well as 72 h, whereas paclitaxel showed time-dependent cytotoxicity with an IC₅₀ of around 40 nM within 24 h but an IC₅₀ of around 20 nM within 48 h, and an IC₅₀ of around 3 nM within 72 h (**Table 3-1**, **Table S 8**). Indicating, that paclitaxel efficacy depends on proliferation, while P-alkaloids exhibit another mode of action. Interestingly, cytotoxicity of P-alkaloids is comparable in MB-231 and MCF10A, whereas anti-mitotic paclitaxel has a slightly higher IC₅₀ of 56.6 ± 18.41 nM in MCF10A. However, TYLO-3 and TYLO-4 did not affect cell viability of MCF10A, although they were cytotoxic to cancer cells (**Table S 8**).

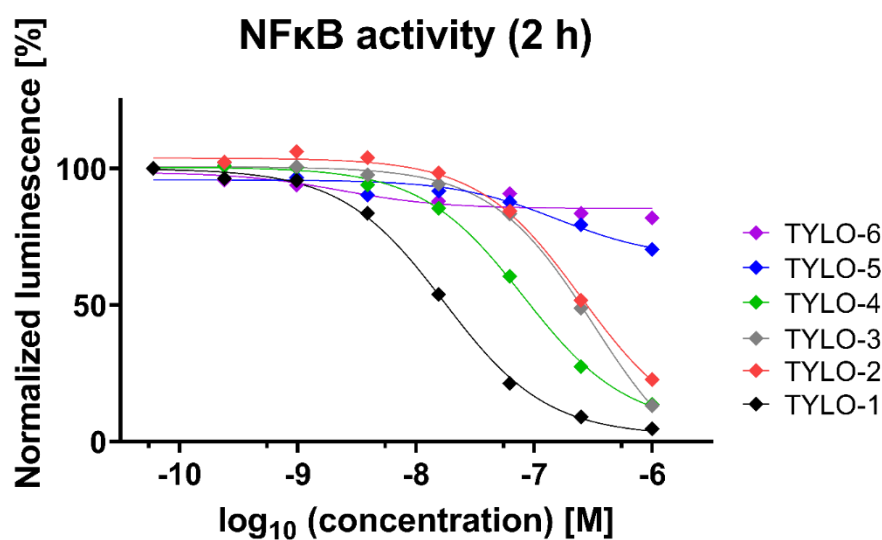
When evaluating modulation of tumour initiation, we found a dose-dependent blockade with a strong reduction of colonies at a concentration of 10 nM for both compounds, TYLO-1 and paclitaxel (**Figure S 4**). We decreased the concentration range for TYLO-1 (2.5 – 12.5nM) and found efficacious blockade of colony formation at concentrations < 10 nM. Blockade of colony formation correlates with the IC₅₀ measured for NF κ B inhibition. Noteworthy, colony formation may rely on blocking NF κ B signalling rather than reducing cell viability.

In conclusion, P-alkaloids block TNF α - and LPS-induced transcriptional activity of NF κ B in TNBC in a time- and dose-dependent manner. While the derivatives TYLO-1 and TYLO-1s exhibit superior NF κ B blockade, compound TYLO-3 may act through another mechanism. NF κ B blockade is mediated through stabilization of its inhibitor I κ B α . NF κ B may play a substantial role in the anti-tumour effects of P-alkaloids by regulating cell viability as well as tumour initiation potential.

Table 3-1 IC₅₀-values determined for P-alkaloids in NF κ B-inhibition and reduction of cell viability in TNBC

Compound	NF κ B-inhibition		Reduction of cell viability
	2 h ¹	24 h ²	24 h ^{3,4}
	IC ₅₀ [nM]	IC ₅₀ [nM]	IC ₅₀ [nM]
TYLO-1	17.1 \pm 2	3.7 \pm 1	13.6 \pm 0.4 ³
TYLO-2	211.8 \pm 69.9	38.2 \pm 14.2	117.9 \pm 35 ³
TYLO-3	284.9 \pm 60.4	114.5 \pm 17.9	55.3 \pm 13.2 ³
TYLO-4	83 \pm 14.7	28.3 \pm 5.6	127 \pm 21.4 ³
TYLO-5	>1000	>1000	>1,000 ³
TYLO-6	>1000	>1000	>1,000 ³
Paclitaxel	>1000	>1000	38.1 \pm 9.3 ³
TYLO-1s	3.3 \pm 0.2 ⁴	n.t. ⁵	4.2 \pm 1 ⁴

Compounds were tested in ¹ NF κ B-MB-231-NanoLuc, ² MB-231-Firefly using the NF κ B-inhibition assay or in MB-231 using the 2D PrestoBlue assay at a ³ high or ⁴ low seeding density. Mean \pm SD ($n=3$). ⁵ Not tested (n.t.)



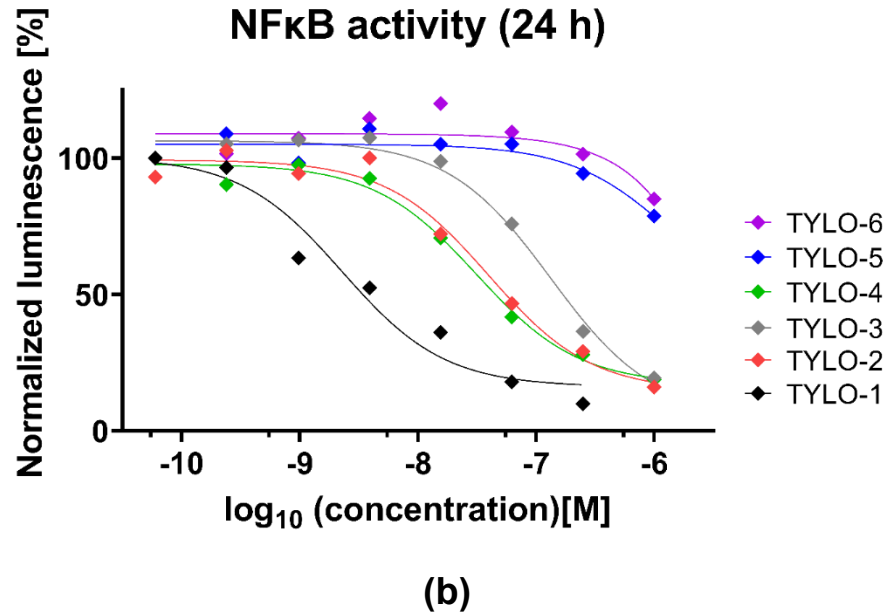


Figure 3-1 P-alkaloids blocked NFκB-mediated gene transcription in TNBC in a dose-dependent manner. The NFκB-dependent luminescence [RLU] was determined after **(a)** 2 h or **(b)** 24 h treatment according to the NFκB-inhibition assay. Concentration of compounds ranged in a four-fold serial dilution starting at 1000 nM. After 20 min pre-treatment with the compounds, cells were stimulated for further **(a)** 2 h using 1 μg/ml LPS or **(b)** 24 h using 20 ng/ml TNFα. In each independent experiment, luminescence was normalized to the RLU value of the lowest concentration applied (0.06 nM; 100%). Each data point represents the mean ($n=3$).

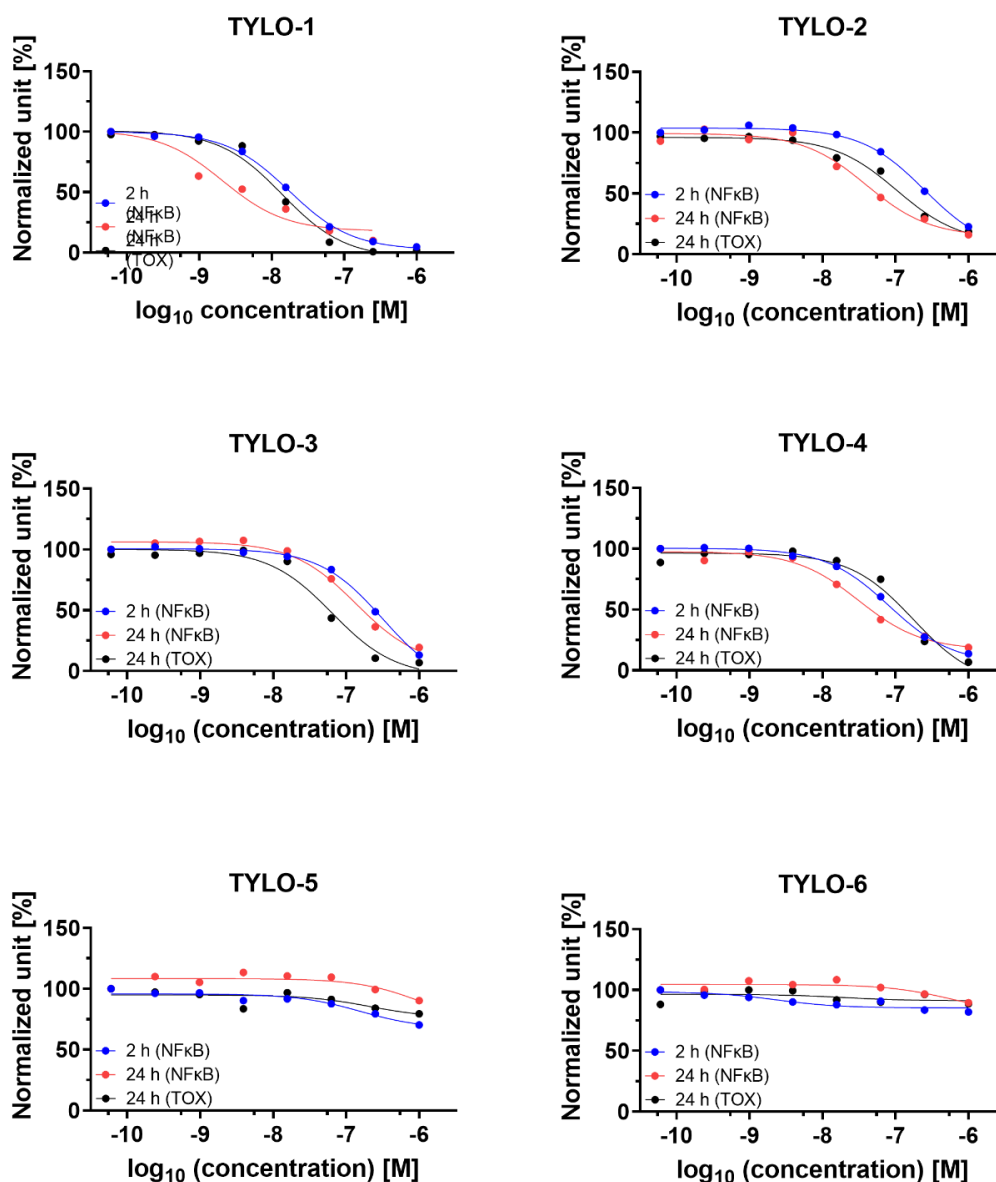


Figure 3-2 Time- and dose-dependent NFκB blockade by P-alkaloids in TNBC. Concentration of compounds ranged in a four-fold serial dilution from 1000 nM to 0.06 nM. (blue, red) NFκB-dependent luminescence [RLU] was determined post-treatment according to the NFκB-inhibition assay. After 20 min pre-incubation with the compounds, cells were stimulated for 2 h using 1 µg/ml LPS (blue) or for 24 h using 20 ng/ml TNFα (red). In each independent experiment, RLU values were normalized to the RLU value at the lowest concentration applied (0.06 nM; which was set to 100%; normalized unit). MB-231 cell viability-dependent fluorescence [RFU] was determined 24 h post-treatment according to the 2D PrestoBlue assay (TOX; black). Untreated cells and cytotoxic staurosporine at 20 µM served as control. In each independent experiment, RFU values were normalized to the highest RFU value (which was set to 100%) and to the lowest RFU value (which was set to 0%) (normalized unit). Each data point represents the mean of at least three independent experiments. Illustration from Reimche *et al.* (2022) [187].

3.1.1.2 Structure activity relationship (SAR) based on NFκB-inhibition

Evaluating differences in the chemical structures of P-alkaloids (TYLO-1 to TYLO-6), we identified critical functional groups that hint to a SAR. Chemical structure and distinct characteristics for a compound structure that promotes anti-inflammatory potential are summarized in **Figure 3-3**.

Differences in chemical structures of P-alkaloids are depicted in (**Figure 2-4**) and summarized in the following description: The core structure of all molecules is based on the scaffold of TYLO-1, which comprises a tricyclic phenanthrene ring fused to the bicyclic indolizidine ring. An α-hydroxyl group at the indolizidine ring is found in TYLO-1, TYLO-2, and TYLO-3. In comparison to TYLO-1, demethylation of one of the methoxyl groups at the phenanthrene ring is found in TYLO-2, TYLO-3, and TYLO-6. Unlike the other compounds, the nitrogen at the indolizidine ring in TYLO-5 and TYLO-6 is positively charged.

When comparing compounds to TYLO-1 regarding reduction of cell viability, loss of the methyl group at C-3 in compound TYLO-3 hints to an anti-tumour effect, which is NFκB-independent and needs further clarification.

When comparing compounds to TYLO-1 regarding NFκB blockade within 2 h, it is evident that loss of the methyl group at the phenanthrene ring decreased activity by a factor of 12 and 17 for TYLO-2 and TYLO-3, respectively. Presumably, activity is diminished through increased polarity resulting from methyl group loss in the methoxyl residuals at position C-3 (ring A) in compound TYLO-3 and at C-6 (ring C) in compound TYLO-2. Lacking the hydroxyl group at C-14 in the indolizidine ring, as found in compound TYLO-4, diminished NFκB suppression in comparison to compound TYLO-1 by a factor of 5. The compounds TYLO-5 and TYLO-6 possess a dehydrated nitrogen at ring D which results in a rigid and planar structure that significantly decreases activity when compared to TYLO-1 and TYLO-4, respectively. Thus, a positively charged nitrogen represents the most critical alteration regarding its anti-tumour and anti-inflammatory potential in TNBC.

In conclusion, initial SAR reveals that anti-tumour potential of P-alkaloids is enhanced in TNBC when possessing a hydroxyl group at position C-14 in the indolizidine ring and methoxyl groups at the phenanthrene ring at position C-3 and C-6. The planar structure and positively charged nitrogen at the indolizidine ring are dominant alterations that result in functional loss, as observed for compound TYLO-5 and TYLO-6.

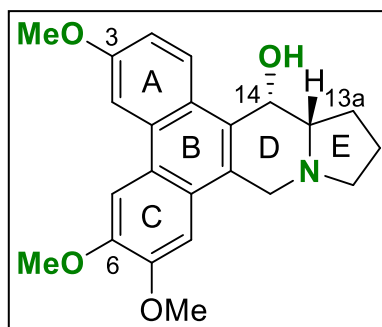


Figure 3-3 Initial structure-activity relationship (SAR) for P-alkaloids in TNBC. The scaffold of TYLO-1 to TYLO-6 is depicted with emphasis to the chemical groups that show major influence on blocking NF κ B signalling (green). Illustration was drawn with ChemDraw and is adapted from Reimche *et al.* (2022) [187].

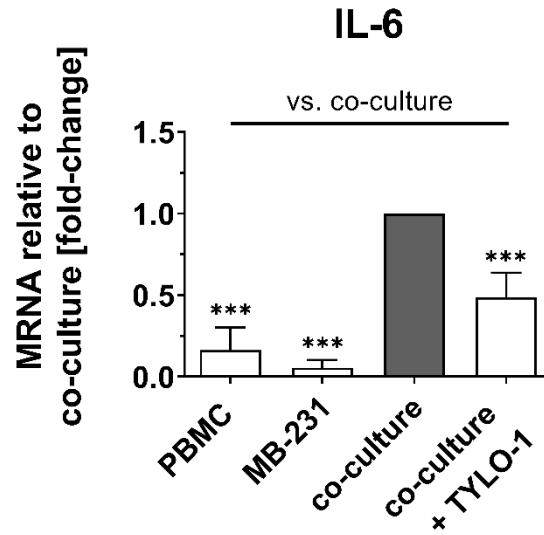
3.1.1.3 TYLO-1 suppresses NF κ B target gene expression to block paracrine signalling in a 2D co-culture of MB-231:PBMCs

To elucidate the bidirectional communication via cytokines in the TME, we assessed cytokine expression upon treatment with the anti-inflammatory TYLO-1.

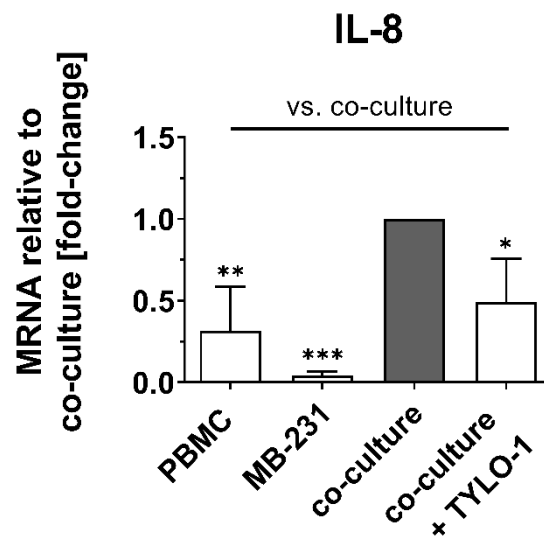
Expression of IL-6 and IL-8 were quantified in a 2D co-culture of MB-231 and PBMCs (1:1) using RT-qPCR (**Figure 3-4**). Remarkably, cytokine expression was significantly enhanced in the co-culture compared to the cell types alone. We could not detect cytokine expression in MB-231, whereas expression in solely naïve PBMCs varied by up to 32%. When exposing MB-231 to 100 nM TYLO-1 prior to co-culture, cytokine expression is significantly decreased by average 51% when compared to the untreated co-culture group.

Our results are inconclusive regarding the attribution of the individual cell type on cytokine expression and also in which cell type cytokine expression is mainly blocked in the co-culture. Thus, we aimed to investigate modulation of cytokine expression in MB-231 alone using a multiplex ELISA and RT-qPCR. First, we evaluated LPS-induced secretion of IL-8 in MB-231 and observed suppression at 10 nM, 100 nM and significant reduction in at 1000 nM TYLO-1 (**Figure 3-5**). Our data indicate dose-dependent suppression of IL-8 secretion, although, our data do not demonstrate statistical significance at non-cytotoxic concentrations. To examine modulation of cytokine expression we assessed the mRNA level after exposure to 7 nM TYLO-1 and observed a moderate reduction of expression for IL-6, but not for IL-8 (**Figure S 5**).

In conclusion, the 2D co-culture of PBMCs and MB-231 reconstituted the paracrine signalling with upregulation of the pro-inflammatory cytokines, IL-6 and IL-8. TYLO-1 was efficaciously blocking paracrine signalling through diminishing cytokine expression.



(a)



(b)

Figure 3-4 TYLO-1 significantly inhibited cytokine expression in a 2D co-culture of MB-231 and PBMCs. MB-231 were pre-incubated for 20 min without or with 100 nM TYLO-1, before PBMCs were applied at a ratio of 1:1 (co-culture). After 24 h incubation expression of (a) IL-6 or (b) IL-8 was quantified with RT-qPCR. Based on the $2^{-\Delta\Delta CT}$ method, fold change in cytokine expression was calculated by initial normalization to the housekeeping gene GAPDH and following normalization to the untreated co-culture group (which was set to 1). Bars represents the mean \pm SD of (a) ($n=4$) or (b) ($n=3$). Statistical difference vs. co-culture was calculated with one-way-ANOVA (* $p < 0.05$, ** $p < 0.01$, *** $p < 0.001$).

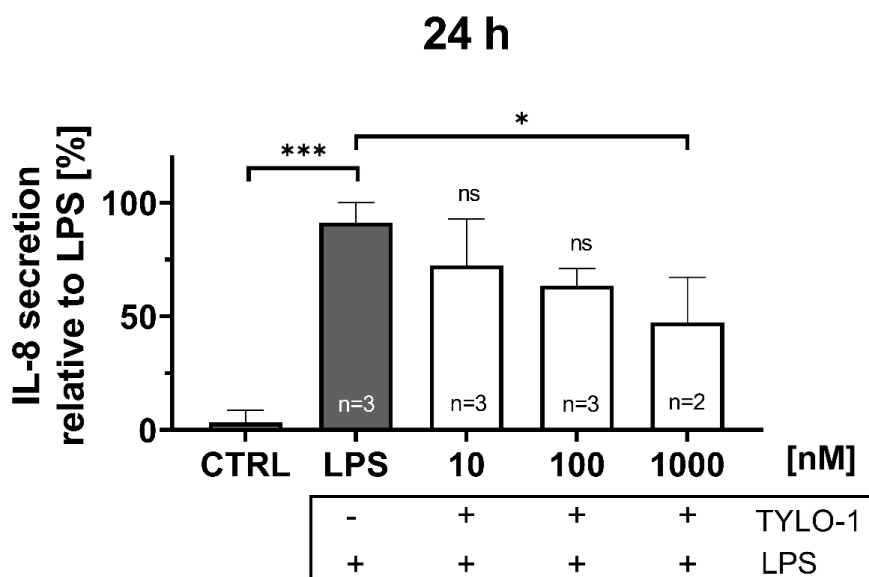


Figure 3-5 TYLO-1 decreased interleukin (IL)-8 secretion from MB-231. IL-8 secretion was determined 24 h post-treatment according to the multiplex ELISA assay. Cells were pre-incubated for 20 min with 10 nM, 100 nM or 1000 nM TYLO-1 before stimulation with 50 ng/ml LPS. Untreated (CTRL) or LPS stimulated cells served as control. IL-8 protein level was normalized to the lowest value (which was set to 0%) and highest value (which was set to 100%). Statistical difference was calculated vs. LPS using one-way-ANOVA (ns = not significant, * $p < 0.05$, *** $p < 0.001$). Bars represent the mean \pm SD ($n=3$).

3.1.1.4 RelA/p65 is dispensable for TYLO-1-induced cytotoxicity

To evaluate relevance of NF κ B (RelA/p65) expression for cytotoxicity of TYLO-1, p65 translation was blocked in MB-231 based on siRNA interference. Knockdown reduced p65 expression by up to 51% (**Figure 3-6**).

Reduction of MB-231 viability in the non-targeted group with an IC_{50} of 12.6 nM was comparable to the p65 targeted group with an IC_{50} value of 13.1 nM, respectively. However, the basic level of cell viability in the untreated non-targeted or p65-targeted group is also comparable. Indicating, that expression of p65 is irrelevant for the cell viability or that knockdown could be improved, due to a low reduction of p65 expression (**Figure 3-7**).

Summarized, these data suggest no relevance of p65 expression in compound activity, although TYLO-1 blocks NF κ B activity, presumably through post-translational modulation, such as inhibition of upstream regulators. Moreover, the lack of dependence on p65 indicates, that compound activity could rely on targeting multiple sites. Notably, knockdown studies could be improved, because our studies show low efficacy in protein diminution.

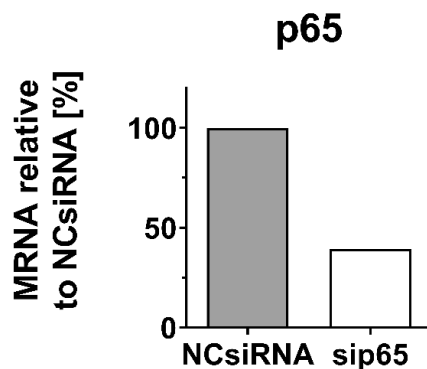


Figure 3-6 RelA/p65 knockdown in MB-231. P65 knockdown was induced in MB-231 with transfection of non-targeting siRNA (NCsiRNA) or p65-targeting siRNA (sip65). 72 h post-transfection, p65 mRNA level was quantified in duplicates with RT-qPCR. Based on the $2^{-\Delta\Delta CT}$ method, the p65 mRNA level was normalized to GAPDH, followed by normalization of the sip65 group against the NCsiRNA group. Bars indicate the mean of one individual experiment.

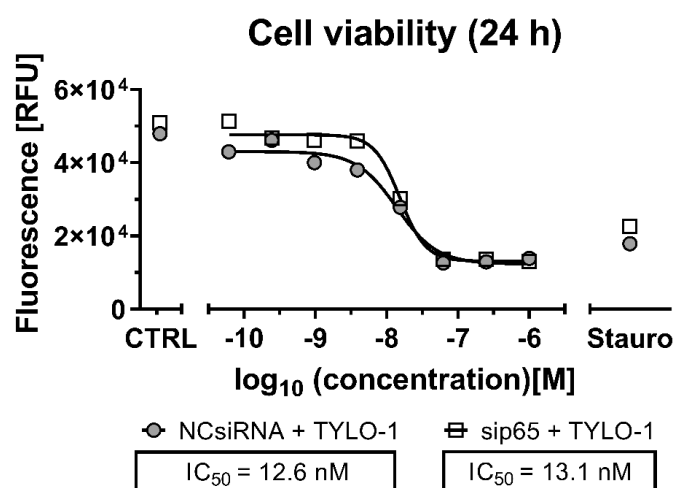


Figure 3-7 TYLO-1 mediated reduction in cell viability is p65-independent. P65 knockdown was induced in MB-231 with transfection of non-targeting siRNA (NCsiRNA) or p65-targeting siRNA (sip65). 48 h post-transfection, cells were treated for 24 h with TYLO-1. Compound concentration was applied in triplicates and ranged in a four-fold serial dilution from 1000 nM to 0.06 nM. Culture medium (CTRL) and 20 μ M of cytotoxic staurosporine (Stauro). Cell viability-dependent fluorescence [RFU] was determined according to the 2D PrestoBlue assay. Data points represent the mean \pm SD of one independent experiment.

3.1.1.5 TYLO-1s delays cell cycle phase transition with arrest at the G0/G1 phase

In our previous work, we report, that TYLO-1 blocks MB-231 proliferation in a time- and dose-dependent manner at an IC₅₀ of 18 nM within 24 h [187]. Based on these findings, we aimed to explore modulation of the cell cycle transition under normoxic and hypoxic conditions by using the chemically prepared compound TYLO-1s.

After treating MB-231 with TYLO-1s under normoxic conditions, we did not detect a shift in cell cycle populations within 24 h (**Figure S 6**). To investigate, whether cell cycle is modulated in a time-dependent manner, we extended compound exposure to 48 h and 72 h. Within 48 h, there was no significant increase in the S- or G2/M phase population although the G0/G1 population was significantly decreased at 20 nM, 500 nM, and 1000 nM TYLO-1s (**Figure 3-8**). After 72 h treatment, cell populations significantly decreased in the G0/G1-state at a concentration ≥ 5 nM TYLO-1s and increased in the S-state at 20 nM, 50 nM, 100 nM, and 500 nM TYLO-1s (**Figure 3-9**). Of note, DMSO had no effect on the cell cycle state (**Figure S 7**).

To further investigate cell cycle progression under normoxic as well as hypoxic conditions we utilized MB-468-UnaG cells and compared TYLO-1s to paclitaxel. Under normoxia, we observed a time-and dose-dependent cell cycle modulation when exposed to TYLO-1s and a dose-dependent cell cycle modulation when exposed to paclitaxel. With TYLO-1s we confirmed a cell cycle regulation in MB-468-UnaG with a significant increase in the G2/M-state at 10 nM, 20 nM and 50 nM TYLO-1s after 48 h (**Figure 3-10**, **Figure 3-11**). Concomitant with already published data paclitaxel significantly induced a G2/M arrest in MB-231 and MB-468-UnaG within 24 h (**Figure 3-12**, **Figure 3-13**) [197]. To evaluate anti-proliferative effects under hypoxic conditions, hypoxia was mimicked in MB-468-UnaG cells by inducing HIF-signalling with exposure to 100 μ M CoCl₂ (**Figure 3-27**). Hypoxia was reported to enhance G2/M arrest in MB-231 [198] and we validated increase in G2/M population under CoCl₂-simulated hypoxia in MB-468-UnaG cells (**Figure 3-14**). Within 72 h, cell cycle progression was not modulated under hypoxic conditions, although 20 nM TYLO-1s moderately increased G0/G1 population, supporting our observation, that cell cycle population is arrested at the G0/G1 state (**Figure 3-14**). Nevertheless, both, TYLO-1s and paclitaxel, reduce cell viability within 24 h under hypoxia (**Figure 3-15**). Interestingly, hypoxia strongly decreased cytotoxic effects of paclitaxel by a factor of ≥ 100 , whereas hypoxia barely affected cytotoxic potential of TYLO-1s. Of note, under normoxia, paclitaxel and TYLO-1s increased cell population at the sub-G0/G1-state, indicating DNA fragmentation (**Figure S 8**), initiated through apoptosis [197].

In conclusion, TYLO-1s blocks TNBC proliferation by arresting the cell cycle at G0/G1 state in a dose- and time-dependent manner, resulting in a delayed progression towards the S

and G2/M phase. Compound characterization under hypoxia, revealed, that in contrast to paclitaxel anti-tumour efficacy of TYLO-1s is not significantly reduced under hypoxic conditions. Furthermore, our data indicate apoptosis induction by TYLO-1, which remains to be confirmed with future studies.

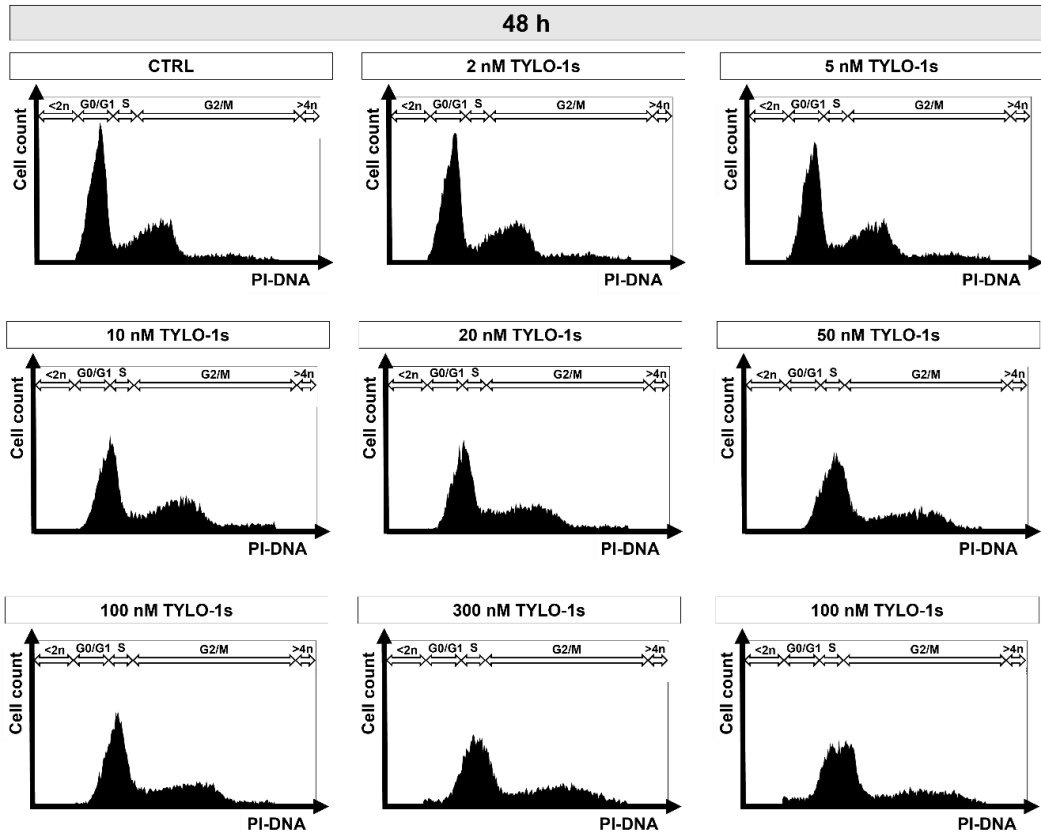
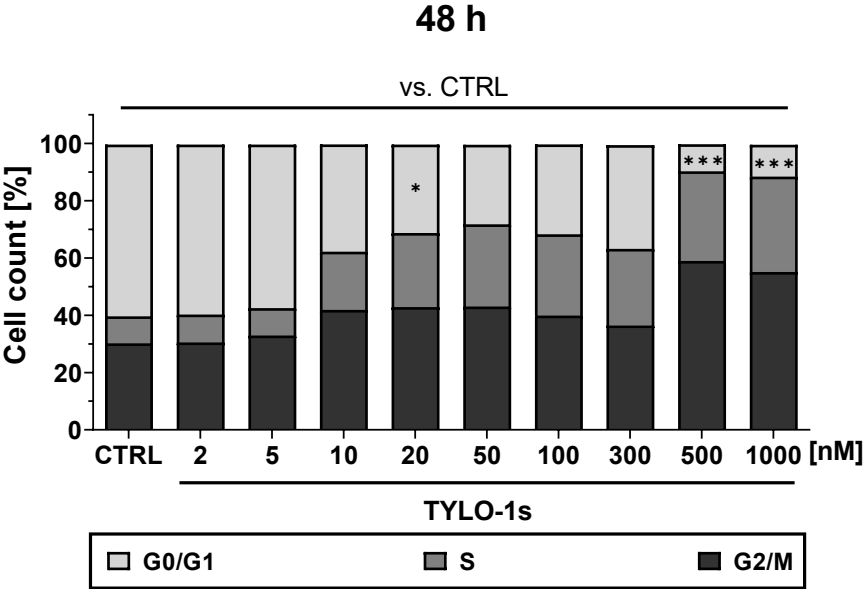
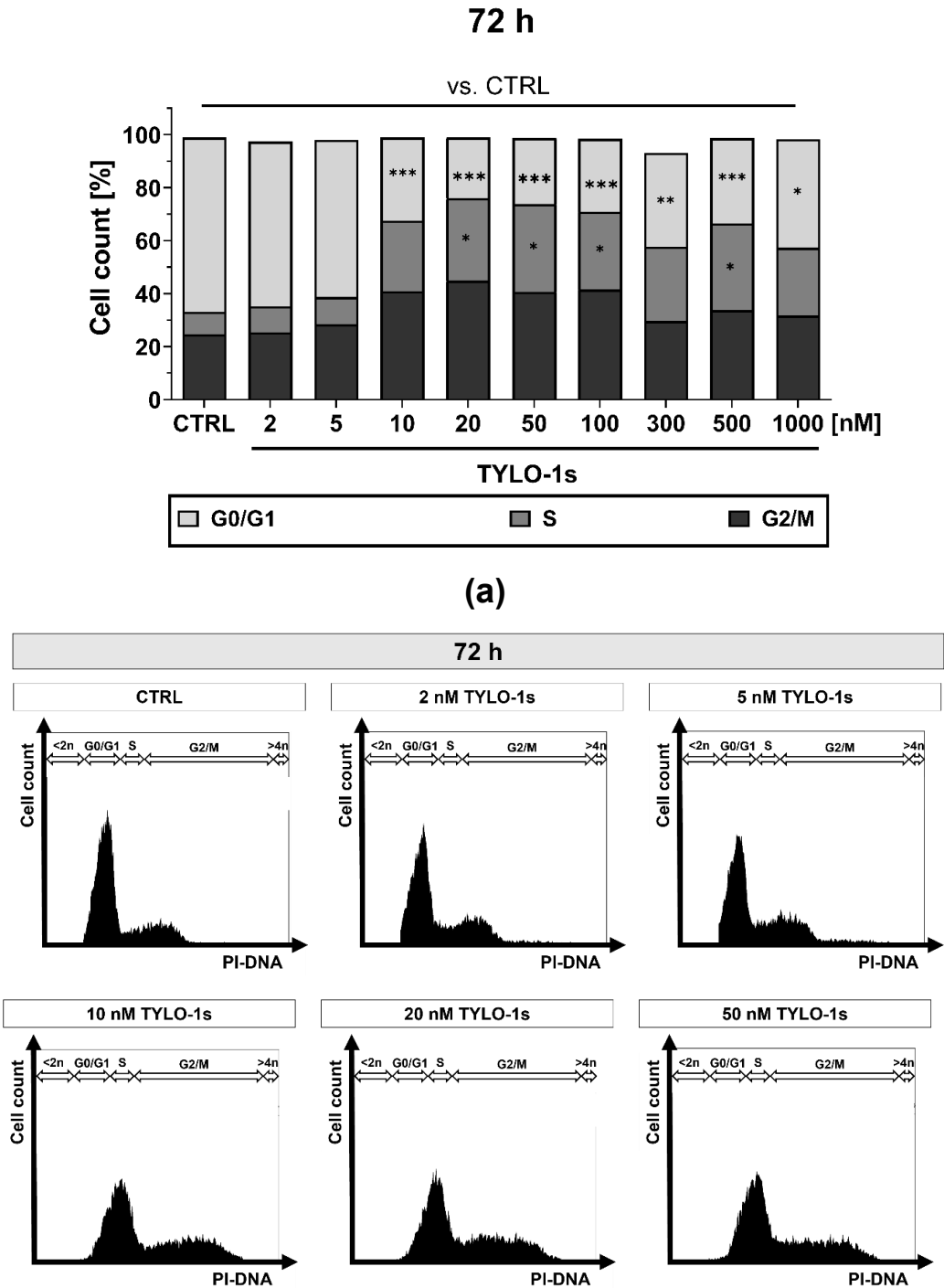


Figure 3-8 TYLO-1s modulated cell cycle populations in MB-231 within 48 h. Cells were left untreated (CTRL) or treated for 48 h with TYLO-1s at the indicated concentration. Cell cycle phase population (G0/G1; S; G2/M) was determined based on the signal of the PI-DNA complex using CytExpert. **(a)** Stacked bars represent the mean ($n=3$). Statistical difference vs. CTRL was calculated with two-way-ANOVA (* $p < 0.05$, *** $p < 0.001$). **(b)** Histograms depicting the cell count within the PI-signal were illustrated with CytExpert.



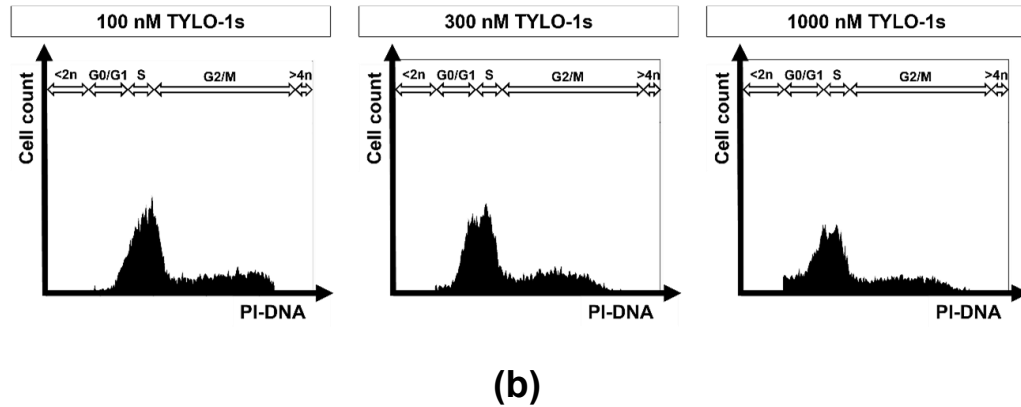
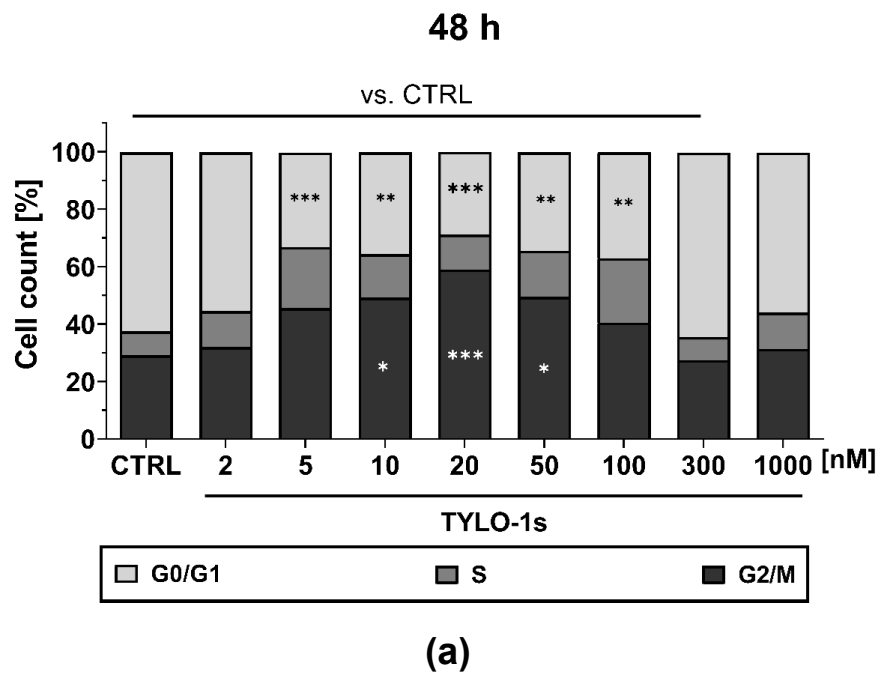


Figure 3-9 TYLO-1s modulated cell cycle populations in MB-231 within 72 h. Cells were left untreated (CTRL) or treated for 72 h with TYLO-1s at the indicated concentration. Cell cycle phase population (G0/G1; S; G2/M) was determined based on the signal of the PI-DNA complex using CytExpert. **(a)** Stacked bars represent the mean ($n=3$). Statistical difference vs. CTRL was calculated with two-way-ANOVA (* $p < 0.05$, ** $p < 0.01$, *** $p < 0.001$). **(b)** Histograms depicting the cell count within the PI-signal were illustrated with CytExpert.



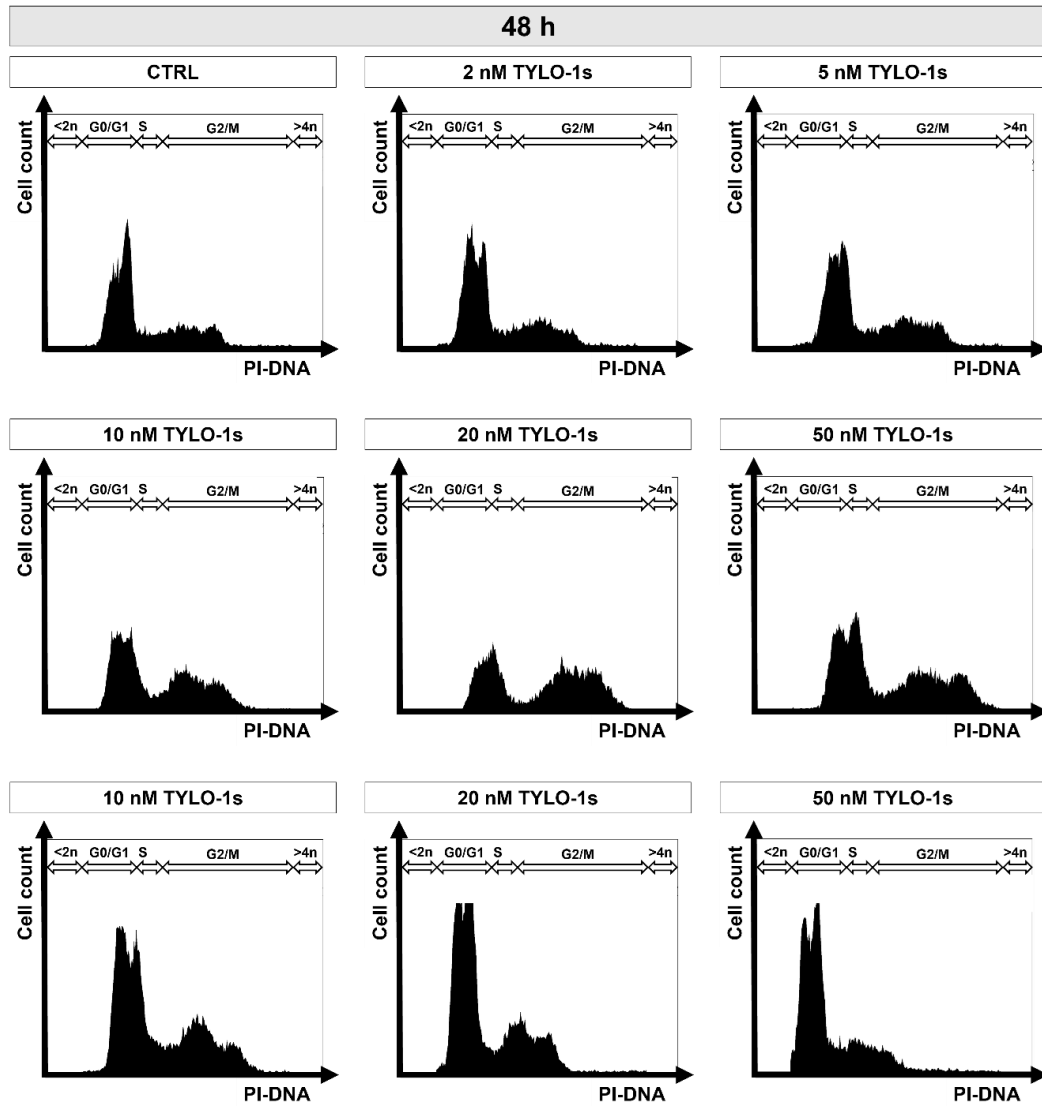
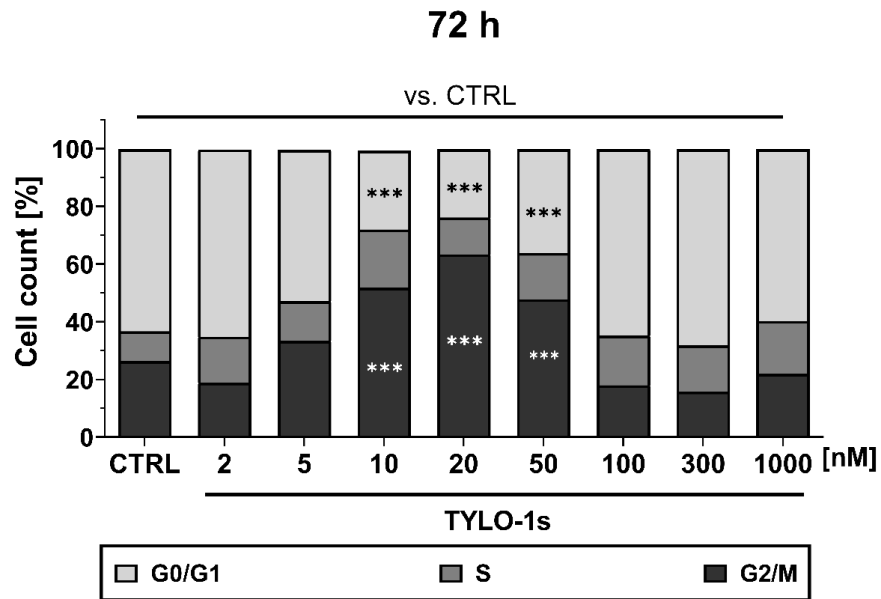
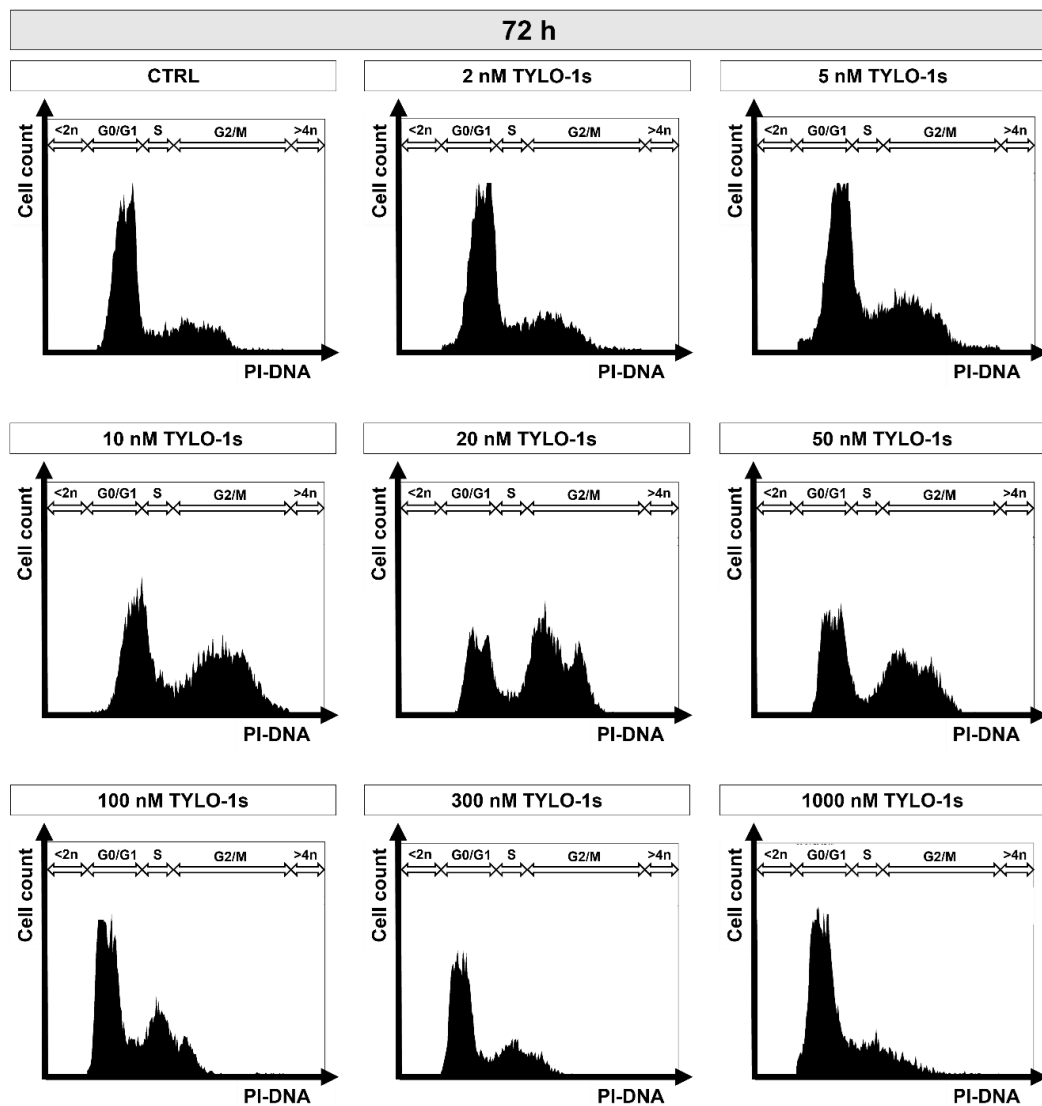


Figure 3-10 TYLO-1s modulated cell cycle populations in MB-468-UnaG within 48 h. Cells were left untreated (CTRL) or treated for 48 h with TYLO-1s at the indicated concentration. Cell cycle phase population (G0/G1; S; G2/M) was determined based on the signal of the PI-DNA complex using CytExpert. **(a)** Stacked bars represent the mean ($n=3$). Statistical difference vs. CTRL was calculated with two-way-ANOVA (* $p < 0.05$, ** $p < 0.01$, *** $p < 0.001$). **(b)** Histograms depicting the cell count within the PI-signal were illustrated with CytExpert.

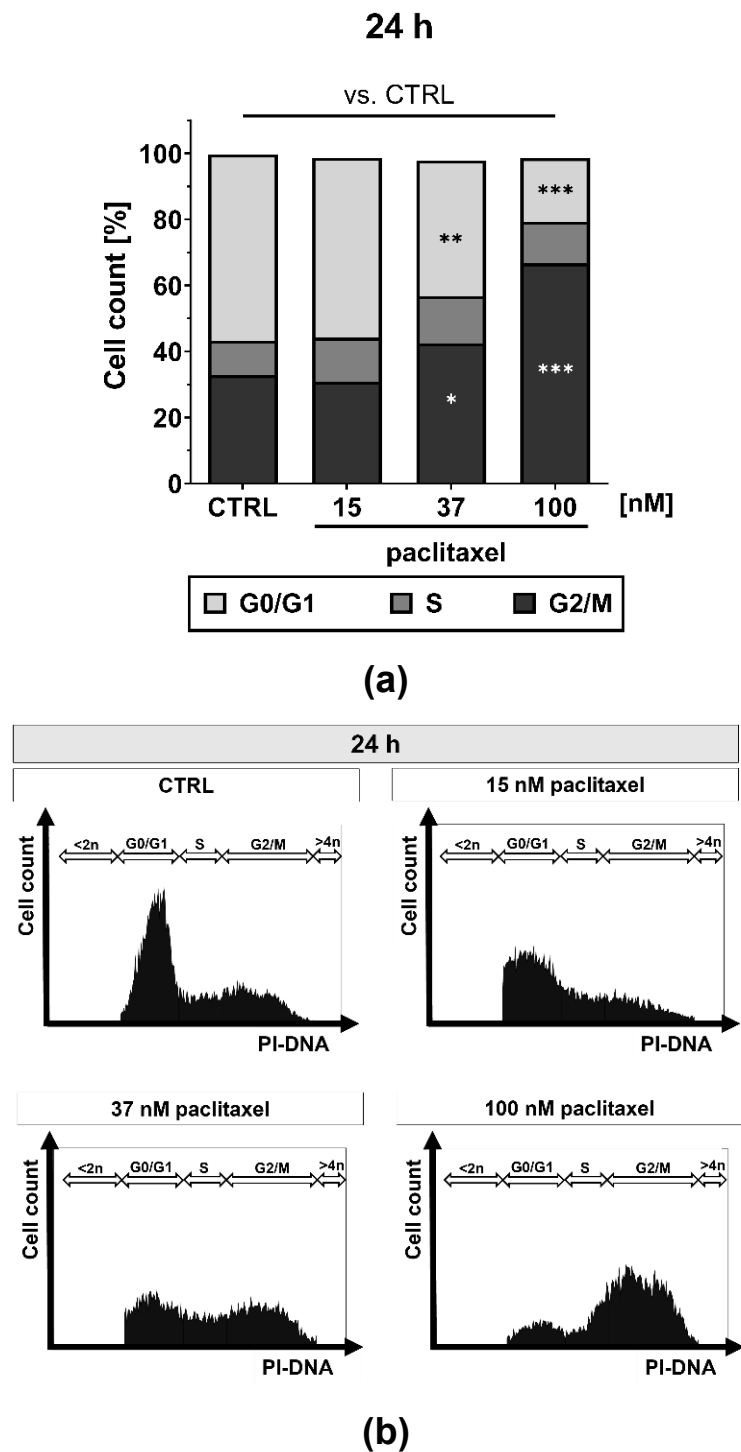


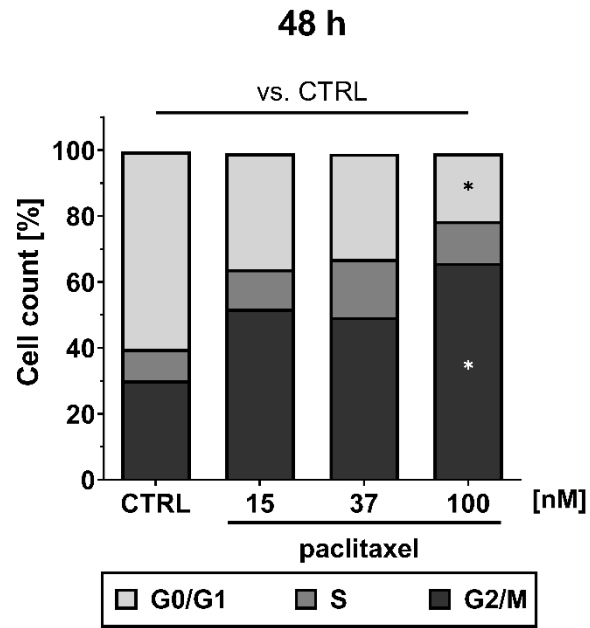
(a)



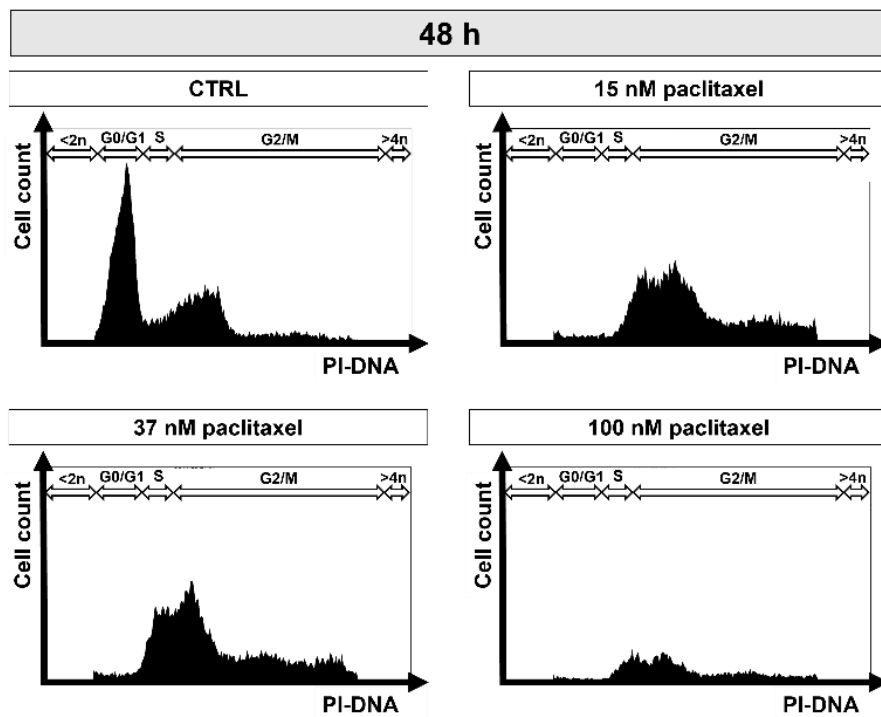
(b)

Figure 3-11 TYLO-1s modulated cell cycle populations in MB-468-UnaG within 72 h. Cells were left untreated (CTRL) or treated for 72 h with TYLO-1s at the indicated concentration. Cell cycle phase population (G0/G1; S; G2/M) was determined based on the signal of the PI-DNA complex using CytExpert. **(a)** Stacked bars represent the mean ($n=3$). Statistical difference vs. CTRL was calculated with two-way-ANOVA (** $p < 0.001$). **(b)** Histograms depicting the cell count within the PI-signal were illustrated with CytExpert.

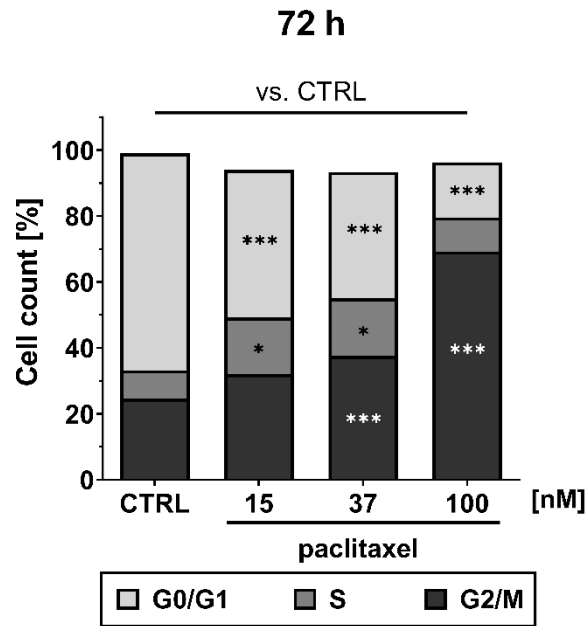




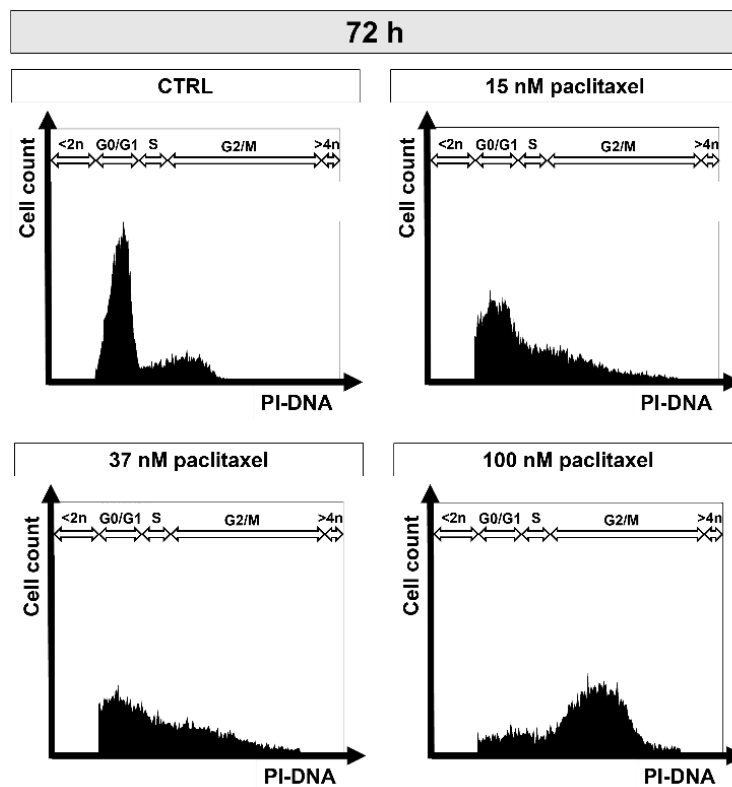
(c)



(d)



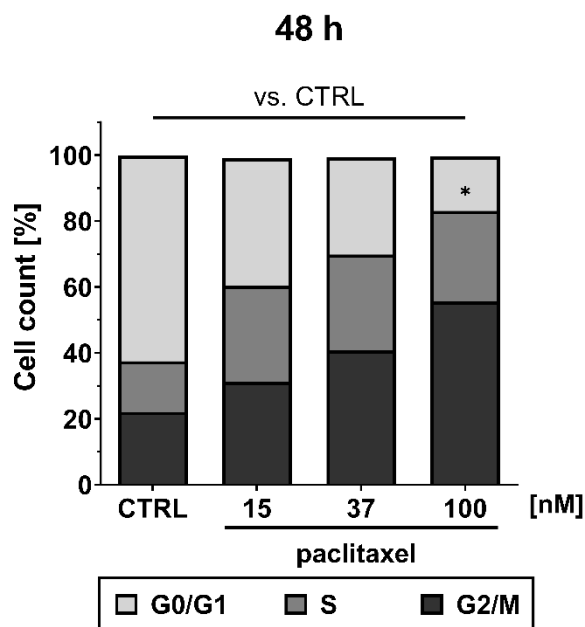
(e)



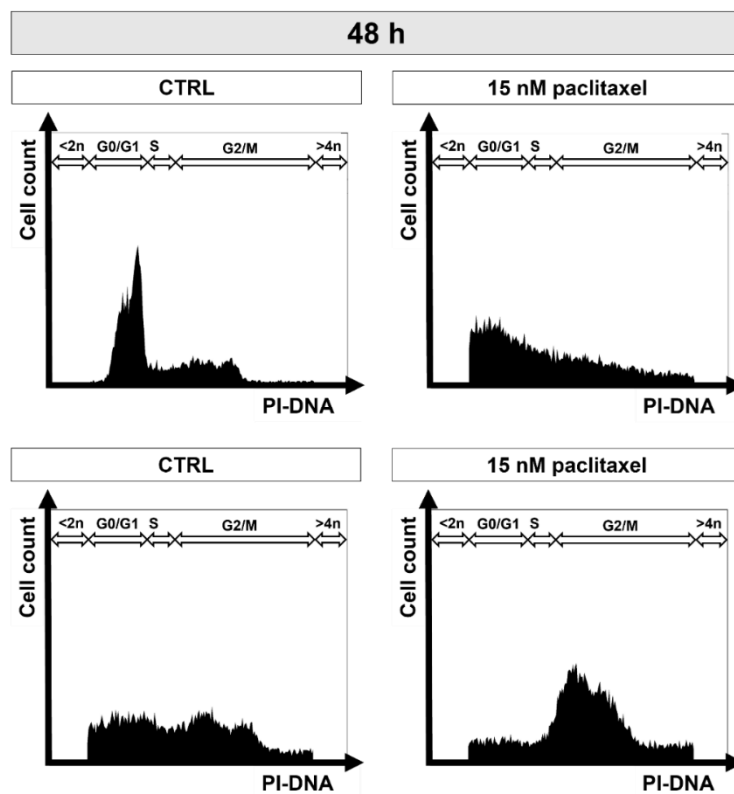
(f)

Figure 3-12 Paclitaxel arrested cell cycle progression at the G2/M-state in MB-231. Cells were left untreated (CTRL) or were treated for (a,b) 24h, (c,d) 48 h and (e,f) 72 h with paclitaxel at the indicated concentration. Cell cycle phase population (G0/G1; S; G2/M) was determined based on the signal of the PI-DNA complex using CytExpert. (a,c,e) Stacked

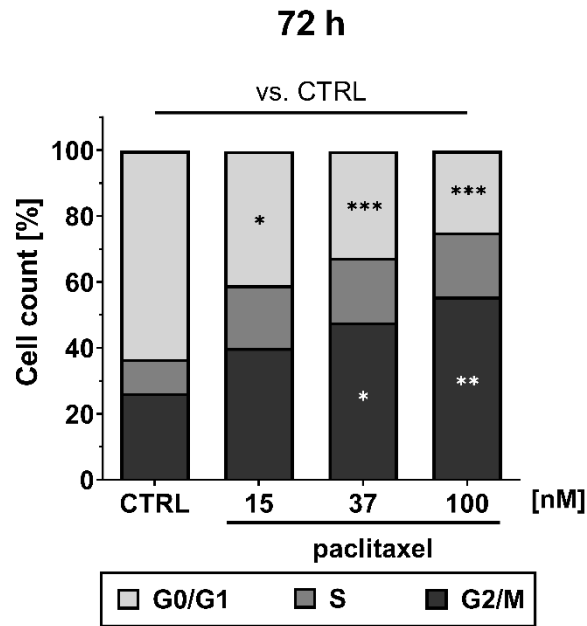
bars represent **(a)** (24 h) one independent experiment or **(c,e)** (48 h, 72 h) three independent experiments. Statistical difference vs. CTRL was calculated with two-way-ANOVA (* $p < 0.05$, ** $p < 0.01$, *** $p < 0.001$). **(b,d,f)** Histograms depicting the cell count within the PI-signal were illustrated with CytExpert.



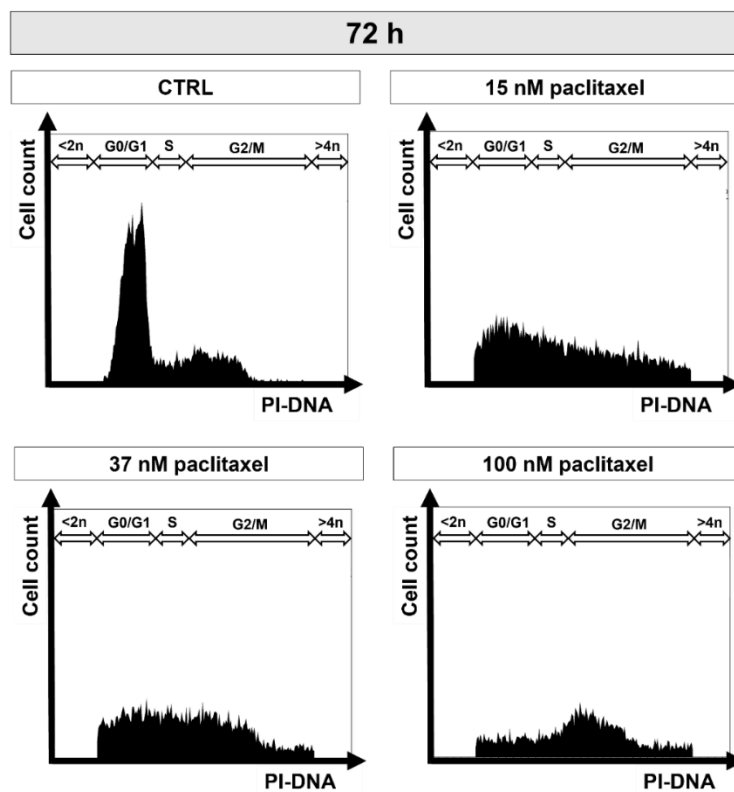
(a)



(b)



(c)



(d)

Figure 3-13 Anti-mitotic paclitaxel arrested cell cycle transition at the G2/M-state in MB-468-UnaG. Cells were left untreated (CTRL) or treated for (a,b) 48 h or (c,d) 72 h with paclitaxel at the indicated concentration. Cell cycle phase population (G0/G1; S; G2/M) was determined based on the signal of the PI-DNA complex using CytExpert. (a,c) Stacked bars represent the mean ($n=3$). Statistical difference vs. CTRL was calculated with two-way-

ANOVA (* $p < 0.05$, ** $p < 0.01$, *** $p < 0.001$). **(b,d)** Histograms depicting the cell count within the PI-signal were illustrated with CytExpert.

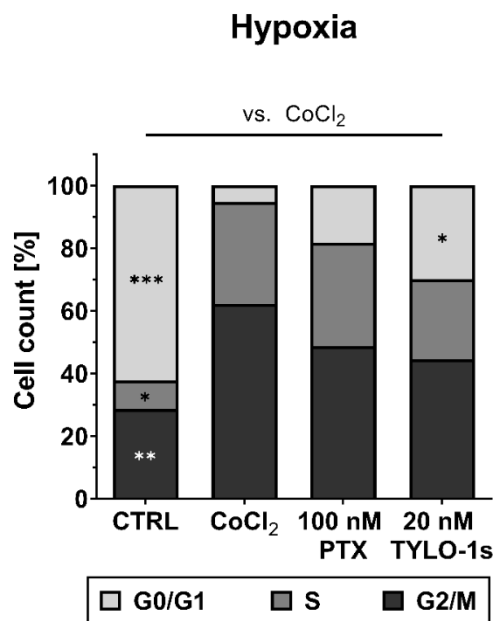
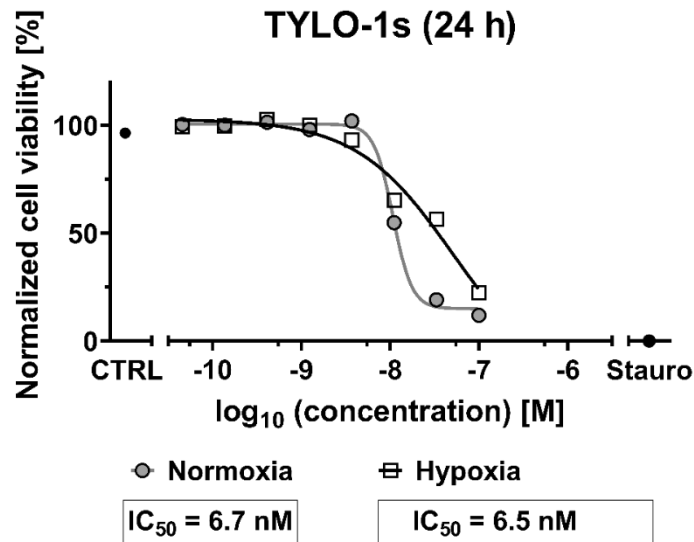
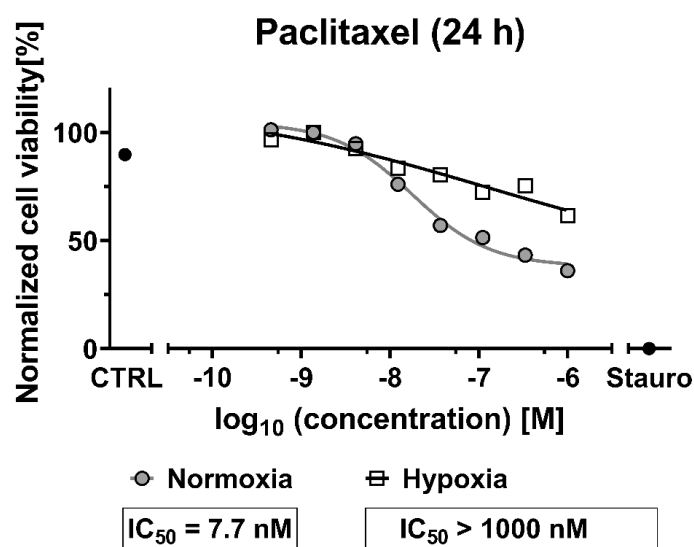


Figure 3-14 CoCl_2 -simulated hypoxia arrested cell cycle progression at the G2/M phase. For hypoxia simulation, MB-468-UnaG cells were pre-treated with 100 μM CoCl_2 for 24h. Cells were left untreated (CTRL) or treated for 24 h with 100 nM paclitaxel or 20 nM TYLO-1s. Cell cycle phase population (G0/G1; S; G2/M) was determined based on the signal of the PI-DNA complex using CytExpert. Stacked bars represent the mean ($n=3$). Statistical difference vs. CoCl_2 was calculated using two-way-ANOVA (* $p < 0.05$, ** $p < 0.01$, *** $p < 0.001$). Illustration with minor modifications from Reimche *et al.* (2022) [187].





(b)

Figure 3-15 CoCl₂-simulated hypoxia affects cytotoxicity of paclitaxel but not TYLO-1s in MB-468-UnaG. For HIF1 α -stabilization, cells were grown for 24 h in the presence of 100 μ M CoCl₂ (hypoxia) or left unstimulated (normoxia). Compound treatment was done (a) for TYLO-1s in a three-fold serial dilution starting at 100 nM and (b) for paclitaxel at a three-fold serial dilution starting at 1,000 nM. Untreated (CTRL) and 10 μ M staurosporine (Stauro) treated groups served as control. Cell viability was determined as relative fluorescence unit and was normalized in each independent experiment to the lowest (0%) and highest (100%) value (normalized cell viability). Data points represent one independent experiment. Illustration with minor modifications from Reimche *et al.* (2022) [187].

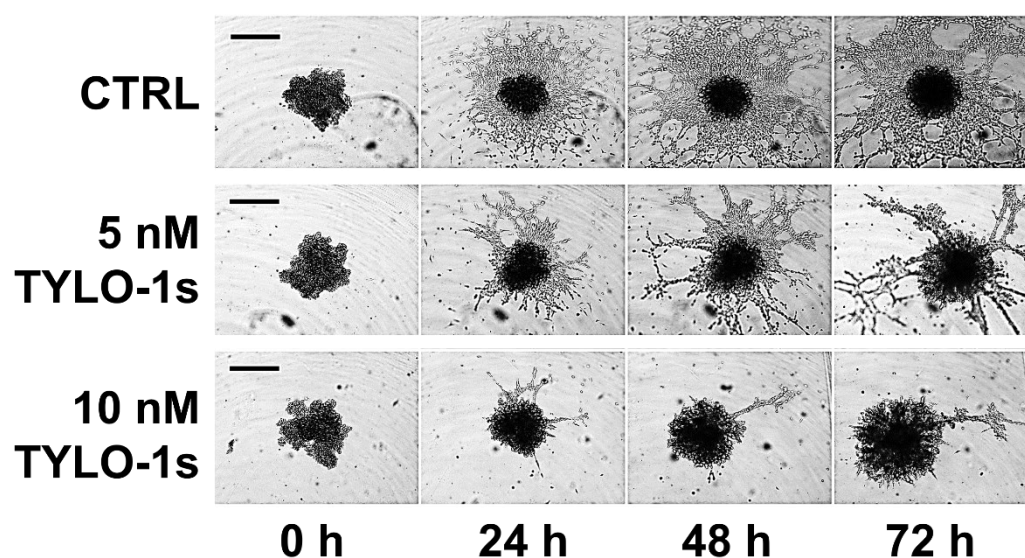
3.1.2 3D TNBC monoculture studies

3.1.2.1 TYLO-1s suppresses TNBC monoculture spheroid invasion in a dose-dependent manner

To investigate anti-migratory effects of P-alkaloids, we tested the natural product TYLO-1 with its chemically synthesized equivalent TYLO-1s regarding inflammatory driven migration of 2D monolayer cells and invasion of 3D monoculture spheroids, respectively. To investigate the role of inflammation in TNBC migration, a 2D wound healing assay was established. MB-231 migration was observed within 8 h and TNF α enhanced migratory behaviour by an average of 20%. TNF α -induced migration was decreased by an average of 15% with 10 nM TYLO-1 and by an average of 5% with 5.5 μ M BAY 11-7085 (**Figure S 9**). For studying the role of tumour-promoting CAFs, we applied conditioned medium from CAFs (CAF-CM), which, in contrast to our expectations, decreased migratory behaviour (**Figure S 10**).

To mimic the multicellular organisation of a tumour, TNBC monoculture spheroids composed of MB-231 were generated in a matrigel®-based matrix. Matrigel® is a commercially available mixture derived from a mouse sarcoma and comprises ECM components, such as growth factors and collagen IV, which is reported to drive motility in TNBC [199] and is also upregulated upon paclitaxel-based chemotherapy [200]. In our model, untreated control cells invaded into the surrounding matrigel® in a time frame of 72 h (**Figure 3-16**). The spheroid area post-treatment (invaded area) was normalized to the spheroid area pre-treatment (0 h). Within 72 h, invasion of untreated spheroids was 5-fold increased when comparing to the spheroid size pre-treatment. Invasion was suppressed by TYLO-1s in a dose-dependent manner (**Figure 3-16**). Compared to the untreated group, invasion was reduced at 5 nM and significantly blocked at 10 nM TYLO-1s. Compared to the untreated group, 10 nM TYLO-1s decreased invasion by around 70% within 48 h as well as within 72 h. Of note, a low-cytotoxic concentration of TYLO-1s was applied to study anti-migratory effects, whereas invasion was reduced at concentrations similar to the IC₅₀ of NFκB-inhibition in MB-231 (**Table 3-1**), but not at lower concentrations, including 2 nM TYLO-1s (**Figure S 11**).

In conclusion, O-methyltylophorinidine (TYLO-1/TYLO-1s) is a potent inhibitor of migration and invasion presumably by targeting the TNFα/NFκB axis in a dose-dependent manner. Moreover, TYLO-1 exhibits superior anti-migratory effects compared to the commercially available NFκB inhibitor BAY 11-7085.



(a)

Monoculture spheroid invasion

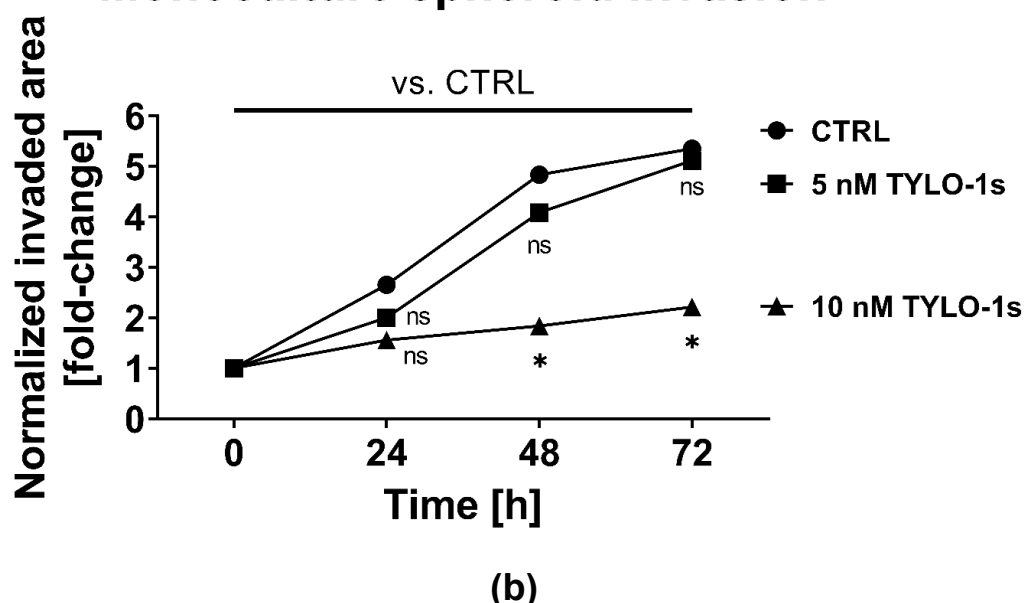


Figure 3-16 TYLO-1s blocked TNBC monoculture spheroid invasion into a matrigel®-based extracellular matrix (ECM). Monoculture spheroids composed of MB-231 were generated for 72 h before matrigel® was applied for ECM formation. Spheroids were grown for another 72 h without (CTRL) or with 5 nM and 10 nM TYLO-1s. **(a)** Representative brightfield images. Scale bar: 500 μ m. **(b)** To calculate invaded area, the spheroid area post-treatment is normalized to the spheroid area pre-treatment (0 h; which was set to 1; fold-change). Statistical difference within all groups was calculated with two-way-ANOVA (ns = not significant, * $p < 0.05$). Data points represent the mean ($n=3$). Illustration with minor modifications from Reimche *et al.* (2022) [187].

3.1.2.2 TYLO-1 blocks TNBC monoculture spheroid growth in a dose-dependent manner

To investigate anti-proliferative effects of P-alkaloids in a 3D model, we tested TYLO-1 regarding TNBC monoculture spheroid growth in a matrigel®-based environment.

Growth behaviour was explored after treatment with TYLO-1 or the MEK1/2 inhibitor, U0126, (**Figure 3-17**). TYLO-1 blocked spheroid growth in a dose-dependent manner. Compared to the untreated control, spheroid size was significantly reduced by $28.9 \pm 16.6\%$ at 25 nM, by $46.3 \pm 7.0\%$ at 50 nM and by $47.0 \pm 9.5\%$ at 100 nM. Growth blockade at 50 nM and 100 nM TYLO-1 was comparable to the anti-proliferative agent U0126 with reduction of spheroid size by $41 \pm 5\%$ when compared to the untreated group. Spheroid size and growth was significantly blocked at 25 nM with reducing growth by approximately 50%, indicating the half maximal growth inhibition (GI_{50}) to be around 25 nM (**Figure 3-17**, **Figure S 12**).

In conclusion, dose-dependent anti-proliferative effects of TYLO-1 was validated in a TNBC monoculture spheroid model. Based on significant growth blockade by TYLO-1, we estimated a GI_{50} of around 25 nM. TYLO-1 exhibits superior growth inhibition potential than the commercially available MEK1/2 inhibitor U0126 and thus implies targets that are different to or additional to the MAPK pathway.

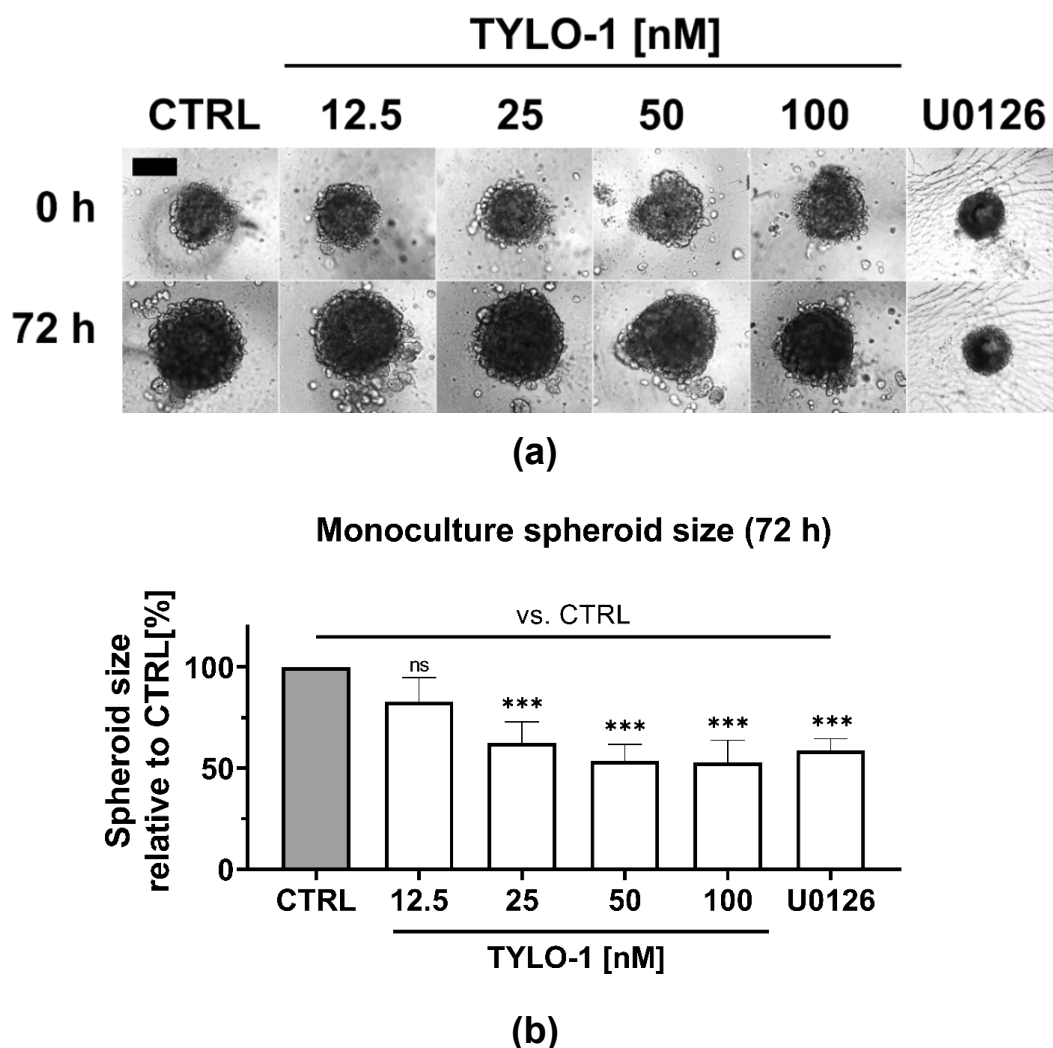


Figure 3-17 TYLO-1 blocked TNBC monoculture spheroid growth in a dose-dependent manner. Monoculture spheroids composed of MB-231 cells were formed for 72 h in 2.5% matrigel®. For another 72 h, spheroids were grown without (CTRL), with 10 μ M U0126 or with TYLO-1 at 12.5 nM, 25 nM, 50 nM and 100 nM. **(a)** Representative brightfield images. Scale bar: 300 μ m. **(b)** 72 h post-treatment, the spheroid size was determined based on the spheroid area that was measured in the brightfield images. In each independent experiment, the spheroid size was normalized to the CTRL (which was set to 100%). Bars represent the mean of at least three independent experiments \pm SD. Statistical difference vs. CTRL was calculated with one-way ANOVA analysis using Šidák's multiple comparison test (ns = not significant, *** $p < 0.001$).

3.1.3 3D TNBC co-culture spheroid model establishment

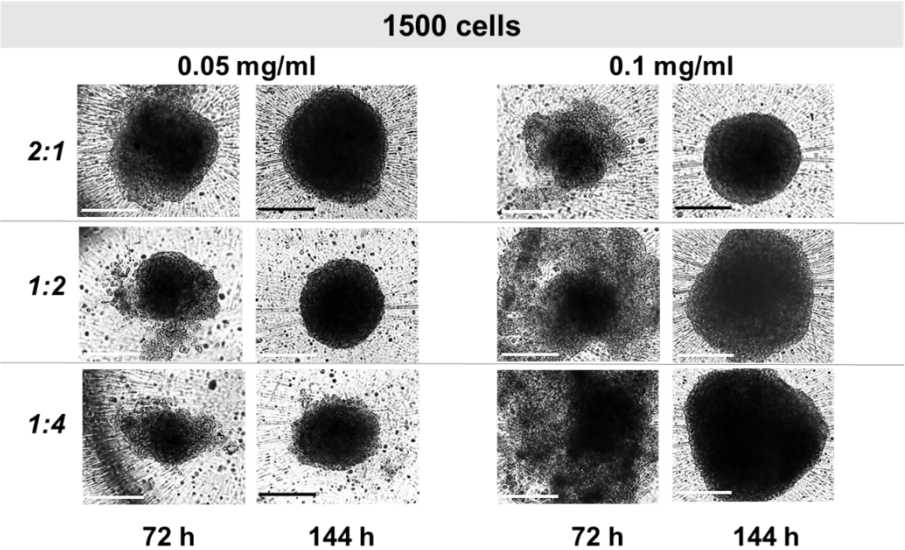
To mimic the physiological TNBC microenvironment in a simplified model, we aimed to generate co-culture spheroids encompassing MB-231 and primary murine CAFs in the presence of collagen type I. Various cell seeding conditions were primarily tested with alteration of the total cell number (1500 cells or 3000 cells), the cell type ratio of MB-231:CAF (2:1, 1:1, 1:2, 1:4), the collagen type I concentration (0.05 mg/ml, 0.1 mg/ml, 0.3 mg/ml) and without or with centrifugation ($136 \times g$). First, it was determined an optimal cell seeding condition to create solid and round spheroids (3.1.3.1). Secondly, spheroids were generated under optimized conditions and were characterized regarding the cell type distribution within the co-culture spheroids (3.1.3.2). Finally, we evaluated the spheroid growth behaviour to determine the time point of treatment and to investigate dependency on collagen for growth (3.1.3.2). Spheroids were grown for a total of 144 h, which is equivalent for the endpoint of treatment.

3.1.3.1 Optimizing cell seeding conditions to form round shaped spheroids

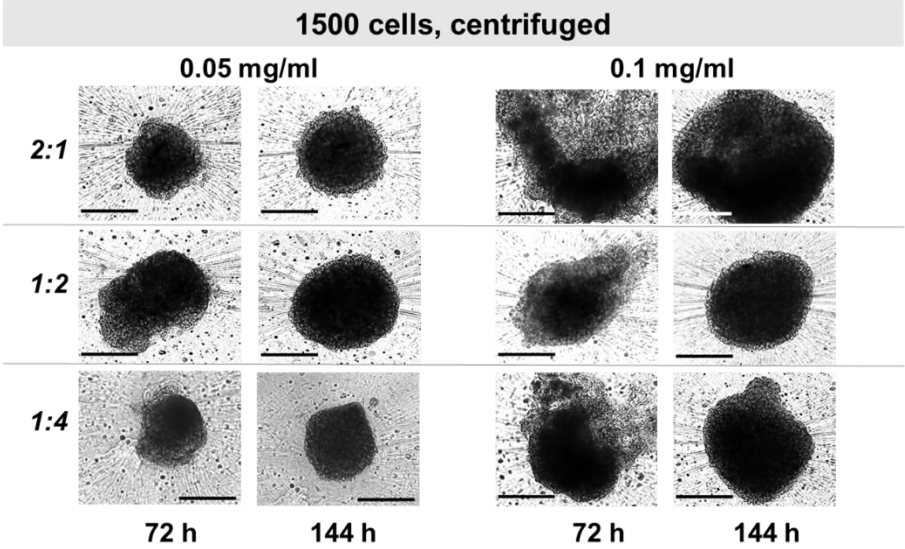
We tested various co-culture seeding conditions by altering the total cell number (1500 or 3000 cells), cell type ratios (MB-231:CAF at 2:1, 1:1, 1:2, 1:4) and collagen type I concentrations (0.05 mg/ml, 0.1 mg/ml or 0.3 mg/ml) without or with centrifugation ($136 \times g$) (**Figure 3-18**). To determine the optimal seeding condition, spheroids were favored when displaying a densely packed and round shape.

First of all, we observed, that centrifugation was not mandatory for spheroid generation and, moreover, was not physiologic. Interestingly, collagen was a predicting factor for the size and cell compactness. After 72 h formation, spheroids grown in the highest collagen concentration, 0.3 mg/ml, displayed a diameter of up to 2 mm with forming the least solid spheroids with loosely connected cells (**Figure 3-18e**). Spheroids grown in a low collagen concentration, 0.05 and 0.1 mg/ml, gained a size of 0.5 mm to 1 mm with displaying compact and round shapes. Regarding the cell number, a low total cell number (1500 cells) exhibited irregularly shaped and loosely packed spheroids, whereas a high total cell number (3000 cells) exhibited round shaped and more densely packed spheroids; especially when comparing the spheroids formed for 72 h. Within a total cell number of 3000 cells, round and compact spheroids were observed at a cell type ratio of 1:2 (MB-231:CAF) in 0.05 mg/ml collagen, but also at a cell ratio of 1:1 (MB-231:CAF) in 0.1 mg/ml collagen. Solid spheroids formed at the cell type ratio of 1:1 and 1:2 exhibited a diameter of around 500 μm already after 72 h formation. Interestingly, spheroids at a ratio of 1:4 barely reached the size of 500 μm after 144 h formation. This observation indicates, that CAFs build an encapsulating barrier to restrict spheroid growth. In contrast to that barrier, spheroids that contained higher or equal amount of MB-231 compared to CAF (2:1 and 1:1) showed

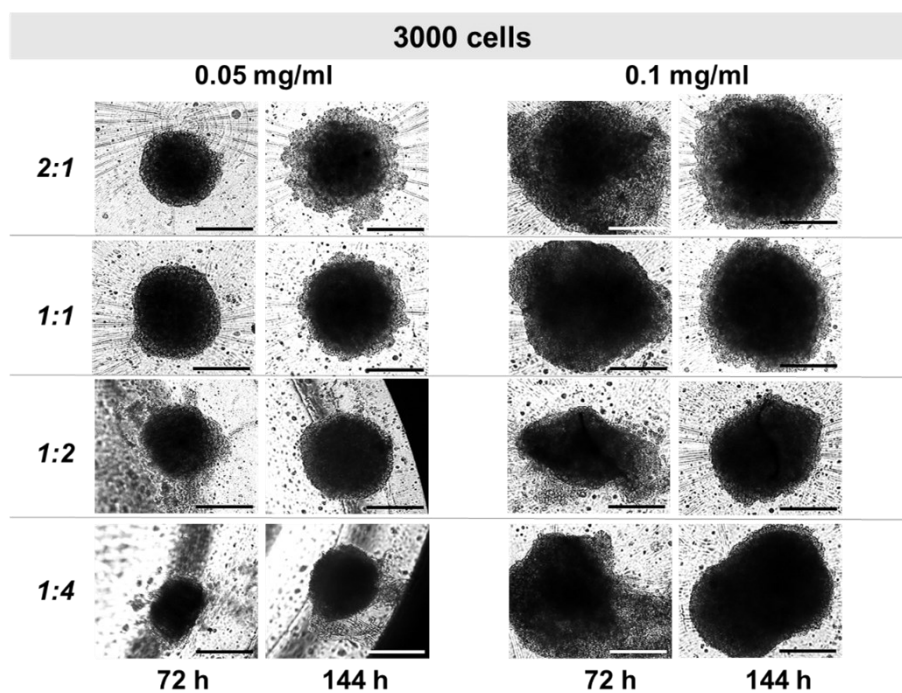
detachment of cells after 144 h formation. Cell detachment was not further characterized, but might indicate general cell aggregation, migration or induction of apoptosis. Summarized, co-culture spheroid formation starting with 3000 cells generated reproducible spheroids without requiring mechanical forces for formation. Nevertheless, optimal cell type ratios and collagen concentrations needed to be determined. Thus, we chose the following conditions for further examinations: MB-231:CAF at the cell type ratio of 1:1 and 1:2 that were grown in a low collagen concentration of 0.05 mg/ml and 0.1 mg/ml.



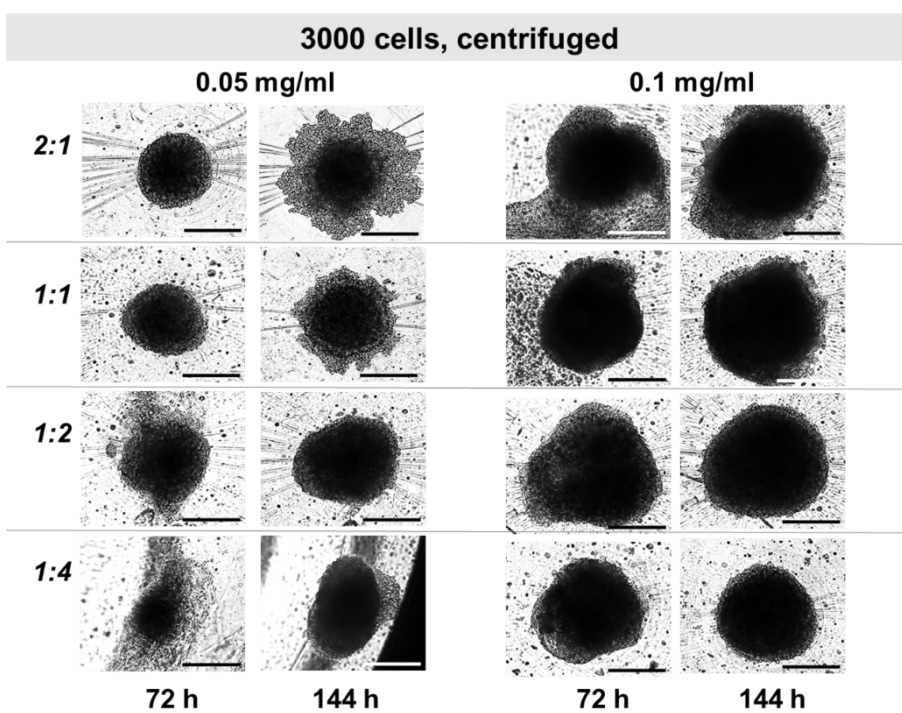
(a)



(b)



(c)



(d)

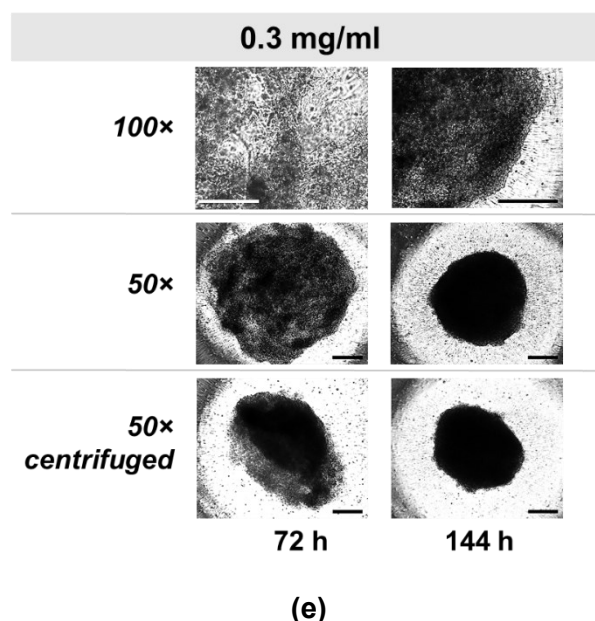


Figure 3-18 3D TNBC co-culture spheroid formation at various seeding conditions.

Co-culture spheroids of a total of (a,b) 1500 cells or (c,d) 3000 cells are composed of MB-231 (MDA) and CAFs at different cell type ratios (MB-231:CAF = 2:1, 1:1, 1:2 and 1:4). Spheroids were grown in total for 144 h in culture media supplemented with various type I collagen concentrations. After seeding, (a,c,e) plates were either directly incubated or (b,d,e) plates were centrifuged at $136 \times g$ for 10 min prior to spheroid growth. (a-e) Representative brightfield images for spheroids grown in 0.05 mg/ml or 0.1 mg/ml. Magnification: 100 \times . (e) Representative brightfield images for spheroids grown in 0.3 mg/ml type I collagen. Spheroids are composed of 3000 cells with a MB-231:CAF ratio of 1:2. Magnification: 50 \times and 100 \times . (a-e) Scale bar: 500 μ m.

3.1.3.2 Characterization of the co-culture spheroids

After selecting cell seeding conditions to form reproducible co-culture spheroids, cellular distribution within the spheroids was determined for each cell type at the following seeding conditions: A total of 3000 cells with a MB-231:CAF ratio of 1:1 or 1:2 was grown in either 0.05 mg/ml or 0.1 mg/ml collagen type I. Cell type distribution was evaluated in addition to the spheroid shape and growth behaviour. To determine the optimal time point of treatment, we evaluated the spheroid size after 72 h as well as 96 h, which would be equivalent to the start point of treatment, and after 144 h, which would be equivalent to the endpoint of treatment.

As observed in the previous spheroid formation (**Figure 3-18**), a more irregular shape correlates with the collagen concentration and mainly spheroids grown in 0.05 mg/ml collagen type I showed reproducible round and compact spheroids (**Figure 3-19**). Of note, the spheroids also displayed a slightly irregular shape with spreading cells from the tumour edge. However, the irregular shape diminished during spheroid formation within 144 h. In

this experiment, we additionally changed the seeding volume from 50 μ l to 90 μ l. We assumed, that spheroid formation was influenced by the initial amount of collagen, which was increased to 90 μ l for cell seeding. Thus, for further experiments, a seeding volume of 50 μ l was maintained with a final collagen concentration of 0.05 mg/ml.

With immunologically staining for the cell types, we localized MB-231 cells in the core of the spheroids that was coated with a cell layer of CAFs regardless of the cell type ratio, which was 1:1 or 1:2 (**Figure 3-20**, **Figure S 13**, **Figure S 14**). The irregular cell branches surrounding the spheroids may be mainly composed of the CAFs (**Figure S 14**). To reflect the TME, which is characterized by a high proportion of CAFs, a cell type ratio of 1:2 / MB-231:CAF) was favoured and maintained for the following studies.

To evaluate spheroid growth, we compared the spheroid size after 72 h or 96 h formation to the endpoint of treatment (144 h). The spheroid size was approximately doubled regardless of the duration of spheroid formation, collagen concentration or cell type ratio (**Figure 3-21**). The spheroid formation for 72 h was sufficient to generate round shaped spheroids, that are coated by CAFs and exhibit spheroid growth. Thus, to examine anti-proliferative potential in the following experiments, compound application was conducted after 72 h spheroid formation.

To investigate collagen dependency concerning the spheroid growth behaviour, we formed co-culture spheroids in the absence or presence of collagen. We compared spheroid size after 72 h or 144 h formation. When spheroids were formed in 0.05 mg/ml collagen, spheroid size was increased by 30-50%, but when spheroids were formed in the absence of collagen, there was no growth detected. (**Figure 3-22**). Remarkably, spheroids grown without collagen showed detached cells at the outer cell layer. This event was previously observed in spheroids grown in a cell type ratio of 2:1 or 1:1 (3.1.3.1), thus implying, that these spheroids are rather aggregates or that cells migrate or enter apoptosis. However, collagen supplementation was maintained in the following 3D growth studies.

All in all, we determined optimal cell seeding conditions to generate 3D TNBC co-culture spheroids with the tumour core (MB-231) which is encapsulated by CAFs. Round shaped and compact spheroids were reproduced at a cell type ratio of MB-231:CAF at 1:2 in a total number of 3000 cells and grown in a low collagen type I concentration (0.05 mg/ml). Regarding growth studies, collagen is indispensable for spheroid formation. For compound testing, we determined the time point of compound treatment, which is after 72 h spheroid formation.

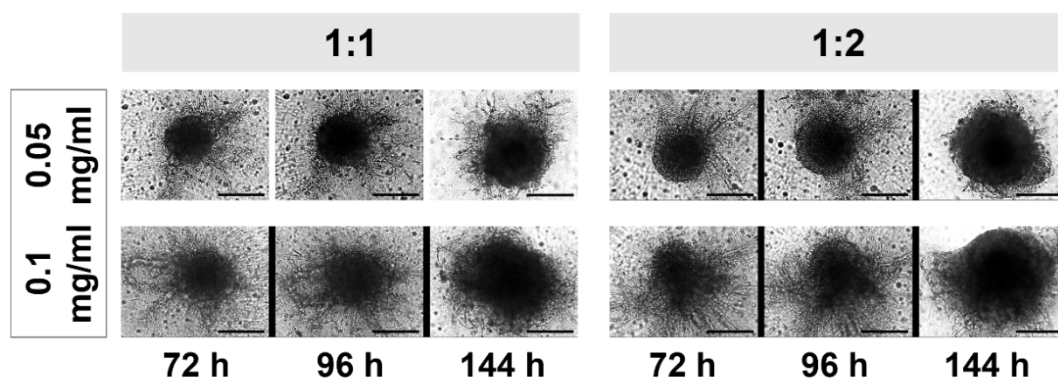


Figure 3-19 Co-culture spheroids showed best reproducibility in a low collagen concentration. Co-culture spheroids with a total of 3000 cells are composed of MB-231:CAFs at a ratio of 1:1 or 1:2. Spheroids were grown for 144 h in culture media supplemented with 0.05 mg/ml or 0.1 mg/ml type I collagen. Representative brightfield images. Scale bar: 500 μ m.

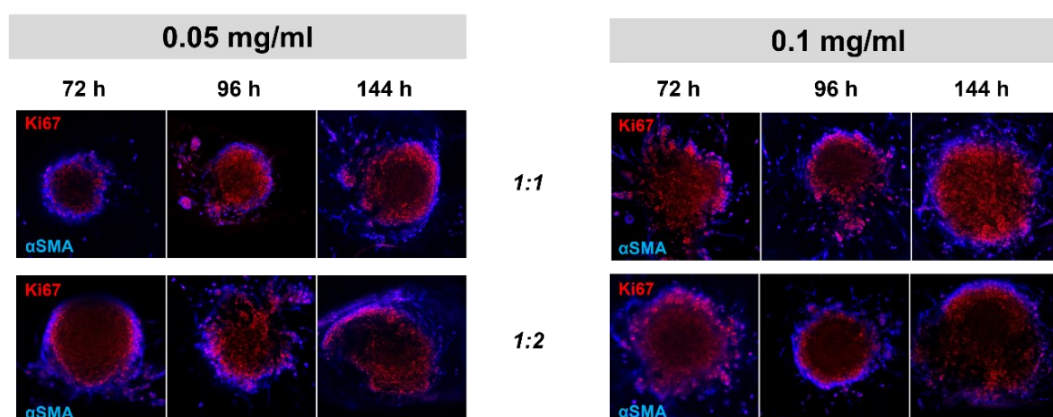


Figure 3-20 CAFs encapsulate MB-231 cells within the co-culture spheroids. Co-culture spheroids were formed with seeding 3000 cells at a MB-231:CAF cell ratio of 1:1 or 1:2. Spheroids were grown in total for 144 h in 0.05 mg/ml or 0.1 mg/ml type I collagen. Fluorescence was recorded after immunologically staining the spheroids for Ki67 (red, MB-231) and α SMA (blue, CAFs). Representative digital cross section of the spheroids. Magnification: 200 \times .

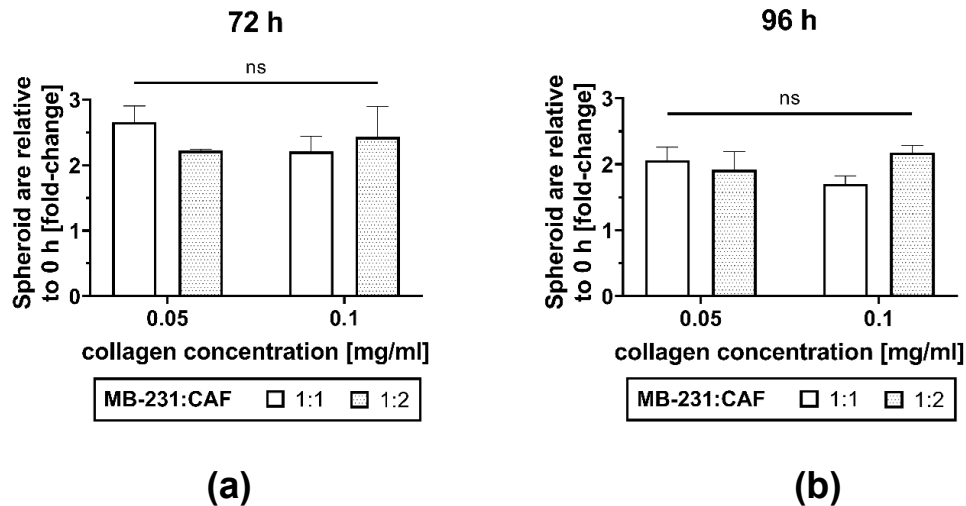


Figure 3-21 Co-culture spheroid growth is comparable after 72 h and 96 h formation. Co-culture spheroids were formed with seeding 3000 cells (MB-231:CAF at 1:1 or 1:2). Spheroids were grown in total for 144 h in either 0.05 mg/ml or 0.1 mg/ml collagen type I. The spheroid size was measured by determining the spheroid area in the brightfield images. Fold-change of the spheroid size was calculated by normalizing the spheroid size after 144 h formation to the spheroids formed for (a) 72 h or (b) 96 h. Bars represent the mean \pm SD of one independent experiment including two imaged spheroids per seeding condition. Statistical difference within all groups was calculated with two-way-ANOVA using šidáks multiple comparison test (ns = not significant).

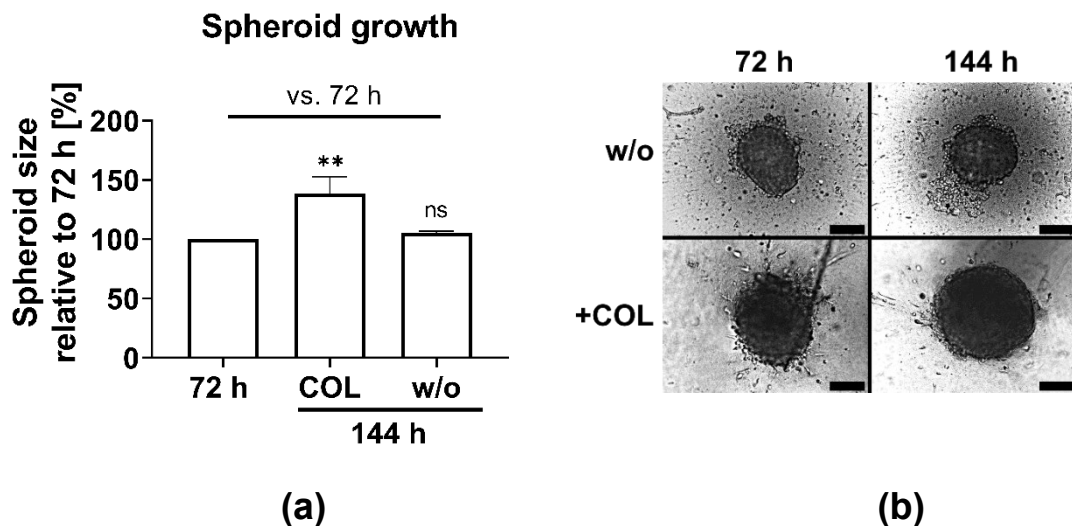


Figure 3-22 Co-culture spheroid growth depends on the collagen-based matrix. Co-culture spheroids (3000 cells; MB-231:CAF at 1:2) were grown for 144 h without (w/o) or in the presence of 0.05 mg/ml collagen type I (COL). (a) The spheroid size was measured by determining the spheroid area in the brightfield images. Average spheroid size at 144 h was normalized to the average spheroid size at 72 h (which was set to 100%). Bars represent the mean \pm SD of one independent experiment including three imaged spheroids

per each seeding condition. Statistical significance vs. 72 h was calculated using two-way-ANOVA (ns = not significant, ** $p < 0.01$). (b) Representative brightfield images. Scale bar: 200 μm .

3.1.4 3D co-culture studies

3.1.4.1 *P-alkaloids decrease cell viability in the 3D TNBC co-culture*

To study drug response under physiological conditions, the TNBC TME was emulated with generating co-culture spheroids composed of MB-231 and primary murine CAFs, that were grown in a collagen-based matrix.

To investigate anti-tumour potential of compounds in the simplified TNBC TME model, we evaluated the cell viability after exposure to P-alkaloids and paclitaxel (**Table 3-2, Figure 3-23**). Reduction in cell viability was observed for TYLO-1s and TYLO-1 to TYLO-4, with TYLO-1 and TYLO-1s displaying the most potent compound with an IC_{50} value of 22.7 ± 2.5 nM and 11.2 ± 2.13 nM, respectively. When compared to TYLO-1, the compounds TYLO-2, TYLO-3, and TYLO-4 were active with an at least 20-fold higher concentration resulting in an IC_{50} of 441.5 ± 70.8 nM, 476.7 ± 160.4 nM, and 517.7 ± 76.8 nM, respectively. Within the concentration tested, neither TYLO-5 nor TYLO-6 were effective. Activity of the compounds in 3D co-culture spheroids is comparable with their activities in 2D cultures of MB-231 (**Table 3-1, Figure S 15**). Regarding the effect on each cell type of the co-culture separately, bioactivity of TYLO-1 to TYLO-4 was slightly stronger on CAFs (**Table 3-3**) but still comparable with their activities in MB-231 (**Table 3-1**). In CAFs, TYLO-1 exhibited an IC_{50} of 2.7 ± 0.9 nM and TYLO-2 to TYLO-4 exhibited an $\text{IC}_{50} < 50$ nM. Noticeably, effects on CAFs were cell-density dependent with showing no activity when CAFs were grown at a cell density that was similar to 2D cultures of MB-231 (**Table 3-3**).

Paclitaxel reduced the cell viability in the co-culture model with an IC_{50} of 43 ± 14.3 nM (**Table 3-2**), which was comparable to its activity in cell monolayer of MB-231 (**Table 3-1**). However, cytotoxic potential stagnated at a concentration of 1 μM regarding the co-culture spheroids, because at a concentration starting from 1 μM up to 100 μM , no additional decrease in cell viability was observed (**Table S 10**). Furthermore, comparing cytotoxicity of TYLO-1 to paclitaxel in both, cell monolayer and co-culture, we detected a cell population that is not affected by the treatment with paclitaxel (**Figure 3-24**). Paclitaxel was ineffective against CAFs regardless of the cell-density, which highlights the differences between targeting CAFs and MB-231 and further indicates a different mode of action when comparing anti-mitotic paclitaxel to P-alkaloids.

In conclusion, the dose-drug response of P-alkaloids in a simplified TNBC TME model was comparable to its efficacy in 2D cell monolayer studies. In the 3D co-culture, TYLO-1 was

the most potent compound whereas TYLO-2, TYLO-3 and TYLO-4 showed major loss of efficacy. Within co-culture spheroids, MB-231 cells present the main target for paclitaxel, while P-alkaloids additionally target CAFs in a cell-density dependent manner. However, TYLO-1 shows superior efficacy in targeting the 3D co-culture, whereas the standard-of-care agent paclitaxel exhibits limited effects.

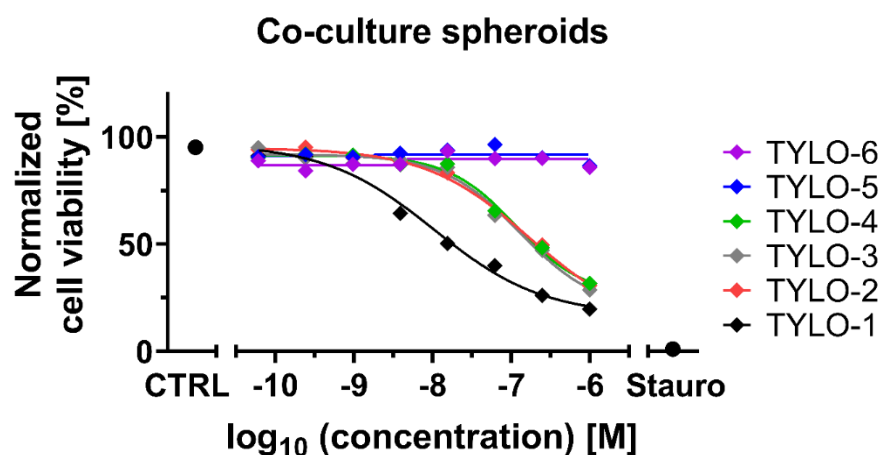


Figure 3-23 P-alkaloids reduce cell viability of 3D co-culture spheroids. Co-culture spheroids were formed for 72 h with seeding 3000 cells at a MB-231:CAF ratio of 1:2 in a total of 0.05 mg/ml collagen type I. Spheroids were exposed for additional 72 h to 100 nM TYLO-1, 100 nM paclitaxel (PTX). Co-culture medium served as a negative control (CTRL) and 20 μ M staurosporine served as a positive control (Stauro). The cell viability was determined 72 h post-treatment according to the 3D CellTiterGlo assay. In each independent experiment, cell viability-dependent luminescence [RLU] was normalized to the smallest value (which was set to 0%) and to the highest value (which was set to 100%). Each data point represents the mean of at least three independent experiments.

Table 3-2 IC₅₀-values determined for reduction of cell viability in co-culture spheroids

Compound	3D co-culture ¹ IC ₅₀ [nM] ²
TYLO-1s	11.2 \pm 2.11 ³
TYLO-1	21.7 \pm 2.5 ⁴
TYLO-2	441.5 \pm 70.8 ⁴
TYLO-3	476.7 \pm 160.4 ⁴
TYLO-4	517.7 \pm 76.8 ⁴
TYLO-5	>1000 ⁴
TYLO-6	>1000 ⁴
Paclitaxel	43 \pm 14.3 ⁴

¹ Spheroids were treated for 72 h. ² Tested in 3D TNBC co-culture spheroids according to the 3D CellTiterGlo assay. ³ Mean \pm SD (*n*=2). ⁴ Mean \pm SD (*n*=3).

Table 3-3 IC₅₀-values determined for reduction of cell viability in primary murine cancer-associated fibroblasts (CAFs)

Compound	CAFs IC ₅₀ [nM] ¹	
	Low seeding density	High seeding density
TYLO-1	2.7 ± 0.9 ²	>1000 ³
TYLO-2	19.7 ± 3.7 ²	>1000 ³
TYLO-3	26.7 ± 3.1 ²	>1000 ²
TYLO-4	33.5 ± 12.7 ²	>1000 ²
TYLO-5	>1000 ²	>1000 ⁴
TYLO-6	>1000 ²	>1000 ⁴

¹ Determined in CAFs 24 h post-treatment according to the 2D PrestoBlue assay. Mean ± SD of ² (n=3), ³ (n=2). or ⁴ (n=1).

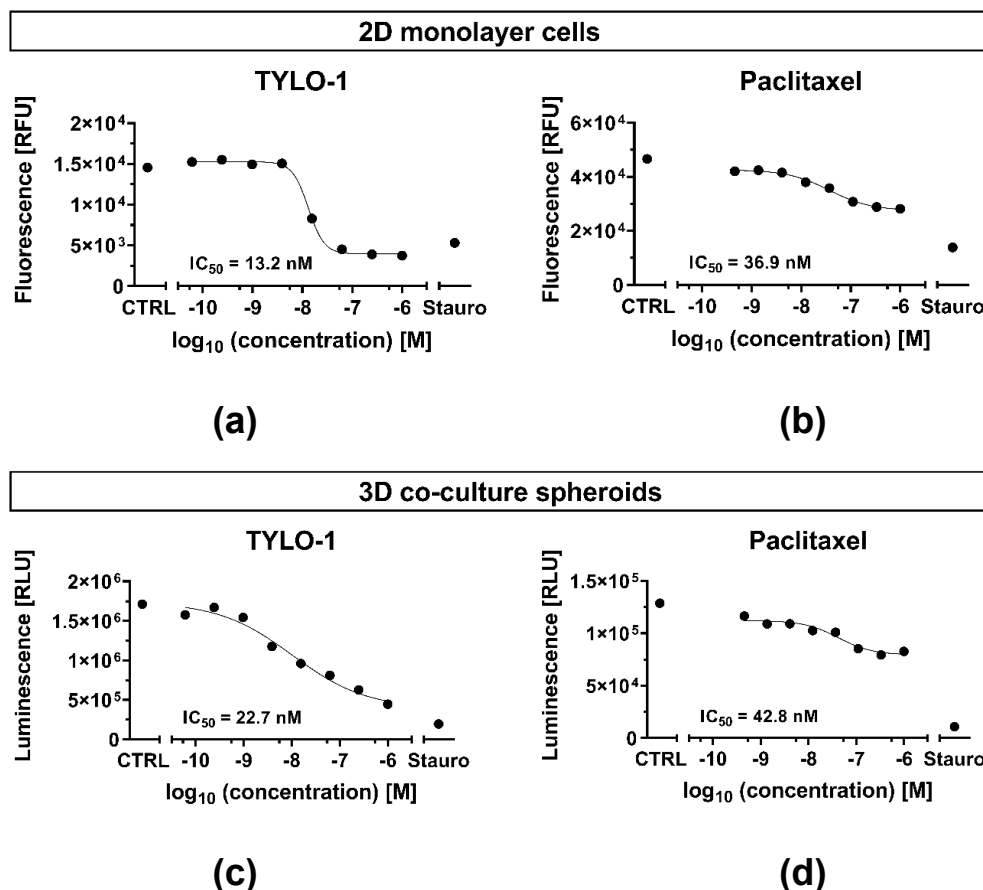


Figure 3-24 Representative dose-response inhibition in MB-231 monolayer cells and 3D co-culture spheroids for TYLO-1 and paclitaxel. (a,b) TYLO-1 was applied in a four-fold serial dilution in the concentration ranging from 1000 nM to 0.06 nM and paclitaxel was applied in a three-fold serial dilution in the concentration ranging from 1000 nM to 0.5 nM. Untreated cells and spheroids (CTRL) or treatment with 20 µM of cytotoxic staurosporine (Stauro) served as control. Data points and IC₅₀ represent one independent experiment. **(a)** MB-231 were treated for 24 h in the presence of TYLO-1 or paclitaxel. Cell viability-dependent fluorescence [RFU] was determined post-treatment according to the 2D

PrestoBlue assay. **(b)** The co-culture spheroids were formed for 72 h before treated for another 72 h with TYLO-1 or paclitaxel. Cell viability-dependent luminescence [RLU] was determined post-treatment according to the 3D cell viability assay.

3.1.4.2 TYLO-1 blocks co-culture spheroid growth

To investigate the modulation of 3D co-culture spheroid growth upon TYLO-1 and paclitaxel, we applied 100 nM of each compound and found superior potential for TYLO-1 when compared to paclitaxel. TYLO-1 significantly suppressed spheroid growth by an average of 40% compared to the untreated spheroids, while paclitaxel did not significantly reduce growth by an average of 25% (**Figure 3-25**). We also tested TYLO-1 and paclitaxel at a low-toxic concentration (10 nM) and found no significant decrease in spheroid size for both compounds (**Figure S 16**). Regarding the cellular organisation within the spheroids, encapsulation of CAFs was maintained during treatment, even though the spheroid shape was irregularly disrupted when compared to the untreated control (**Figure 3-26**). Modulation of the spheroid shape may result from targeting both, MB-231 and CAFs (compare **Table 3-1**, **Table 3-3**).

In conclusion, the plant-derived TYLO-1 has superior anti-growth effects in TNBC co-culture spheroids compared to paclitaxel. Thus, P-alkaloids may serve as novel drug candidates for treating TNBC.

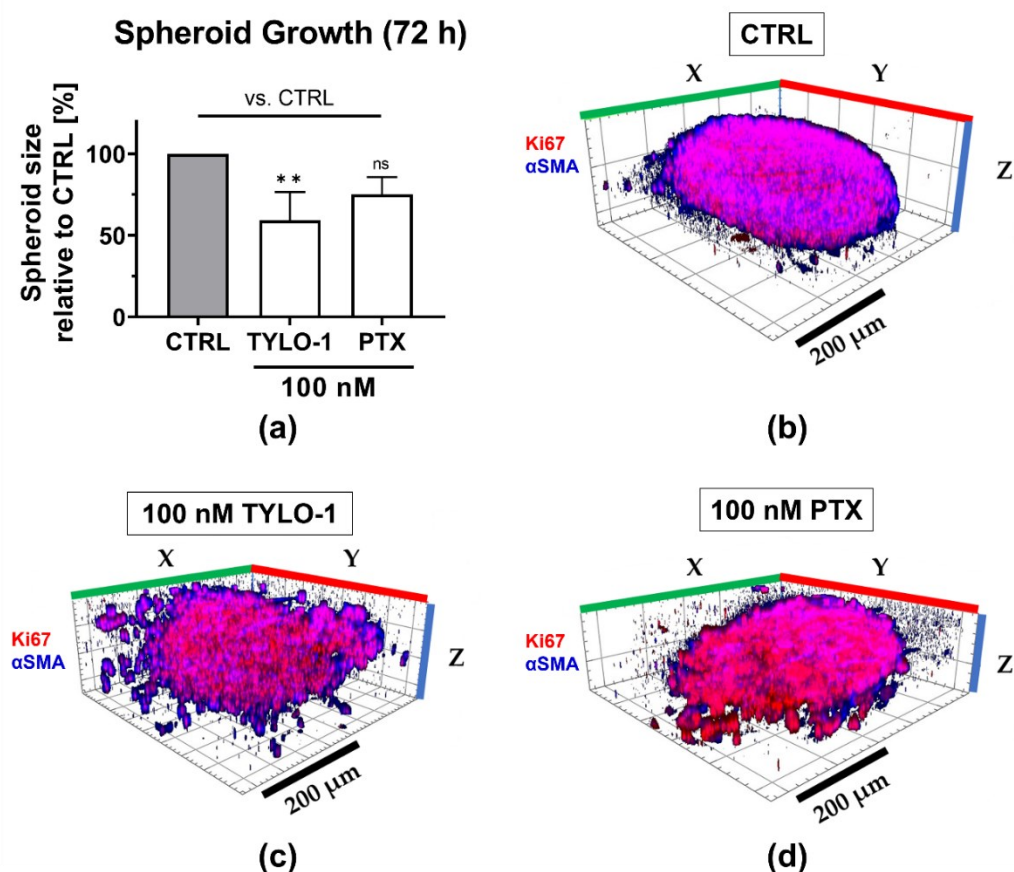


Figure 3-25 3D co-culture spheroid growth is significantly blocked with TYLO-1 but not paclitaxel. Co-culture spheroids were formed for 72 h with seeding 3000 cells at a MB-231:CAF ratio of 1:1 with a total of 0.05 mg/ml collagen type I. Subsequently, spheroids were exposed for another 72 h to 100 nM TYLO-1, 100 nM paclitaxel (PTX) or left untreated (CTRL). The spheroid size post-treatment was measured by determining the spheroid area in the brightfield images. In each independent experiment, average spheroid size per treatment group was normalized to the average spheroid size of CTRL. Bars represent the mean \pm SD ($n=3$). Statistical difference vs. CTRL was calculated using one-way-ANOVA (ns = not significant, ** $p < 0.01$). Illustration with minor modifications from Reimche *et al.* (2022) [187].

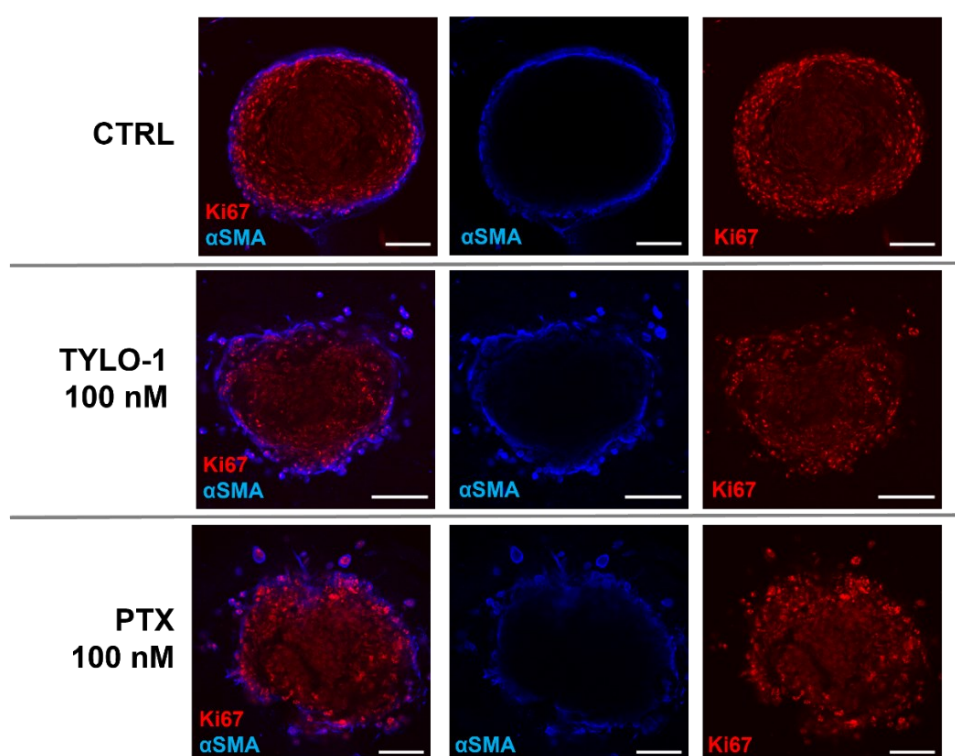


Figure 3-26 CAF encapsulation in co-culture spheroids is maintained post-treatment with TYLO-1 and paclitaxel. Co-culture spheroids were formed for 72 h with seeding 3000 cells at a MB-231:CAF cell ratio of 1:1 with a total of 0.05 mg/ml collagen type I. Subsequently, spheroids were exposed for another 72 h to 100 nM TYLO-1, 100 nM paclitaxel (PTX) or left untreated (CTRL). Fluorescence was recorded after immunologically staining the spheroids for Ki67 (red, MB-231) and αSMA (blue, CAFs). Representative digital cross section of the spheroids. Scale bar: 100 μ m.

3.1.5 Pathway crosstalk: HIF and NFκB

3.1.5.1 *TYLO-1s suppresses hypoxia-inducible factor (HIF)-mediated transcription in a dose-dependent manner*

To explore effects of P-alkaloids under hypoxia, anti-inflammatory potential as well as hypoxia-associated HIF-activity was evaluated in 2D cultures. To study tumour growth under hypoxia, we aimed to create a 3D co-culture model.

HIF-1α-mediated transcription was evaluated using a second TNBC cell line, MB-468-UnaG, expressing the fluorescence protein UnaG under the control of a synthetic hypoxia responsive promotor [82]. To simulate hypoxia, 100 μM CoCl₂ was applied. CoCl₂ is described to inhibit HIF-1α hydroxylation and degradation under normoxic conditions, thereby stabilizing HIF-1α driven gene expression [198,201,202]. In MB-468-UnaG we confirmed hypoxia induction with 100 μM CoCl₂ by increasing HIF-regulated UnaG expression (**Figure 3-27**). To investigate the interplay between the NFκB and the HIF pathway under normoxic as well as hypoxic conditions, we tested TYLO-1s and the NFκB inhibitor BAY 11-7085. Reduction of cell viability by both compounds in MB-468-UnaG (**Figure 3-28b,c, Table S 6**) was comparable to MB-231 (**Table 3-1**). Under normoxia, TYLO-1s significantly decreased HIF-1α-mediated UnaG expression by 11 ± 3% at 10 nM and by 13 ± 4% at 20 nM, while BAY 11-7085 had no significant effects (**Figure 3-29a,b**). When cells were pre-treated with compounds before inducing CoCl₂-simulated hypoxia, the increase in HIF-1α activity was blocked in the presence of 6 μM BAY 11-7085 as well as by 2 nM, 5nM, 10 nM and 20 nM of TYLO-1s. Solely TYLO-1s significantly reduced HIF-1α activity by 14 ± 4% at 20 nM (**Figure 3-29c,d**).

To investigate the role of hypoxia in tumour growth and to characterize P-alkaloids under hypoxic conditions, a simplified 3D co-culture model was established comprising the hypoxia-sensor cell clone MB-468-UnaG and the primary murine CAFs. We tested different cell proportions and collagen type I concentration, similar to the co-culture establishment of spheroids comprising MB-231 (**Figure S 17**). In general, increase in collagen resulted in a more irregular spheroid shape, and increased CAF proportion correlated with a more densely packed spheroid. Within all conditions, round shaped and densely packed spheroids that exhibited spheroid growth were generated with a cell seeding number of 3000 cells at a MB-468:CAF ratio of 1:2 and with a total of 0.05 mg/ml collagen type I (**Figure S 18**). To induce hypoxia, co-culture spheroids were exposed to 100 μM and 200 μM CoCl₂ for 72 h. Concerning the cell type distribution within spheroids, tumour cells were encapsulated with CAFs under normoxic as well as hypoxia simulated conditions (**Figure S 19a**). The growth of spheroids was rather decreased upon CoCl₂-induced hypoxia (**Figure S 19b,c**).

All in all, blockade of CoCl_2 -induced HIF signalling by TYLO-1s and BAY 11-7985 indicates a key role of the NF κ B-pathway in CoCl_2 -mediated hypoxia. Different to NF κ B-targeting compounds, decreased HIF-1 α activity was solely found for TYLO-1s under normoxic as well as hypoxic conditions. Thus, P-alkaloids present a class of compounds with multiple target sites. However, our 3D co-culture model was not suitable to investigate drug response on tumour growth within a hypoxic TME.

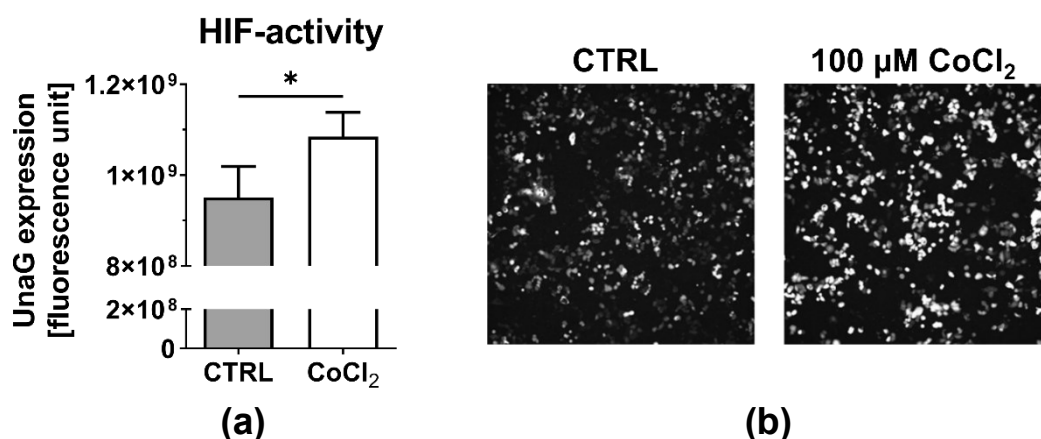


Figure 3-27 CoCl_2 simulated hypoxia by enhancing hypoxia inducible factor (HIF) transcriptional activity. MB-468-UnaG cells were left untreated (CTRL) or exposed to 100 μM CoCl_2 for 24 h. **(a)** Fluorescence intensity of HIF-mediated UnaG expression was determined in UnaG-expressing cell clones. Statistical difference was calculated with a paired two-tailed t -test (* $p < 0.05$). Bars represent the mean \pm SEM ($n=3$). **(b)** Representative images for UnaG fluorescence (white area) recorded at 100 \times magnification. Illustration from Reimche *et al.* (2022) [187].

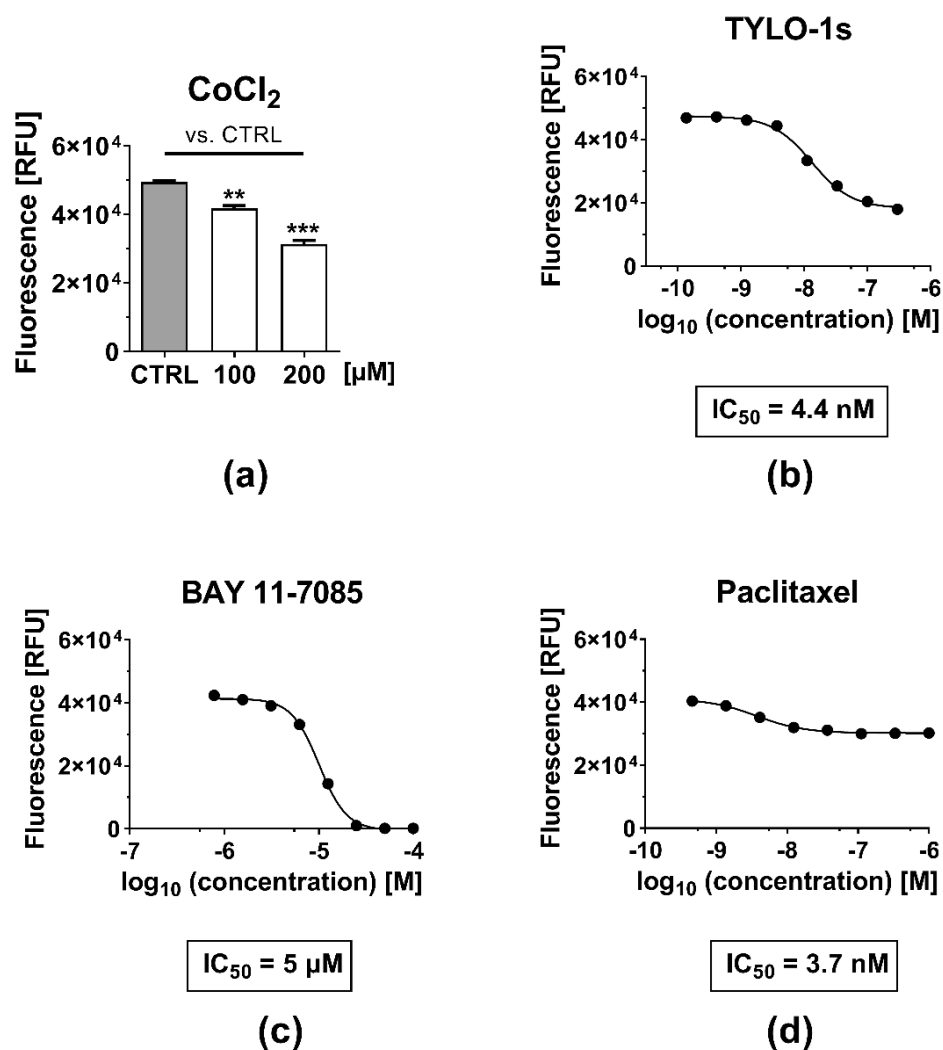
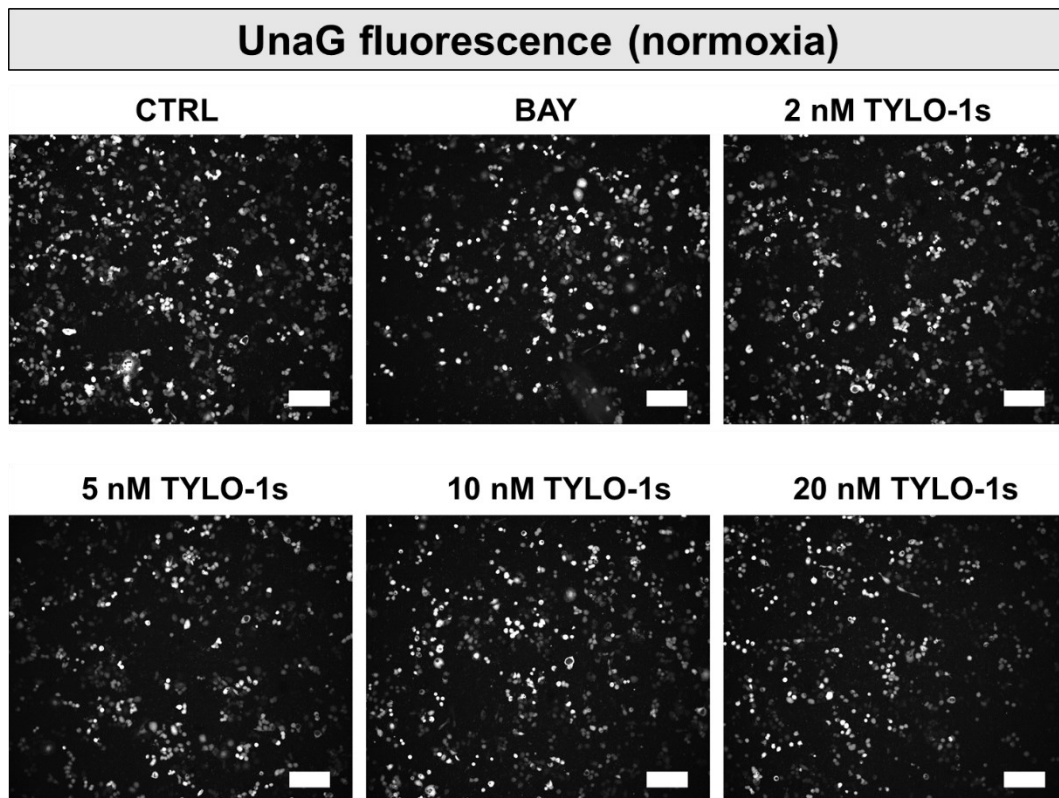
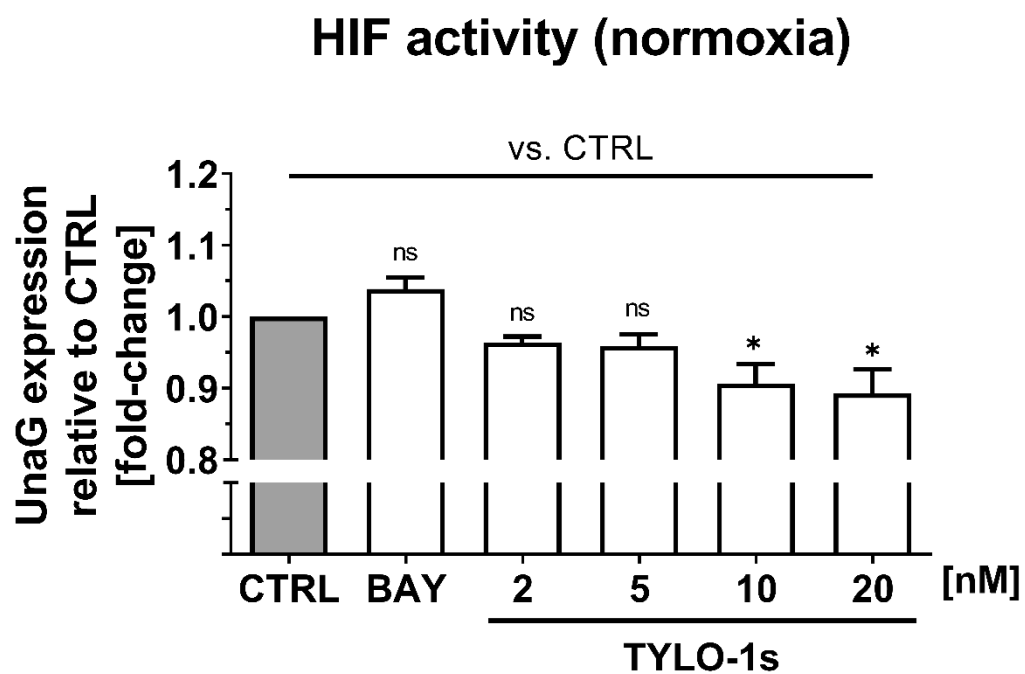


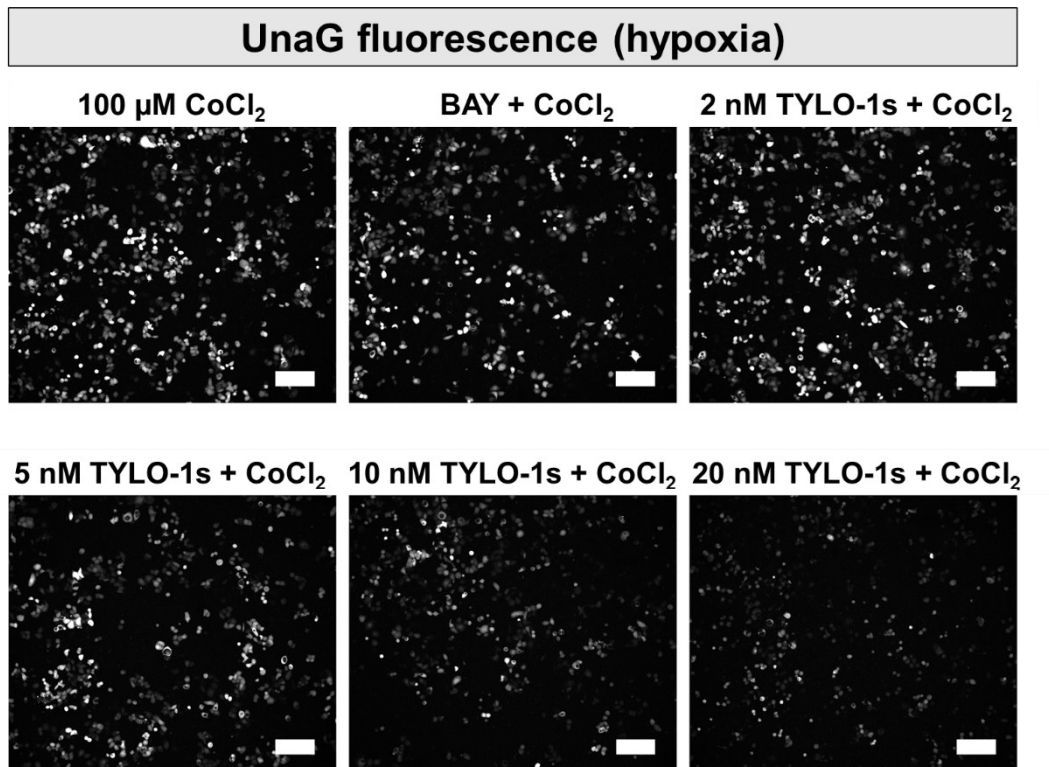
Figure 3-28 Dose-response inhibition in MB-468-UnaG for CoCl₂, TYLO-1s, BAY 11-7085 and paclitaxel. Cell viability was determined 24 h post-treatment according to the 2D PrestoBlue assay. Cells were untreated (CTRL) or exposed to (a) CoCl₂, (b) TYLO-1s, (c) paclitaxel or (d) BAY 11-7085. Final compound concentration was applied in triplicates in a three-fold serial dilution starting at 100 nM for TYLO-1s, at 1000 nM for paclitaxel and at 50 μM for BAY 11-7085. (a) Bars represent the mean of one independent experiment ± SEM. (b-d) Data points represent the mean of one independent experiment. (a) Statistical difference vs. CTRL was calculated with two-way-ANOVA (** $p < 0.01$, *** $p < 0.001$). Illustration with minor modifications from Reimche *et al.* (2022) [187].



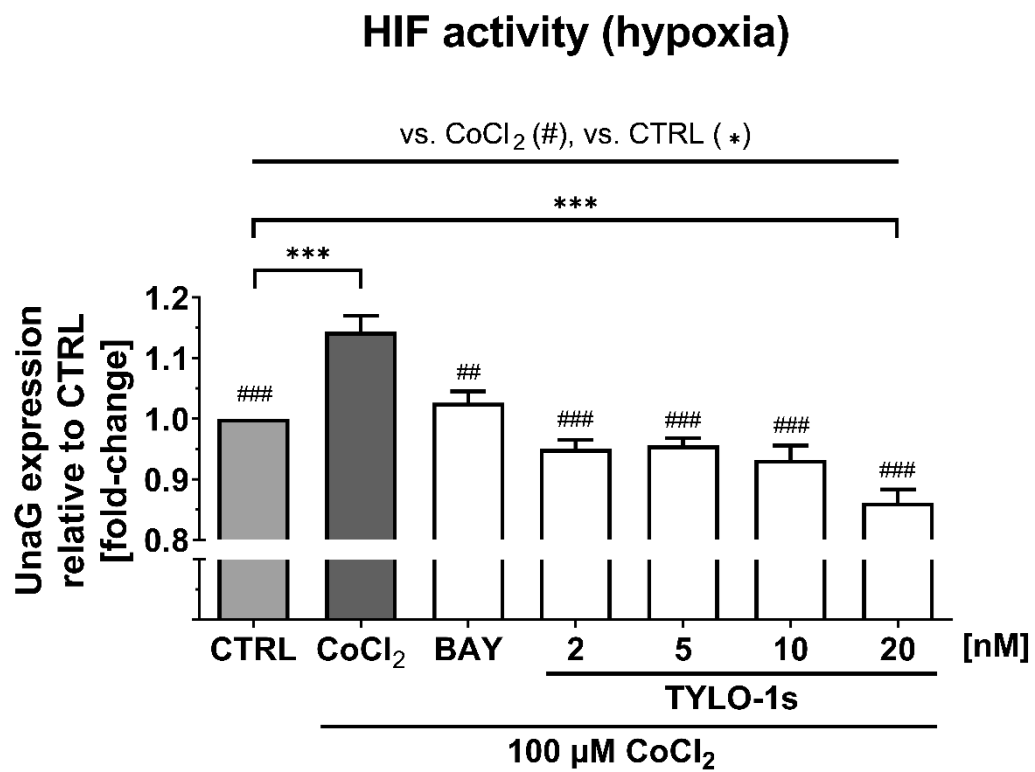
(a)



(b)



(c)



(d)

Figure 3-29 TYLO-1s decreased HIF-mediated transcription in MB-468-UnaG. Cells were left untreated (CTRL) or pre-treated for 1 h with TYLO-1s or BAY 11-7085 (BAY) at the indicated concentration. For further 24 h, cells were **(a,b)** left unstimulated (normoxia) or **(c,d)** exposed to 100 μ M CoCl₂ (hypoxia). **(a,c)** Representative fluorescence images depicting UnaG expression under normoxia and hypoxia. Scale bar: 200 μ m. **(b,d)** Total fluorescence intensity of HIF-dependent UnaG is depicted relative to the CTRL group (which was set to 1; fold-change). Bars represent the mean \pm SEM ($n=3$). Statistical difference was calculated with one-way-ANOVA **(b)** vs. CTRL (normoxia) (* $p < 0.05$). **(d)** vs. CTRL (hypoxia) (** $p < 0.001$); vs. CoCl₂ (## $p < 0.01$, ### $p < 0.001$). Illustration with minor modifications from Reimche *et al.* (2022) [187].

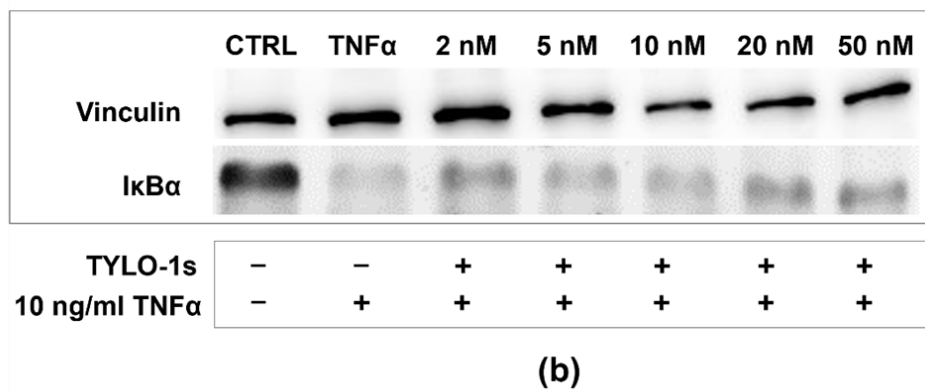
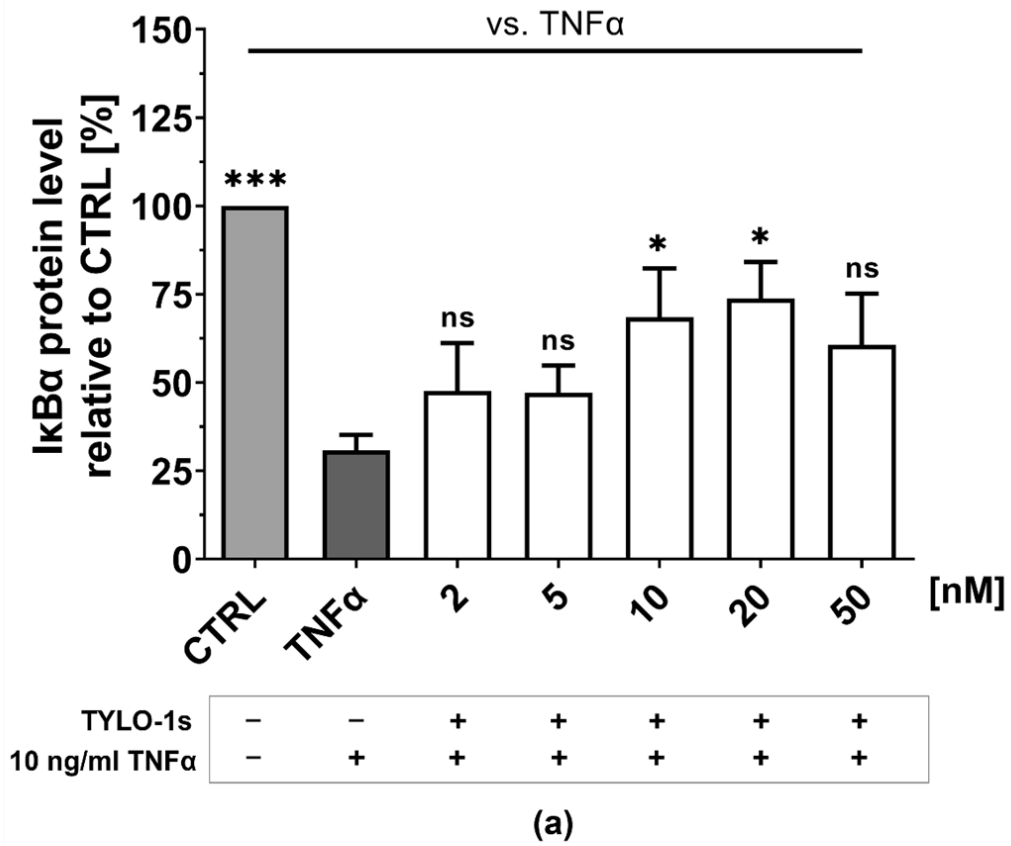
3.1.5.2 TYLO-1s suppresses NF κ B under hypoxic conditions via I κ B α stabilization

We aimed to investigate NF κ B modulation under normoxic as well hypoxic conditions. For that, the protein level of the NF κ B inhibitor I κ B α was assessed in the hypoxia sensor cell line MB-468-UnaG (**Figure 3-30**).

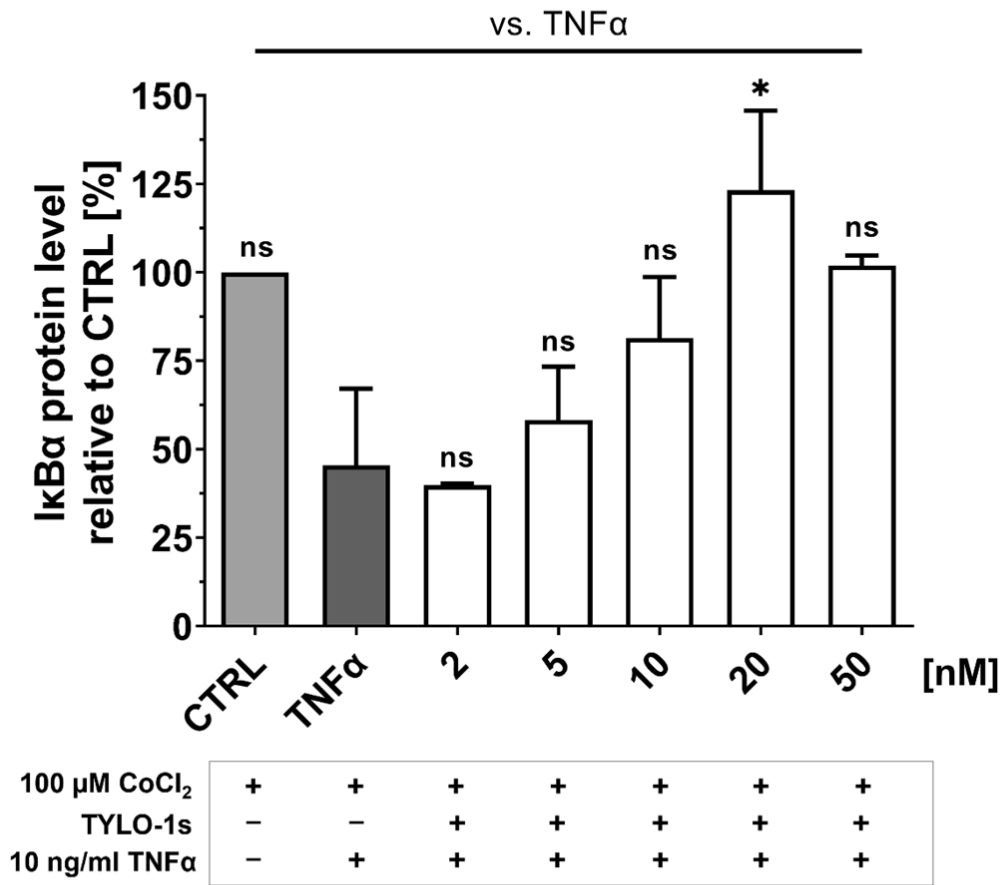
Under normoxia, TNF α stimulation reduced the I κ B α protein level to $31 \pm 6\%$ when compared to the untreated control. After pre-stimulation with TYLO-1s, TNF α -mediated I κ B α degradation was reverted. Compared to the untreated group, TYLO-1s significantly stabilized I κ B α at 10 nM and 20 nM to a protein level of $69 \pm 20\%$ and $74 \pm 15\%$, respectively. Furthermore, to investigate compound effects under hypoxia, hypoxia was induced with a pre-treatment using 100 μ M CoCl₂. Interestingly, CoCl₂ downregulated I κ B α , which suggests additional induction of the NF κ B pathway (**Figure S 20**). Under CoCl₂-simulated hypoxia, TNF α reduced I κ B α to a protein level of $55 \pm 22\%$, and again, I κ B α degradation was reverted by TYLO-1s. I κ B α was significantly stabilized at 20 nM TYLO-1s to a I κ B α protein level of $123 \pm 22\%$, i.e., enhancing the I κ B α level by average 20% when compared to the untreated control. Nevertheless, the dose-dependent reversion of I κ B α degradation was limited at short time exposure, presumably due to cytotoxic effects at high concentrations (50 nM).

In conclusion, under both conditions, normoxia as well as hypoxia, I κ B α was stabilized with TYLO-1s, thus, indicating enhanced sequestration of NF κ B in the cytoplasm. As we investigated short time exposure, we postulate, that NF κ B-inhibition is not mediated on the transcriptional level but post-translation by targeting upstream regulators.

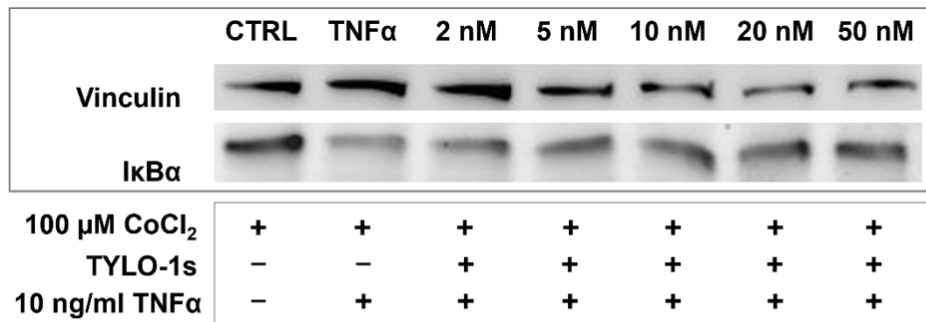
Normoxia



Hypoxia



(c)



(d)

Figure 3-30 TYLO-1s stabilizes the inhibitor κ B α protein (I κ B α) under normoxic and hypoxic conditions. MB-468-UnaG cells were (a,b) left unstimulated or (c,d) exposed to 100 μ M CoCl₂ for 24 h prior to treatment. (a-d) Cells were left untreated (CTRL), stimulated with solely 10 ng/ml TNF α for 30 min (TNF α) or pre-incubated with TYLO-1s at the indicated concentration for 1 h before stimulation with TNF α for 30 min. (a,c) Normalized I κ B α protein level is displayed relative to the CTRL group. Statistical difference vs. TNF α was calculated with one-way-ANOVA (ns = not significant, * $p < 0.05$, *** $p < 0.001$). Bars represent the

mean \pm SEM of **(a)** ($n=3$) or **(b)** ($n=2$). **(b, d)** Representative western blot with protein lysates that are immunologically stained for I κ B α (39 kDa) and the housekeeper protein vinculin (124 kDa).

3.1.6 Pathway crosstalk: YAP and NF κ B

3.1.6.1 TYLO-1 modulates YAP in a contradictory manner in MB-231

To explore YAP as a target for P-alkaloids, we determined transcriptional activity of YAP by analysing the nuclear YAP protein level. For YAP knockdown studies, YAP protein translation was blocked based on siRNA interference. Of note, non-targeted siRNA transfection neither affected YAP activity (**Figure S 21**) nor YAP expression (**Figure S 22**). Compared to the non-cancerous epithelial cell line HMEC, YAP activity was increased in the cancerous cell line MB-231 (**Figure S 23**). Further, YAP modulation was analysed after exposure to 100 nM TYLO-1 and activity was significantly decreased by 10% in NF κ B-MB-231-Firefly and by 35% in MB-231 when compared to the untreated control (**Figure S 24**). To investigate modulation of YAP, YAP knockdown was performed, resulting in a decrease of YAP activity by $41\pm 9\%$ in NF κ B-MB-231-Firefly and by 73% in MB-231. TYLO-1 reduced YAP activity in the non-targeted group by $57\pm 19\%$ in NF κ B-MB-231-Firefly and by 65% in MB-231, but TYLO-1 had no additional effects to the YAP-targeted group. YAP modulation after solely YAP knockdown and solely TYLO-1 treatment was comparable with a reduction by 40-50% in NF κ B-MB-231-Firefly and by 60-70% in MB-231, indicating a similar mechanism, i.e., reduced YAP expression, which needs further clarification (**Figure S 25**). We questioned whether modulation of YAP is cancer specific and investigated TYLO-1 in MB-231 compared to the non-cancerous cell line MCF10A. Upon siYAP transfection, YAP was significantly reduced by at least 68% in both cell lines (**Figure S 26**). Additionally, we evaluated TYLO-1 in YAP knockdown cells. In the non-targeted group, TYLO-1 reduced YAP activity by 60% in MB-231, but did not significantly decrease YAP activity in MCF10A. In the YAP targeted group, TYLO-1 did not additionally modulate YAP activity in MB-231 nor MCF10A (**Figure S 27**).

To address whether TYLO-1 modulates YAP activity on the transcriptional level, YAP expression was quantified in NF κ B-MB-231-Firefly and MB-231. YAP knockdown resulted in decreased YAP expression by at least 65% in both cell lines (**Figure 3-31**). Interestingly, TYLO-1 increased YAP expression in both cell lines in the non-targeted group as well as YAP targeted group by at least doubling expression.

In summary, our data reveal YAP as a novel target for TYLO-1, which is specific to cancerous cell lines. However, YAP is modulated in a contradictory manner on the transcriptional and post-translational level with enhancing expression, while reducing activity. Further investigations are required to unravel the mode of action involving YAP .

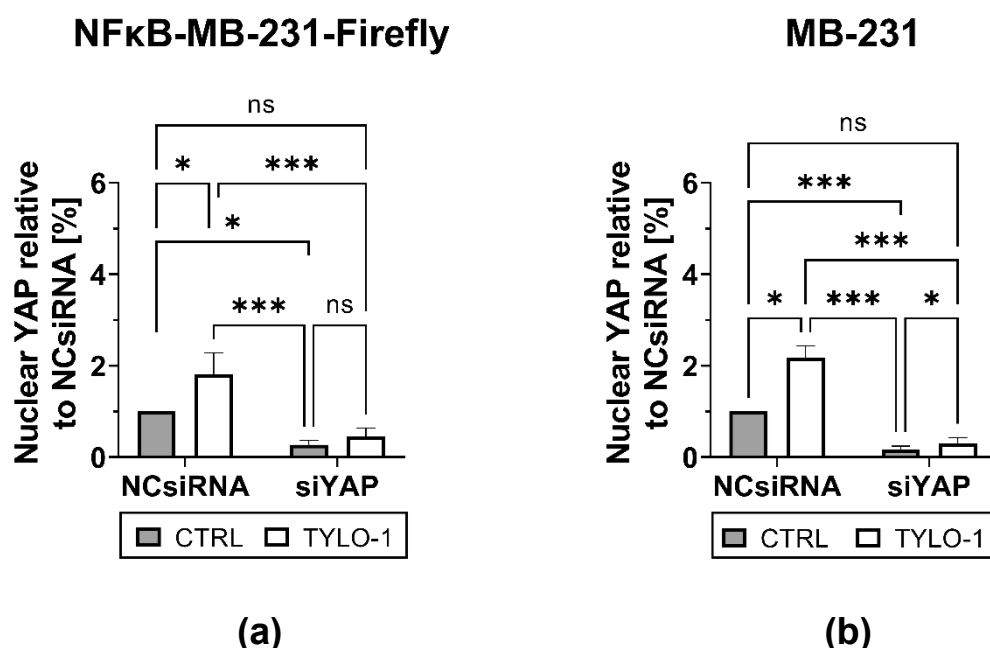


Figure 3-31 TYLO-1 enhances YAP expression in TNBC. YAP knockdown was performed in **(a)** NFκB-MB-231-Firefly and **(b)** MB-231 with transfection of non-targeting siRNA (NCsiRNA) or YAP-targeting siRNA (siYAP). 48 h-post transfection, cells were treated for 24 h with 100 nM TYLO-1. YAP expression was quantified with RT-qPCR. Based on the $2^{-\Delta\Delta CT}$ method, the YAP mRNA level was normalized to GAPDH, followed by normalization of all groups to the untreated NCsiRNA group. Bars represent the mean \pm SD ($n=3$). Statistical difference within all groups was calculated with one-way-ANOVA (ns = not significant, * $p < 0.05$, *** $p < 0.001$).

3.1.6.2 YAP is dispensable for anti-tumour effects by TYLO-1

After we observed altered YAP activity upon TYLO-1 stimulation, we questioned whether YAP is relevant for the anti-inflammatory and cytotoxic effects of TYLO-1.

TYLO-1 blocks TNF α induced NFκB activity with a comparable IC₅₀ value in the non-targeted and YAP-targeted group with 4.9 nM and 4.1 nM, respectively (**Figure 3-32**). Regarding cell viability after TYLO-1 treatment, IC₅₀ value was also comparable in the non-targeted and YAP-targeted group with 7.9 nM and 8.2 nM, respectively (**Figure 3-33**). YAP knockdown in the untreated group was neither affecting potential for NFκB inhibition nor reduction in cell viability in MB-231 (**Figure 3-32**, **Figure 3-33**).

To sum it up, our results exclude a key role of YAP for the anti-tumour and anti-inflammatory potential of TYLO-1.

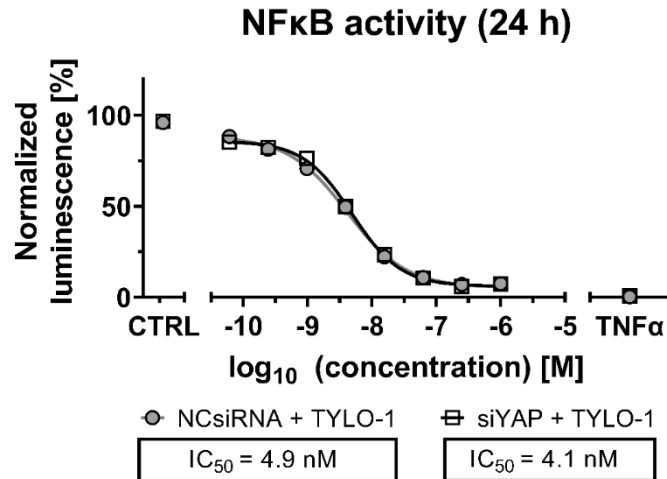


Figure 3-32 TYLO-1 induced NFκB-inhibition is YAP-independent. YAP knockdown was performed in NFκB-MB-231-Firefly using non-targeting siRNA (NCsiRNA) or YAP-targeting siRNA (siYAP). 48 h-post transfection, cells were pre-treated for 20 min with TYLO-1 in a four-fold serial dilution starting at a concentration of 1 μM. For stimulating NFκB, it was applied 20 ng/ml TNFα for another 24 h. Untreated cells served as negative control (CTRL), TNFα treated cells served as positive control (TNFα). NFκB activity was assessed according to the NFκB-inhibition assay. NFκB-dependent luminescence was normalized to the average luminescence of the CTRL group (which was set to 100%) and of the TNFα (which was set to 0%). Data points represent the mean ± SD (*n*=3).

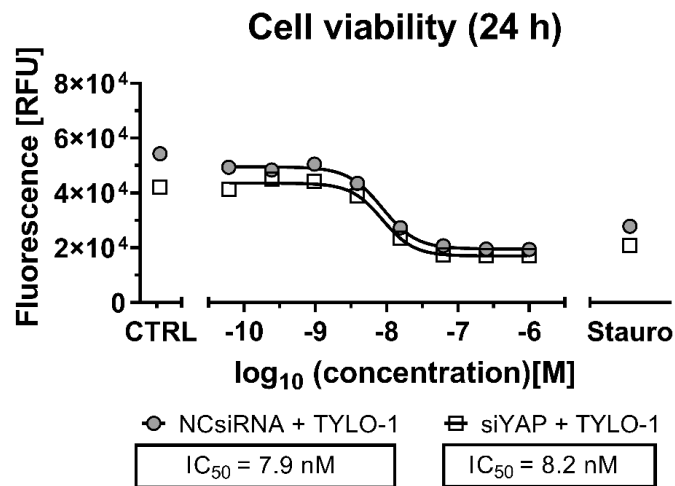


Figure 3-33 TYLO-1 mediated reduction in cell viability is YAP-independent. YAP knockdown was induced in MB-231 with transfection of non-targeting siRNA (NCsiRNA) or YAP-targeting siRNA (siYAP). 48 h post-transfection, cells were treated with TYLO-1 for 24 h. TYLO-1 concentration was applied in triplicates ranged in a four-fold serial dilution from 1000 nM to 0.06 nM. Culture medium (CTRL) and 20 μM of cytotoxic staurosporine (Stauro). Cell viability-dependent fluorescence [RFU] was determined according to the 2D PrestoBlue assay. Data points represent the mean ± SD of one independent experiment.

3.2 Anti-tumour characterization of fungus-derived metabolites in TNBC

To characterize anti-tumour potential of fungus-derived substances, bioactivity was explored regarding inflammation (3.2.1., 3.2.3) and migration (3.2.2). Fungal compounds were isolated from *A. falconensis* (3.2.1., 3.2.2) and *Didymella* sp. IEA-3B.1 (3.2.3).

3.2.1 Azaphilones isolated from the fungus *A. falconensis* suppress NFκB-mediated gene transcription in TNBC

Azaphilones were extracted from the marine-derived fungus *Aspergillus falconensis* and anti-tumour potential against TNBC was published in our previous work [171].

To investigate anti-inflammatory potential TNFα-induced transcriptional activity of NFκB was assessed for nine isolated compounds: Falconensin O, A, M, N, H, Q, R; S and I. NFκB blockade was found for all compounds with an IC₅₀ at a two-digit micromolar concentration in the range of 15 - 72 μM (**Table 3-4, Figure 3-34**). Falconensin O, Q and R showed strongest NFκB-inhibition with an IC₅₀ of 15.7 ± 0.7 μM, 11.9 ± 2.1 μM and 14.6 ± 1.7 μM, respectively. To exclude cytotoxicity as a cause of decreased NFκB transcription, we evaluated cell viability of MB-231. Falconensin O, M, N, H, Q, S and I did not affect cell viability in the concentration range tested (IC₅₀ > 200 μM). Falconensin A and R reduced cell viability with an IC₅₀ of 89.7 ± 9.1 μM and 126.8 ± 5.4 μM, respectively. Falconensin A and R displayed a distinct NFκB-inhibiting potential at a 9-times and 2-times lower concentration compared to reduction of cell viability.

In conclusion, fungal-derived azaphilones exhibit anti-inflammatory potential in TNBC through suppressing TNFα-induced transcriptional activity of NFκB at a two-digit micromolar concentration, with falconensin Q as one of the most potent metabolites.

Table 3-4 IC₅₀-values for azaphilones in NFκB-inhibition and reduction of cell viability

Compound	NFκB-inhibition ¹	Reduction of cell viability ²
	IC ₅₀ [μM] ³	IC ₅₀ [μM] ³
Falconensin A	53.2 ± 21.4	89.7 ± 9.1
Falconensin H	72 ± 28.1	> 400
Falconensin I	19.5 ± 2.5	> 400
Falconensin M	56.5 ± 8.3	> 200
Falconensin N	71 ± 7.3	> 200
Falconensin O	15.7 ± 0.7	> 200
Falconensin Q	11.9 ± 2.1	> 200
Falconensin R	14.6 ± 1.7	126.8 ± 5.4
Falconensin S	20.1 ± 5.6	> 200

Compounds were tested in ¹ NFκB-MB-231-Firefly according to the NFκB-inhibition assay or in ² MB-231 according to the 2D CellTiter Glo (384-well format). ³ Average IC₅₀ ± SD (*n* ≥ 3) tested in the concentration range of 400 μM to 0.78 μM (falconensin A, H, I) and 200 μM to 0.78 μM (falconensin M, N, O, Q, R, S) in a two-fold serial dilution. Adapted from El-Kashef *et al.* (2020) [171].

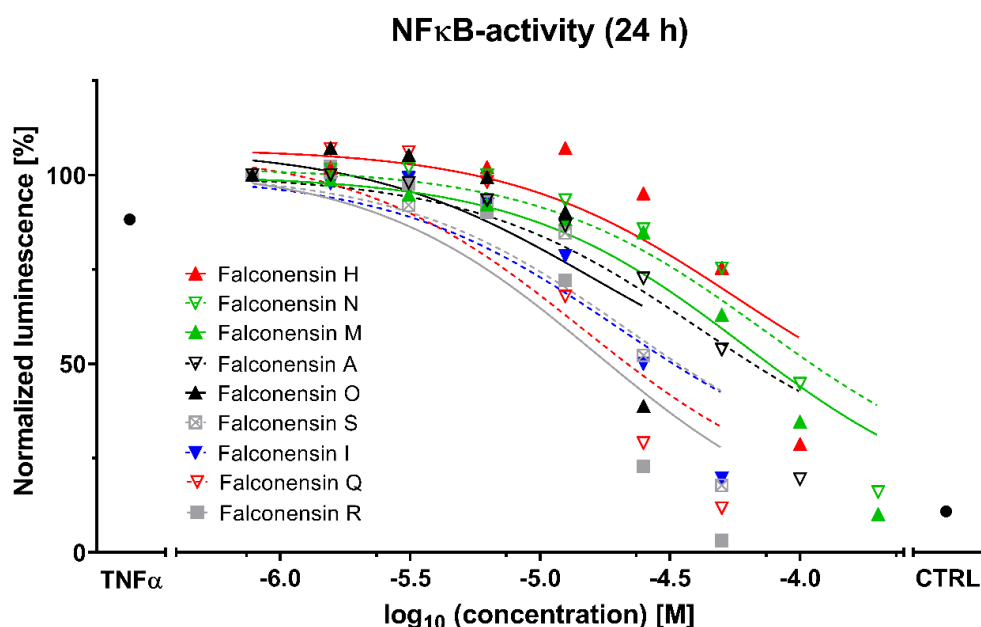


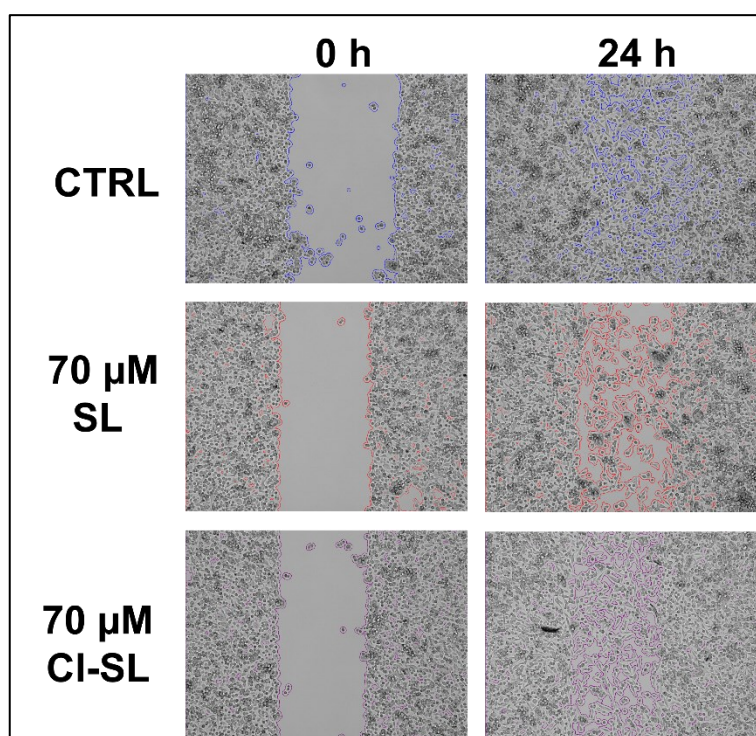
Figure 3-34 Azaphilones suppressed NFκB-mediated gene transcription in a dose-dependent manner. The NFκB-dependent luciferase activity was recorded 24 h post-stimulation in NFκB-MB-231-Firefly. Cells were left untreated (CTRL), treated for 24 h with solely 20 ng/ml TNFα (TNFα) or pre-treated for 20 min with compounds before stimulation for 24 h with 20 ng/ml TNFα. Final compound concentration in a two-fold serial dilution starting ranged from 100 μM to 0.78 μM (falconensin H, A, O, S, I, Q, R) or from 200 μM to 0.78 μM (falconensin N, M). In each independent experiment, the NFκB-dependent luminescence [RLU] was normalized to the RLU value of the lowest concentration applied (0.78 μM; which was set to 100%). Each data point represents the mean of at least three independent experiments.

3.2.2 Polyketides isolated from the fungus *A. falconensis* suppress TNBC migration

Polyketides were derived from the marine-derived fungus *Aspergillus falconensis* and anti-tumour potential against TNBC was published in our previous work. Studies revealed inhibition of MMP-13 [141].

Based on these findings anti-migratory potential of polyketides was examined in a 2D wound healing assay (**Figure 3-35**). MB-231 cell migration was significantly blocked by $57.9 \pm 11.8\%$ at 70 μM sulochrin and moderate, non-significant reduction in migration was observed at 70 μM monochlorsulochrin. Both compounds, sulochrin and monochlorsulochrin were non-toxic to MB-231 (**Figure 3-36**).

In conclusion, sulochrin serves as a potent anti-migratory compound to block TNBC migration at a two-digit micromolar concentration.



(a)

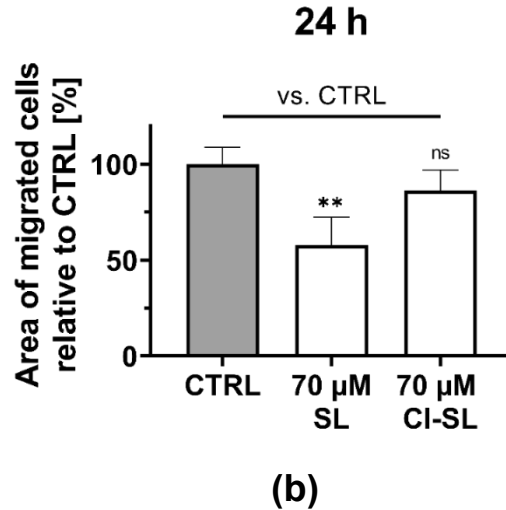


Figure 3-35 Sulochrin suppressed migration of MB-231 cells. Migration was evaluated according to the 2D wound healing assay. Monolayer cells were left untreated (CTRL) or incubated for 24 h with 70 μ M sulochrin (SL) or monochlorsulochrin (CI-SL). **(a)** Representative brightfield images of the migration gap were recorded pre-treatment (0 h) and post-treatment (24 h) using the high-content imager CQ1. Magnification: 100 \times . The cell area and cell free area were identified based on a machine learning recognition using the software CellPathfinder. The border between the cell area and cell free area is depicted as a colourful outline (blue, red, or violet). **(b)** The area of migrated cells was quantified based on the reduction of the cell free area within the migration gap. The cell free area was determined in brightfield images using the software CellPathfinder and normalized to the CTRL group post-treatment (which was set to 100%). Bars represent the mean \pm SD ($n=3$). Statistical difference vs. CTRL was calculated with one-way-ANOVA (ns = not significant, ** $p < 0.01$).

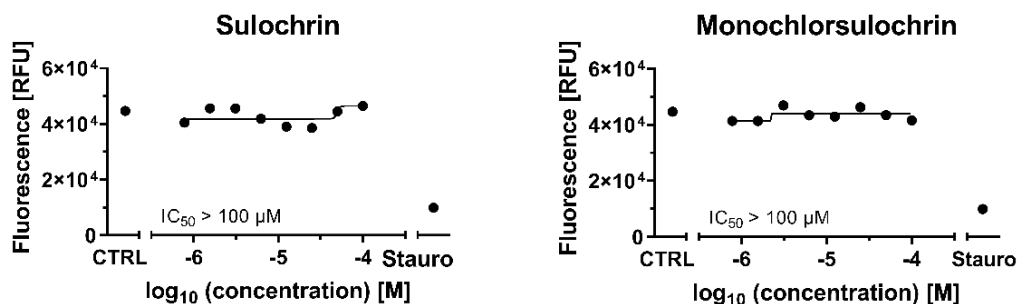


Figure 3-36 Representative dose-response inhibition of cell viability for sulochrin and monochlorsulochrin in MB-231. Cells were treated for 24 h in triplicates of sulochrin and monochlorsulochrin at a two-fold serial dilution ranging from 100 μ M to 0.78 μ M. Untreated cells (CTRL) or treatment with 20 μ M of cytotoxic staurosporine (Stauro) served as control. Cell viability-dependent fluorescence [RFU] was recorded according to the 2D

PrestoBlue assay. Data points represent one independent experiment. IC₅₀ is representative for reduction of cell viability within 24 h as well as 48 h (*n*=3).

3.2.3 Decahydrofluorenes isolated from the fungus *Didymella* sp. IEA-3B.1 inhibit NFκB-mediated gene expression in TNBC

Decahydrofluorenes were derived from the fungus *Didymella* sp. IEA-3B.1 and anti-tumour potential against TNBC was published in our previous work for one of the tested compounds, namely didymellanosine [168].

To investigate anti-inflammatory potential, we assessed LPS-induced transcriptional activity of NFκB for three isolated metabolites: Didymellanosine, phomapyrrolidone A and ascomylactam C. To exclude cytotoxicity as a cause of decreased NFκB signalling, we additionally evaluated cell viability of MB-231 (**Figure 3-37, Table 3-5**). Didymellanosine and phomapyrrolidone A showed a strong NFκB-inhibition with an IC₅₀ of 15.5 ± 1.1 μM, 54.1 ± 5.4 μM and reduction of cell viability with a at least two-fold higher concentration showing an IC₅₀ of 45.4 ± 8.1 μM and > 100 μM, respectively. Ascomylactam C reduced cell viability with an IC₅₀ of 47.5 ± 8.5 μM, that is comparable to NFκB-inhibition at 45.0 ± 11.6 μM, indicating a strong dependence on NFκB-blockade for its anti-tumour effects.

In conclusion, decahydrofluorenes exhibit anti-inflammatory potential in TNBC through suppressing LPS-induced transcriptional activity of NFκB at a two-digit micromolar concentration, with didymellanosine as the most potent metabolite.

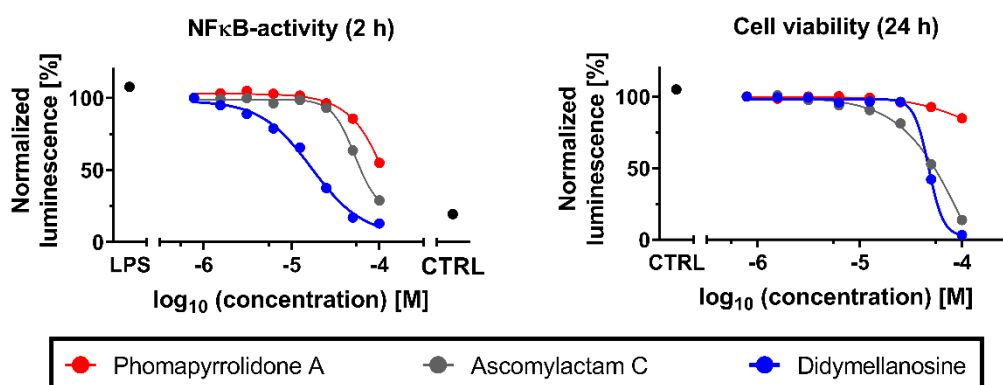


Figure 3-37 Dose-response inhibition of NFκB-activity and cell viability for decahydrofluorenes. (a) NFκB-MB-231-NanoLuc were left untreated (CTRL), treated for 2 h with solely 1 μg/ml LPS (LPS) or pre-treated for 20 min with compounds before stimulation for 2 h with 1 μg/ml LPS. NFκB-dependent luminescence [RLU] was recorded according to the NFκB-inhibition assay. (b) MB-231 were left untreated (CTRL) or treated for 24 h with compounds. Cell viability-dependent luminescence [RLU] was recorded according to the 2D CellTiterGlo (384-well format). (a,b) Final compound concentration

ranged in a two-fold serial dilution from 100 μM to 0.78 μM . In each independent experiment, RLU values were normalized to the RLU value of the lowest concentration applied (0.78 μM ; which was set to 100%; normalized luminescence). Each data point represents the mean of at least four independent experiments.

Table 3-5 IC₅₀-values for decahydrofluorenes in NF κ B-inhibition and reduction of cell viability

Compound	NF κ B-inhibition ¹	Reduction of cell viability ²
	2 h ³	24 h ³
	IC ₅₀ [μM] ⁴	IC ₅₀ [μM] ⁴
Didymellanosine	15.5 \pm 1.1	45.4 \pm 8.1
Phomapyrrolidone A	54.1 \pm 5.4	> 100
Ascomylactam C	45 \pm 11.6	47.5 \pm 8.5

Compounds were tested in ¹ NF κ B-MB-231-NanoLuc using the NanoGlo assay or in ² MB-231 using the 2D CellTiterGlo assay (384-well format). ³ Duration of treatment. ⁴ Average IC₅₀ of at least four independent experiments \pm SD tested in the concentration range from 100 μM to 0.78 μM in a two-fold serial dilution.

3.3 Anti-tumour characterization of engineered and chemically prepared histone deacetylase inhibitors (HDACIs) in TNBC

To explore anti-tumour potential against TNBC, cell viability of MB-231 was assessed after treatment with the synthetically prepared HDACIs, namely, LAK41, LAK107, LAK110, LAK121, LAK-ZnFD, KSK64, KSK75 and MPK26. Reduction in cell viability was observed for LAK41, KSK64 and MPK265 with an IC₅₀ value of 4.5 \pm 1.7 μM , 10.2 \pm 4.9 μM and 38.7 \pm 1.8 μM , respectively (**Figure 3-38, Table 3-6**). These three synthetic compounds were proven to simultaneously target HDAC1 and HDAC6 at a nanomolar concentration (compare **Table 2-14**). Other HDACIs, which solely impact HDAC1 (LAK110, LAK121) or HDAC6 (LAK-ZnFD, KSK75) did not affect cell viability (IC₅₀ > 100 μM). Cell viability was also not affected by additionally targeting HDAC2 (LAK110) or HDAC8 (KSK75) or targeting HDAC3 alone (LAK107). Compound KSK75 was proven to solely target HDAC6 but showed no selectivity to HDAC1. However, the compounds that with proven selectivity to solely HDAC1 (LAK110, LAK121) or solely HDAC6 (Lak-ZnFD) were not yet examined whether they additionally target HDAC6 or HDAC1, respectively.

In conclusion, HDACIs have anti-tumour potential against TNBC at a low micromolar concentration. Effects in TNBC was only found for HDACIs that simultaneously targeted HDAC1 and HDAC6. Further studies are suggested to investigate simultaneous targeting both, HDAC1 and HDAC6, for compounds that were proven to solely target HDAC1 (LAK110, LAK121) or HDAC6 (Lak-ZnFD).

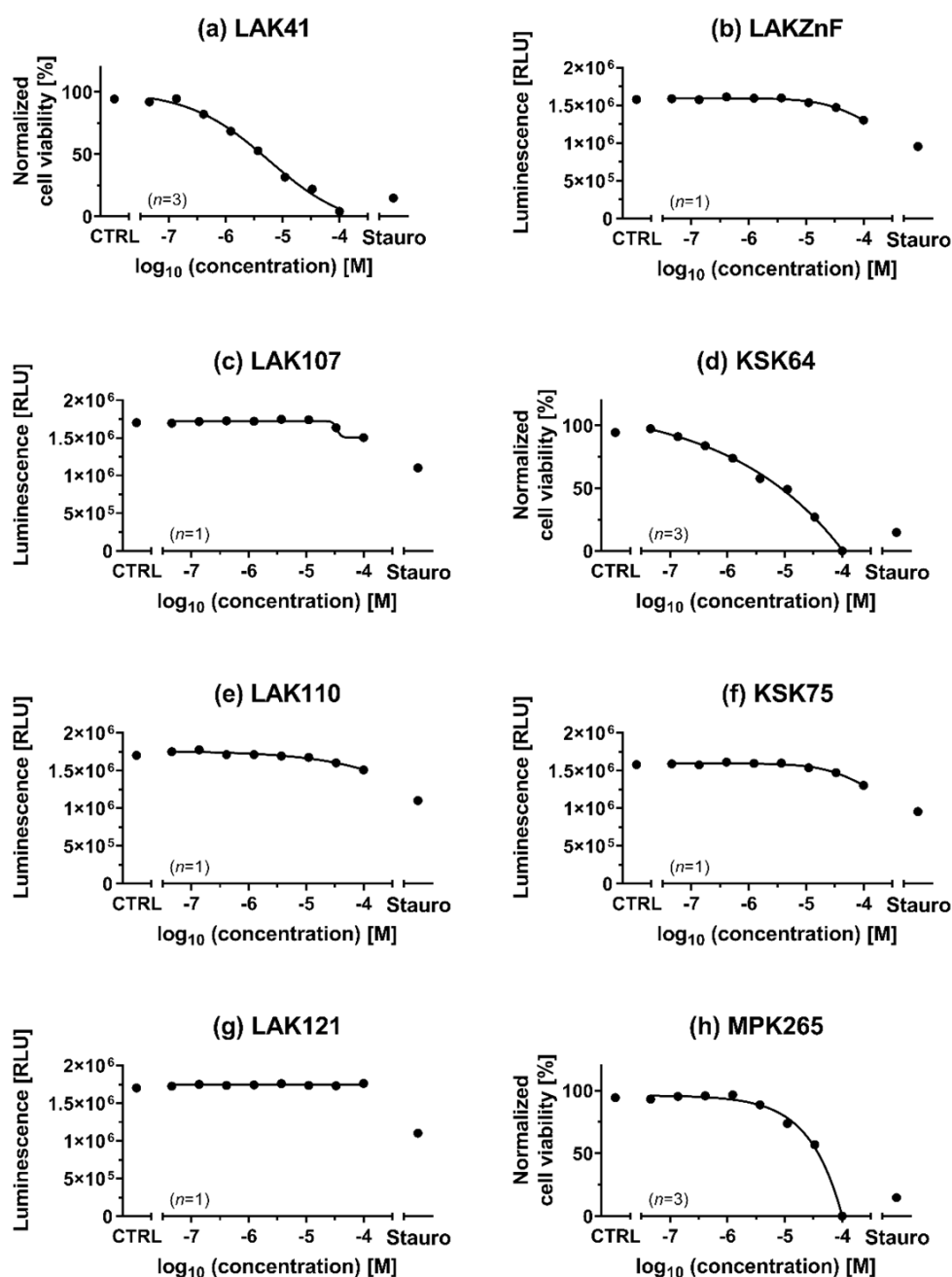


Figure 3-38 HDACIs display dose-response reduction of MB-231 cell viability. Cell viability was determined in MB-231 24 h post-treatment using a 2D CellTiterGlo on a 384-well format. Applied concentration in triplicates ranged in a three-fold serial dilution starting at 100 μ M. Untreated cells served as negative control, (CTRL), 20 μ M staurosporine served as positive control (Stauro). In each independent experiment, the Relative Light Unit (RLU) was normalized to the smallest value (which was set to 0%) and to the highest value (which was set to 100%) (cell viability). Each data point represents (b,c,e,f,g) (n=1) one independent experiment or (a,d,h) (n=3) the mean of three independent experiments.

Table 3-6 IC₅₀-values of HDACIs for reduction of cell viability in MB-231

HDACI	Reduction of cell viability
	IC ₅₀ [μM] ¹
LAK41	4.5 ± 1.7
LAK107	> 100
LAK110	> 100
LAK121	> 100
LAK-ZnFD	> 100
KSK64	10.2 ± 4.9
KSK75	> 100
MPK265	38.7 ± 1.8

¹ Average IC₅₀ of at least three independent experiments ± SD. The cell viability was determined 24 h post-treatment of MB-231 according to the 2D CellTiterGlo (384-well format). Compound concentration ranged from 100 μM to 0.78 μM in a two-fold serial dilution.

4 Discussion

4.1 Characterization of P-alkaloids in TNBC

4.1.1 Anti-tumour mechanism of P-alkaloids against TNBC

P-alkaloids exhibit growth blockade [203] and cytotoxicity against MB-231 or MB-468 [203–205], with no mechanism elucidated yet. To characterize the anti-cancer potential of P-alkaloids isolated from *T. ovata* in TNBC, we evaluated cell viability, apoptosis, and potential for tumour initiation. Our data reveal a different mode of action for P-alkaloids compared to paclitaxel, presumably due to targeting multiple sites to suppress TNBC progression (Figure 4-1).

In this study, TYLO-1 reduced cell viability in cancerous as well as non-cancerous cells at a similar concentration with an IC_{50} around 10 nM. Nevertheless, performed assays can't distinguish whether compound activity relies on anti-proliferative or pro-apoptotic effects, because cell viability measurement depended on the proportion of viable cells. To address this ambiguity, we interpreted drug response over time (48 h) regarding cell viability and found, that TYLO-1 maintained its IC_{50} of around 10 nM, while paclitaxel, which is an anti-mitotic compound, showed increased efficacy over time. These results suggest, that TYLO-1 acts differently, because its efficacy was not time-dependent and thus not solely depending on proliferation. Additionally, we concluded from our cell cycle studies, that TYLO-1s induces apoptosis in TNBC through arrest at the G1-state during cell cycle progression. Concomitant with our findings, pro-apoptotic features were ascribed to the tylophorine derivative, NK007, by involving the p38/MAPK signalling and arresting cells at the G1/S-state in ovarian cancer [149]. Moreover, cell death induction was found to rely on downregulation of Bcl-2 [206]. However, no pro-apoptotic features were attributed to antofine, a derivative of tylophorine, in colon cancer [153] or the synthetic tylophorine analogue, DCB-3503 in hepatocellular carcinoma [179]. Thus, hypothesizing, that the compound mechanism might strictly rely on the distinct SAR, and on the distinct molecular features of cancer entities. In TNBC, cytotoxicity through TYLO-1/TYLO-1s might depend on anti-inflammatory features, because NF κ B-blockade strongly correlated with the reduction of cell viability. Distinct from P-alkaloids, paclitaxel showed no inhibitory effects on NF κ B signalling, neither at short- nor long-time exposure. This further strengthens our observation, that P-alkaloids act in a different way than paclitaxel.

To further characterize anti-proliferative potential in TNBC, we studied tumour initiation upon TYLO-1 or paclitaxel treatment in a simplified colony formation assay. Both compounds suppressed cell growth, which correlated with their specific IC_{50} value for reduced cell viability, 10.6 nM and 3.2 nM, respectively. Recently, we reported proliferation

blockade at an average IC_{50} of 18 nM in MB-231, which is slightly higher compared to the IC_{50} for the reduction in cell viability [187]. Thus, we hypothesize, that suppressed colony formation does not solely rely on proliferation blockade. When testing TYLO-1 at lower concentrations to evaluate tumour initiation, suppressed cell growth was observed at a concentration, which is comparable to the average IC_{50} for NF κ B-inhibition, 4 nM within 24 h. Of note, experiments had different time windows with evaluating colony formation after ten days and NF κ B-inhibition after one day treatment. Anti-inflammatory effects of P-alkaloids were time-dependent, thus we cannot exclude, that the definite average IC_{50} might even fall short of the determined IC_{50} value within 24 h. Concerning other studies including P-alkaloids, colony formation blockade at a low-toxic and low two-digit nanomolar concentration were also described for the natural tylophorine derivative, NK007, which was sufficient to block tumour initiation in ovarian carcinoma and even in paclitaxel-resistant cells [149]. Interestingly, basal-like BC and ovarian carcinoma share molecular features, including loss of activity for p53, Rb, BRCA1 and high activation of the HIF-1 α [23], MAPK and AKT signalling [207]. Hence, we hypothesize, that P-alkaloids are likewise potent to reverse chemotherapy resistance, which was already reported [154], but needs further validation in TNBC. Tumour initiation is an attributed feature of CSC [32]. In this study, paclitaxel-induced pathways, which are linked to CSC features, namely NF κ B, HIF [31] as well as YAP [48], are blocked by TYLO-1/TYLO-1s. Concluding from these results, we hypothesize, that P-alkaloids might overcome drug resistance by targeting CSC.

In vivo, P-alkaloids suppress tumour growth [150] and inflammatory response [208]. Anti-inflammatory features might depend on intervention with cellular signalling, because tylophorine administration exhibited *in vivo* effects shortly after administration [208]. In line with these findings, our data revealed anti-inflammatory effects after short-time exposure to TYLO-1s, caused by decreased upstream signalling of NF κ B. Furthermore indicating, that pathways are modulated by post-translational modifications rather than a reduced expression of the transcription factors.

In conclusion, P-alkaloids prevent proliferation and tumour initiation by a different mechanism than currently applied drugs in TNBC therapy. Anti-inflammatory features are more relevant than blockade of proliferation, while bioactivity relies on modulation of post-translation protein modifications to reduce cell signalling. Further investigations are required to validate pro-apoptotic effects of P-alkaloids, whereas the mechanism is still not well understood. Although P-alkaloids reverse drug resistance, general cytotoxicity to non-cancerous cells is disadvantageous for clinical application. Nevertheless, we recommend combinational treatment of P-alkaloids with chemotherapeutics to evaluate their potential to increase drug sensitivity in TNBC. The generation of chemotherapeutic agent-resistant cell lines and assessment of CSC markers could help to address this issue.

potential of TYLO-3, which was already reported in nasopharyngeal, lung and colorectal cancer cells [164] as well as in BC cells regarding HIF signalling [157], our data indicate, that the activity of TYLO-3 does not depend on NFkB-blockade. Compound activity corresponds to the chemical structure [150,209] and for the synthetic compound TYLO- 1s we report similar NFkB blockade ($IC_{50} = 3.3 \pm 0.2$ nM) and reduction of cell viability ($IC_{50} = 4.2 \pm 1$ nM) compared to the natural equivalent TYLO-1. Initial SAR of compound TYLO-1 to TYLO-6 reveals that bioactivity in TNBC is enhanced due to the following characteristics in their chemical structure: (I) A hydroxyl moiety in the indolizidine ring at position C-14, (II) a methoxyl moiety in the phenanthrene ring at position C-3 and C-6 and (III) an uncharged nitrogen in the indolizidine ring, with (III) being the most crucial feature that determines anti-tumour potential against TNBC.

Our findings come in agreement with various reported studies [150,157,162,164,204], and next, the relevance of functional groups within the compounds will be discussed regarding *in vitro* anti-cancer mechanisms and *in vivo* activity.

Concerning the indolizidine ring, unshared electrons of the nitrogen might be crucial for its anti-cancer activity [162] through interaction with proteins [158]. For example, Rao and colleagues hypothesize, that the indolizidine moiety participates in the alignment to the active site of the enzyme thymidylate synthase [210], which was reported as a target for TYLO-2 [166], causing reduced nucleic acid synthesis. A low pH level was described to decrease anti-tumour potential of P-alkaloids, presumably due to protonation. It is suggested, that the unprotonated nitrogen, mainly associated with non-planar compounds, is important for transportation into the cell and for interaction with receptors [208]. Studies from Yang *et al.* postulate, that anti-inflammatory potential, which was investigated in murine macrophages (RAW264.7) is increased in non-planar compounds, compared to rigid and planar molecules [211]. Concomitant with these findings, our data revealed reduced anti-cancer as well as anti-inflammatory potential for the planar compounds, such as those found in TYLO-5 and TYLO-6, and thereby validating, that the positively charged nitrogen is the most critical alteration in the chemical structure resulting in activity loss. Other studies confirmed our observation and state, that TYLO-5 had no effects against tumours, including the luminal BC (T47D) [157,162]. Interestingly, a distinct mode of action was reported for TYLO-5 and TYLO-6 through blocking telomerase activity by promoting telomeric DNA folding into G-quadruplex at a two-digit micromolar concentration [165]. It was reported, that planar molecules with a positively charged nitrogen possess enhanced binding affinity to DNA, and binding affinity was increased with a methoxyl group at C-2, C-3 as well as C-6 in the phenanthrene ring [165]. However, DNA binding was also reported as a mechanism to reduce NFkB binding to the DNA for the non-planar tylophorine analogue, DCB-3503 [151], as well as phenanthrene-based compounds (PTBs) [212]. For the non-covalent DNA

binding of the stereoisomer of TYO-4, namely (+)-(13a*S*)-deoxytylophorinine, hydrophobic methoxy substitutes at the phenanthrene ring are important for intercalation into double-stranded DNA, while the hydrophilic nitrogen atom sticks out into the DNA groove to interact and block proteins that are involved in DNA replication and gene transcription [158].

Regarding the phenanthrene ring, some studies conclude, that the position of the hydroxyl and methoxyl groups at the phenanthrene ring is crucial for its activity [150], while other studies conclude, that there is no marked difference given by the particular position or that the number of these functional groups is more relevant than the position [213]. Amongst diverse SAR studies, a hydroxyl group at the C-7 position in the phenanthrene ring was increasing compound activity [213]. This is an interesting finding for the compounds tested in this study, because the most potent compound TYLO-1/TYLO-1s possesses a methoxyl group at C-7. Hence, it would be interesting to investigate if replacement with a hydroxyl group could further TYLO-1 compound efficacy.

P-alkaloid derivatives that are solely generated based on the phenanthrene ring [214] or the indolizidine ring [215] exhibit anti-cancer features, although there were controversial findings regarding their mode of action. Concerning PTBs, Lin and colleagues found NFκB-blockade, which is caused by suppressed upstream AKT/IKKα signalling, thus, resulting in accumulation of IκBα which sequesters NFκB. They report, that PTBs activate an alternative NFκB pathway (IKKα/RelB) to suppress the canonical p65/p50 signalling [216]. Effects of P-alkaloids were not yet investigated towards the alternative NFκB signalling and could be considered in future studies. All in all, compounds, that are based on solely one moiety, the phenanthrene or indolizidine ring might act differently, presumably based on the different functions of each moiety, by either interacting with DNA or proteins [158].

Diverse SAR studies involving P-alkaloids report functional groups that may or may not improve compound activity. It was also found, that compound efficacy corresponds to the stereochemistry of e.g. the hydrogen at C-13 [213]. Apart from this, the stereochemistry of functional groups is relevant, because it may determine and alter the impact of the residual functional groups for compound activities [208].

Despite the efficacious anti-tumour effects of P-alkaloids, including the anti-inflammatory potential [217], severe toxicity *in vivo* is a major obstacle regarding utilization for clinical purposes [212]. There are controversial findings regarding SAR *in vivo*. Gao and colleagues, observed, that compounds carrying a hydroxylation at C-14 exhibited greater anti-tumour effects *in vivo*. The conclusion was based on increased activity *in vitro* as well as *in vivo* of TYLO-2 compared to (*R*)-(+)-deoxytylophorinidine, the isomer of TYLO-4 [150]. In contrast to that, the synthetically prepared YPC-10157, which is similar to the molecule structure of TYLO-3, lacks a hydroxyl group at the C-14 and displays mild toxicity *in vivo* with greater growth suppression compared to the hydroxylated analogues [203]. Additional

SAR studies confirmed the observation, that compound efficacy and tolerability *in vivo* increases, when derivatives lack hydroxylation at C-14 [164,203]. However, *in vivo* SAR might also depend on the compound scaffold used for engineering of synthetic analogues, thus SAR should be interpreted with caution. Regarding toxic side effects *in vivo*, polar analogues, i.e. hydroxylated molecules, are hypothesized to clear the blood-brain-barrier (BBB) to a lesser extent [208] and thereby showing decreased neurotoxicity [218]. This hypothesis might explain, why TYLO-3 was more tolerable *in vivo* in addition to a stronger growth inhibition compared to tylophorinine, the stereoisomer of TYLO-1 [163]. Notably, methoxyl groups at the phenanthrene ring might influence metabolic stability, while there are controversial findings whether the impact is positive or negative [203].

All in all, P-alkaloids isolated from the plant *T. ovata* display a SAR regarding their anti-inflammatory and anti-cancer potential against TNBC. Functional groups at the phenanthrene ring might be relevant for non-covalent binding to DNA; while functional groups at the indolizidine ring might be important for interactions with proteins. Concerning future perspectives, additional SAR studies are inevitable to optimize bioactivity while simultaneously increasing safety for clinical utilization e.g., in cancer therapy.

4.1.3 The anti-inflammatory potential of P-alkaloids is maintained under hypoxic conditions

The tumour niche of TNBC is characterized by increased inflammation and reduced oxygen levels [62]. Hitherto, transcription blockade was reported for P-alkaloids regarding inflammation-associated NF κ B-pathway in HepG2 [150] and hypoxia-associated HIF-1 α pathway in T47D [157], but none of the studies included TNBC.

In this study, examination of upstream regulation of NF κ B revealed that TYLO-1s stabilizes I κ B α in TNBC under normoxia as well as CoCl₂-simulated hypoxia. Additional blockade of HIF-regulated transcription presents P-alkaloids as multi-targeting compounds in TNBC. Regarding NF κ B-mediated transcription, studies from Gao *et al.* report inhibition in HepG2 cells for TYLO-2 and the epimer of TYLO-1, namely tylophorinine [150]. However, the mode of action for transcriptional blockade in TNBC remains elusive. We evaluated compound TYLO-1s regarding the upstream regulation of NF κ B and found dose-dependent stabilization of the NF κ B inhibitor I κ B α . Because both, I κ B α and NF κ B are substrates of IKK, we hypothesize that P-alkaloids affect NF κ B through blocking activating phosphorylation by IKK. Findings from Shiah *et al.* support our hypothesis regarding NF κ B-inhibition in pancreatic ductal adenocarcinoma cancer cell line, PANC-1, using the synthetic tylophorine analogue DCB-3503. They report decreased NF κ B activity through suppression of phosphorylation by IKK α /IKK β . As a consequence, reduced phosphorylation events of I κ B α and NF κ B result in stabilization of I κ B α and enhanced sequestration of NF κ B in the

cytoplasm to block its transcriptional activity [151]. Concluded from our results, P-alkaloids inhibit NFκB through sequestration by IκBα in the cytoplasm rather than by decreasing RelA/p65 transcription or blockade of DNA binding after translocation to the nucleus. Reduced NFκB binding affinity to DNA was also excluded by studies from Shiah and colleagues, where they suggested, that phosphorylated p65/NFκB is at least partially eliminated through proteasome-mediated degradation [151].

NFκB activity induces drug resistance and is triggered during paclitaxel therapy [61] but also by hypoxia [92]. Inhibition of NFκB in HepG2 [150] and inhibition of HIF-1α in T47D [157] were reported separately for P-alkaloids, e.g. TYLO-2. In addition, we questioned whether the anti-inflammatory potential of compound TYLO-1s is maintained under hypoxic conditions. Our findings reveal a significant NFκB suppression at 20 nM via stabilization of IκBα under normoxia as well as under CoCl₂-simulated hypoxia. Indeed, we found modulation of HIF-mediated transcription by TYLO-1s and investigated the role of NFκB-inhibition on HIF-activity. Under normoxic as well as hypoxic conditions HIF was significantly blocked at a low nanomolar concentration (20 nM). Accordingly, data from Chen *et al.* support our findings, reporting blockade of HIF induction under low oxygen levels in the luminal BC cell line T47D for tylophorinine, TYLO-1, TYLO-2 as well as for TYLO-3 but not for TYLO-5 [157]. These results match with the SAR identified for our NFκB inhibition studies. NFκB blockade with the NFκB inhibitor BAY 11-7085 or TYLO-1s was sufficient to block CoCl₂-simulated hypoxia, whereas blockade of NFκB alone using Bay 11-7085 was not sufficient to suppress HIF, indicating that NFκB is involved in inducing CoCl₂-induced HIF-activity, which has already been reported [219], and that P-alkaloids act distinct from the commercially available NFκB inhibitors by impacting multiple targets, e.g. NFκB and HIF in TNBC.

Both, NFκB as well as the HIF pathway, are triggered upon paclitaxel-based chemotherapy and are involved in mediating chemoresistance [59,61,62,220], which is a major feature of CSCs [31]. Targeting key pathways in CSC may be a promising approach to combat TNBC, which is enriched in CSC [34]. Findings from Chen *et al.* describe HIF-blockade at a low nanomolar concentration [157], which matches our results with NFκB inhibition and HIF-inhibition by TYLO-1s at a low nanomolar concentration, hence, indicating that a common upstream regulator of both pathways may be modulated by P-alkaloids. The effects of P-alkaloids on upstream signalling of both NFκB and HIF as well as effects on the crosstalk between both pathways has not been elucidated yet. NFκB is involved in the transcriptional regulation of HIF-1α [89] and HIF-1α triggers NFκB activity by inducing nuclear translocation [92] through enhancing IKK/NFκB signalling [62]. But it remains unclear if (I) NFκB blockade by P-alkaloids affects HIF expression, (II) NFκB is involved in modulation of HIF-inhibition by P-alkaloids, (III) HIF-blockade would affect NFκB-inhibition by P-alkaloids. Knockdown

studies could help to address these hypotheses. However, both pathways share triggers for activation, TNF α and CoCl₂ [92], as well as target genes including cyclin D1 [219]. AKT is a common upstream regulator of NF κ B and HIF [221] and was reported as a target for P-alkaloids by blocking kinase activity [222]. It is poorly understood, how P-alkaloids regulate phosphorylation events [151] and whether P-alkaloids act as allosteric kinase inhibitors [152,179,223]. Nevertheless, approaches with *in silico* docking studies postulate kinase inhibition through binding to the ATP-binding site as a pharmacological mode-of-action for P-alkaloids. Studies from Liu *et al.* report blockade of AKT for the epimer of TYLO-1, namely HTBP1 [222], and Mostafa *et al.* showed blockade of Aurora A and B kinases for tylophorine and TYLO-2 [224]. Moreover, tylophorine was found to bind to the ATP-binding site of the vascular endothelial growth factor receptor (VEGFR) in endothelial cells, thus suppressing downstream signalling pathways including AKT and Erk [152]. Indicating, that AKT might not be the only molecular target to orchestrate inhibition of NF κ B and HIF signalling, which needs further clarification.

In conclusion, P-alkaloids are multi-targeting compounds in TNBC with the most efficacious compounds, TYLO-1 and TYLO-1s, exhibiting NF κ B-inhibition by a significant blockade of I κ B degradation that was maintained under hypoxia. Our SAR studies regarding NF κ B-inhibition might predict the anti-tumour potential for a variety of different types of cancer. Like many other natural product families, P-alkaloids represent a compound class targeting key cell signalling pathways in drug resistance e.g., NF κ B and HIF, which is distinct from their previously reported cytotoxicity. Finally, further studies are needed to identify the distinct pharmacological target(s) in the molecular interplay of both NF κ B and HIF in TNBC, also regarding CSC features.

4.1.4 P-alkaloids block proliferation in TNBC through arrest at the G0/G1-state, thereby, delaying cell cycle progression

Proliferation is a multi-step process comprising the interphase (G1, S, G2) and mitosis (M) while non-proliferative cells are resting at a G0 state. Cell cycle phase transition is regulated by the balance of cyclins as well as cyclin-dependent kinases and checkpoint proteins controlling DNA damage and chromosomal segregation as well as modulating the cell fate towards progression or apoptosis [225]. Although the anti-proliferative effects of P-alkaloids were reported for BC cell lines, including MB-231 [148], regulation of the cell cycle remains unclear in TNBC. For P-alkaloids, affecting the cell cycle arrest at the G1 or S-phase is reported for various cancer entities [149,154,179,226]. Cell cycle arrest resulting from the downregulation of cell cycle-related cyclins [227] and downregulation of cell cycle regulatory proteins by P-alkaloids [203] was reported for the following targets: cyclin D1 (G1-progression) by e.g. TYLO-2 [150], cyclin E1 (G1/S-transition) by the tylophorine analogue

DCB-3503 [223] or cyclin A2 (G1/S; S/G2-transition) by tylophorine [226]. In our recent publication, we report anti-proliferative effects of TYLO-1 in TNBC [187]. To investigate modulation of the cell cycle state in TNBC, we tested the chemically prepared TYLO-1s and found a time- and dose-dependent accumulation of S- and G2-phase cell populations presumably through retardation in G1/S transition. The delay in G1-progression [227] might rely on downregulation of cyclin D1 by targeting NFκB [150], which is described as a key player in the G1/S phase transition by regulating cyclin D1 and CDK4/6 expression [228]. NFκB blockade was also reported for a tylophorine analogue in pancreatic [151] and hepatocellular [150] cancer cell lines, thus we assume a common mode of action regarding proliferation blockade in diverse cancer entities. Concomitant with our findings, there was no shift detected in the cell cycle population within 24 h when exposing T47D cells to tylophorine [154]. Indicating, that within 24 h cells might arrest at the G1-state, resulting in retardation of cell cycle progression. In contrast, studies from Gao *et al.* claimed a cell cycle arrest to be cancer type dependent [179].

Overall, the mechanism of P-alkaloids in cell cycle modulation differs significantly from the M-phase inhibitor paclitaxel, known to arrest progression at the G2/M state by preventing depolymerization of mitotic spindles during cell division [229]. In contrast, proliferation blockade by P-alkaloids might rely on inhibiting checkpoint proteins in the cell cycle or inhibiting DNA replication [150,158,159]. Recently, Aurora A and B kinases were found as novel targets for the stereoisomer of TYLO-1, namely tylophorinine, and for TYLO-2 at low micromolar concentration in MCF7 [224]. As a direct substrate of Aurora kinases, p53 is phosphorylated and subsequently degraded [230]. Downregulation of p53 and its target genes coding for p21 was also reported for tylophorine and its analogue DCB-3503 [179,223], while studies from Gao *et al.* assume that cell cycle arrest is independent of p53 activity and thus independent of DNA damage [179]. Additional studies are needed to clarify the role of p53 and DNA damage concerning the anti-proliferative P-alkaloids in TNBC. Furthermore, blockade of DNA replication was reported for (+)-(13aS)-deoxytylophorinine, the stereoisomer of TYLO-4, through intercalation into nucleic acid [158,159] and for tylophorinine and TYLO-2 through blockade of the nucleic acid synthesis [166,231]. Preferably, (+)-(13aS)-deoxytylophorinine intercalates at AT-rich sequences, which is mainly found upstream of the transcription start site [158,159]. Hydrophobic methoxyl substitutes at the phenanthrene ring are suggested to be important for binding to nucleic acid [158] and might explain the general blockade of protein synthesis [203]. On the contrary, findings from Wang *et al.* assume that reduced DNA replication is a side effect of downregulating proteins involved in DNA synthesis [232].

Studies with tylophorine revealed a G1 arrest which was sufficient to abrogate the G2/M arrest of doxorubicin, thereby inducing cell death [154]. In this study, each compound was

tested separately, hence, for future studies, combinational treatment of paclitaxel with O-methyltylophorinidine (TYLO-1/TYLO1s) is proposed to evaluate the impact on drug sensitivity in TNBC, considering their different mechanism of action in the cell cycle.

Hypoxia was reported to induce G1-arrest by downregulation of cyclin A, resulting in paclitaxel resistance [220]. In our artificial hypoxia model, simulation with CoCl₂ at a low-toxic concentration resulted in a different modulation by inducing a G2/M arrest. However, we cannot exclude that a low-toxic concentration of CoCl₂ conducted cytotoxic effects at long-time exposure or that CoCl₂ activates pathways, that are differently regulated under oxygen shortage.

In conclusion, cell cycle modulation by P-alkaloids is distinct from the standard-of-care agent paclitaxel, presumably by blocking DNA replication and blocking or downregulating proteins involved in cell cycle transition with all events resulting in G0/G1-arrest to delay cell cycle progression.

4.1.5 P-alkaloids have multiple target sites in TNBC, including YAP

P-alkaloids were reported to block *de novo* RNA synthesis [208] and inhibit protein synthesis [203], by blocking protein translation [223]. However, transcription, as the initial step of gene expression, is regulated by transcription factors, and for TNBC we reported suppression of NFκB as well as HIF activity in our recent work [187]. To our knowledge, this study was the first to identify the transcriptional coactivator YAP as a novel target for P-alkaloids. In the following, we will discuss potential upstream regulators of the targeted pathways by P-alkaloids, including mechanisms involved in protein degradation.

In line with our initial observation, YAP is highly activated in cancer cells compared to non-cancerous cells [233]. In addition to that, YAP has ascribed a fundamental role in the TME, because the increased transcriptional activity of the heterodimeric YAP/TAZ complex was found in stromal cells, [134], including tumour infiltrated cells [51], which is linked to tumour-promoting features [122]. In stiff matrices, YAP functions as a mechanotransducer to promote proliferation and metastasis in TNBC cells (MB-231), whilst YAP shows no tumour-promoting role in non-TNBC cells (MCF7) [234]. In our studies, we observed contradictory modulation of YAP signalling. On the one hand, TYLO-1 enhanced YAP expression in MB-231, but on the other hand, TYLO-1 decreased YAP activity. However, we cannot exclude adverse cytotoxic effects, because we applied a concentration of TYLO-1, which was found to reduce cell viability in 2D cultures (100 nM). Concomitant with our findings, other studies confirm the controversial role in TNBC: YAP ablation was either reducing paclitaxel sensitivity in TNBC (MB-231) [235] or sensitizing TNBC cells for radiotherapy [236] and chemotherapy, including paclitaxel as well as doxorubicin [63]. Differences in prognosis could be explained by the complex regulation of YAP, including the physical properties in

the ECM [53,237] and transactivation by diverse cellular pathways, which are involved in tumour progression [48]. Of note, within the interaction of mechanical and chemical cues, soluble factors may partially have a greater impact on cellular signalling [131].

Mechanotransduction via YAP also transactivates key pathways in cancer, e.g. NF κ B [238] and HIF-1 α [132]. Within the inflammatory TME in BC, TNF α /IKK β signalling not triggers YAP as well as NF κ B activation, resulting in a YAP/TEAD/p65 triplet complex to modulate glucose metabolism, which benefits cell migration. Remarkably, YAP has a special role by partially regulating the expression of NF κ B-regulated genes [48]. To investigate the role of YAP as well as the role of p65 in the effects of P-alkaloids, we performed knockdown studies to downregulate p65 or YAP based on siRNA interference. YAP was dispensable for the anti-inflammatory activity of TYLO-1 and we found, that the anti-tumour features of TYLO-1 is maintained irrespective of p65 or YAP expression. Indicating, that the anti-tumour potential does not solely rely on the modulation of these proteins, which furthermore highlights the relevance of multiple target sites of P-alkaloids in TNBC. Our hypothesis is supported by studies from Bhattacharjee and colleagues, where they demonstrate that various proteins can be affected at a different degree of inhibition [239], suggesting, that the interplay is important for compound activity. Nonetheless, the interplay between targeted pathways in TNBC, including NF κ B, HIF as well as YAP, remains unclear in the pharmacological mechanism of P-alkaloids and needs further examinations.

Regarding upstream factors of NF κ B, HIF, as well as YAP, the impact on kinase activities by P-alkaloids is not well understood in BC. AKT was earlier introduced as a potential target of P-alkaloids [222] and a common upstream regulator of NF κ B, HIF [221], and in addition to that also YAP [240]. However, to date, there is no molecular target identified for P-alkaloids, which explains a decrease in nuclear translocation of YAP. Aurora kinases were identified as potential targets of P-alkaloids [224]. These kinases negatively regulate YAP signalling by phosphorylation [241]. While targeting Aurora A should suppress YAP phosphorylation, hence should increase nuclear YAP levels, our study shows decreased YAP activity upon TYLO-1 treatment. Concluding from our results, Aurora A is not the main target to affect downstream YAP activity. Concerning YAP, our results exclude decreased gene expression in response to TYLO-1, thus, suggesting post-transcriptional regulation as a mechanism to interfere with YAP activity. Indicating, that YAP is blocked through either enhanced inactivating phosphorylation, enhanced proteasomal degradation or decreased protein translation. Non-coding RNAs also play a role in suppressing protein translation [54], but their relevance is not understood in the mechanism of P-alkaloids.

Regarding the reduced activity of NF κ B, HIF and YAP, we questioned how the proteasome is involved to decrease transcriptional activity by P-alkaloids. Concerning NF κ B blockade, our data show stabilization of its inhibitor I κ B α after short time exposure to TYLO-1s,

indicating decreased I κ B α phosphorylation and further a decrease in proteasomal degradation. In line with our findings, Shiah and colleagues postulate, that increased I κ B α stability is caused by reduced phosphorylation rather than involving the proteasome. In contrast to that, NF κ B is degraded by the proteasome [151]. Concerning CoCl₂-simulated hypoxia, our study revealed decreased HIF signalling in response to TYLO-1s, which could either result from lowered HIF expression or enhanced proteasomal degradation. Regarding YAP, we observed increased expression but decreased activity. Indicating, that either protein translation is blocked or that proteasomal degradation is increased as a result of enhanced YAP phosphorylation. Hence, the role of the proteasome in lowered HIF and YAP activity needs further clarification. The proteasomal machinery is differently involved in the targeted pathways of P-alkaloids, suggesting, that the proteasome is no specific molecular target. Studies from Wang *et al.* support our findings and report, that anti-tumour features do not rely on enhanced protein degradation by the proteasomal machinery [232].

In conclusion, we identified YAP as a novel target for P-alkaloids. Noteworthy, the role of the pathway crosstalk between YAP, NF κ B and HIF is still poorly understood regarding the compound activity and the main molecular targets. There are further studies required to conduct a better understanding of upstream regulators, that might orchestrate simultaneous pathway inhibition. Nevertheless, we did not address cellular processes that are involved in suppression of protein activities by lowering the protein level, such as mRNA degradation, but we exclude a key role for the proteasomal machinery.

4.1.6 TYLO-1 interferes with the tumour-stroma crosstalk by mitigating cytokines production

The inflammatory TME in TNBC [100] is linked to malignant features and poor clinical outcomes [110,242–244]. Paracrine signalling leads to the attraction of TAMS which interact with TNBC cells via the secretion of second messengers such as IL-8 or IL-6 [245]. Previously, studies from Sperlich and Teusch described the elevated expression of cytokines IL-6 and IL-8 in a 2D co-culture of MB-231 and PBMCs at a cell type ratio of 1:1. The crosstalk based on cytokines could be suppressed by NF κ B blockade [79]. Based on these findings, we aimed to examine the most efficacious P-alkaloid, TYLO-1, regarding its impact on the TME crosstalk via cytokines. Reconstituting this 2D co-culture model, our data reproduced enhanced IL-6 and IL-8 levels in the co-culture, which was diminished in the presence of TYLO-1, presumably by blocking NF κ B, and thus, cytokines induced forward feedback loop via NF κ B signalling. Notably, our studies involved cytotoxic concentration of TYLO-1 for MB-231 as well as PBMCs, thus we cannot exclude cytotoxic effects on cytokines level. However, when applying TYLO-1 at low-toxic concentrations, our data show diminished IL-6 and IL-8 levels in the tumour cells. Nevertheless, our results may

not distinguish the targeted cell type involved in cytokine upregulation or downregulation. Concomitant with our findings, other studies examined co-cultures of MB-231 as well as macrophages and present tumour cells are the main source for cytokines, which were upregulated in the crosstalk in an NF κ B/p65 dependent manner [115]. Although, NF κ B presents the main target to block the tumour-stroma crosstalk, we suggest knockdown studies to confirm the relevance of NF κ B for blocking the paracrine signalling by TYLO-1. Not to be neglected, the PBMC is a heterogeneous mixture of monocytes and lymphocytes with no determined proportion of each cell type. Additionally, neither the activation status of the immune cells nor the markers that define tumour-associated character were determined. The crosstalk with TNBC and macrophages is rather complex by displaying two differentiation states of macrophages: Tumour-suppressive M1-like that releases pro-inflammatory cytokines and chemokines including TNF α , IL-1 β and IL-6, and the tumour-promoting M2-like that releases anti-inflammatory cytokines including IL-10 to mediate tissue remodelling, angiogenesis and immunosuppression [246]. Moreover M2-types correlate with increased proliferation, EMT, migration and invasion and poor prognosis in TNBC [247]. There are unclear findings about the TAM polarization, because co-culture with MB-231 was reported to polarize macrophages towards the M2-type [247], while other studies discovered, that TAMs possess a mixed status of M1-like and M2-like which drive TNBC growth and aggressiveness [246]. To date, regulation of tumour-promoting features of stromal cells is unclear for P-alkaloids. Elucidation of the TAM polarization upon treatment could address if the tumour-associated status can be reverted. Moreover, further studies are required to validate, that intervention with the tumour-stroma crosstalk is sufficient to reduce tumour aggressiveness, and in particular, chemotherapy resistance. In summary, targeting NF κ B disturbs the bidirectional crosstalk of tumour and stromal cells via reducing the level of inflammatory cytokines. Thereby, presenting anti-inflammatory P-alkaloids as a potent candidate to disturb the inflammatory TME.

4.1.7 3D cultures as preclinical drug screening models for TNBC

To evaluate the drug efficacy of O-methyltylophoridine (TYLO-1/TYLO-1s) regarding TNBC growth and invasion, we utilized 3D spheroids. In the following, the utilization of 2D cultures will be discussed, in addition to the 3D monoculture and co-culture model that were generated in an ECM-like matrix, including our approach to generate a 3D model to study tumour growth under hypoxia. Also, some recent advances in preclinical 3D studies are introduced.

The 2D cultures may display an artificial drug response, hence, providing a low predictability for the clinical potential of drugs. In our studies, a cell density-dependent drug-dose response of P-alkaloids was observed on CAFs. In addition to that, comparing drug-dose

response of paclitaxel in 2D monoculture vs. 3D co-culture, we detected a limited cytotoxicity, presumably due to the heterogenic nature of the cell line population, including a proportion of drug resistant cells. Concomitant with that finding, Niepel *et al.* postulate a distinguished drug response at the single-cell level, thereby recommending consideration of unique molecular features of single cells to increase higher accuracy in HTS [248].

Based on the unique limitations of current preclinical models in cancer research, spheroids represent a predictive HTS model for solid tumours by mimicking physiological conditions within the TME that drive drug resistance [83]. TNBC sensitivity to chemotherapeutics and targeted therapy agents, e.g. EGFR inhibitor or HDACI, differs in 2D and 3D models [27,249]. Drug resistance in 3D [27] might be explained by an altered gene expression profile in comparison to monolayer cells [207] in addition to a lowered drug uptake in 3D [250]. In general, drug uptake is negatively affected by the hypoxic and acidic TME [251], including the desmoplastic tissue [33].

Studies of Badea *et al.* characterized MB-231 spheroids, grown in a matrigel-based matrix, because monoculture spheroids of MB-231, grown without any scaffolds, rather form aggregates than spheroids due to a low E-cadherin level, hence, due to low intercellular connections. Badea *et al.* confirmed the similarity of the 3D physiology with microtumours *in vivo*: Within the organisation of multi-cell layers, proliferative cells are located at the edge of the spheroids and a necrotic and hypoxic core is observed at a spheroid size of $\geq 400\ \mu\text{m}$ [181]. Distinguished cell zones within the spheroid might also explain a lower growth rate compared to 2D cultures [180], presumably by a decreased overall expression of cell cycle-related genes, including CDKs and Aurora kinases [252]. In our studies, the 3D monoculture spheroids, grown in matrigel, as well as the 3D co-culture spheroids, grown in a collagen-based-matrix, exhibited a similar size with a diameter of at least $400\ \mu\text{m}$. Badea *et al.* concluded, that these microtumours resembled *in vivo* conditions with reproducing gradients in nutrients and oxygen supply, which causes a necrotic core and affects drug response in 3D studies [181]. Indeed, drug penetration anti-proportionally decreases with the tumour size [207], and drug diffusion within the tumour is another limiting factor for drug efficacy [253].

To increase predictability for drug response we established 3D TNBC co-cultures to mimic the TME by incorporating MB-231 cells and the predominant stromal cell type, CAFs, as well as the predominant structural protein within the ECM, collagen type I. Tumour-promoting CAFs were recently classified in murine [104] and human BC [104]. Classification from Bartoschek *et al.* describes four subtypes of CAFs which were isolated from the murine MMTV-PyMT BC model. Amongst two αSMA^+ types, matrix CAFs are associated with increased expression of ECM-related proteins, such as collagens as well as lysyl oxidases, and vascular CAFs correlate with increased expression of transcription factors and proteins

involved in angiogenesis. The matrix CAFs, which make up to 89% of the mammary gland fibroblasts, were mainly located at the invasive front, whereas vascular CAFs, which make up to 40% of the CAF pool, were predominantly infiltrated into the tumour [104]. Regarding the proposed categories, the murine α SMA+ CAFs used in our 3D model may be ascribed to the matrix CAF subtype, which presumably arose from the resident fibroblasts [104]. In previous studies by Jungwirth *et al.* the murine CAFs we used in our studies, i.e. matrix CAFs, promote spheroid growth of murine TNBC (4T1) and drive metastasis [191]. Noteworthy, in this study, the matrix CAFs did not impact TNBC migration, which was investigated by implementation of an indirect 2D co-culture in a wound healing assay. In the course of 3D co-culture model establishment, our data showed, that CAFs were needed for a compact cellular organisation by encompassing the tumour cell core. However, ECM deposition by the matrix CAFs was not sufficient to drive growth of 3D co-culture spheroids, which was rather dependent on collagen type I, hence, highlighting the important role of the ECM within the TME.

The ECM, in particular collagen, is relevant for BC spheroid organisation in 3D models and influencing drug efficacy [207]. However, the amount of ECM components, such as collagen, is distinct between tumour patients, and the composition, as well as architecture of the ECM, might be relevant for drug response, because some studies including predominant ECM components, such as collagen I and IV, did not recapitulate drug resistance in a 3D TNBC [254]. We observed, that the growth of our co-culture spheroids depended on collagen type I, and indeed, collagen concentration correlates with the tumour size [255]. Future 3D studies should consider ECM mixtures with the incorporation of e.g. hyaluronic acid, due to their contribution to tumour metastasis and drug resistance [181], mainly by maintaining CSC features [124]. Noteworthy, the arrangement of the ECM should be considered with caution, because the degree of stiffness determines the impact on tumour progression, which is either inhibiting or promoting [256].

Tumour growth is restricted to a size of 2-3 mm [90] and hypoxia-induced HIF-signalling a compensatory mechanism to sustain oxygen and nutrient supply [89,257] by initiating e.g. angiogenesis as well as tumour cell migration towards blood vessels [90]. In the hypoxic TME, HIF is a key player and correlates with tumour aggressiveness [81], including growth [89]. To evaluate drug efficacy in a hypoxic environment, we aimed to establish a 3D TNBC co-culture model under CoCl_2 -simulated hypoxia. We adjusted our co-culture by replacing the TNBC cell line using the HIF-sensor cell clone MB-468-UnaG. However, our approach did not apply to studying drug response in hypoxia-driven spheroid growth, because, in contrast to our expectations, growth of the co-culture spheroid was diminished when exposed to CoCl_2 . While some studies postulate that reduced oxygen levels do not affect cell viability [258], CoCl_2 is an artificial system that performs dose-dependent cytotoxicity

with minor toxic effects at the concentration applied in our study (100 μ M and 200 μ M) [198]. Nevertheless, there are also controversial findings about the role of HIF. Diverse studies describe hypoxia as a tumour-promoting condition [259], whilst HIF-inhibition could suppress TNBC growth [93,260] as well as migration [261]. On the other hand, some studies report that HIF-silencing resulted in the upregulation of collagen fibres, which are linked to increased metastasis [260]. A context-dependent role of HIF may be partially explained by the severity of oxygen reduction. This may be due to the different roles of HIF isomers, knowing, that in the course of angiogenesis HIF-2 α is required for effective vessel remodelling and induction of a mature, functional vascular network [257]. HIF-2 α is upregulated under intermediate hypoxia (5% O₂) expression, whereas HIF-1 α is upregulated at severe hypoxia (< 1%) [257]. Thus, it is not surprising, that the vascular system is abnormal with functional deficiencies in cancer [89,257]. To date, tylophorine was reported to inhibit angiogenesis *in vitro* and *in vivo* by blocking migration and proliferation of human or murine vascular cells, presumably by inhibition of VEGFR signalling [152,262]. However, the role of VEGFR and downstream signalling was not yet addressed in cancer, hence highlighting, that the molecular mechanism of P-alkaloids is not fully understood. Hypoxia (HIF) is a critical mediator of chemotherapy-induced resistance [60], thus, preclinical studies should consider the role of hypoxia to study drug response. Regarding a simplified HTS model, Badea and colleagues suggest that TNBC spheroids grown in matrigel are a suitable model to study hypoxia due to the maintenance of hypoxia markers [181]. Another hypoxia model is presented by Grist and colleagues. They generated a microfluidic system to mimic cycled hypoxia as well as reoxygenation and cycled drug application [263].

Inventing novel technologies, that consider relevant factors in clinical administration are milestones for optimizing drug response predictability in preclinical studies. Nevertheless, cycles of drug administration, as performed in cancer therapy, may immensely impact on drug response, especially when observed over long periods of time. There are approaches to mimicking dynamic drug administration by altering the culture condition such as exemplified in a tumour-on-a-chip [182]. Not to be neglected, a crucial step in drug discovery is the assessment of the toxicity profile before utilization in clinical trials. To examine clinical safety in early preclinical models, Wang *et al.* introduced a 3D neural model to evaluate drug neurotoxicity [264]. These advances in preclinical studies head towards an animal-free drug screening, that may further save costs and time for discovering novel drug candidates. Moreover, these progresses accelerate the “war on cancer” [265].

In conclusion, 3D models are beneficial in drug discovery, in particular by providing predictive drug response *in vitro* and by partially replacing or avoiding unnecessary animal models. Thus, accelerating the identification of potent drug candidates for a therapeutic use

by saving time and costs. However, animal models are still indispensable to guarantee clinical safety regarding adverse side effects in the clinical use. With respect to precision medicine, incorporation of patient-derived tissue in 3D models may further enhance prediction of a drug response, and thereby improving customized therapy options to improve patients' outcomes and overall survival.

4.1.8 P-alkaloids maintain anti-tumour potential in a 3D TNBC co-culture model and block growth as well as invasion of 3D TNBC spheroids

As drug efficacy differs in monolayer cells compared to the respective 3D biology [83,176], we characterized TYLO-1/TYLO-1s in a 3D TNBC spheroid model that incorporates predominant TME components that drive drug resistance [83]. During spheroid formation, NFκB activity is enhanced [266] and promotes chemotherapy resistance, tumour growth and metastasis [267]. In our study, the examination of anti-inflammatory P-alkaloids showed diminished tumour progression by blocking migration of 2D cultures and growth as well as invasion of 3D spheroids. Potentially, p65 knockdown studies could address to the involvement of NFκB in TNBC progression in more molecular detail.

Our 3D studies suggest, that P-alkaloids are promising drug candidates to block growth of highly proliferative TNBC. The dose-dependent effects of TYLO-1 were maintained in the 3D TNBC monoculture spheroids with an estimated GI_{50} of 25 nM. Growth blockade was superior to the MEK1/2 inhibitor, presumably by targeting NFκB, which is downstream the MAPK pathway as well as downstream of other RTK-induced pathways that drive malignant tumour features [44]. Migration as an early step of metastasis is induced by NFκB-mediated downregulation of E-cadherin or upregulation of ECM-proteolytic enzymes such as matrix metalloprotease (MMP)-9 and EMT-associated markers, e.g. vimentin and snail1 [268]. In MB-231 cells, NFκB drives migratory behaviour [61] and findings from Sperlich and Teusch showed suppression of 3D TNBC invasion by blocking NFκB signalling [79], hence supposedly downregulation of EMT-related factors [269]. Based on these findings, we questioned whether the anti-inflammatory TYLO-1s is sufficient to suppress TNBC invasion. So far, anti-migrative behaviour in cancer cells was reported for tylophorine [206], the tylophorine analogue, NK007 [149] and also for the chemically prepared phenanthrene-based molecules YS206 and YS306 [270]. Hitherto, migration or invasion studies of P-alkaloids were conducted *in vitro* using 2D cell monolayers, thus, neglecting the ECM composition and stiffness. In this study, initial examination of TYLO-1 in a wound healing assay revealed a blockade of TNFα-induced TNBC migration, presumed by targeting the TNFα/NFκB axis. Further, TYLO-1s was examined regarding invasion of TNBC monoculture spheroids into a matrigel®-based matrix and showed a significant invasion

blockade at 10 nM, presumably by blocking NFκB. Indeed, P-alkaloids reduce migratory behaviour by downregulation of the NFκB target gene MMP-9 [206]. Interestingly, newly identified targets of P-alkaloids, Aurora kinases, are also involved in mediating EMT via activation of NFκB [230,271]. But to date, no *in vitro* studies included the role of P-alkaloids in the crosstalk of Aurora A/B and NFκB. However, as drug resistance is a major cause for therapy failure, targeting NFκB-regulated EMT, which is a key process for maintaining cancer stemness and drug resistance [31], is promising in TNBC therapy for recurrent cancer.

Our 3D TNBC monoculture model may not fully reflect physiological conditions, thus we aimed to investigate the anti-cancer features of TYLO-1 by mimicking the TNBC TME by the inclusion of tumour-specific stromal cells and ECM-matrix components [272]. Spheroids were grown with additional type I collagen, the main component in the stroma of TNBC patients [273], mainly secreted by CAFs [109] and elevated in BC [274]. Regarding cytotoxicity, the anti-tumour potential of P-alkaloids in the 3D co-culture spheroids was predictable based on the SAR studies for NFκB-inhibition with TYLO-1 and TYLO-1s showing a striking reduction of cell viability at an IC₅₀ of 21.7 ± 2.5 nM and 11.2 ± 2.1 nM, respectively. Regarding the SAR in 3D co-culture models, compared to the TYLO-1 scaffold, compounds with a hydroxyl group in the phenanthrene ring (TYLO-2 and TYLO-3) or lacking the hydroxyl moiety in the indolizidine ring (TYLO-4) lost efficacy in the 3D model by a factor of 4 for TYLO-2 and TYLO-4 and by a factor of 8 for TYLO-3, resulting in an IC₅₀ of around 450 nM for all three compounds.

The hypoxic and immunosuppressive TME is linked to enhanced inflammation [65,81,92,112], and NFκB as well as HIF, which are both highly activated in spheroids [252,266], and are crucial to maintain tumour-promoting features of CAFs. In this work, CAFs are not targeted by paclitaxel whereas bioactive P-alkaloids TYLO-1 to TYLO-4 maintain dose-dependent anti-proliferative effects presumably by blocking NFκB and HIF signalling, thus reverting CAF activation. Because αSMA+ CAFs have been widely described as tumour-promoting and correlating with worse prognosis [125,275], we assume that mainly paracrine signalling enhances inflammation [98], i.e., NFκB, which might lead to increased vulnerability of co-culture spheroids to a treatment with NFκB-inhibiting agents. All in all, we generated a simplified 3D model to evaluate the efficacy of P-alkaloids and the main potent compound O-methyltylophorinidine (TYLO-1/TYLO-1s) was maintaining its potential. Regarding the decreased TNBC growth by P-alkaloids, we hypothesize, that suppression of tumour progression may partially rely on a reversed activation status of CAFs, which needs further validation.

4.1.9 TYLO-1/TYLO-1s exhibits superior anti-tumour potential compared to the chemotherapeutic agent paclitaxel

TYLO-1/TYLO-1s exhibits superior anti-tumour potential in TNBC compared to paclitaxel regarding cytotoxicity in 2D monolayer cells as well as in 3D-co-culture spheroids. Furthermore, TYLO-1s is more efficacious under hypoxia.

TYLO-1/TYLO-1s displays superiority compared to paclitaxel by targeting NFκB and HIF which are both involved in paclitaxel resistance [20]. Under hypoxia, the bioactivity of TYLO-1 was merely affected and maintains NFκB blockade via stabilization of the IκBα inhibitor presumably by additionally targeting HIF. In contrast, paclitaxel loses cytotoxic potential under hypoxia, presumably due to HIF-related resistance [276]. For paclitaxel a reduced induction of apoptosis was reported by diminishing the arrest at the G2/M cell cycle state under hypoxia [220]. Under hypoxia as well as under normoxia paclitaxel induces autophagy [277], potentially mediating paclitaxel resistance [278]. On the other hand, blockade of the HIF-pathway, a driving force for drug resistance, was reported to sensitize tumour cells to paclitaxel [59]. Hypoxia is also involved in enhancing NFκB activity and blocking both pathways might be sufficient to suppress tumour progression [62] and to reverse drug resistance [59,61,62].

Although our data indicate that the pharmacological mode of action for NFκB blockade by P-alkaloids might be different from the underlying mode of action resulting in proliferation inhibition, further research needs to be done to develop novel analogues with reduced cytotoxicity while maintaining the NFκB blocking potential. A major obstacle for P-alkaloids in clinical application is based on the neurotoxicity of these compounds. To date, *in vivo* activity in BC was so far described for cryptopleurine, but a clinical trial at phase I was discontinued due to central nervous system toxicity [212]. General cytotoxicity of P-alkaloids was excluded on an epithelial BC cell line MCF10A *in vitro* for the compound 3-O-demethyltylophorinidine [279]. On the contrary, we observed reduced cell viability in non-cancerous cell lines after exposure to TYLO-1 at a similar concentration compared to cancerous-cells, however, additional studies are needed to distinguish proliferation blockade from cell death. Furthermore, severe neurotoxicity and contradictory findings emphasize the relevance of extended SAR studies to optimize drug specificity and drug safety *in vivo*.

In summary, the TYLO-1 exhibits superior anti-tumour potential compared to paclitaxel and maintains efficacy under hypoxia. Superiority is attributed to the distinguished mode of action that relies on multiple target sites in P-alkaloids. Further studies might include combinational treatments of P-alkaloids specifically addressing the resistance development of paclitaxel. Nevertheless, SAR studies and drug design are inevitable to optimize drug efficacy for clinical application.

4.2 Fungus-derived metabolites possess anti-inflammatory and anti-migratory potential, suggesting a SAR in TNBC

Despite the numerous species of the kingdom fungi, hitherto, there are no metabolites approved as anti-cancer agents [280]. To screen for drug candidates in TNBC therapy, we evaluated the isolated metabolites from *A. falconensis* (azaphilones and polyketides) and *Didymella* sp. (decahydrofluorenes), which were isolated upon changing the culture conditions, hence, affording novel molecules. All natural products showed anti-tumour effects in TNBC with a hint towards a SAR. In general, anti-tumour effects of fungal compounds were detected at a two-digit micromolar concentration, while cytotoxicity was conducted at an at least two-fold higher concentration.

The compound classes, azaphilones or decahydrofluorenes, blocked TNF α - or LPS-induced NF κ B-mediated gene transcription in a dose-dependent manner. Regarding decahydrofluorenes, the strongest NF κ B-blockade was found for didymellanosine due to its polar and aromatic tail, which was different compared to the other two molecules. An altered stereochemistry and incorporation of one hydroxyl group, as found in ascomylactam C, increased cytotoxicity with no affection on NF κ B-inhibitory capacity, when compared to phomapyrrolidone A. Meanwhile, ascomylactam C displayed a strong anti-inflammatory dependency for reduced cell viability with a comparable IC₅₀ in both assays.

Having a closer look into the structural differences of azaphilones, reduced cell viability within 200 μ M, though distinct from NF κ B-blockade, is solely observed for metabolites possessing two methoxyl groups, as found in falconensin A and R. On the other hand, no cytotoxicity was observed, when compounds have solely one methoxyl group in addition to either two hydroxyl groups, as found in falconensin I and N, or one hydroxyl group as well as acetoxy group, as found in falconensin O and S, regardless of chlorine residues. In addition, compounds bearing only one methoxyl group in addition to one hydroxyl group, as found for falconensin H, M and Q, showed no cytotoxicity. However, the anti-inflammatory potential diminished by a factor of five, when chlorine was bound, as found in compound M and H. When comparing falconensin M and H with Q, it is evident, that brominated derivatives, as found in compound Q, exhibit best NF κ B-inhibitory features. This observation is confirmed by comparison of the similar structure from falconensin A and R, revealing, that bromide, as found in compound R, improved NF κ B-inhibition by a factor of 2. Moreover, when comparing falconensin I with N, it was also observed that anti-inflammatory potential of falconensin N decreased by a factor of 3, although this metabolite neither possesses bromide nor chlorine residuals. Noteworthy to mention that when metabolites bear an acetoxy group, NF κ B inhibition was unaffected by chlorine, as found in falconensin O, or lack of halogenated residues, as found in falconensin S. Hence, to sum it up, halogens are dispensable for anti-inflammatory features of azaphilones, however, brominated

metabolites displayed superior effects compared to chlorinated metabolites. Interestingly, an acetoxy group immensely increase efficacy, regardless of chlorine residuals. Based on that, it is unclear if acetoxy groups could additionally increase potential of brominated compounds. Finally, bromination or acetoxylation, in particular in chlorinated compounds, is the marked characteristic for anti-inflammatory features against TNBC.

Polyketides were tested against TNBC migration and showed efficacious blockade for sulochrin, indicating that an additional chlorine, as found in monochlorsulochrin, diminishes anti-cancer capacity. Both derivatives were found to be selective inhibitors of MMP-13, which was determined *in silico* by performing molecular docking studies [141]. In BC, MMP-13 correlates with metastasis and a poor clinical outcome [281]. NFκB is a main regulator of metastasis via upregulation of MMPs, including MMP-9 [282] and MMP-13 [283]. It is an open question whether polyketides might block other MMPs that are involved in TNBC aggressiveness. However, efficacy of polyketides is cancer type dependent, because sulochrin exhibited strong cytotoxicity against mouse lymphoma cells (L5178Y) with an IC₅₀ value of 5.1 μM [141], while our data do not detect cytotoxicity in TNBC within 100 μM.

Concluded from our studies, fungus-derived secondary metabolites are potent anti-inflammatory and anti-migratory agents in TNBC with hint to a SAR. Remarkably, their drug dose is not comparable to currently applied standard therapeutics in TNBC, because activities are observed at a micromolar concentration, which is a huge disadvantage regarding drug isolation or synthetic preparation. We suggest further SAR studies, including generation of novel compound analogues, to improve anti-cancer efficacy.

4.3 SAR studies of synthetically engineered HDACIs

Pan-HDACIs, including vorinostat (SAHA), were first approved by the Food and Drug Administration (FDA) in 2006 [284]. Vorinostat

stops TNBC proliferation and leads to cell death [26], but still, no HDACI were yet approved for TNBC treatment. However, pan-HDACI application is challenging due to unpredictable side effects and a pleiotropic role in cells, including the regulating of non-cancer related processes, that lead to an increasing relevance for SAR studies towards HDAC-selective isoforms. HDACIs are designed according to the targeted enzyme structure, hence, they have an aromatic tail, referred to as the cap group, a central lipophilic linker, and a zinc binding group (ZBG), which mainly determines their selectivity: carboxylic acid, thiols, benzamides or hydroxamic acids (**Figure 4-2a**) [26].

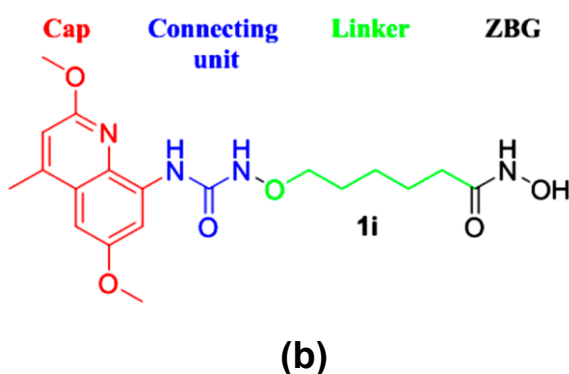
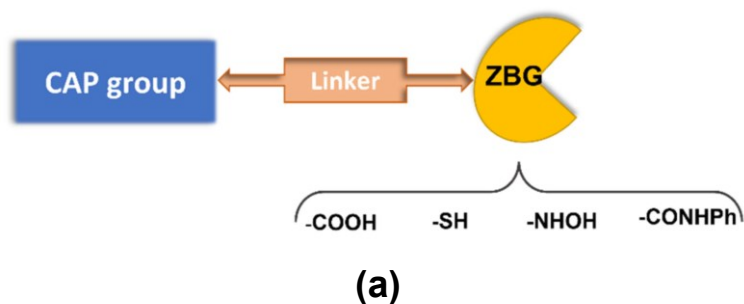


Figure 4-2 Pharmacophoric compartments of HDACIs. (a) Illustration from Maccallini *et al.* (2022) [26]. (b) KSK64 (1i) is exemplary shown for novel synthetic HDACI. The structure comprises an aromatic tail (cap group, red), an alkoxyurea connecting unit (blue), a lipophilic linker (green) and an hydroxamic acid zinc binding group (ZBG, black). Illustration with minor modifications from Stenzel *et al.* (2017) [189].

In this study, eight novel synthetically engineered HDACIs were examined in TNBC, namely LAK41, LAK107, LAK110, LAK121, LAK-ZnFD, KSK64, KSK75 and MPK265. According to their molecular targets, they are ascribed to HDACIs with specificity to class I HDACs, including HDAC1, HDAC2, HDAC3, HDAC8, or specificity to class IIb HDACs, including HDAC6 as well as HDAC10. So far, investigations in other cancer types revealed anti-tumour potential for LAK41 by cell killing [188] and for LAK41 as well as KSK64 by enhancing sensitivity towards cisplatin treatment [188,189]. Concerning TNBC, our data suggest a key role for HDAC1 and HDAC6, because only dual targeting reduced cell viability, which was observed for LAK41, KSK64 and MPK265. These HDACIs display an amid (LAK41), alkoxyurea (KSK64) or alkoxyamide (MPK265) group as a connecting unit between the CAP and linker region (**Figure 4-2b**). The most distinct structural feature for all three active molecules is a hydroxamic acid as the ZBG. Characteristics of inactive agents in TNBC include chlorine residues (KSK75), a ketone group (LAK-ZnFD) or sulfones (LAK107, LAK110, LAK121).

Regarding HDACI selectivity, other studies report growth and metastasis blockade in TNBC, *in vitro* as well as *in vivo*, when solely targeting HDAC1 or targeting class IIb HDACs, including HDAC6 and HDAC10 [26]. Moreover, class I HDACs are overexpressed in BC

[285] and selective inhibition by e.g. entinostat reverses the ER⁻ state by upregulation of ER in TNBC, which would enable endocrine therapy using e.g. letrozole [26]. HDACIs also reverse the CSC state and enhance sensitivity towards paclitaxel [27]. Furthermore, HDACIs are also suggested in combinational treatment with immunotherapy, due to their immunomodulatory activity [286]. Thus, presenting HDACIs as potent chemosensitizer. In conclusion, our data reveal a key role for HDAC1 and HDAC6 in TNBC. Additional studies are required to explore if active HDACIs against TNBC, namely LAK41, KSK64 and MPK265, are sufficient to prevent tumour aggressiveness or induce cell death. In general, pan-HDACIs present an unpredictable treatment approach, thus, drug design aims to strengthen HDAC selectivity. HDACIs could be a promising therapy option to improve clinical outcome for TNBC patients by overcoming drug resistance and providing a new treatment route with endocrine therapy.

4.4 Chemical synthesis of natural products, including derivatives and novel analogues, to improve drug efficacy for clinical purposes

Natural products are promising drug candidates for diverse medicinal applications due to their various activities [287,288]. The fact, that still new species and compounds are discovered [140,168], sheds light on the potential of natural sources for therapeutic purposes. However, utilization of natural products is challenging due to their toxicity profile and a low availability, i.e. tedious isolation procedures [287].

Early research involving natural products was restricted to the methodology to isolate secondary metabolites, thereby, bioactivity was entirely determined by nature. Natural sources provide molecules with a highly complex molecule structure, while additional compound derivatives present a huge structural diversity [287]. Exemplary for plants, compound isolation is an elaborating procedure, in which a high amount of plant material is needed in order to obtain solely a small amount of isolated products [289]. On the other hand, chemical synthesis enables molecule production at lower costs and shorter time, and in addition to that, is declared to be more sustainable, while exhibiting a high yield in compound product [187,287]. Regarding P-alkaloids, to increase overall yield of natural products [290], various chemical synthesis techniques were reported [290–292], including the anti-tumour substances TYLO-3 [163] and TYLO-1/TYLO-1s, which was examined in our recent work [187]. In addition to that, chemical synthesis provides a possible route to generate novel compound analogues [150,270]. However, *in vitro* generation of natural products may be challenging due to a complex molecule structure, as found for the chemotherapeutics paclitaxel and vincristine. To overcome this limitation, semi-synthetic preparation is performed with using natural compound intermediates, which are much

easier to isolate from natural sources and additionally offer the opportunity to synthesize novel molecule analogues [287]. Also biological systems e.g. yeast are used and modified for synthesis of complex molecule structures [289]. Furthermore, advances in synthesis protocols are shortening the time required to prepare novel synthetic molecules [293]. Creating novel derivatives based on a natural equivalents may either enhance or reduce a compound's activity [150], while generation of novel synthetic analogues often correlates with unknown adverse side effects and low therapeutic efficacy [287]. Hence, accentuating the relevance of SAR studies.

Moreover, synthetically engineered molecules can be tailored in order to increase *in vivo* efficacy through mitigating undesired toxic side effects [294], and simultaneously increasing the half-life of molecules, and thereby, compound bioavailability [295]. Regarding P-alkaloids, neurotoxicity in clinical studies is a major challenge for a clinical application [212] and some researchers suggest, that drug design of P-alkaloids should consider generation of compounds possessing a higher polarity to prevent penetration through the BBB [208]. Meanwhile, passing the BBB is mandatory for brain diseases, such as glioblastoma. Being aware of this limitation, the group of Wang *et al.* tailored a derivative of TYLO-4 to form nano emulsion droplets, and as a consequence, decreasing toxicity *in vivo*, while increasing the compound's bioavailability, which was determined by an enhanced compound level in the blood plasma and at the tumour site [294]. Noteworthy, chemically engineered nano vectors of chemical and biological nature enhance drug efficacy and safety after systemic administration, thus offering improved strategies for therapeutic purposes [296]. Generally, nano vectors, including organic and inorganic systems, were reported to improve the delivery of natural products in BC in regard to enhance poor stability, aqueous solubility and bioavailability, factors that might limit clinical efficacy [297]. While some researcher aim to alter already known secondary metabolites [150], other studies aim to design drugs based on the targeted protein, also referred to as structure-based rational drug design [298]. Irrespective of the original source, compounds are classified according to their functional groups and numerous natural as well as synthetic compounds are currently evaluated for BC therapy [288,299]. Natural products and novel analogues raise hope for treating resistant TNBC, thus, improving clinical outcome.

In conclusion, synthetic molecule preparation is beneficial compared to compound isolation from natural sources in regard to (I) compound yield, (II) costs, (III) time consumption and (IV) generation of novel analogues. Nevertheless, protocols for molecule synthesis are limited considering the complex chemical structures of natural products and there are still novel techniques discovered to facilitate compound production, especially by taking advantage of biological systems. All in all, sophisticated drug design and SAR studies are inevitable to improve safety and bioavailability *in vivo*.

4.5 Current and future perspectives for TNBC therapy

Besides surgery and radiation, chemotherapy is the main option for TNBC treatment [300]. Although, targeted inhibitors are perceived as a promising solution in regard to precision medicine, the failure rate in preclinical studies is immense with only 2.3% of all drugs tested were approved for the clinical use [27]. Novel agents were mainly approved for metastatic diseases (76%), including for TNBC, but predominantly for HR+/HER2- BC [13]. In the last decades, TNBC therapy recorded a substantial success by finally presenting novel treatment regimens, although these achievements are limited to patients with a metastatic disease or tumour recurrence [300]. In 2013, FDA approved the first targeted therapy option for TNBC, which is an antibody-drug conjugate sacituzumab govitecan (Trodelvy®) targeting TROP-2, but only permitted for patients that already experienced prior treatment of two or more lines of systemic therapy [301]. In 2019, FDA further approved two novel regimens: PARP-inhibitors olaparib (Lynparza®) as well as talazoparib (Talzenna®), which are limited for patients carrying germline BRCA mutations [13], and the PD-L1 targeting antibody atezolizumab (Tecentriq®) for immunotherapy in combination with nab-paclitaxel (Abraxane®) [302]. Although, novel agents seem promising, there are some limitations given by the intrinsic cancer heterogeneity. Only a small number of TNBC patients bear BRCA mutations (30%), thus, are predisposed for PARP-inhibitor based therapy [23,300]. In general, immune cells are enriched in BC [303] and T-cell lymphocytes infiltration is associated with good prognosis in TNBC [304]. However, TNBC is characterized by a low level of infiltrated lymphocytes, referred to as immunologically “cold”, hence, immunotherapy is impeded [302]. Besides that, targeted therapy causes a high incidence of adverse events, including nausea, hair loss as well as reduction of blood cells. Immunotherapy could even result in autoimmune reactions [300]. Although, novel therapy strategies prolong TNBC patient’s survival, there is still an unmet need for a cure in TNBC. Current clinical trials for TNBC investigate novel targeted strategies concerning cell cycle progression (CDK4/6 inhibitor palbociclib), angiogenesis (anti-VEGF antibody bevacizumab) and highly activated signalling pathways (anti-EGFR antibody cetuximab; AKT inhibitor ipatasertib; hedgehog/SMO-inhibitor sonidegib; androgen receptor inhibitor enzalutamide). Research of epigenetic modifications is far behind with currently performing preclinical studies involving inhibitors for DNA-methyl transferases as well as HDACIs [288,305]. According to the heterogeneous nature of TNBC, each targeted strategy is limited to a specific cancer subtype (**Figure 4-3**).

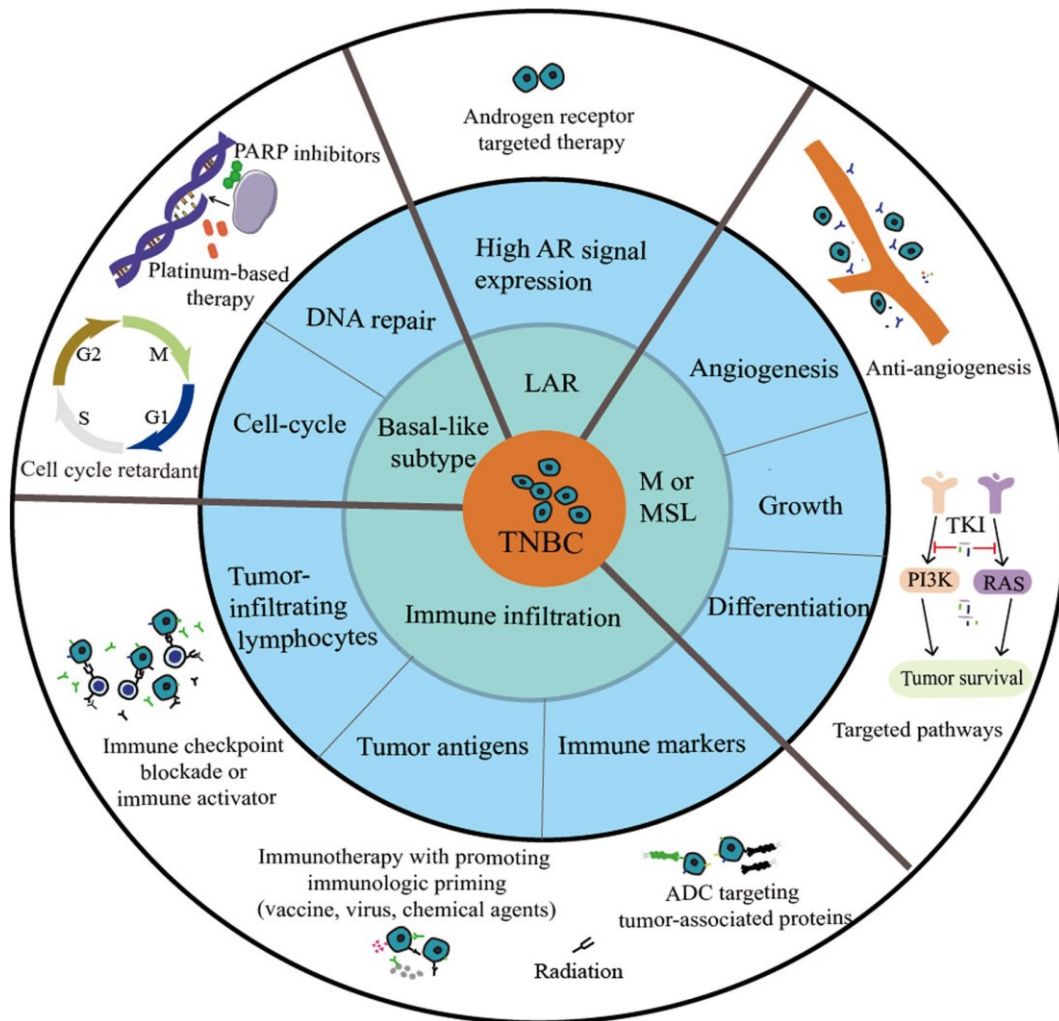


Figure 4-3 Therapeutic options for TNBC according to the intrinsic subtypes. TNBC subtypes: luminal androgen receptor (LAR), mesenchymal (M), mesenchymal-stem-like (MSL), basal-like and immune-infiltrated. Targeted therapy options are recommended according to the intrinsic molecular features of TNBC. ADC: antibody–drug conjugates; AR: androgen receptor; PARP: poly-adenosine diphosphate ribose polymerase; TKI: tyrosine kinase inhibitor. Illustration from Li *et al.* (2022) [306].

Currently, inter- and intratumoural heterogeneity is a major obstacle in therapy success [7], hence, new insights into molecular TNBC subtypes is the basis for the route of novel therapy options. Poor results in clinical trials involving tyrosine kinase inhibitors and monoclonal antibodies in BC treatment, in addition to conventional chemotherapeutic agents, is ascribed to activation of compensation mechanisms, i.e. alternative downstream pathways [32]. Concerning this resistance mechanism, crosstalk between Ras/Raf/MAPK and PI3K/AKT/mTOR pathway plays a major role. Notably, the inflammatory, hypoxic and desmoplastic TME, including NFκB and HIF [44] and YAP [307] activity, are involved in mediating RTK inhibitor (RTKI) resistance. Based on these findings, a combinational treatment with RTKIs and the before mentioned factors, that mediate resistance, is

recommended for improved TNBC eradication [44,308]. To improve efficacy of RTKIs or chemotherapeutics, some approaches aim to inactivate anti-apoptotic factors [309] or target CSC [32]. In particular, resistance to RTKIs is ascribed to NFκB, which is considered as the main node of resistance (**Figure 4-4**), because compensated pathways converge in NFκB signalling [44]. Acquired resistance via NFκB is also triggered by chemotherapeutics, e.g. paclitaxel [61]. Hence, presenting NFκB as one of the most critical factors in TNBC. In the last decades, natural compounds are considered as potential novel drug candidates in cancer given by their broad activities in combination with a low adverse side effect profile as well as the potency to reduce chemotherapy resistance [288].

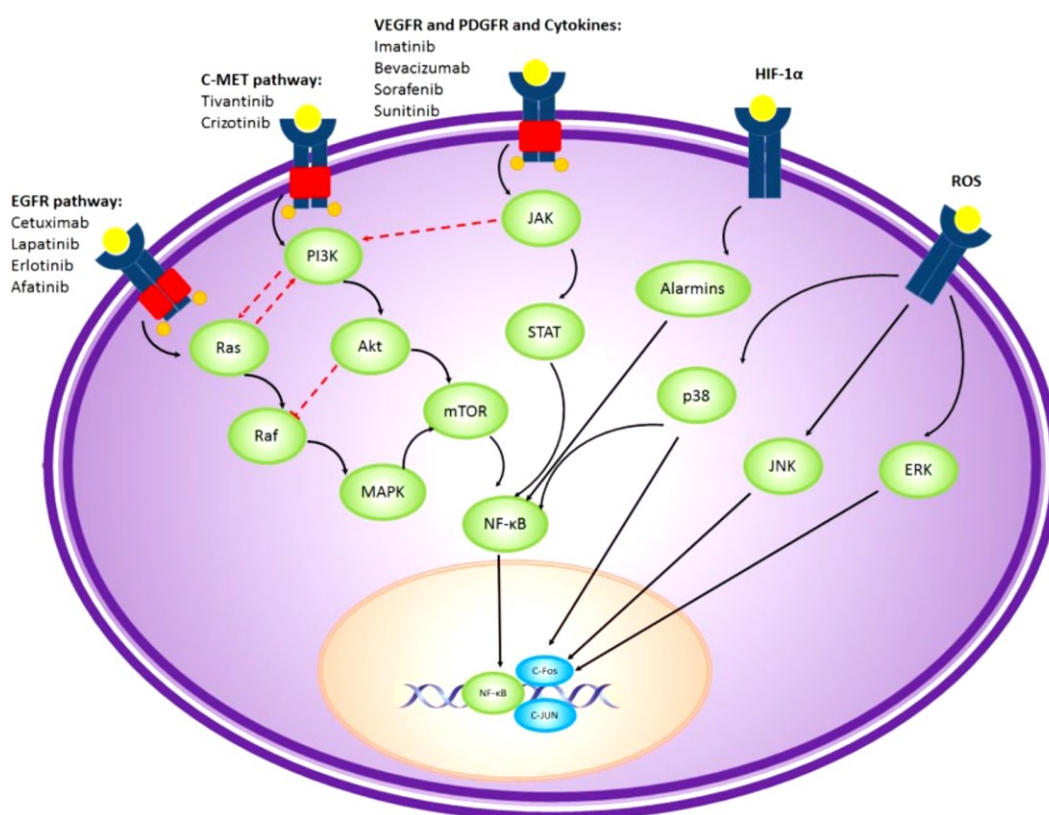


Figure 4-4 NF-κB as the main node of resistance to receptor tyrosine kinase inhibitors in TNBC . Potential inhibitors of the receptor signaling are listed for the epidermal growth factor receptor (EGFR), c-Met and other RTKIs, including VEGFR and PDGFR. Illustration from Darvishi *et al.* (2017) [44].

In this study, we presented anti-tumour potential for fungal-derived metabolites by inhibiting NFκB activity and migration, which is a crucial step of metastasis. Compared to currently applied drugs, efficiency of fungal substances is low due to the high drug concentrations needed for distinguished effects, whereas the mechanism of action in TNBC is not fully elucidated yet. Nevertheless, single targeting of NFκB is discouraged due to the broad range of upstream regulators and target genes, that are also involved in non-pathological processes [64]. In this context, our study presents P-alkaloids as advantageous anti-cancer agents by targeting multiple sites, including NFκB, HIF and YAP. Moreover, activities of these plant-derived molecules at a low nanomolar concentration are comparable to currently used drugs in the clinic, and for TYLO-1 we demonstrated superiority to paclitaxel. Another reason for therapy failure includes off-target effects on stromal cells in the TME, resulting in tumour-promotion rather than tumour eradication [122]. A paradigm shift in cancer therapy reveals the TME as a potential target to suppress tumour progression. There are diverse approaches for reversing the CAF phenotype in order to disrupt the stromal-tumoural interaction, including targeting e.g. CAF metabolism [52] or the CAF's secretome, e.g. TGF-β [310]. However, targeting stromal cells should be considered with caution due to their ambiguity with negatively or positively regulating tumour progression by presenting both, anti-tumour or pro-tumourigenic features [120]. Hypoxia, inflammation [86] and stromal cells, CAFs [113] as well as TAMs [114], generate an immunosuppressive environment. Other possible routes to target the TME include reactivation of the immune system by utilization of dendritic cell-based vaccines [311] and chimeric antigen receptor T-cells [312].

In conclusion, current advances in targeted therapies record prolonged survival, however, due to a high rate of tumour recurrence, there is an immense need for novel drug candidates to specifically eradicate TNBC. In future therapy, a clear understanding of the inter- and intratumoural heterogeneous TNBC disease, including CSC, and heterogeneity of the TME helps in the context of precision medicine. In our studies, we identified P-alkaloids isolated from *T. ovata* as potential novel drug candidates given by the fact, that these derivatives inhibit multiple cellular processes including transcriptional activity of key factors in CSC maintenance, namely NFκB, HIF and YAP. Lacking targetable therapy options, chemosensitisation plays a major role to suppress tumour recurrence. In this context, combinational treatment with chemotherapeutics is superior in eliminating tumour cells by targeting both drug resistant cells, i.e., CSC, as well as the proliferative tumour bulk.

4.6 Conclusions

P-alkaloids show a broad range of bioactivities in a variety of cancers. In TNBC we validated dose-dependent anti-inflammatory, anti-hypoxic, anti-migratory and anti-proliferative activities with an initial SAR for the anti-inflammatory activity displaying TYLO-1/TYLO-1s, namely *O*-methyltylophorinidine, as the most efficacious compound. This study determines P-alkaloids as a multi-targeting class of natural products with efficacious inhibition of NFκB and HIF, thus, modulating chemoresistance driving pathways. Although it is already known, that P-alkaloids are able to address NFκB in various disease settings, this study demonstrates, that NFκB blockade in TNBC is maintained under hypoxic conditions, presumably by targeting HIF. Limiting factors for drug sensitivity include the inflammatory and hypoxic TME, as well as YAP signalling, which this study revealed as a novel target. Inhibition of pathways by P-alkaloids, which are involved in drug resistance, might enhance chemotherapy sensitivity in TNBC. P-alkaloids serve as capable modulators of the tumour-promoting TME through blocking the bidirectional communication of tumour and stroma cells by suppressing NFκB-regulated cytokine expression. Furthermore, P-alkaloids maintain blockade of tumour growth and invasion in a 3D model while their mode of action may differ from the mode of action of paclitaxel. Further studies need to focus on combinational treatment approaches and more in-depth SAR studies are inevitable for drug design to prevent neurotoxicity and optimize drug application.

Fungus-derived compounds display broad anti-tumour activities. Within TNBC we found anti-migratory features for polyketides as well as dose-dependent anti-inflammatory effects for azaphilones and decahydrofluorenes, which indicates a SAR within each compound class. Nevertheless, drug efficacy at micromolar concentrations is not comparable to currently applied chemotherapeutics, hence, recommending further SAR studies and drug design to improve compound activity.

Hitherto, preclinical cancer research aims to identify novel strategies for targeted therapies, including HDACIs to regulate epigenetic modifications. HDACIs are potent chemosensitizer in TNBC therapy and drug design is indispensable to improve selectivity. In this study, synthetically engineered HDACIs with target selectivity were examined and hint to a SAR. Our data reveal a substantial role for a simultaneous inhibition of HDAC1 and HDAC6, however further studies are required to characterize their effects on tumour progression. Nevertheless, HDACIs are potent chemosensitizer in TNBC therapy.

5 References

1. Sung, H.; Ferlay, J.; Siegel, R.L.; Laversanne, M.; Soerjomataram, I.; Jemal, A.; Bray, F. Global cancer statistics 2020: GLOBOCAN estimates of incidence and mortality worldwide for 36 cancers in 185 countries. *CA Cancer J. Clin.* **2021**, *71*, 209–249, doi:10.3322/caac.21660.
2. The American Cancer Society Medical and Editorial Content Team. Triple-negative Breast Cancer. Available online: <https://www.cancer.org/cancer/breast-cancer/about/types-of-breast-cancer/triple-negative.html> (accessed on 19 June 2022).
3. Wang, X.; Guda, C. Integrative exploration of genomic profiles for triple negative breast cancer identifies potential drug targets. *Medicine (Baltimore)* **2016**, *95*, e4321–e4332, doi:10.1097/MD.00000000000004321.
4. Shoemaker, M.L.; White, M.C.; Wu, M.; Weir, H.K.; Romieu, I. Differences in breast cancer incidence among young women aged 20–49 years by stage and tumor characteristics, age, race, and ethnicity, 2004–2013. *Breast Cancer Res. Treat.* **2018**, *169*, 595–606, doi:10.1007/s10549-018-4699-9.
5. Hwang, K.-T.; Kim, J.; Jung, J.; Chang, J.H.; Chai, Y.J.; Oh, S.W.; Oh, S.; Kim, Y.A.; Park, S.B.; Hwang, K.R. Impact of breast cancer subtypes on prognosis of women with operable invasive breast cancer: a population-based study using SEER database. *Clin. Cancer Res.* **2019**, *25*, 1970–1979, doi:10.1158/1078-0432.CCR-18-2782.
6. Pal, S.K.; Childs, B.H.; Pegram, M. Triple negative breast cancer: unmet medical needs. *Breast Cancer Res. Treat.* **2011**, *125*, 627–636, doi:10.1007/s10549-010-1293-1.
7. Savard, M.-F.; Khan, O.; Hunt, K.K.; Verma, S. Redrawing the Lines: The Next Generation of Treatment in Metastatic Breast Cancer. *Am. Soc. Clin. Oncol. Educ. Book* **2019**, *39*, e8–e21, doi:10.1200/EDBK_237419.
8. Mani, S.; Hande, A.; Boichuk, S. Triple-Negative Breast Cancer: the Current Aspects of Pathogenesis and Therapies. *BioNanoSci.* **2022**, 1–32, doi:10.1007/s12668-022-00991-1.
9. Lebert, J.M.; Lester, R.; Powell, E.; Seal, M.; McCarthy, J. Advances in the systemic treatment of triple-negative breast cancer. *Curr. Oncol.* **2018**, *25*, 142–150, doi:10.3747/co.25.3954.
10. Lee, K.-L.; Chen, G.; Chen, T.-Y.; Kuo, Y.-C.; Su, Y.-K. Effects of Cancer Stem Cells in Triple-Negative Breast Cancer and Brain Metastasis: Challenges and Solutions. *Cancers (Basel)* **2020**, *12*, 2122, doi:10.3390/cancers12082122.

11. Wu, Q.; Siddharth, S.; Sharma, D. Triple Negative Breast Cancer: A Mountain Yet to Be Scaled Despite the Triumphs. *Cancers (Basel)* **2021**, *13*, 3697, doi:10.3390/cancers13153697.
12. American Cancer Society. Breast Cancer Facts & Figures 2019-2020. *Atlanta. American Cancer Society, Inc.* **2019**.
13. Duranti, S.; Fabi, A.; Filetti, M.; Falcone, R.; Lombardi, P.; Daniele, G.; Franceschini, G.; Carbognin, L.; Palazzo, A.; Garganese, G.; et al. Breast Cancer Drug Approvals Issued by EMA: A Review of Clinical Trials. *Cancers (Basel)* **2021**, *13*, doi:10.3390/cancers13205198.
14. International Agency for Research on Cancer. Global Cancer Observatory. Available online: <https://gco.iarc.fr/> (accessed on 7 October 2022).
15. Nascimento, R.G.d.; Otoni, K.M. Histological and molecular classification of breast cancer: what do we know? *Mastology* **2020**, *30*, doi:10.29289/25945394202020200024.
16. Picornell, A.C.; Echavarria, I.; Alvarez, E.; López-Tarruella, S.; Jerez, Y.; Hoadley, K.; Parker, J.S.; Del Monte-Millán, M.; Ramos-Medina, R.; Gayarre, J.; et al. Breast cancer PAM50 signature: correlation and concordance between RNA-Seq and digital multiplexed gene expression technologies in a triple negative breast cancer series. *BMC Genomics* **2019**, *20*, 452, doi:10.1186/s12864-019-5849-0.
17. Kolečková, M.; Vomacková, K.; Kolar, Z. Molecular Prognostic and Predictive Markers in Triple - Negative Breast Cancer. In *Breast Cancer - Evolving Challenges and Next Frontiers*; T. Valarmathi, M., Ed.; IntechOpen, 2021, ISBN 978-1-83969-202-4.
18. Ensenyat-Mendez, M.; Llinàs-Arias, P.; Orozco, J.I.J.; Íñiguez-Muñoz, S.; Salomon, M.P.; Sesé, B.; DiNome, M.L.; Marzese, D.M. Current Triple-Negative Breast Cancer Subtypes: Dissecting the Most Aggressive Form of Breast Cancer. *Front. Oncol.* **2021**, *11*, 681476, doi:10.3389/fonc.2021.681476.
19. Elango, R.; Vishnubalaji, R.; Shaath, H.; Alajezi, N.M. Molecular subtyping and functional validation of TTK, TPX2, UBE2C, and LRP8 in sensitivity of TNBC to paclitaxel. *Mol. Ther. Methods Clin. Dev.* **2021**, *20*, 601–614, doi:10.1016/j.omtm.2021.01.013.
20. Jiang, Y.-Z.; Ma, D.; Suo, C.; Shi, J.; Xue, M.; Hu, X.; Xiao, Y.; Yu, K.-D.; Liu, Y.-R.; Yu, Y.; et al. Genomic and Transcriptomic Landscape of Triple-Negative Breast Cancers: Subtypes and Treatment Strategies. *Cancer Cell* **2019**, *35*, 428-440.e5, doi:10.1016/j.ccell.2019.02.001.

21. Abramson, V.G.; Lehmann, B.D.; Ballinger, T.J.; Pietenpol, J.A. Subtyping of triple-negative breast cancer: implications for therapy. *Cancer* **2015**, *121*, 8–16, doi:10.1002/cncr.28914.
22. Prat, A.; Adamo, B.; Cheang, M.C.U.; Anders, C.K.; Carey, L.A.; Perou, C.M. Molecular characterization of basal-like and non-basal-like triple-negative breast cancer. *Oncologist* **2013**, *18*, 123–133, doi:10.1634/theoncologist.2012-0397.
23. The Cancer Genome Atlas Network. Comprehensive molecular portraits of human breast tumours. *Nature* **2012**, *490*, 61–70, doi:10.1038/nature11412.
24. Temian, D.C.; Pop, L.A.; Irimie, A.I.; Berindan-Neagoe, I. The Epigenetics of Triple-Negative and Basal-Like Breast Cancer: Current Knowledge. *J. Breast Cancer* **2018**, *21*, 233–243, doi:10.4048/jbc.2018.21.e41.
25. Mendaza, S.; Guerrero-Setas, D.; Monreal-Santesteban, I.; Ulazia-Garmendia, A.; Cordoba Iturriagoitia, A.; La Cruz, S. de; Martín-Sánchez, E. A DNA Methylation-Based Gene Signature Can Predict Triple-Negative Breast Cancer Diagnosis. *Biomedicines* **2021**, *9*, doi:10.3390/biomedicines9101394.
26. Maccallini, C.; Ammazalorso, A.; Filippis, B. de; Fantacuzzi, M.; Giampietro, L.; Amoroso, R. HDAC Inhibitors for the Therapy of Triple Negative Breast Cancer. *Pharmaceuticals (Basel)* **2022**, *15*, doi:10.3390/ph15060667.
27. Matossian, M.D.; Burks, H.E.; Elliott, S.; van Hoang, T.; Bowles, A.C.; Sabol, R.A.; Wahba, B.; Anbalagan, M.; Rowan, B.; Abazeed, M.E.; et al. Drug resistance profiling of a new triple negative breast cancer patient-derived xenograft model. *BMC Cancer* **2019**, *19*, 205, doi:10.1186/s12885-019-5401-2.
28. Garrido-Castro, A.C.; Lin, N.U.; Polyak, K. Insights into Molecular Classifications of Triple-Negative Breast Cancer: Improving Patient Selection for Treatment. *Cancer Discov.* **2019**, *9*, 176–198, doi:10.1158/2159-8290.CD-18-1177.
29. Abou-Bakr, A.A.; Eldweny, H.I. p16 expression correlates with basal-like triple-negative breast carcinoma. *Ecancermedicalscience* **2013**, *7*, 317, doi:10.3332/ecancer.2013.317.
30. Xu, H.; Tian, Y.; Yuan, X.; Liu, Y.; Wu, H.; Liu, Q.; Wu, G.S.; Wu, K. Enrichment of CD44 in basal-type breast cancer correlates with EMT, cancer stem cell gene profile, and prognosis. *Onco. Targets. Ther.* **2016**, *9*, 431–444, doi:10.2147/OTT.S97192.
31. Zhang, H.; Steed, A.; Co, M.; Chen, X. Cancer stem cells, epithelial-mesenchymal transition, ATP and their roles in drug resistance in cancer. *Cancer Drug Resist.* **2021**, *4*, 684–709, doi:10.20517/cdr.2021.32.
32. Li, J.; Qi, D.; Hsieh, T.-C.; Huang, J.H.; Wu, J.M.; Wu, E. Trailblazing perspectives on targeting breast cancer stem cells. *Pharmacol. Ther.* **2021**, *223*, 107800, doi:10.1016/j.pharmthera.2021.107800.

33. Lee, K.-L.; Kuo, Y.-C.; Ho, Y.-S.; Huang, Y.-H. Triple-Negative Breast Cancer: Current Understanding and Future Therapeutic Breakthrough Targeting Cancer Stemness. *Cancers (Basel)* **2019**, *11*, 1334, doi:10.3390/cancers11091334.
34. Fultang, N.; Chakraborty, M.; Peethambaran, B. Regulation of cancer stem cells in triple negative breast cancer. *Cancer Drug Resist.* **2021**, *4*, 321–342, doi:10.20517/cdr.2020.106.
35. Hua, Z.; White, J.; Zhou, J. Cancer stem cells in TNBC. *Semin. Cancer Biol.* **2022**, *82*, 26–34, doi:10.1016/j.semcancer.2021.06.015.
36. Strietz, J.; Stepputtis, S.S.; Follo, M.; Bronsert, P.; Stickeler, E.; Maurer, J. Human Primary Breast Cancer Stem Cells Are Characterized by Epithelial-Mesenchymal Plasticity. *IJMS* **2021**, *22*, 1808, doi:10.3390/ijms22041808.
37. Park, S.-Y.; Choi, J.-H.; Nam, J.-S. Targeting Cancer Stem Cells in Triple-Negative Breast Cancer. *Cancers (Basel)* **2019**, *11*, doi:10.3390/cancers11070965.
38. Sulaiman, A.; McGarry, S.; Han, X.; Liu, S.; Wang, L. CSCs in Breast Cancer-One Size Does Not Fit All: Therapeutic Advances in Targeting Heterogeneous Epithelial and Mesenchymal CSCs. *Cancers (Basel)* **2019**, *11*, doi:10.3390/cancers11081128.
39. Lee, C.H. Reversal of Epithelial-Mesenchymal Transition by Natural Anti-Inflammatory and Pro-Resolving Lipids. *Cancers (Basel)* **2019**, *11*, doi:10.3390/cancers11121841.
40. Kumari, N.; Dwarakanath, B.S.; Das, A.; Bhatt, A.N. Role of interleukin-6 in cancer progression and therapeutic resistance. *Tumor Biology* **2016**, *37*, 11553–11572, doi:10.1007/s13277-016-5098-7.
41. Hartman, Z.C.; Poage, G.M.; den Hollander, P.; Tsimelzon, A.; Hill, J.; Panupinthu, N.; Zhang, Y.; Mazumdar, A.; Hilsenbeck, S.G.; Mills, G.B.; et al. Growth of triple-negative breast cancer cells relies upon coordinate autocrine expression of the proinflammatory cytokines IL-6 and IL-8. *Cancer Res.* **2013**, *73*, 3470–3480, doi:10.1158/0008-5472.CAN-12-4524-T.
42. Mehraj, U.; Ganai, R.A.; Macha, M.A.; Hamid, A.; Zargar, M.A.; Bhat, A.A.; Nasser, M.W.; Haris, M.; Batra, S.K.; Alshehri, B.; et al. The tumor microenvironment as driver of stemness and therapeutic resistance in breast cancer: New challenges and therapeutic opportunities. *Cell. Oncol. (Dordr)* **2021**, *44*, 1209–1229, doi:10.1007/s13402-021-00634-9.
43. Diep, S.; Maddukuri, M.; Yamauchi, S.; Geshow, G.; Delk, N.A. Interleukin-1 and Nuclear Factor Kappa B Signaling Promote Breast Cancer Progression and Treatment Resistance. *Cells* **2022**, *11*, 1673–1688, doi:10.3390/cells11101673.

44. Darvishi, B.; Farahmand, L.; Eslami-S, Z.; Majidzadeh-A, K. NF- κ B as the main node of resistance to receptor tyrosine kinase inhibitors in triple-negative breast cancer. *Tumor Biology* **2017**, *39*, 1010428317706919, doi:10.1177/1010428317706919.
45. Espinoza-Sánchez, N.A.; Enciso, J.; Pelayo, R.; Fuentes-Pananá, E.M. An NF κ B-dependent mechanism of tumor cell plasticity and lateral transmission of aggressive features. *Oncotarget* **2018**, *9*, 26679–26700, doi:10.18632/oncotarget.25465.
46. Bossennec, M.; Di Roio, A.; Caux, C.; Ménétrier-Caux, C. MDR1 in immunity: friend or foe? *Oncoimmunology* **2018**, *7*, e1499388, doi:10.1080/2162402X.2018.1499388.
47. Jia, D.; Li, L.; Andrew, S.; Allan, D.; Li, X.; Lee, J.; Ji, G.; Yao, Z.; Gadde, S.; Figeys, D.; et al. An autocrine inflammatory forward-feedback loop after chemotherapy withdrawal facilitates the repopulation of drug-resistant breast cancer cells. *Cell Death Dis.* **2017**, *8*, e2932, doi:10.1038/cddis.2017.319.
48. Gao, Y.; Yang, Y.; Yuan, F.; Huang, J.; Xu, W.; Mao, B.; Yuan, Z.; Bi, W. TNF α -YAP/p65-HK2 axis mediates breast cancer cell migration. *Oncogenesis* **2017**, *6*, e383, doi:10.1038/oncsis.2017.83.
49. Calvo, F.; Ranftl, R.; Hooper, S.; Farrugia, A.J.; Moeendarbary, E.; Bruckbauer, A.; Batista, F.; Charras, G.; Sahai, E. Cdc42EP3/BORG2 and Septin Network Enables Mechano-transduction and the Emergence of Cancer-Associated Fibroblasts. *Cell Rep.* **2015**, *13*, 2699–2714, doi:10.1016/j.celrep.2015.11.052.
50. Cao, L.; Sun, P.-L.; Yao, M.; Jia, M.; Gao, H. Expression of YES-associated protein (YAP) and its clinical significance in breast cancer tissues. *Hum. Pathol.* **2017**, *68*, 166–174, doi:10.1016/j.humpath.2017.08.032.
51. Wang, Y.; Xu, X.; Maglic, D.; Dill, M.T.; Mojumdar, K.; Ng, P.K.-S.; Jeong, K.J.; Tsang, Y.H.; Moreno, D.; Bhavana, V.H.; et al. Comprehensive Molecular Characterization of the Hippo Signaling Pathway in Cancer. *Cell Rep.* **2018**, *25*, 1304-1317.e5, doi:10.1016/j.celrep.2018.10.001.
52. Li, Y.; Wang, S.; Wei, X.; Zhang, S.; Song, Z.; Chen, X.; Zhang, J. Role of inhibitor of yes-associated protein 1 in triple-negative breast cancer with taxol-based chemoresistance. *Cancer Sci.* **2019**, *110*, 561–567, doi:10.1111/cas.13888.
53. Yamaguchi, H.; Taouk, G.M. A Potential Role of YAP/TAZ in the Interplay Between Metastasis and Metabolic Alterations. *Front. Oncol.* **2020**, *10*, 928, doi:10.3389/fonc.2020.00928.
54. Li, Y.; Wang, Z.; Ajani, J.A.; Song, S. Drug resistance and Cancer stem cells. *Cell Commun. Signal.* **2021**, *19*, 19, doi:10.1186/s12964-020-00627-5.
55. Filser, C. *Die Epithelial-Mesenchymale Transition (EMT) in Karzinosarkomen des Ovars und Endometriums: Immunhistochemische Untersuchungen mit Korrelation zum Überleben*, 2016.

56. Fedele, M.; Cerchia, L.; Chiappetta, G. The Epithelial-to-Mesenchymal Transition in Breast Cancer: Focus on Basal-Like Carcinomas. *Cancers (Basel)* **2017**, *9*, doi:10.3390/cancers9100134.
57. D'Ignazio, L.; Rocha, S. Hypoxia Induced NF- κ B. *Cells* **2016**, *5*, doi:10.3390/cells5010010.
58. Culver, C.; Sundqvist, A.; Mudie, S.; Melvin, A.; Xirodimas, D.; Rocha, S. Mechanism of hypoxia-induced NF- κ B. *Mol. Cell. Biol.* **2010**, *30*, 4901–4921, doi:10.1128/MCB.00409-10.
59. You, L.; Wu, W.; Wang, X.; Fang, L.; Adam, V.; Nepovimova, E.; Wu, Q.; Kuca, K. The role of hypoxia-inducible factor 1 in tumor immune evasion. *Med. Res. Rev.* **2021**, *41*, 1622–1643, doi:10.1002/med.21771.
60. Samanta, D.; Gilkes, D.M.; Chaturvedi, P.; Xiang, L.; Semenza, G.L. Hypoxia-inducible factors are required for chemotherapy resistance of breast cancer stem cells. *Proc. Natl. Acad. Sci. U. S. A.* **2014**, *111*, E5429-38, doi:10.1073/pnas.1421438111.
61. Esparza-López, J.; Longoria, O.; La Cruz-Escobar, E.N. de; Garibay-Díaz, J.C.; León-Rodríguez, E.; Jesús Ibarra-Sánchez, M. de. Paclitaxel resistance is mediated by NF- κ B on mesenchymal primary breast cancer cells. *Oncol. Lett.* **2022**, *23*, 50, doi:10.3892/ol.2021.13168.
62. Wu, H.; Chu, Y.; Sun, S.; Li, G.; Xu, S.; Zhang, X.; Jiang, Y.; Gao, S.; Wang, Q.; Zhang, J.; et al. Hypoxia-Mediated Complement 1q Binding Protein Regulates Metastasis and Chemoresistance in Triple-Negative Breast Cancer and Modulates the PKC-NF- κ B-VCAM-1 Signaling Pathway. *Front. Cell Dev. Biol.* **2021**, *9*, 607142, doi:10.3389/fcell.2021.607142.
63. Oku, Y.; Nishiya, N.; Shito, T.; Yamamoto, R.; Yamamoto, Y.; Oyama, C.; Uehara, Y. Small molecules inhibiting the nuclear localization of YAP/TAZ for chemotherapeutics and chemosensitizers against breast cancers. *FEBS Open Bio* **2015**, *5*, 542–549, doi:10.1016/j.fob.2015.06.007.
64. Zhang, T.; Ma, C.; Zhang, Z.; Zhang, H.; Hu, H. NF- κ B signaling in inflammation and cancer. *MedComm (2020)* **2021**, *2*, 618–653, doi:10.1002/mco2.104.
65. Liubomirski, Y.; Lerrer, S.; Meshel, T.; Rubinstein-Achiasaf, L.; Morein, D.; Wiemann, S.; Körner, C.; Ben-Baruch, A. Tumor-Stroma-Inflammation Networks Promote Pro-metastatic Chemokines and Aggressiveness Characteristics in Triple-Negative Breast Cancer. *Front. Immunol.* **2019**, *10*, 757, doi:10.3389/fimmu.2019.00757.
66. Biswas, T.; Efird, J.T.; Prasad, S.; James, S.E.; Walker, P.R.; Zagar, T.M. Inflammatory TNBC Breast Cancer: Demography and Clinical Outcome in a Large

- Cohort of Patients With TNBC. *Clin. Breast Cancer* **2016**, *16*, 212–216, doi:10.1016/j.clbc.2016.02.004.
67. Wang, X.; Belguise, K.; Kersual, N.; Kirsch, K.H.; Mineva, N.D.; Galtier, F.; Chalbos, D.; Sonenshein, G.E. Oestrogen signalling inhibits invasive phenotype by repressing RelB and its target BCL2. *Nature Cell Biology* **2007**, *9*, 470–478, doi:10.1038/ncb1559.
 68. Agrawal, A.K.; Pielka, E.; Lipinski, A.; Jelen, M.; Kielan, W.; Agrawal, S. Clinical validation of nuclear factor kappa B expression in invasive breast cancer. *Tumour Biol.* **2018**, *40*, 1010428317750929, doi:10.1177/1010428317750929.
 69. Arora, R.; Yates, C.; Gary, B.D.; McClellan, S.; Tan, M.; Xi, Y.; Reed, E.; Piazza, G.A.; Owen, L.B.; Dean-Colomb, W. Panepoxydone targets NF- κ B and FOXM1 to inhibit proliferation, induce apoptosis and reverse epithelial to mesenchymal transition in breast cancer. *PLoS ONE* **2014**, *9*, e98370, doi:10.1371/journal.pone.0098370.
 70. Smith, S.M.; Lyu, Y.L.; Cai, L. NF- κ B affects proliferation and invasiveness of breast cancer cells by regulating CD44 expression. *PLoS ONE* **2014**, *9*, e106966, doi:10.1371/journal.pone.0106966.
 71. Prajoko, Y.W.; Aryandono, T. Expression of nuclear factor kappa B (NF- κ B) as a predictor of poor pathologic response to chemotherapy in patients with locally advanced breast cancer. *Asian Pac. J. Cancer Prev.* **2014**, *15*, 595–598, doi:10.7314/apjcp.2014.15.2.595.
 72. Ossovskaya, V.; Wang, Y.; Budoff, A.; Xu, Q.; Lituev, A.; Potapova, O.; Vansant, G.; Monforte, J.; Daraselia, N. Exploring molecular pathways of triple-negative breast cancer. *Genes Cancer* **2011**, *2*, 870–879, doi:10.1177/1947601911432496.
 73. Gaptulbarova, K.A.; Tsyganov, M.M.; Pevzner, A.M.; Ibragimova, M.K.; Litviakov, N.V. NF- κ B as a potential prognostic marker and a candidate for targeted therapy of cancer. *Exp. Oncol.* **2020**, *42*, 263–269, doi:10.32471/exp-oncology.2312-8852.vol-42-no-4.15414.
 74. Cogswell, P.C.; Guttridge, D.C.; Funkhouser, W.K.; Baldwin, A.S. Selective activation of NF- κ B subunits in human breast cancer: potential roles for NF- κ B B2/p52 and for Bcl-3. *Oncogene* **2000**, *19*, 1123–1131, doi:10.1038/sj.onc.1203412.
 75. Xia, L.; Tan, S.; Zhou, Y.; Lin, J.; Wang, H.; Oyang, L.; Tian, Y.; Liu, L.; Su, M.; Wang, H.; et al. Role of the NF κ B-signaling pathway in cancer. *Onco. Targets. Ther.* **2018**, *11*, 2063–2073, doi:10.2147/OTT.S161109.
 76. Jayatilaka, H.; Tyle, P.; Chen, J.J.; Kwak, M.; Ju, J.; Kim, H.J.; Lee, J.S.H.; Wu, P.-H.; Gilkes, D.M.; Fan, R.; et al. Synergistic IL-6 and IL-8 paracrine signalling pathway infers a strategy to inhibit tumour cell migration. *Nat. Commun.* **2017**, *8*, 15584, doi:10.1038/ncomms15584.

77. Pires, B.R.B.; Mencalha, A.L.; Ferreira, G.M.; Souza, W.F. de; Morgado-Díaz, J.A.; Maia, A.M.; Corrêa, S.; Abdelhay, E.S.F.W. NF-kappaB Is Involved in the Regulation of EMT Genes in Breast Cancer Cells. *PLoS ONE* **2017**, *12*, e0169622, doi:10.1371/journal.pone.0169622.
78. Hoesel, B.; Schmid, J.A. The complexity of NF-κB signaling in inflammation and cancer. *Mol. Cancer* **2013**, *12*, 86, doi:10.1186/1476-4598-12-86.
79. Sperlich, J.; Teusch, N. Pseudopterosin Inhibits Proliferation and 3D Invasion in Triple-Negative Breast Cancer by Agonizing Glucocorticoid Receptor Alpha. *Molecules* **2018**, *23*, 1992, doi:10.3390/molecules23081992.
80. Wei Wang; Subhasree A. Nag; Ruiwen Zhang. Targeting the NFκB Signaling Pathways for Breast Cancer Prevention and Therapy.
81. Vaupel, P. Hypoxia and aggressive tumor phenotype: implications for therapy and prognosis. *Oncologist* **2008**, *13*, 21–26, doi:10.1634/theoncologist.13-S3-21.
82. Erapaneedi, R.; Belousov, V.V.; Schäfers, M.; Kiefer, F. A novel family of fluorescent hypoxia sensors reveal strong heterogeneity in tumor hypoxia at the cellular level. *EMBO J.* **2016**, *35*, 102–113, doi:10.15252/embj.201592775.
83. Nunes, A.S.; Barros, A.S.; Costa, E.C.; Moreira, A.F.; Correia, I.J. 3D tumor spheroids as in vitro models to mimic in vivo human solid tumors resistance to therapeutic drugs. *Biotechnol. Bioeng.* **2019**, *116*, 206–226, doi:10.1002/bit.26845.
84. Farina, A.R.; Cappabianca, L.; Sebastiano, M.; Zelli, V.; Guadagni, S.; Mackay, A.R. Hypoxia-induced alternative splicing: the 11th Hallmark of Cancer. *J. Exp. Clin. Cancer Res.* **2020**, *39*, 110, doi:10.1186/s13046-020-01616-9.
85. Hanahan, D.; Weinberg, R.A. Hallmarks of cancer: the next generation. *Cell* **2011**, *144*, 646–674, doi:10.1016/j.cell.2011.02.013.
86. Giatromanolaki, A.; Gkegka, A.G.; Pouliliou, S.; Biziota, E.; Kakolyris, S.; Koukourakis, M. Hypoxia and anaerobic metabolism relate with immunologically cold breast cancer and poor prognosis. *Breast Cancer Res. Treat.* **2022**, *194*, 13–23, doi:10.1007/s10549-022-06609-0.
87. Zhang, Y.; Zhang, H.; Wang, M.; Schmid, T.; Xin, Z.; Kozhuharova, L.; Yu, W.-K.; Huang, Y.; Cai, F.; Biskup, E. Hypoxia in Breast Cancer-Scientific Translation to Therapeutic and Diagnostic Clinical Applications. *Front. Oncol.* **2021**, *11*, 652266, doi:10.3389/fonc.2021.652266.
88. Semenza, G.L. The hypoxic tumor microenvironment: A driving force for breast cancer progression. *Biochim. Biophys. Acta* **2016**, *1863*, 382–391, doi:10.1016/j.bbamcr.2015.05.036.
89. D'Ignazio, L.; Batie, M.; Rocha, S. Hypoxia and Inflammation in Cancer, Focus on HIF and NF-κB. *Biomedicines* **2017**, *5*, 21, doi:10.3390/biomedicines5020021.

90. Fouad, Y.A.; Aanei, C. Revisiting the hallmarks of cancer. *Am. J. Cancer Res.* **2017**, *7*, 1016–1036.
91. Soleymani Abyaneh, H.; Gupta, N.; Radziwon-Balicka, A.; Jurasz, P.; Seubert, J.; Lai, R.; Lavasanifar, A. STAT3 but Not HIF-1 α Is Important in Mediating Hypoxia-Induced Chemoresistance in MDA-MB-231, a Triple Negative Breast Cancer Cell Line. *Cancers (Basel)* **2017**, *9*, doi:10.3390/cancers9100137.
92. Zhang, J.; Ma, X.; Fan, D. Ginsenoside CK Inhibits Hypoxia-Induced Epithelial-Mesenchymal Transformation through the HIF-1 α /NF- κ B Feedback Pathway in Hepatocellular Carcinoma. *Foods* **2021**, *10*, 1195, doi:10.3390/foods10061195.
93. Shi, Y.; Chang, M.; Wang, F.; Ouyang, X.; Jia, Y.; DU, H. Role and mechanism of hypoxia-inducible factor-1 in cell growth and apoptosis of breast cancer cell line MDA-MB-231. *Oncol. Lett.* **2010**, *1*, 657–662, doi:10.3892/ol_00000115.
94. Sulaiman, A.; McGarry, S.; Chambers, J.; Al-Kadi, E.; Phan, A.; Li, L.; Mediratta, K.; Dimitroulakos, J.; Addison, C.; Li, X.; et al. Targeting Hypoxia Sensitizes TNBC to Cisplatin and Promotes Inhibition of Both Bulk and Cancer Stem Cells. *IJMS* **2020**, *21*, doi:10.3390/ijms21165788.
95. Kim, I.S.; Zhang, X.H.-F. One microenvironment does not fit all: heterogeneity beyond cancer cells. *Cancer Metastasis Rev.* **2016**, *35*, 601–629, doi:10.1007/s10555-016-9643-z.
96. Gupta, S.; Roy, A.; Dwarakanath, B.S. Metabolic Cooperation and Competition in the Tumor Microenvironment: Implications for Therapy. *Front. Oncol.* **2017**, *7*, 68, doi:10.3389/fonc.2017.00068.
97. Hanahan, D.; Coussens, L.M. Accessories to the crime: functions of cells recruited to the tumor microenvironment. *Cancer Cell* **2012**, *21*, 309–322, doi:10.1016/j.ccr.2012.02.022.
98. López de Andrés, J.; Griñán-Lisón, C.; Jiménez, G.; Marchal, J.A. Cancer stem cell secretome in the tumor microenvironment: a key point for an effective personalized cancer treatment. *J. Hematol. Oncol.* **2020**, *13*, 136, doi:10.1186/s13045-020-00966-3.
99. Fernández-Nogueira, P.; Fuster, G.; Gutierrez-Uzquiza, Á.; Gascón, P.; Carbó, N.; Bragado, P. Cancer-Associated Fibroblasts in Breast Cancer Treatment Response and Metastasis. *Cancers (Basel)* **2021**, *13*, doi:10.3390/cancers13133146.
100. Place, A.E.; Jin Huh, S.; Polyak, K. The microenvironment in breast cancer progression: biology and implications for treatment. *Breast Cancer Res.* **2011**, *13*, 227, doi:10.1186/bcr2912.
101. Moorman, A.M.; Vink, R.; Heijmans, H.J.; van der Palen, J.; Kouwenhoven, E.A. The prognostic value of tumour-stroma ratio in triple-negative breast cancer. *European*

- Journal of Surgical Oncology (EJSO)* **2012**, 38, 307–313, doi:10.1016/j.ejso.2012.01.002.
102. Kalluri, R. The biology and function of fibroblasts in cancer. *Nat. Rev. Cancer* **2016**, 16, 582–598, doi:10.1038/nrc.2016.73.
 103. Louault, K.; Bonneaud, T.L.; Séveno, C.; Gomez-Bougie, P.; Nguyen, F.; Gautier, F.; Bourgeois, N.; Loussouarn, D.; Kerdraon, O.; Barillé-Nion, S.; et al. Interactions between cancer-associated fibroblasts and tumor cells promote MCL-1 dependency in estrogen receptor-positive breast cancers. *Oncogene* **2019**, 38, 3261–3273, doi:10.1038/s41388-018-0635-z.
 104. Bartoschek, M.; Oskolkov, N.; Bocci, M.; Lövrot, J.; Larsson, C.; Sommarin, M.; Madsen, C.D.; Lindgren, D.; Pekar, G.; Karlsson, G.; et al. Spatially and functionally distinct subclasses of breast cancer-associated fibroblasts revealed by single cell RNA sequencing. *Nat. Commun.* **2018**, 9, doi:10.1038/s41467-018-07582-3.
 105. Costa, A.; Kieffer, Y.; Scholer-Dahirel, A.; Pelon, F.; Bourachot, B.; Cardon, M.; Sirven, P.; Magagna, I.; Fuhrmann, L.; Bernard, C.; et al. Fibroblast Heterogeneity and Immunosuppressive Environment in Human Breast Cancer. *Cancer Cell* **2018**, 33, 463-479.e10, doi:10.1016/j.ccell.2018.01.011.
 106. Foster, D.S.; Jones, R.E.; Ransom, R.C.; Longaker, M.T.; Norton, J.A. The evolving relationship of wound healing and tumor stroma. *JCI Insight* **2018**, 3, doi:10.1172/jci.insight.99911.
 107. D'Arcangelo, E.; Wu, N.C.; Cadavid, J.L.; McGuigan, A.P. The life cycle of cancer-associated fibroblasts within the tumour stroma and its importance in disease outcome. *Br. J. Cancer* **2020**, 122, 931–942, doi:10.1038/s41416-019-0705-1.
 108. Mehraj, U.; Dar, A.H.; Wani, N.A.; Mir, M.A. Tumor microenvironment promotes breast cancer chemoresistance. *Cancer Chemother. Pharmacol.* **2021**, 87, 147–158, doi:10.1007/s00280-020-04222-w.
 109. Deepak, K.; Vempati, R.; Nagaraju, G.P.; Dasari, V.R.; S., N.; Rao, D.N.; Malla, R.R. Tumor microenvironment: Challenges and opportunities in targeting metastasis of triple negative breast cancer. *Pharmacological Research* **2020**, 153, 104683, doi:10.1016/j.phrs.2020.104683.
 110. Yu, T.; Di, G. Role of tumor microenvironment in triple-negative breast cancer and its prognostic significance. *Chin. J. Cancer Res.* **2017**, 29, 237–252, doi:10.21147/j.issn.1000-9604.2017.03.10.
 111. Hendrayani, S.-F.; Al-Harbi, B.; Al-Ansari, M.M.; Silva, G.; Aboussekhra, A. The inflammatory/cancer-related IL-6/STAT3/NF-κB positive feedback loop includes AUF1 and maintains the active state of breast myofibroblasts. *Oncotarget* **2016**, 7, 41974–41985, doi:10.18632/oncotarget.9633.

112. Gok Yavuz, B.; Gunaydin, G.; Gedik, M.E.; Kosemehmetoglu, K.; Karakoc, D.; Ozgur, F.; Guc, D. Cancer associated fibroblasts sculpt tumour microenvironment by recruiting monocytes and inducing immunosuppressive PD-1+ TAMs. *Sci. Rep.* **2019**, *9*, 3172, doi:10.1038/s41598-019-39553-z.
113. Monteran, L.; Erez, N. The Dark Side of Fibroblasts: Cancer-Associated Fibroblasts as Mediators of Immunosuppression in the Tumor Microenvironment. *Front. Immunol.* **2019**, *10*, 1835, doi:10.3389/fimmu.2019.01835.
114. Qiu, S.-Q.; Waaijer, S.J.H.; Zwager, M.C.; Vries, E.G.E. de; van der Vegt, B.; Schröder, C.P. Tumor-associated macrophages in breast cancer: Innocent bystander or important player? *Cancer Treat. Rev.* **2018**, *70*, 178–189, doi:10.1016/j.ctrv.2018.08.010.
115. Liubomirski, Y.; Lerrer, S.; Meshel, T.; Morein, D.; Rubinstein-Achiasaf, L.; Sprinzak, D.; Wiemann, S.; Körner, C.; Ehrlich, M.; Ben-Baruch, A. Notch-Mediated Tumor-Stroma-Inflammation Networks Promote Invasive Properties and CXCL8 Expression in Triple-Negative Breast Cancer. *Front. Immunol.* **2019**, *10*, 804, doi:10.3389/fimmu.2019.00804.
116. Sperlich, J.; Kerr, R.; Teusch, N. The Marine Natural Product Pseudopterosin Blocks Cytokine Release of Triple-Negative Breast Cancer and Monocytic Leukemia Cells by Inhibiting NF- κ B Signaling. *Mar. Drugs* **2017**, *15*, 262–277, doi:10.3390/md15090262.
117. Yuan, Z.-Y.; Luo, R.-Z.; Peng, R.-J.; Wang, S.-S.; Xue, C. High infiltration of tumor-associated macrophages in triple-negative breast cancer is associated with a higher risk of distant metastasis. *Onco. Targets. Ther.* **2014**, *7*, 1475–1480, doi:10.2147/OTT.S61838.
118. Matsumoto, H.; Koo, S.; Dent, R.; Tan, P.H.; Iqbal, J. Role of inflammatory infiltrates in triple negative breast cancer. *J. Clin. Pathol.* **2015**, *68*, 506–510, doi:10.1136/jclinpath-2015-202944.
119. Chen, K.G.; Sikic, B.I. Molecular pathways: regulation and therapeutic implications of multidrug resistance. *Clin. Cancer Res.* **2012**, *18*, 1863–1869, doi:10.1158/1078-0432.CCR-11-1590.
120. Jin, K.; Pandey, N.B.; Popel, A.S. Crosstalk between stromal components and tumor cells of TNBC via secreted factors enhances tumor growth and metastasis. *Oncotarget* **2017**, *8*, 60210–60222, doi:10.18632/oncotarget.19417.
121. Liu, Q.; Li, A.; Tian, Y.; Wu, J.D.; Liu, Y.; Li, T.; Chen, Y.; Han, X.; Wu, K. The CXCL8-CXCR1/2 pathways in cancer. *Cytokine Growth Factor Rev.* **2016**, *31*, 61–71, doi:10.1016/j.cytogfr.2016.08.002.

122. Linares, J.; Marín-Jiménez, J.A.; Badia-Ramentol, J.; Calon, A. Determinants and Functions of CAFs Secretome During Cancer Progression and Therapy. *Front. Cell Dev. Biol.* **2020**, *8*, 621070, doi:10.3389/fcell.2020.621070.
123. Karagiannis, G.S.; Poutahidis, T.; Erdman, S.E.; Kirsch, R.; Riddell, R.H.; Diamandis, E.P. Cancer-associated fibroblasts drive the progression of metastasis through both paracrine and mechanical pressure on cancer tissue. *Mol. Cancer Res.* **2012**, *10*, 1403–1418, doi:10.1158/1541-7786.MCR-12-0307.
124. Nallanthighal, S.; Heiserman, J.P.; Cheon, D.-J. The Role of the Extracellular Matrix in Cancer Stemness. *Front. Cell Dev. Biol.* **2019**, *7*, 86, doi:10.3389/fcell.2019.00086.
125. Mollah, F.; Varamini, P. Overcoming Therapy Resistance and Relapse in TNBC: Emerging Technologies to Target Breast Cancer-Associated Fibroblasts. *Biomedicines* **2021**, *9*, 1921, doi:10.3390/biomedicines9121921.
126. Acerbi, I.; Cassereau, L.; Dean, I.; Shi, Q.; Au, A.; Park, C.; Chen, Y.Y.; Liphardt, J.; Hwang, E.S.; Weaver, V.M. Human breast cancer invasion and aggression correlates with ECM stiffening and immune cell infiltration. *Integr. Biol. (Camb)* **2015**, *7*, 1120–1134, doi:10.1039/c5ib00040h.
127. Hupfer, A.; Brichkina, A.; Koeniger, A.; Keber, C.; Denkert, C.; Pfefferle, P.; Helmpobst, F.; Pagenstecher, A.; Visekruna, A.; Lauth, M. Matrix stiffness drives stromal autophagy and promotes formation of a protumorigenic niche. *Proc. Natl. Acad. Sci. U. S. A.* **2021**, *118*, doi:10.1073/pnas.2105367118.
128. Lee, J.Y.; Chang, J.K.; Dominguez, A.A.; Lee, H.-P.; Nam, S.; Chang, J.; Varma, S.; Qi, L.S.; West, R.B.; Chaudhuri, O. YAP-independent mechanotransduction drives breast cancer progression. *Nat. Commun.* **2019**, *10*, 1848, doi:10.1038/s41467-019-09755-0.
129. Zhang, Q.; Han, X.; Chen, J.; Xie, X.; Xu, J.; Zhao, Y.; Shen, J.; Hu, L.; Xu, P.; Song, H.; et al. Yes-associated protein (YAP) and transcriptional coactivator with PDZ-binding motif (TAZ) mediate cell density-dependent proinflammatory responses. *J. Biol. Chem.* **2018**, *293*, 18071–18085, doi:10.1074/jbc.RA118.004251.
130. Oudeck, M.G.; Kumar, A.; Placone, J.K.; Plunkett, C.M.; Matte, B.F.; Wong, K.C.; Fattet, L.; Yang, J.; Engler, A.J. Dynamically stiffened matrix promotes malignant transformation of mammary epithelial cells via collective mechanical signaling. *Proc. Natl. Acad. Sci. U. S. A.* **2019**, *116*, 3502–3507, doi:10.1073/pnas.1814204116.
131. Mendez, M.G.; Janmey, P.A. Transcription factor regulation by mechanical stress. *Int. J. Biochem. Cell Biol.* **2012**, *44*, 728–732, doi:10.1016/j.biocel.2012.02.003.
132. Zhang, X.; Li, Y.; Ma, Y.; Yang, L.; Wang, T.; Meng, X.; Zong, Z.; Sun, X.; Hua, X.; Li, H. Yes-associated protein (YAP) binds to HIF-1 α and sustains HIF-1 α protein stability

- to promote hepatocellular carcinoma cell glycolysis under hypoxic stress. *J. Exp. Clin. Cancer Res.* **2018**, *37*, 216, doi:10.1186/s13046-018-0892-2.
133. Kim, J.-G.; Islam, R.; Cho, J.Y.; Jeong, H.; Cap, K.-C.; Park, Y.; Hossain, A.J.; Park, J.-B. Regulation of RhoA GTPase and various transcription factors in the RhoA pathway. *J. Cell. Physiol.* **2018**, *233*, 6381–6392, doi:10.1002/jcp.26487.
 134. Calvo, F.; Ege, N.; Grande-Garcia, A.; Hooper, S.; Jenkins, R.P.; Chaudhry, S.I.; Harrington, K.; Williamson, P.; Moeendarbary, E.; Charras, G.; et al. Mechanotransduction and YAP-dependent matrix remodelling is required for the generation and maintenance of cancer-associated fibroblasts. *Nature Cell Biology* **2013**, *15*, 637–646, doi:10.1038/ncb2756.
 135. Bu, L.; Baba, H.; Yoshida, N.; Miyake, K.; Yasuda, T.; Uchihara, T.; Tan, P.; Ishimoto, T. Biological heterogeneity and versatility of cancer-associated fibroblasts in the tumor microenvironment. *Oncogene* **2019**, *38*, 4887–4901, doi:10.1038/s41388-019-0765-y.
 136. Turley, E.A. HIPPO and Hyaluronan: Partners in Tumor Resistance? *Bioessays* **2020**, *42*, e2000090, doi:10.1002/bies.202000090.
 137. Erkisa, M.; Sariman, M.; Geyik, O.G.; Geyik, C.; Stanojkovic, T.; Ulukaya, E. Natural Products as a Promising Therapeutic Strategy to Target Cancer Stem Cells. *Curr. Med. Chem.* **2022**, *29*, 741–783, doi:10.2174/0929867328666210628131409.
 138. Newman, D.J.; Cragg, G.M. Natural Products as Sources of New Drugs over the Nearly Four Decades from 01/1981 to 09/2019. *J. Nat. Prod.* **2020**, *83*, 770–803, doi:10.1021/acs.jnatprod.9b01285.
 139. Kordestani, Z.; Shahrokhi-Farjah, M.; Yazdi Rouholamini, S.E.; Saberi, A. Reduced IKK/NF- κ B Expression by Nigella Sativa Extract in Breast Cancer. *Middle East Journal of Cancer* **2020**, *11*, doi:10.30476/mejc.2019.82140.1059.
 140. Tseng, Y.-H.; Chao, C.-T. *Tylophora lui* (Apocynaceae), a new species from Taiwan. *Annales Botanici Fennici* **2011**, *48*.
 141. El-Kashef, D.H.; Youssef, F.S.; Reimche, I.; Teusch, N.; Müller, W.E.G.; Lin, W.; Frank, M.; Liu, Z.; Proksch, P. Polyketides from the marine-derived fungus *Aspergillus falconensis*: In silico and in vitro cytotoxicity studies. *Bioorg. Med. Chem.* **2021**, *29*, 115883, doi:10.1016/j.bmc.2020.115883.
 142. Jia, X.-H.; Zhao, H.-X.; Du, C.-L.; Tang, W.-Z.; Wang, X.-J. Possible pharmaceutical applications can be developed from naturally occurring phenanthroindolizidine and phenanthroquinolizidine alkaloids. *Phytochem. Rev.* **2021**, *20*, 845–868, doi:10.1007/s11101-020-09723-3.
 143. Hemsley, H.; Happ, H.; Hoyopsis, H.L.; Hemsley, N. *Tylophora*. *Flora of China* **1995**, *16*, 253–262.

144. Endress, M.E.; Bruyns, P.V. A revised classification of the Apocynaceae s.l. *The Botanical Review* **2000**, *66*.
145. Nazar, S.; Hussain, M.A.; Khan, A.; Muhammad, G.; Bukhari, S. Alkaloid-rich plant *Tylophora indica*; current trends in isolation strategies, chemical profiling and medicinal applications. *Arabian Journal of Chemistry* **2020**, *13*, 6348–6365, doi:10.1016/j.arabjc.2020.05.037.
146. Cyriac, A.; Thomas, T.; Thomas, T.D. Tylophorine: Sources, Properties, Applications and Biotechnological Production. In *Plant-derived Bioactives*; Swamy, M.K., Ed.; Springer Singapore: Singapore, 2020; pp 167–176, ISBN 978-981-15-1760-0.
147. Mayank Gupta, Hayat M. Mukhtar, Sayeed Ahmad. Phyto-pharmacological and plant tissue culture overview of *Tylophora indica* (burm f.) Merrill. *Journal of Pharmaceutical Sciences and Research* **2010**, *2*, 401–411.
148. NCI human tumor cell line growth inhibition assay. Data for the MDA-MB-231/ATCC Breast cell line. Available online: <https://pubchem.ncbi.nlm.nih.gov/bioassay/95> (accessed on 22 July 2019).
149. Li, Z.; Tang, X.; Luo, Y.; Chen, B.; Zhou, C.; Wu, X.; Tang, Z.; Qi, X.; Cao, G.; Hao, J.; et al. NK007 helps in mitigating paclitaxel resistance through p38MAPK activation and HK2 degradation in ovarian cancer. *J. Cell. Physiol.* **2019**, 16178–16190, doi:10.1002/jcp.28278.
150. Gao, W.; Bussom, S.; Grill, S.P.; Gullen, E.A.; Hu, Y.-C.; Huang, X.; Zhong, S.; Kaczmarek, C.; Gutierrez, J.; Francis, S.; et al. Structure-activity studies of phenanthroindolizidine alkaloids as potential antitumor agents. *Bioorg. Med. Chem. Lett.* **2007**, *17*, 4338–4342, doi:10.1016/j.bmcl.2007.05.021.
151. Shiah, H.-S.; Gao, W.; Baker, D.C.; Cheng, Y.-C. Inhibition of cell growth and nuclear factor-kappaB activity in pancreatic cancer cell lines by a tylophorine analogue, DCB-3503. *Mol. Cancer Ther.* **2006**, *5*, 2484–2493, doi:10.1158/1535-7163.MCT-06-0146.
152. Saraswati, S.; Kanaujia, P.K.; Kumar, S.; Kumar, R.; Alhaider, A.A. Tylophorine, a phenanthroindolizidine alkaloid isolated from *Tylophora indica* exerts antiangiogenic and antitumor activity by targeting vascular endothelial growth factor receptor 2-mediated angiogenesis **2013**, *12*:82, 1–16.
153. Min, H.-Y.; Chung, H.-J.; Kim, E.-H.; Kim, S.; Park, E.-J.; Lee, S.K. Inhibition of cell growth and potentiation of tumor necrosis factor- α (TNF- α)-induced apoptosis by a phenanthroindolizidine alkaloid antofine in human colon cancer cells. *Biochem. Pharmacol.* **2010**, *80*, 1356–1364, doi:10.1016/j.bcp.2010.07.026.
154. Pratama, N.P.; Wulandari, S.; Nugroho, A.E.; Fakhrudin, N.; Astuti, P.; Sudarsono. Tylophorine Abrogates G2/M Arrest Induced by Doxorubicine and Promotes

- Increased Apoptosis in T47D Breast Cancer Cells. *Asian Pac. J. Cancer Prev.* **2018**, *19*, 3065–3069, doi:10.31557/APJCP.2018.19.11.3065.
155. NCI human tumor cell line growth inhibition assay. Data for the MCF7 Breast cell line. Available online: <https://pubchem.ncbi.nlm.nih.gov/bioassay/83> (accessed on 22 July 2019).
156. NCI human tumor cell line growth inhibition assay. Data for the T-47D Breast cell line. Available online: <https://pubchem.ncbi.nlm.nih.gov/bioassay/91> (accessed on 22 July 2019).
157. Chen, C.-Y.; Zhu, G.-Y.; Wang, J.-R.; Jiang, Z.-H. Phenanthroindolizidine alkaloids from *Tylophora atrofolliculata* with hypoxia-inducible factor-1 (HIF-1) inhibitory activity. *RSC Adv.* **2016**, *6*, 79958–79967, doi:10.1039/C6RA16455B.
158. Liu, Z.; Lv, H.; Li, H.; Zhang, Y.; Zhang, H.; Su, F.; Xu, S.; Li, Y.; Si, Y.; Yu, S.; et al. Interaction studies of an anticancer alkaloid, (+)-(13aS)-deoxytylophorinine, with calf thymus DNA and four repeated double-helical DNAs. *Chemotherapy* **2011**, *57*, 310–320, doi:10.1159/000329506.
159. Liu, Z.-J.; Lv, H.-N.; Li, H.-Y.; Zhang, Y.; Zhang, H.-J.; Su, F.-Q.; Si, Y.-K.; Yu, S.-S.; Chen, X.-G. Anticancer effect and neurotoxicity of S-(+)-deoxytylophorinidine, a new phenanthroindolizidine alkaloid that interacts with nucleic acids. *J. Asian Nat. Prod. Res.* **2011**, *13*, 400–408, doi:10.1080/10286020.2011.566868.
160. Peraza-Sánchez, S.R.; Chai, H.-B.; Geun Shin, Y.; Santisuk, T.; Reutrakul, V.; Farnsworth, N.R.; Cordell, G.A.; Pezzuto, J.M.; Kinghorn, A.D. Constituents of the Leaves and Twigs of *Ficus hispida*. *Planta Med.* **2001**, *68*, 186–188.
161. Xie, B.; Hänsel, J.; Mundorf, V.; Betz, J.; Reimche, I.; Erkan, M.; Büdeyri, I.; Gesell, A.; Kerr, R.G.; Ariantari, N.P.; et al. Pseudopterosin and O-Methyltylophorinidine Suppress Cell Growth in a 3D Spheroid Co-Culture Model of Pancreatic Ductal Adenocarcinoma. *Bioengineering (Basel)* **2020**, *7*, doi:10.3390/bioengineering7020057.
162. Huang, X.; Gao, S.; Fan, L.; Yu, S.; Liang, X. Cytotoxic alkaloids from the roots of *Tylophora atrofolliculata*. *Planta Med.* **2004**, *70*, 441–445, doi:10.1055/s-2004-818973.
163. Ikeda, T.; Yaegashi, T.; Matsuzaki, T.; Hashimoto, S.; Sawada, S. Asymmetric synthesis of phenanthroindolizidine alkaloids with hydroxyl group at the C14 position and evaluation of their antitumor activities. *Bioorg. Med. Chem. Lett.* **2011**, *21*, 342–345, doi:10.1016/j.bmcl.2010.11.008.
164. Ikeda, T.; Yaegashi, T.; Matsuzaki, T.; Yamazaki, R.; Hashimoto, S.; Sawada, S. Synthesis of phenanthroindolizidine alkaloids and evaluation of their antitumor

- activities and toxicities. *Bioorg. Med. Chem. Lett.* **2011**, *21*, 5978–5981, doi:10.1016/j.bmcl.2011.07.120.
165. Chen, C.-Y.; Bai, L.-P.; Ke, Z.-F.; Liu, Y.; Wang, J.-R.; Jiang, Z.-H. G-Quadruplex DNA-binding quaternary alkaloids from *Tylophora atrofolliculata*. *RSC Adv.* **2016**, *6*, 114135–114142, doi:10.1039/C6RA21056B.
166. Rao, K.N.; Bhattacharya, R.; Venkatachalam, S. Thymidylate synthase activity in leukocytes from patients with chronic myelocytic leukemia and acute lymphocytic leukemia and its inhibition by phenanthroindolizidine alkaloids pergularinine and tylophorinidine. *Cancer letters* **1998**, 183–188.
167. Zhong, J.-J.; Xiao, J.-H. Secondary metabolites from higher fungi: discovery, bioactivity, and bioproduction. *Adv. Biochem. Eng. Biotechnol.* **2009**, *113*, 79–150, doi:10.1007/10_2008_26.
168. Ariantari, N.P.; Ancheeva, E.; Frank, M.; Stuhldreier, F.; Meier, D.; Gröner, Y.; Reimche, I.; Teusch, N.; Wesselborg, S.; Müller, W.E.G.; et al. Didymellanosine, a new decahydrofluorene analogue, and ascolactone C from *Didymella* sp. IEA-3B.1, an endophyte of *Terminalia catappa*. *RSC Adv.* **2020**, *10*, 7232–7240, doi:10.1039/c9ra10685e.
169. Chen, Y.; Liu, Z.; Huang, Y.; Liu, L.; He, J.; Wang, L.; Yuan, J.; She, Z. Ascomylactams A-C, Cytotoxic 12- or 13-Membered-Ring Macrocyclic Alkaloids Isolated from the Mangrove Endophytic Fungus *Didymella* sp. CYSK-4, and Structure Revisions of Phomapyrrolidones A and C. *J. Nat. Prod.* **2019**, *82*, 1752–1758, doi:10.1021/acs.jnatprod.8b00918.
170. Julia Sperlich. *Pharmacological characterization of pseudopterosin, azaphilone and teleocidin as novel drug candidates for the treatment of triple negative breast cancer.*, 2018. Available online: <https://docserv.uni-duesseldorf.de/servlets/DocumentServlet?id=48165> (accessed on 15 September 2022).
171. El-Kashef, D.H.; Youssef, F.S.; Hartmann, R.; Knedel, T.-O.; Janiak, C.; Lin, W.; Reimche, I.; Teusch, N.; Liu, Z.; Proksch, P. Azaphilones from the Red Sea Fungus *Aspergillus falconensis*. *Mar. Drugs* **2020**, *18*, doi:10.3390/md18040204.
172. Bladt, T.T.; Frisvad, J.C.; Knudsen, P.B.; Larsen, T.O. Anticancer and antifungal compounds from *Aspergillus*, *Penicillium* and other filamentous fungi. *Molecules* **2013**, *18*, 11338–11376, doi:10.3390/molecules180911338.
173. Edmondson, R.; Broglie, J.J.; Adcock, A.F.; Yang, L. Three-dimensional cell culture systems and their applications in drug discovery and cell-based biosensors. *Assay Drug Dev. Technol.* **2014**, *12*, 207–218, doi:10.1089/adt.2014.573.

174. Roarty, K.; Echeverria, G.V. Laboratory Models for Investigating Breast Cancer Therapy Resistance and Metastasis. *Front. Oncol.* **2021**, *11*, 645698, doi:10.3389/fonc.2021.645698.
175. Boix-Montesinos, P.; Soriano-Teruel, P.M.; Armiñán, A.; Orzáez, M.; Vicent, M.J. The past, present, and future of breast cancer models for nanomedicine development. *Adv. Drug Deliv. Rev.* **2021**, *173*, 306–330, doi:10.1016/j.addr.2021.03.018.
176. Abu-Jamous, B.; Buffa, F.M.; Harris, A.L.; Nandi, A.K. In vitro downregulated hypoxia transcriptome is associated with poor prognosis in breast cancer. *Mol. Cancer* **2017**, *16*, 1–19, doi:10.1186/s12943-017-0673-0.
177. Mak, I.W.Y.; Evaniew, N.; Ghert, M. Lost in translation: animal models and clinical trials in cancer treatment. *Am. J. Transl. Res.* **2014**, *6*, 114–118.
178. Okano, M.; Oshi, M.; Butash, A.; Okano, I.; Saito, K.; Kawaguchi, T.; Nagahashi, M.; Kono, K.; Ohtake, T.; Takabe, K. Orthotopic Implantation Achieves Better Engraftment and Faster Growth Than Subcutaneous Implantation in Breast Cancer Patient-Derived Xenografts. *J. Mammary Gland Biol. Neoplasia* **2020**, *25*, 27–36, doi:10.1007/s10911-020-09442-7.
179. Gao W.; Lam, W.; Zhong, S.; Kaczmarek, C.; Baker, D.C.; Cheng, Y.-C. Novel Mode of Action of Tylophorine Analogs as Antitumor Compounds. *Cancer Res.* **2004**, *64*, 678–688, doi:10.1158/0008-5472.CAN-03-1904.
180. Huang, Z.; Yu, P.; Tang, J. Characterization of Triple-Negative Breast Cancer MDA-MB-231 Cell Spheroid Model. *Onco. Targets. Ther.* **2020**, *13*, 5395–5405, doi:10.2147/OTT.S249756.
181. Badea, M.A.; Balas, M.; Hermenean, A.; Ciceu, A.; Herman, H.; Ionita, D.; Dinischiotu, A. Influence of Matrigel on Single- and Multiple-Spheroid Cultures in Breast Cancer Research. *SLAS Discov.* **2019**, *24*, 563–578, doi:10.1177/2472555219834698.
182. Clegg, J.; Koch, M.K.; Thompson, E.W.; Haupt, L.M.; Kalita-de Croft, P.; Bray, L.J. Three-Dimensional Models as a New Frontier for Studying the Role of Proteoglycans in the Normal and Malignant Breast Microenvironment. *Front. Cell Dev. Biol.* **2020**, *8*, doi:10.3389/fcell.2020.569454.
183. Kapałczyńska, M.; Kolenda, T.; Przybyła, W.; Zajączkowska, M.; Teresiak, A.; Filas, V.; Ibbs, M.; Bliźniak, R.; Łuczewski, Ł.; Lamperska, K. 2D and 3D cell cultures - a comparison of different types of cancer cell cultures. *Arch. Med. Sci.* **2018**, *14*, 910–919, doi:10.5114/aoms.2016.63743.
184. Pierce, J.W.; Schoenleber, R.; Jesmok, G.; Best, J.; Moore, S.A.; Collins, T.; Gerritsen, M.E. Novel inhibitors of cytokine-induced IkappaBalpha phosphorylation

- and endothelial cell adhesion molecule expression show anti-inflammatory effects in vivo. *J. Biol. Chem.* **1997**, 272, 21096–21103, doi:10.1074/jbc.272.34.21096.
185. Nasu, K.; Nishida, M.; Ueda, T.; Yuge, A.; Takai, N.; Narahara, H. Application of the nuclear factor-kappaB inhibitor BAY 11-7085 for the treatment of endometriosis: an in vitro study. *Am. J. Physiol. Endocrinol. Metab.* **2007**, 293, E16-23, doi:10.1152/ajpendo.00135.2006.
 186. Karthikeyan, S.; Bharanidharan, G.; Ragavan, S.; Kandasamy, S.; Chinnathambi, S.; Udayakumar, K.; Mangaiyarkarasi, R.; Suganya, R.; Aruna, P.; Ganesan, S. Exploring the Binding Interaction Mechanism of Taxol in β -Tubulin and Bovine Serum Albumin: A Biophysical Approach. *Molecular Pharmaceutics* **2019**, 16, 669–681, doi:10.1021/acs.molpharmaceut.8b00948.
 187. Reimche, I.; Yu, H.; Ariantari, N.P.; Liu, Z.; Merkens, K.; Rotfuß, S.; Peter, K.; Jungwirth, U.; Bauer, N.; Kiefer, F.; et al. Phenanthroindolizidine Alkaloids Isolated from *Tylophora ovata* as Potent Inhibitors of Inflammation, Spheroid Growth, and Invasion of Triple-Negative Breast Cancer. *IJMS* **2022**, 23, 10319, doi:10.3390/ijms231810319.
 188. Alves Avelar, L.A.; Schrenk, C.; Sönnichsen, M.; Hamacher, A.; Hansen, F.K.; Schliehe-Diecks, J.; Borkhardt, A.; Bhatia, S.; Kassack, M.U.; Kurz, T. Synergistic induction of apoptosis in resistant head and neck carcinoma and leukemia by alkoxyamide-based histone deacetylase inhibitors. *Eur. J. Med. Chem.* **2021**, 211, 113095, doi:10.1016/j.ejmech.2020.113095.
 189. Stenzel, K.; Hamacher, A.; Hansen, F.K.; Gertzen, C.G.W.; Senger, J.; Marquardt, V.; Marek, L.; Marek, M.; Romier, C.; Remke, M.; et al. Alkoxyurea-Based Histone Deacetylase Inhibitors Increase Cisplatin Potency in Chemoresistant Cancer Cell Lines. *J. Med. Chem.* **2017**, 60, 5334–5348, doi:10.1021/acs.jmedchem.6b01538.
 190. Schindelin, J.; Arganda-Carreras, I.; Frise, E.; Kaynig, V.; Longair, M.; Pietzsch, T.; Preibisch, S.; Rueden, C.; Saalfeld, S.; Schmid, B.; et al. Fiji: an open-source platform for biological-image analysis. *Nat. Methods* **2012**, 9, 676–682, doi:10.1038/nmeth.2019.
 191. Jungwirth, U.; van Weverwijk, A.; Jenkins, L.; Alexander, J.; Vicente, D.; Gao, Q.; Haider, S.; Iravani, M.; Isacke, C.M. Impairment of a distinct cancer-associated fibroblast population limits tumour growth and metastasis **2020**, 23, 1–17, doi:10.1101/2020.05.17.100412.
 192. Jungwirth, U.; van Weverwijk, A.; Melake, M.J.; Chambers, A.F.; Gao, Q.; Fivaz, M.; Isacke, C.M. Generation and characterisation of two D2A1 mammary cancer sublines to model spontaneous and experimental metastasis in a syngeneic BALB/c host. *Disease Models & Mechanisms* **2018**, 11, doi:10.1242/dmm.031740.

193. Keller, F.; Rudolf, R.; Hafner, M. Towards optimized breast cancer 3D spheroid mono- and co-culture models for pharmacological research and screening. *JCB* **2019**, *5*, 89–101, doi:10.3233/JCB-199001.
194. Livak, K.J.; Schmittgen, T.D. Analysis of relative gene expression data using real-time quantitative PCR and the 2(-Delta Delta C(T)) Method. *Methods* **2001**, *25*, 402–408, doi:10.1006/meth.2001.1262.
195. Hawsawi, N.M.; Ghebeh, H.; Hendrayani, S.-F.; Tulbah, A.; Al-Eid, M.; Al-Tweigeri, T.; Ajarim, D.; Alaiya, A.; Dermime, S.; Aboussekhra, A. Breast carcinoma-associated fibroblasts and their counterparts display neoplastic-specific changes. *Cancer Res.* **2008**, *68*, 2717–2725, doi:10.1158/0008-5472.CAN-08-0192.
196. LI-COR Biosciences. Housekeeping Protein Normalization Protocol. Available online: <https://www.licor.com/documents/kijrkoh8oqvw212577slsljldl74og16> (accessed on 9 March 2022).
197. Sunters, A.; Fernández de Mattos, S.; Stahl, M.; Brosens, J.J.; Zoumpoulidou, G.; Saunders, C.A.; Coffey, P.J.; Medema, R.H.; Coombes, R.C.; Lam, E.W.-F. FoxO3a transcriptional regulation of Bim controls apoptosis in paclitaxel-treated breast cancer cell lines. *J. Biol. Chem.* **2003**, *278*, 49795–49805, doi:10.1074/jbc.M309523200.
198. Rana, N.K.; Singh, P.; Koch, B. CoCl₂ simulated hypoxia induce cell proliferation and alter the expression pattern of hypoxia associated genes involved in angiogenesis and apoptosis. *Biol. Res.* **2019**, *52*, 1–13, doi:10.1186/s40659-019-0221-z.
199. Fatherree, J.P.; Guarín, J.R.; McGinn, R.A.; Naber, S.P.; Oudin, M.J. Chemotherapy-Induced Collagen IV Drives Cancer Cell Motility through Activation of Src and Focal Adhesion Kinase. *Cancer Res* **2022**, *82*, 2031–2044, doi:10.1158/0008-5472.CAN-21-1823.
200. Fatherree, J.P.; Guarín, J.; McGinn, R.; Oudin, M.J. Abstract LT001: Paclitaxel-induced collagen IV drives local invasion in the post-chemotherapy tumor microenvironment in triple-negative breast cancer. *Cancer Res* **2021**, *81*, LT001-LT001, doi:10.1158/1538-7445.TME21-LT001.
201. Befani, C.; Mylonis, I.; Gkoutinakou, I.-M.; Georgoulas, P.; Hu, C.-J.; Simos, G.; Liakos, P. Cobalt stimulates HIF-1-dependent but inhibits HIF-2-dependent gene expression in liver cancer cells. *Int. J. Biochem. Cell Biol.* **2013**, *45*, 2359–2368, doi:10.1016/j.biocel.2013.07.025.
202. Yuan, Y.; Hilliard, G.; Ferguson, T.; Millhorn, D.E. Cobalt inhibits the interaction between hypoxia-inducible factor- α and von Hippel-Lindau protein by direct binding to hypoxia-inducible factor- α . *J. Biol. Chem.* **2003**, *278*, 15911–15916, doi:10.1074/jbc.M300463200.

203. Ueno, S.; Yamazaki, R.; Ikeda, T.; Yaegashi, T.; Matsuzaki, T. Antitumor Effect of a Novel Phenanthroindolizidine Alkaloid Derivative Through Inhibition of Protein Synthesis. *Anticancer Research* **2014**, *34*, 3391–3398.
204. Yap, V.A.; Loong, B.-J.; Ting, K.-N.; Loh, S.H.-S.; Yong, K.-T.; Low, Y.-Y.; Kam, T.-S.; Lim, K.-H. Hispidacine, an unusual 8,4'-oxyneolignan-alkaloid with vasorelaxant activity, and hispiloscine, an antiproliferative phenanthroindolizidine alkaloid, from *Ficus hispida* Linn. *Phytochemistry* **2015**, *109*, 96–102, doi:10.1016/j.phytochem.2014.10.032.
205. Al-Khdhairawi, A.A.Q.; Krishnan, P.; Mai, C.-W.; Chung, F.F.-L.; Leong, C.-O.; Yong, K.-T.; Chong, K.-W.; Low, Y.-Y.; Kam, T.-S.; Lim, K.-H. A Bis-benzopyrroloisoquinoline Alkaloid Incorporating a Cyclobutane Core and a Chlorophenanthroindolizidine Alkaloid with Cytotoxic Activity from *Ficus fistulosa* var. *tengerensis*. *J. Nat. Prod.* **2017**, *80*, 2734–2740, doi:10.1021/acs.jnatprod.7b00500.
206. Haryanti, S.; Murwanti, R.; Putri, H.; Pradani Nur Imawati, Gagas: Pramono, Suwijjiyo; Meiyanto, E. Different 4T1 Cells Migration under *Caesalpinia sappan* L. and *Ficus septica* Burm.f Ethanolic Extracts. *Indonesian Journal of Cancer Chemoprevention*, **2017**, *8*, 21–26.
207. Amirghasemi, F.; Adjei-Sowah, E.; Pockaj, B.A.; Nikkhah, M. Microengineered 3D Tumor Models for Anti-Cancer Drug Discovery in Female-Related Cancers. *Ann. Biomed. Eng.* **2021**, *49*, 1943–1972, doi:10.1007/s10439-020-02704-9.
208. Chemler, S.R. Phenanthroindolizidines and Phenanthroquinolizidines: Promising Alkaloids for Anti-Cancer Therapy. *Curr. Bioact. Compd.* **2009**, *5*, 2–19, doi:10.2174/157340709787580928.
209. Niphakis, M.J.; Gay, B.C.; Hong, K.H.; Bleeker, N.P.; Georg, G.I. Synthesis and evaluation of the anti-proliferative and NF- κ B activities of a library of simplified tylophorine analogs. *Bioorg. Med. Chem.* **2012**, *20*, 5893–5900, doi:10.1016/j.bmc.2012.07.044.
210. K. N. Rao, R. K. Bhattacharya, S. R. Venkatachalam. Inhibition of thymidylate synthase and cell growth by the phenanthroindolizidine alkaloids pergularinine and tylophorinidine. *Chemico-biological interactions* **1997**, 201–212.
211. Yang, C.-W.; Chuang, T.-H.; Wu, P.-L.; Huang, W.-H.; Lee, S.-J. Anti-inflammatory effects of 7-methoxycryptopleurine and structure-activity relations of phenanthroindolizidines and phenanthroquinolizidines. *Biochemical and Biophysical Research Communications* **2007**, *354*, 942–948, doi:10.1016/j.bbrc.2007.01.065.
212. Lin, J.-C.; Yang, S.-C.; Hong, T.-M.; Yu, S.-L.; Shi, Q.; Wei, L.; Chen, H.-Y.; Yang, P.-C.; Lee, K.-H. Phenanthrene-based tylophorine-1 (PBT-1) inhibits lung cancer cell

- growth through the Akt and NF-kappaB pathways. *J. Med. Chem.* **2009**, *52*, 1903–1911, doi:10.1021/jm801344j.
213. Abe, F.; Hirokawa, M.; Yamauchi, T.; Honda, K.; Hayashi, N.; Ishii, M.; Imagawa, S.; Iwahana, M. Further Investigation of Phenanthroindolizidine Alkaloids from *Tylophora tanakea* **1998**, *46*, 767–769.
214. Wei, L.; Brossi, A.; Kendall, R.; Bastow, K.F.; Morris-Natschke, S.L.; Shi, Q.; Lee, K.-H. Antitumor agents 251: synthesis, cytotoxic evaluation, and structure-activity relationship studies of phenanthrene-based tylophorine derivatives (PBTs) as a new class of antitumor agents. *Bioorg. Med. Chem.* **2006**, *14*, 6560–6569, doi:10.1016/j.bmc.2006.06.009.
215. Ishikura, M.; Abe, T.; Choshi, T.; Hibino, S. Simple indole alkaloids and those with a nonrearranged monoterpene unit. *Nat. Prod. Rep.* **2015**, *32*, 1389–1471, doi:10.1039/c5np00032g.
216. Yang, X.; Shi, Q.; Liu, Y.-N.; Zhao, G.; Bastow, K.F.; Lin, J.-C.; Yang, S.-C.; Yang, P.-C.; Lee, K.-H. Antitumor agents 268. Design, synthesis, and mechanistic studies of new 9-substituted phenanthrene-based tylophorine analogues as potent cytotoxic agents. *J. Med. Chem.* **2009**, *52*, 5262–5268, doi:10.1021/jm9009263.
217. Gopalakrishnan, C.; Shankaranarayan, D.; Kameswaran, L.; Natarajan, S. Pharmacological investigations of tylophorine, the major alkaloid of *Tylophora indica*. *Indian J. Med. Res.* **1979**, *69*, 513–520.
218. George R. Pettit/Animesh Goswami/Gordon M. Cragg/Jean M. Schmidt/Ji-Chun Zou. Antineoplastic Agents, 103. The Isolation and Structure of Hypoestestins 1 and 2 From the East African *Hypoestes verticillaris*.
219. Yoshida, T.; Hashimura, M.; Mastumoto, T.; Tazo, Y.; Inoue, H.; Kuwata, T.; Saegusa, M. Transcriptional upregulation of HIF-1 α by NF- κ B/p65 and its associations with β -catenin/p300 complexes in endometrial carcinoma cells. *Lab. Invest.* **2013**, *93*, 1184–1193, doi:10.1038/labinvest.2013.111.
220. Guo, Q.; Lu, L.; Liao, Y.; Wang, X.; Zhang, Y.; Liu, Y.; Huang, S.; Sun, H.; Li, Z.; Zhao, L. Influence of c-Src on hypoxic resistance to paclitaxel in human ovarian cancer cells and reversal of FV-429. *Cell Death Dis.* **2018**, *8*, e3178, doi:10.1038/cddis.2017.367.
221. Ferrari, P.; Scatena, C.; Ghilli, M.; Bargagna, I.; Lorenzini, G.; Nicolini, A. Molecular Mechanisms, Biomarkers and Emerging Therapies for Chemotherapy Resistant TNBC. *Int. J. Mol. Sci.* **2022**, *23*, 1665, doi:10.3390/ijms23031665.
222. Liu, H.; Chen, Q.; Di Lu; Pang, X.; Yin, S.; Wang, K.; Wang, R.; Yang, S.; Zhang, Y.; Qiu, Y.; et al. HTBPI, an active phenanthroindolizidine alkaloid, inhibits liver

- tumorigenesis by targeting Akt. *FASEB J.* **2020**, *34*, 12255–12268, doi:10.1096/fj.202000254R.
223. Wang, Y.; Lam, W.; Chen, S.-R.; Guan, F.-L.; Dutchman, G.E.; Francis, S.; Baker, D.C.; Cheng, Y.-C. Tylophorine Analog DCB-3503 Inhibited Cyclin D1 Translation through Allosteric Regulation of Heat Shock Cognate Protein 70. *Sci. Rep.* **2016**, *6*, 32832, doi:10.1038/srep32832.
 224. Mostafa, E.M.; Mohammed, H.A.; Musa, A.; Abdelgawad, M.A.; Al-Sanea, M.M.; Almahmoud, S.A.; Ghoneim, M.M.; Gomaa, H.A.M.; Rahman, F.E.-Z.S.A.; Shalaby, K.; et al. In Vitro Anti-Proliferative, and Kinase Inhibitory Activity of Phenanthroindolizidine Alkaloids Isolated from *Tylophora indica*. *Plants (Basel)* **2022**, *11*, 1295, doi:10.3390/plants11101295.
 225. Vermeulen, K.; van Bockstaele, D.R.; Berneman, Z.N. The cell cycle: a review of regulation, deregulation and therapeutic targets in cancer. *Cell Prolif.* **2003**, *36*, 131–149, doi:10.1046/j.1365-2184.2003.00266.x.
 226. Wu, C.-M.; Yang, C.-W.; Lee, Y.-Z.; Chuang, T.-H.; Wu, P.-L.; Chao, Y.-S.; Lee, S.-J. Tylophorine arrests carcinoma cells at G1 phase by downregulating cyclin A2 expression. *Biochemical and Biophysical Research Communications* **2009**, *386*, 140–145, doi:10.1016/j.bbrc.2009.05.138.
 227. Lim, S.; Kaldis, P. Cdks, cyclins and CKIs: roles beyond cell cycle regulation. *Development* **2013**, *140*, 3079–3093, doi:10.1242/dev.091744.
 228. Ledoux, A.C.; Perkins, N.D. NF- κ B and the cell cycle. *Biochem. Soc. Trans.* **2014**, *42*, 76–81, doi:10.1042/BST20130156.
 229. Kampan, N.C.; Madondo, M.T.; McNally, O.M.; Quinn, M.; Plebanski, M. Paclitaxel and Its Evolving Role in the Management of Ovarian Cancer. *Biomed Res. Int.* **2015**, *2015*, 413076, doi:10.1155/2015/413076.
 230. Gully, C.P.; Velazquez-Torres, G.; Shin, J.-H.; Fuentes-Mattei, E.; Wang, E.; Carlock, C.; Chen, J.; Rothenberg, D.; Adams, H.P.; Choi, H.H.; et al. Aurora B kinase phosphorylates and instigates degradation of p53. *Proc. Natl. Acad. Sci. U. S. A.* **2012**, *109*, E1513–E1522, doi:10.1073/pnas.1110287109.
 231. Rao, K.N.; Venkatachalam, S. Inhibition of Dihydrofolate Reductase and Cell Growth Activity by the Phenanthroindolizidine Alkaloids Pergularinine and Tylophorinidine: the In Vitro Cytotoxicity of These Plant Alkaloids and their Potential as Antimicrobial and Anticancer Agents. *Toxicology in Vitro* **2000**, 53–59.
 232. Wang, Y.; Gao, W.; Svitkin, Y.V.; Chen, A.P.-C.; Cheng, Y.-C. DCB-3503, a tylophorine analog, inhibits protein synthesis through a novel mechanism. *PLoS ONE* **2010**, *5*, e11607, doi:10.1371/journal.pone.0011607.

233. Morciano, G.; Vezzani, B.; Missiroli, S.; Boncompagni, C.; Pinton, P.; Giorgi, C. An Updated Understanding of the Role of YAP in Driving Oncogenic Responses. *Cancers (Basel)* **2021**, *13*, doi:10.3390/cancers13123100.
234. Chen, W.; Park, S.; Patel, C.; Bai, Y.; Henary, K.; Raha, A.; Mohammadi, S.; You, L.; Geng, F. The migration of metastatic breast cancer cells is regulated by matrix stiffness via YAP signalling. *Heliyon* **2021**, *7*, e06252, doi:10.1016/j.heliyon.2021.e06252.
235. Yuan, M.; Tomlinson, V.; Lara, R.; Holliday, D.; Chelala, C.; Harada, T.; Gangeswaran, R.; Manson-Bishop, C.; Smith, P.; Danovi, S.A.; et al. Yes-associated protein (YAP) functions as a tumor suppressor in breast. *Cell Death Differ.* **2008**, *15*, 1752–1759, doi:10.1038/cdd.2008.108.
236. Andrade, D.; Mehta, M.; Griffith, J.; Panneerselvam, J.; Srivastava, A.; Kim, T.-D.; Janknecht, R.; Herman, T.; Ramesh, R.; Munshi, A. YAP1 inhibition radiosensitizes triple negative breast cancer cells by targeting the DNA damage response and cell survival pathways. *Oncotarget* **2017**, *8*, 98495–98508, doi:10.18632/oncotarget.21913.
237. Wu, L.; Yang, X. Targeting the Hippo Pathway for Breast Cancer Therapy. *Cancers (Basel)* **2018**, *10*, doi:10.3390/cancers10110422.
238. Wang, Q.; Gao, X.; Yu, T.; Yuan, L.; Dai, J.; Wang, W.; Chen, G.; Jiao, C.; Zhou, W.; Huang, Q.; et al. REGγ Controls Hippo Signaling and Reciprocal NF-κB-YAP Regulation to Promote Colon Cancer. *Clin. Cancer Res.* **2018**, *24*, 2015–2025, doi:10.1158/1078-0432.CCR-17-2986.
239. Bhattacharjee, D.; Bakar, J.; Sausville, E.L.; Mendelson, B.E.; Long, K.; Smith, J.C.; Sheltzer, J.M. *A drug's most potent target is not necessarily the source of its anti-cancer activity*, 2022.
240. Takeda, T.; Yamamoto, Y.; Tsubaki, M.; Matsuda, T.; Kimura, A.; Shimo, N.; Nishida, S. PI3K/Akt/YAP signaling promotes migration and invasion of DLD-1 colorectal cancer cells. *Oncol. Lett.* **2022**, *23*, 106, doi:10.3892/ol.2022.13226.
241. Nath, A.; Mitra, S.; Mistry, T.; Pal, R.; Nasare, V.D. Molecular targets and therapeutics in chemoresistance of triple-negative breast cancer. *Med. Oncol.* **2021**, *39*, 14, doi:10.1007/s12032-021-01610-x.
242. Mohamed, M.M.; El-Ghonaimy, E.A.; Nouh, M.A.; Schneider, R.J.; Sloane, B.F.; El-Shinawi, M. Cytokines secreted by macrophages isolated from tumor microenvironment of inflammatory breast cancer patients possess chemotactic properties. *Int. J. Biochem. Cell Biol.* **2014**, *46*, 138–147, doi:10.1016/j.biocel.2013.11.015.

243. Sanguinetti, A.; Santini, D.; Bonafè, M.; Taffurelli, M.; Avenia, N. Interleukin-6 and pro inflammatory status in the breast tumor microenvironment. *World J. Surg. Oncol.* **2015**, *13*, 129, doi:10.1186/s12957-015-0529-2.
244. Zhou, J.; Wang, X.-H.; Zhao, Y.-X.; Chen, C.; Xu, X.-Y.; Sun, Q.; Wu, H.-Y.; Chen, M.; Sang, J.-F.; Su, L.; et al. Cancer-Associated Fibroblasts Correlate with Tumor-Associated Macrophages Infiltration and Lymphatic Metastasis in Triple Negative Breast Cancer Patients. *J. Cancer* **2018**, *9*, 4635–4641, doi:10.7150/jca.28583.
245. Long, X.; Ye, Y.; Zhang, L.; Liu, P.; Yu, W.; Wei, F.; Ren, X.; Yu, J. IL-8, a novel messenger to cross-link inflammation and tumor EMT via autocrine and paracrine pathways (Review). *Int. J. Oncol.* **2016**, *48*, 5–12, doi:10.3892/ijo.2015.3234.
246. Pe, K.C.S.; Saetung, R.; Yodsurang, V.; Chaotham, C.; Suppipat, K.; Chanvorachote, P.; Tawinwung, S. Triple-negative breast cancer influences a mixed M1/M2 macrophage phenotype associated with tumor aggressiveness. *PLoS ONE* **2022**, *17*, e0273044, doi:10.1371/journal.pone.0273044.
247. Chen, Z.; Wu, J.; Wang, L.; Zhao, H.; He, J. Tumor-associated macrophages of the M1/M2 phenotype are involved in the regulation of malignant biological behavior of breast cancer cells through the EMT pathway. *Med. Oncol.* **2022**, *39*, 83, doi:10.1007/s12032-022-01670-7.
248. Niepel, M.; Hafner, M.; Chung, M.; Sorger, P.K. Measuring Cancer Drug Sensitivity and Resistance in Cultured Cells. *Curr. Protoc. Chem. Biol.* **2017**, *9*, 55–74, doi:10.1002/cpch.21.
249. Muguruma, M.; Teraoka, S.; Miyahara, K.; Ueda, A.; Asaoka, M.; Okazaki, M.; Kawate, T.; Kuroda, M.; Miyagi, Y.; Ishikawa, T. Differences in drug sensitivity between two-dimensional and three-dimensional culture systems in triple-negative breast cancer cell lines. *Biochemical and Biophysical Research Communications* **2020**, *533*, 268–274, doi:10.1016/j.bbrc.2020.08.075.
250. Horning, J.L.; Sahoo, S.K.; Vijayaraghavalu, S.; Dimitrijevic, S.; Vasir, J.K.; Jain, T.K.; Panda, A.K.; Labhasetwar, V. 3-D tumor model for in vitro evaluation of anticancer drugs. *Molecular Pharmaceutics* **2008**, *5*, 849–862, doi:10.1021/mp800047v.
251. Ward, C.; Langdon, S.P.; Mullen, P.; Harris, A.L.; Harrison, D.J.; Supuran, C.T.; Kunkler, I.H. New strategies for targeting the hypoxic tumour microenvironment in breast cancer. *Cancer Treat. Rev.* **2013**, *39*, 171–179, doi:10.1016/j.ctrv.2012.08.004.
252. Özkan, H.; Öztürk, D.G.; Korkmaz, G. Transcriptional Factor Repertoire of Breast Cancer in 3D Cell Culture Models. *Cancers (Basel)* **2022**, *14*, doi:10.3390/cancers14041023.

253. Aydın, M.; Özdemir, E.; Altun, Z.; Kılıç, S.; Aktaş, S. Evaluation of Liposomal and Microbubbles Mediated Delivery of Doxorubicin in Two-Dimensional (2D) and Three-Dimensional (3D) Models for Breast Cancer. Available online: <https://www.ncbi.nlm.nih.gov/pmc/articles/PMC8246045/> (accessed on 25 November 2021).
254. Byrne, C.E.; Decombe, J.-B.; Bingham, G.C.; Remont, J.; Miller, L.G.; Khalif, L.; King, C.T.; Hamel, K.; Bunnell, B.A.; Burow, M.E.; et al. Evaluation of Extracellular Matrix Composition to Improve Breast Cancer Modeling. *Tissue Eng. Part A* **2021**, *27*, 500–511, doi:10.1089/ten.tea.2020.0364.
255. Ioachim, E.; Charchanti, A.; Briasoulis, E.; Karavasilis, V.; Tsanou, H.; Arvanitis, D.; Agnantis, N.; Pavlidis, N. Immunohistochemical expression of extracellular matrix components tenascin, fibronectin, collagen type IV and laminin in breast cancer: their prognostic value and role in tumour invasion and progression. *European Journal of Cancer* **2002**, *38*, 2362–2370, doi:10.1016/S0959-8049(02)00210-1.
256. Lam, C.R.I.; Wong, H.K.; Nai, S.; Chua, C.K.; Tan, N.S.; Tan, L.P. A 3D biomimetic model of tissue stiffness interface for cancer drug testing. *Molecular Pharmaceutics* **2014**, *11*, 2016–2021, doi:10.1021/mp500059q.
257. Emami Nejad, A.; Najafgholian, S.; Rostami, A.; Sistani, A.; Shojaeifar, S.; Esparvarinha, M.; Nedaeinia, R.; Haghighi Javanmard, S.; Taherian, M.; Ahmadi, M.; et al. The role of hypoxia in the tumor microenvironment and development of cancer stem cell: a novel approach to developing treatment. *Cancer Cell Int.* **2021**, *21*, 62, doi:10.1186/s12935-020-01719-5.
258. Xie, J.; Xiao, Y.; Zhu, X.; Ning, Z.; Xu, H.; Wu, H. Hypoxia regulates stemness of breast cancer MDA-MB-231 cells. *Med. Oncol.* **2016**, *33*, 1–7, doi:10.1007/s12032-016-0755-7.
259. Riffle, S.; Hegde, R.S. Modeling tumor cell adaptations to hypoxia in multicellular tumor spheroids. *J. Exp. Clin. Cancer Res.* **2017**, *36*, 102, doi:10.1186/s13046-017-0570-9.
260. Goggins, E.; Kakkad, S.; Mironchik, Y.; Jacob, D.; Wildes, F.; Krishnamachary, B.; Bhujwalla, Z.M. Hypoxia Inducible Factors Modify Collagen I Fibers in MDA-MB-231 Triple Negative Breast Cancer Xenografts. *Neoplasia* **2018**, *20*, 131–139, doi:10.1016/j.neo.2017.11.010.
261. Carroll, C.P.; Bolland, H.; Vancauwenberghe, E.; Collier, P.; Ritchie, A.A.; Clarke, P.A.; Grabowska, A.M.; Harris, A.L.; McIntyre, A. Targeting hypoxia regulated sodium driven bicarbonate transporters reduces triple negative breast cancer metastasis. *Neoplasia* **2022**, *25*, 41–52, doi:10.1016/j.neo.2022.01.003.

262. Joa, H.; Blažević, T.; Grojer, C.; Zeller, I.; Heiss, E.H.; Atanasov, A.G.; Feldler, I.; Gruzdaitis, P.; Czaloun, C.; Proksch, P.; et al. Tylophorine reduces protein biosynthesis and rapidly decreases cyclin D1, inhibiting vascular smooth muscle cell proliferation in vitro and in organ culture. *Phytomedicine* **2019**, 152938, doi:10.1016/j.phymed.2019.152938.
263. Grist, S.M.; Nasser, S.S.; Laplatine, L.; Schmok, J.C.; Yao, D.; Hua, J.; Chrostowski, L.; Cheung, K.C. Long-term monitoring in a microfluidic system to study tumour spheroid response to chronic and cycling hypoxia. *Sci. Rep.* **2019**, 9, 17782, doi:10.1038/s41598-019-54001-8.
264. Wang, Q.; Cohen, J.D.; Yukawa, T.; Estrella, H.; Leonard, C.; Nunes, J.; Choi, C.; Lewis, L.; Baker, K.S.; Kuga, K.; et al. Assessment of a 3D neural spheroid model to detect pharmaceutical-induced neurotoxicity. *ALTEX* **2022**, doi:10.14573/altex.2112221.
265. Milestone (1971): President Nixon declares war on cancer. Available online: https://dtp.cancer.gov/timeline/flash/milestones/M4_Nixon.htm (accessed on 9 November 2022).
266. Kopp, S.; Sahana, J.; Islam, T.; Petersen, A.G.; Bauer, J.; Corydon, T.J.; Schulz, H.; Saar, K.; Huebner, N.; Slumstrup, L.; et al. The role of NFκB in spheroid formation of human breast cancer cells cultured on the Random Positioning Machine. *Sci. Rep.* **2018**, 8, 1–17, doi:10.1038/s41598-017-18556-8.
267. Wang, W.; Mani, A.M.; Wu, Z.-H. DNA damage-induced nuclear factor-kappa B activation and its roles in cancer progression. *JCMT* **2017**, 3, 45, doi:10.20517/2394-4722.2017.03.
268. Wang, M.; Zhang, Y.; Xu, Z.; Qian, P.; Sun, W.; Wang, X.; Jian, Z.; Xia, T.; Xu, Y.; Tang, J. RelB sustains endocrine resistant malignancy: an insight of noncanonical NF-κB pathway into breast Cancer progression. *Cell Commun. Signal.* **2020**, 18, 1–17, doi:10.1186/s12964-020-00613-x.
269. Yu, J.; Luo, Y.; Wen, Q. Nalbuphine suppresses breast cancer stem-like properties and epithelial-mesenchymal transition via the AKT-NFκB signaling pathway. *J. Exp. Clin. Cancer Res.* **2019**, 38, 197, doi:10.1186/s13046-019-1184-1.
270. Liu, J.; He, Y.; Zhang, D.; Cai, Y.; Zhang, C.; Zhang, P.; Zhu, H.; Xu, N.; Liang, S. In vitro anticancer effects of two novel phenanthroindolizidine alkaloid compounds on human colon and liver cancer cells. *Mol. Med. Rep.* **2017**, 16, 2595–2603, doi:10.3892/mmr.2017.6879.
271. Kim, C.-H.; Kim, D.-E.; Kim, D.-H.; Min, G.-H.; Park, J.-W.; Kim, Y.-B.; Sung, C.K.; Yim, H. Mitotic protein kinase-driven crosstalk of machineries for mitosis and metastasis. *Exp. Mol. Med.* **2022**, 54, 414–425, doi:10.1038/s12276-022-00750-y.

272. Wang, M.; Feng, R.; Chen, Z.; Shi, W.; Li, C.; Liu, H.; Wu, K.; Li, D.; Li, X. Identification of Cancer-Associated Fibroblast Subtype of Triple-Negative Breast Cancer. *J. Oncol.* **2022**, 2022, 6452636, doi:10.1155/2022/6452636.
273. Kalluri, R.; Zeisberg, M. Fibroblasts in cancer. *Nat. Rev. Cancer* **2006**, 6, 392–401, doi:10.1038/nrc1877.
274. Kauppila, S.; Stenbäck, F.; Risteli, J.; Jukkola, A.; Risteli, L. Aberrant type I and type III collagen gene expression in human breast cancerin vivo. *J. Pathol.* **1998**, 186, 262–268, doi:10.1002/(SICI)1096-9896(1998110)186:3<262:AID-PATH191>3.0.CO;2-3.
275. Li, Q.; Li, M.; Zheng, K.; Tang, S.; Ma, S. Expression pattern analysis and drug differential sensitivity of cancer-associated fibroblasts in triple-negative breast cancer. *Transl. Oncol.* **2021**, 14, 100891, doi:10.1016/j.tranon.2020.100891.
276. Okazaki, M.; Fushida, S.; Tsukada, T.; Kinoshita, J.; Oyama, K.; Miyashita, T.; Ninomiya, I.; Harada, S.; Ohta, T. The effect of HIF-1 α and PKM1 expression on acquisition of chemoresistance. *Cancer Manag. Res.* **2018**, 10, 1865–1874, doi:10.2147/CMAR.S166136.
277. Notte, A.; Ninane, N.; Arnould, T.; Michiels, C. Hypoxia counteracts taxol-induced apoptosis in MDA-MB-231 breast cancer cells: role of autophagy and JNK activation. *Cell Death Dis.* **2013**, 4, e638, doi:10.1038/cddis.2013.167.
278. Wen, J.; Yeo, S.; Wang, C.; Chen, S.; Sun, S.; Haas, M.A.; Tu, W.; Jin, F.; Guan, J.-L. Autophagy inhibition re-sensitizes pulse stimulation-selected paclitaxel-resistant triple negative breast cancer cells to chemotherapy-induced apoptosis. *Breast Cancer Res. Treat.* **2015**, 149, 619–629, doi:10.1007/s10549-015-3283-9.
279. Dhiman, M.; Khanna, A.; Manju, S. A new phenanthroindolizidine alkaloid from *Tylophora indica*. *Chemical Papers* **2013**, 67, 245–248, doi:10.2478/s11696-012-0265-9.
280. Kornienko, A.; Evidente, A.; Vurro, M.; Mathieu, V.; Cimmino, A.; Evidente, M.; van Otterlo, W.A.L.; Dasari, R.; Lefranc, F.; Kiss, R. Toward a Cancer Drug of Fungal Origin. *Med. Res. Rev.* **2015**, 35, 937–967, doi:10.1002/med.21348.
281. Shrivastava, S.; Singh, N.; Sinha, D.; Shrivastava, S.; Kumar, S. Matrix Metalloproteinase-13 (MMP-13): A Novel Tumor Marker for Diagnosis of Breast Carcinoma. *International Journal of Contemporary Medical Research.*
282. Oida, K.; Matsuda, A.; Jung, K.; Xia, Y.; Jang, H.; Amagai, Y.; Ahn, G.; Nishikawa, S.; Ishizaka, S.; Jensen-Jarolim, E.; et al. Nuclear factor- κ B plays a critical role in both intrinsic and acquired resistance against endocrine therapy in human breast cancer cells. *Sci. Rep.* **2014**, 4, 4057, doi:10.1038/srep04057.

283. Li, S.; Pritchard, D.M.; Yu, L.-G. Regulation and Function of Matrix Metalloproteinase-13 in Cancer Progression and Metastasis. *Cancers (Basel)* **2022**, *14*, doi:10.3390/cancers14133263.
284. Su, Y.; Hopfinger, N.R.; Nguyen, T.D.; Pogash, T.J.; Santucci-Pereira, J.; Russo, J. Epigenetic reprogramming of epithelial mesenchymal transition in triple negative breast cancer cells with DNA methyltransferase and histone deacetylase inhibitors. *J. Exp. Clin. Cancer Res.* **2018**, *37*, 314, doi:10.1186/s13046-018-0988-8.
285. Jenke, R.; Reßing, N.; Hansen, F.K.; Aigner, A.; Büch, T. Anticancer Therapy with HDAC Inhibitors: Mechanism-Based Combination Strategies and Future Perspectives. *Cancers (Basel)* **2021**, *13*, doi:10.3390/cancers13040634.
286. Terranova-Barberio, M.; Thomas, S.; Ali, N.; Pawlowska, N.; Park, J.; Krings, G.; Rosenblum, M.D.; Budillon, A.; Munster, P.N. HDAC inhibition potentiates immunotherapy in triple negative breast cancer. *Oncotarget* **2017**, *8*, 114156–114172, doi:10.18632/oncotarget.23169.
287. Lahlou, M. The Success of Natural Products in Drug Discovery. *PP* **2013**, *04*, 17–31, doi:10.4236/pp.2013.43A003.
288. Dewi, C.; Fristiohady, A.; Amalia, R.; Khairul Ikram, N.K.; Ibrahim, S.; Muchtaridi, M. Signaling Pathways and Natural Compounds in Triple-Negative Breast Cancer Cell Line. *Molecules* **2022**, *27*, doi:10.3390/molecules27123661.
289. Zhang, J.; Hansen, L.G.; Gudich, O.; Viehrig, K.; Lassen, L.M.M.; Schrübbers, L.; Adhikari, K.B.; Rubaszka, P.; Carrasquer-Alvarez, E.; Chen, L.; et al. A microbial supply chain for production of the anti-cancer drug vinblastine. *Nature* **2022**, *609*, 341–347, doi:10.1038/s41586-022-05157-3.
290. Wang, R.-B.; Lv, H.-N.; Zhu, S.-S.; Ren, X.-D.; Xu, S.; Ma, S.-G.; Liu, Y.-B.; Qu, J.; Yu, S.-S. A novel and practical synthesis of CAT3: a phenanthroindolizidine alkaloid with potential in treating glioblastoma. *RSC Adv.* **2018**, *8*, 29301–29308, doi:10.1039/c8RA04511A.
291. Jo, Y.-I.; Burke, M.D.; Cheon, C.-H. Modular Syntheses of Phenanthroindolizidine Natural Products. *Org. Lett.* **2019**, *21*, 4201–4204, doi:10.1021/acs.orglett.9b01397.
292. Han, G.; Chen, L.; Wang, Q.; Wu, M.; Liu, Y.; Wang, Q. Design, Synthesis, and Antitobacco Mosaic Virus Activity of Water-Soluble Chiral Quaternary Ammonium Salts of Phenanthroindolizidines Alkaloids. *J. Agric. Food Chem.* **2018**, *66*, 780–788, doi:10.1021/acs.jafc.7b03418.
293. California Institute of Technology. Synthetic Chemistry Takes Anti-Cancer Compounds out of the Sea Slug and into the Lab. Available online: <https://www.caltech.edu/about/news/synthetic-chemistry-takes-anti-cancer-compounds-out-sea-slug-and-lab-85115> (accessed on 28 October 2022).

294. Wang, H.; Li, L.; Ye, J.; Dong, W.; Zhang, X.; Xu, Y.; Hu, J.; Wang, R.; Xia, X.; Yang, Y.; et al. Improved Safety and Anti-Glioblastoma Efficacy of CAT3-Encapsulated SMEDDS through Metabolism Modification. *Molecules* **2021**, *26*, doi:10.3390/molecules26020484.
295. Kwon, Y.; Song, J.; Lee, H.; Kim, E.-Y.; Lee, K.; Lee, S.K.; Kim, S. Design, Synthesis, and Biological Activity of Sulfonamide Analogues of Antofine and Cryptopleurine as Potent and Orally Active Antitumor Agents. *J. Med. Chem.* **2015**, *58*, 7749–7762, doi:10.1021/acs.jmedchem.5b00764.
296. Briolay, T.; Petithomme, T.; Fouet, M.; Nguyen-Pham, N.; Blanquart, C.; Boisgerault, N. Delivery of cancer therapies by synthetic and bio-inspired nanovectors. *Mol. Cancer* **2021**, *20*, 55, doi:10.1186/s12943-021-01346-2.
297. Yap, K.M.; Sekar, M.; Fuloria, S.; Wu, Y.S.; Gan, S.H.; Mat Rani, N.N.I.; Subramaniam, V.; Kokare, C.; Lum, P.T.; Begum, M.Y.; et al. Drug Delivery of Natural Products Through Nanocarriers for Effective Breast Cancer Therapy: A Comprehensive Review of Literature. *Int. J. Nanomedicine* **2021**, *16*, 7891–7941, doi:10.2147/IJN.S328135.
298. Gane, P.J.; Dean, P.M. Recent advances in structure-based rational drug design. *Current Opinion in Structural Biology* **2000**, *10*, 401–404, doi:10.1016/s0959-440x(00)00105-6.
299. Liu, J.; Ming, B.; Gong, G.-H.; Di Wang; Bao, G.-L.; Yu, L.-J. Current research on anti-breast cancer synthetic compounds. *RSC Adv.* **2018**, *8*, 4386–4416, doi:10.1039/C7RA12912B.
300. The American Cancer Society Medical and Editorial Content Team. Treatment of Triple-negative Breast Cancer. Available online: <https://www.cancer.org/cancer/breast-cancer/treatment/treatment-of-triple-negative.html> (accessed on 26 October 2022).
301. Nonneville, A. de; Goncalves, A.; Mamessier, E.; Bertucci, F. Sacituzumab govitecan in triple-negative breast cancer. *Ann Transl Med* **2022**, *10*, 647, doi:10.21037/atm-22-813.
302. Hossain, F.; Majumder, S.; David, J.; Miele, L. Precision Medicine and Triple-Negative Breast Cancer: Current Landscape and Future Directions. *Cancers (Basel)* **2021**, *13*, doi:10.3390/cancers13153739.
303. Wagner, J.; Rapsomaniki, M.A.; Chevrier, S.; Anzeneder, T.; Langwieder, C.; Dykgers, A.; Rees, M.; Ramaswamy, A.; Muenst, S.; Soysal, S.D.; et al. A Single-Cell Atlas of the Tumor and Immune Ecosystem of Human Breast Cancer. *Cell* **2019**, *177*, 1330-1345.e18, doi:10.1016/j.cell.2019.03.005.

304. Huertas-Caro, C.A.; Ramirez, M.A.; Gonzalez-Torres, H.J.; Sanabria-Salas, M.C.; Serrano-Gómez, S.J. Immune Lymphocyte Infiltrate and its Prognostic Value in Triple-Negative Breast Cancer. *Front. Oncol.* **2022**, *12*, 910976, doi:10.3389/fonc.2022.910976.
305. Li, Y.; Zhan, Z.; Yin, X.; Fu, S.; Deng, X. Targeted Therapeutic Strategies for Triple-Negative Breast Cancer. *Front. Oncol.* **2021**, *11*, 731535, doi:10.3389/fonc.2021.731535.
306. Li, Y.; Zhang, H.; Merkhher, Y.; Chen, L.; Liu, N.; Leonov, S.; Chen, Y. Recent advances in therapeutic strategies for triple-negative breast cancer. *J. Hematol. Oncol.* **2022**, *15*, 121, doi:10.1186/s13045-022-01341-0.
307. Nguyen, C.D.K.; Yi, C. YAP/TAZ Signaling and Resistance to Cancer Therapy. *Trends Cancer* **2019**, *5*, 283–296, doi:10.1016/j.trecan.2019.02.010.
308. Song, H.; Wu, T.; Xie, D.; Li, D.; Hua, K.; Hu, J.; Fang, L. WBP2 Downregulation Inhibits Proliferation by Blocking YAP Transcription and the EGFR/PI3K/Akt Signaling Pathway in Triple Negative Breast Cancer. *Cell. Physiol. Biochem.* **2018**, *48*, 1968–1982, doi:10.1159/000492520.
309. Guestini, F.; McNamara, K.M.; Sasano, H. The use of chemosensitizers to enhance the response to conventional therapy in triple-negative breast cancer patients. *Breast Cancer Management* **2017**, *6*, 127–131, doi:10.2217/bmt-2017-0030.
310. Asif, P.J.; Longobardi, C.; Hahne, M.; Medema, J.P. The Role of Cancer-Associated Fibroblasts in Cancer Invasion and Metastasis. *Cancers (Basel)* **2021**, *13*, doi:10.3390/cancers13184720.
311. Gelao, L.; Criscitiello, C.; Esposito, A.; Laurentiis, M. de; Fumagalli, L.; Locatelli, M.A.; Minchella, I.; Santangelo, M.; Placido, S. de; Goldhirsch, A.; et al. Dendritic cell-based vaccines: clinical applications in breast cancer. *Immunotherapy* **2014**, *6*, 349–360, doi:10.2217/imt.13.169.
312. Alard, E.; Butnariu, A.-B.; Grillo, M.; Kirkham, C.; Zinovkin, D.A.; Newnham, L.; Macciochi, J.; Pranjol, M.Z.I. Advances in Anti-Cancer Immunotherapy: Car-T Cell, Checkpoint Inhibitors, Dendritic Cell Vaccines, and Oncolytic Viruses, and Emerging Cellular and Molecular Targets. *Cancers (Basel)* **2020**, *12*, doi:10.3390/cancers12071826.
313. Johns Hopkins Pathology. Staging & Grade - Breast Pathology. Available online: <https://pathology.jhu.edu/breast/staging-grade/> (accessed on 1 November 2022).
314. Mary E. Endress and Peter V. Bruyns. A revised classification of the Apocynaceae s.l. **2000**, 66.
315. A. Bashir, N. Ali, S. Bashir, M. Choudhary. Biological activities of aerial parts of *Tylophora hirsuta* Wall. *African Journal of Biotechnology* **2009**, *8*, 4627–4631.

316. Islam, M.T.; Sarkar, C.; El-Kersh, D.M.; Jamaddar, S.; Uddin, S.J.; Shilpi, J.A.; Mubarak, M.S. Natural products and their derivatives against coronavirus: A review of the non-clinical and pre-clinical data. *Phytother. Res.* **2020**, *34*, 2471–2492, doi:10.1002/ptr.6700.
317. Michael, J.P. Indolizidine and quinolizidine alkaloids. *Nat. Prod. Rep.* **2008**, *25*, 139–165, doi:10.1039/b612166g.
318. Kubo, M.; Yatsuzuka, W.; Matsushima, S.; Harada, K.; Inoue, Y.; Miyamoto, H.; Matsumoto, M.; Fukuyama, Y. Antimalarial Phenanthroindolizine Alkaloids from *Ficus septica*. *Chem. Pharm. Bull. (Tokyo)* **2016**, *64*, 957–960, doi:10.1248/cpb.c16-00181.
319. THAILAND NATURE PROJECT. *Ideopsis similis persimilis* species page. Available online: <https://www.thailandnatureproject.com/ideopsis-similis-persimilis.html> (accessed on 27 September 2022).
320. Komatsu, H.; Watanabe, M.; Ohyama, M.; Enya, T.; Koyama, K.; Kanazawa, T.; Kawahara, N.; Sugimura, T.; Wakabayashi, K. Phenanthroindolizidine alkaloids as cytotoxic substances in a Danaid butterfly, *Ideopsis similis*, against human cancer cells. *J. Med. Chem.* **2001**, *44*, 1833–1836, doi:10.1021/jm0004042.
321. Reddy, B.K.; Balaji, M.; Reddy, P.U.; Sailaja, G.; Vaidyanath, K.; Narasimha, G. Antifeedant and antimicrobial activity of *Tylophora indica*. *International Scholars Journals* **2009**.
322. Ge, Y.; Liu, P.; Yang, R.; Zhang, L.; Chen, H.; Camara, I.; Liu, Y.; Shi, W. Insecticidal Constituents and Activity of Alkaloids from *Cynanchum mongolicum*. *Molecules* **2015**, *20*, 17483–17492, doi:10.3390/molecules200917483.
323. Jang, E.J.; Kim, H.K.; Jeong, H.; Lee, Y.S.; Jeong, M.G.; Bae, S.J.; Kim, S.; Lee, S.K.; Hwang, E.S. Anti-adipogenic activity of the naturally occurring phenanthroindolizidine alkaloid antofine via direct suppression of PPAR γ expression. *Chem. Biodivers.* **2014**, *11*, 962–969, doi:10.1002/cbdv.201300365.
324. Raina, V.; Raina, S. The Responsiveness of Leukocyte Adenyl Cyclase to Tylophorine in Asthmatic Subjects. *Biochemical and Biophysical Research Communications* **1980**, 1074–1077.
325. Dhiman, M.; Parab, R.R.; Manju, S.L.; Desai, D.C.; Mahajan, G.B. Antifungal Activity of Hydrochloride Salts of Tylophorinidine and Tylophorinine. *Nat. Prod. Commun.* **2012**, *7*, 1934578X1200700, doi:10.1177/1934578X1200700916.
326. Yang, C.-W.; Lee, Y.-Z.; Hsu, H.-Y.; Shih, C.; Chao, Y.-S.; Chang, H.-Y.; Lee, S.-J. Targeting Coronaviral Replication and Cellular JAK2 Mediated Dominant NF- κ B Activation for Comprehensive and Ultimate Inhibition of Coronaviral Activity. *Sci. Rep.* **2017**, *7*, 4105, doi:10.1038/s41598-017-04203-9.

327. Nguyen, L.P.; Park, C.; Luong, T.T.D.; Park, E.-M.; Choi, D.-H.; Han, K.M.; Mai, H.N.; Nguyen, H.C.; Lim, Y.-S.; Hwang, S.B. 5-Oxo-1-(2,3,6,7-tetramethoxy-9-phenanthrenyl)methyl-L-proline Inhibits Hepatitis C Virus Entry. *Sci. Rep.* **2019**, *9*, 7288, doi:10.1038/s41598-019-43783-6.
328. Honda, K.; & Ocirmura, H.; Hayashi, N.; Abe, F.; Yamauchi, T. Oviposition-stimulatory activity of phenanthroindolizidine alkaloids of host-plant origin to a danaid butterfly, *Ideopsis similis*. *Physiological Entomology* **2001**, *26*, 6–10, doi:10.1111/j.1365-3032.2001.00208.x.
329. Yang, C.-W.; Chen, W.-L.; Wu, P.-L.; Tseng, H.-Y.; Lee, S.-J. Anti-inflammatory mechanisms of phenanthroindolizidine alkaloids. *Mol. Pharmacol.* **2006**, *69*, 749–758, doi:10.1124/mol.105.017764.
330. Oh, J.; Kim, G.D.; Kim, S.; Lee, S.K. Antofine, a natural phenanthroindolizidine alkaloid, suppresses angiogenesis via regulation of AKT/mTOR and AMPK pathway in endothelial cells and endothelial progenitor cells derived from mouse embryonic stem cells. *Food Chem. Toxicol.* **2017**, *107*, 201–207, doi:10.1016/j.fct.2017.06.036.
331. Gao, W.; Lam, W.; Zhong, S.; Kaczmarek, C.; Baker, D.C.; Cheng, Y.-C. Novel mode of action of tylophorine analogs as antitumor compounds. *Cancer Res.* **2004**, *64*, 678–688, doi:10.1158/0008-5472.can-03-1904.
332. Qiu, Y.-Q.; Yang, C.-W.; Lee, Y.-Z.; Yang, R.-B.; Lee, C.-H.; Hsu, H.-Y.; Chang, C.-C.; Lee, S.-J. Targeting a ribonucleoprotein complex containing the caprin-1 protein and the c-Myc mRNA suppresses tumor growth in mice: an identification of a novel oncotarget. *Oncotarget* **2015**, *6*, 2148–2163, doi:10.18632/oncotarget.3236.

6 Appendix

6.1 Supplementary figures

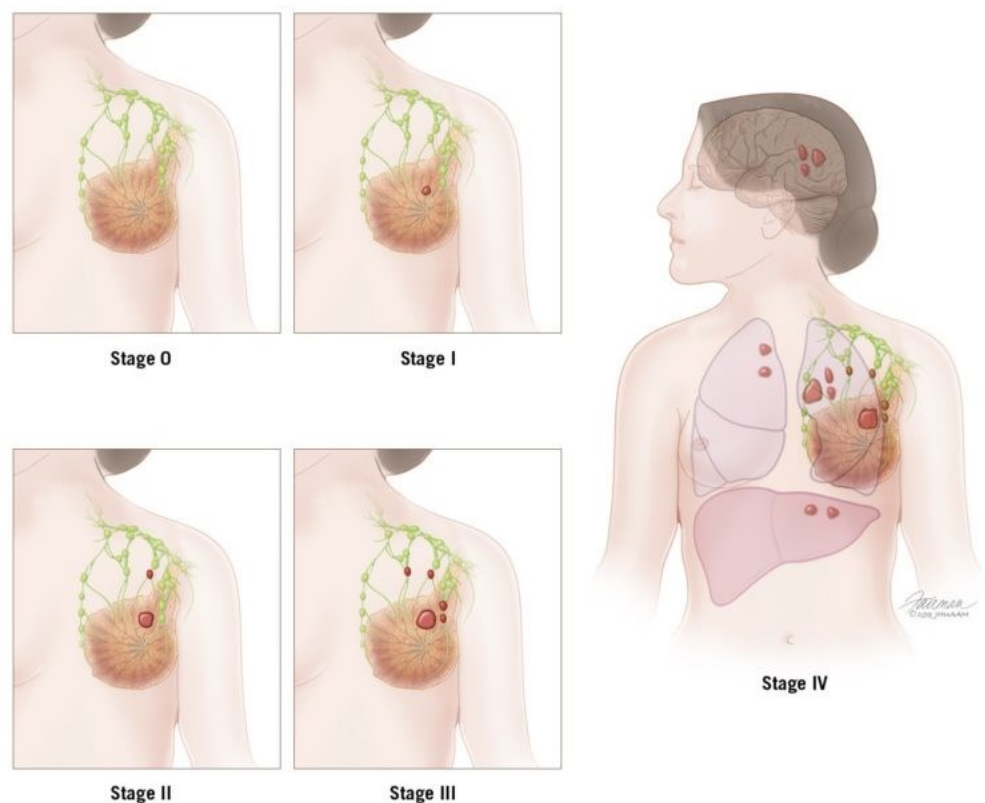
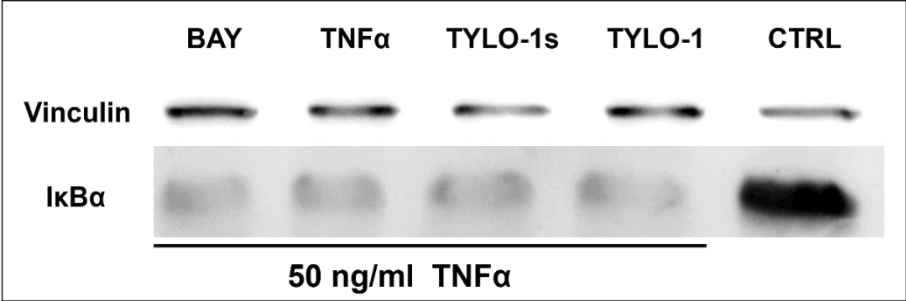
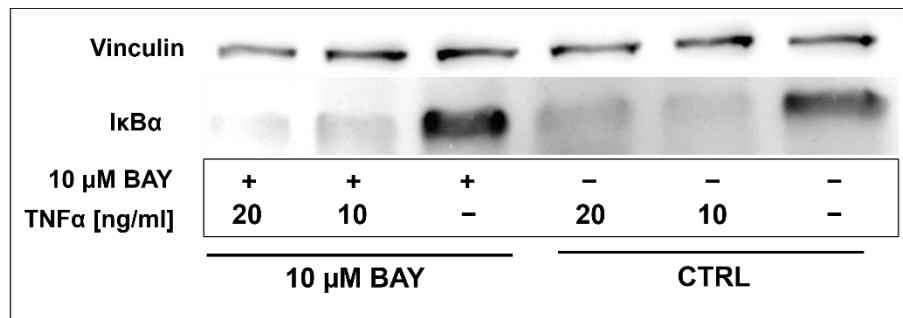


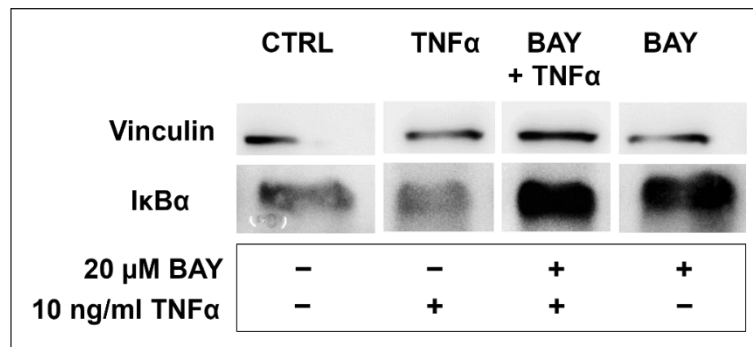
Figure S 1 BC staging. Tumours (red) are depicted in the breast tissue, as well as metastasis within the torso or to the brain. Illustration from Johns Hopkins University (medicine and pathology) [313].



(a)

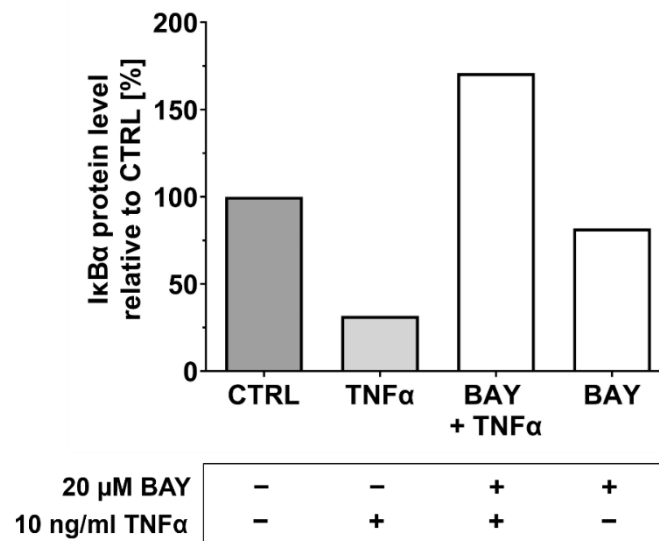


(b)



(c)

BAY 11-7085



(d)

Figure S 2 Optimizing the balance of the NFκB-agonist and antagonist in MB-231. On a 6-well plate, 2.5×10^5 MB-231 cells were seeded and allowed to attach for 48 h. **(a-c)** Western blot with protein lysates that are immunologically stained for IκBα (39 kDa) and the housekeeper protein vinculin (124 kDa). **(a)** Cells were left untreated (CTRL) and pre-incubated for 1 h with 10 nM TYLO-1s, 10 nM TYLO-1 or 10 μM Bay 11-7985 (BAY) before incubation with 50 ng/ml TNFα for 30 min. Anti-inflammatory compounds not impact IκBα degradation. **(b)** Concentration of the NFκB agonist, TNFα, was decreased. Cells were left untreated or treated with 10 μM Bay 11-7985 (BAY) for 1 h before incubated for 30 min

with 10 or 20 ng/ml TNF α . **(c,d)** Concentration of the NF κ B antagonist, BAY, was increased. Cells were left untreated (CTRL), stimulated with solely 10 ng/ml TNF α for 30 min (TNF α) or pre-treated for 1 h with 20 μ M BAY before stimulation with 10 ng/ml TNF α for 30 min. **(d)** Normalized I κ B α protein level is displayed relative to CTRL. Bars represent one independent experiment.

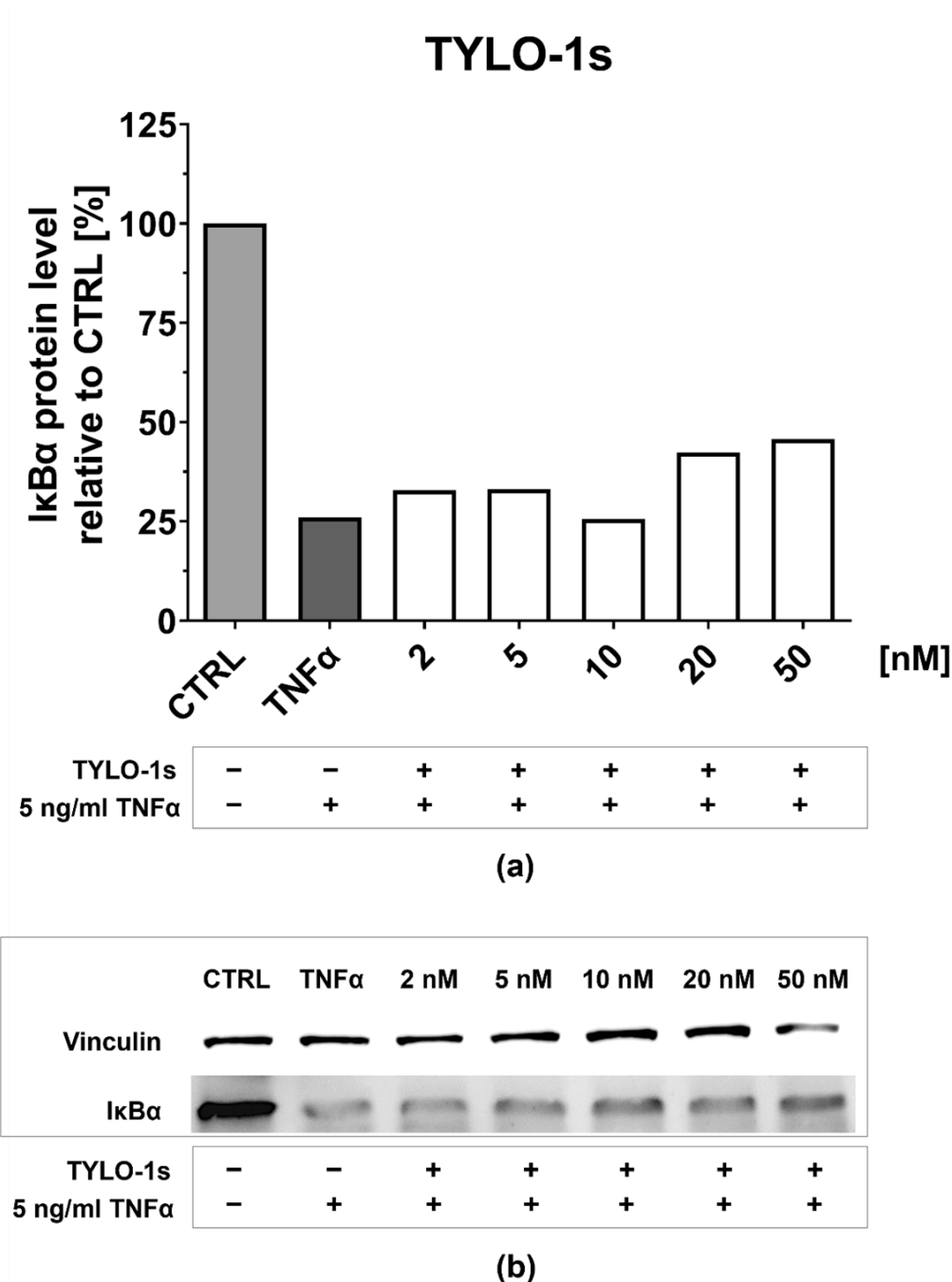


Figure S 3 TYLO-1s moderately stabilized I κ B α in MB-231. Cells were left untreated (CTRL), stimulated with solely 5 ng/ml TNF α for 30 min (TNF α) or pre-incubated with TYLO-1s at the indicated concentration for 1 h before stimulation with 5 ng/ml TNF α for 30 min. **(a)** Normalized I κ B α protein level is displayed relative to CTRL. Bars represent one

independent experiment. **(b)** Representative western blot with protein lysates that are immunologically stained for I κ B α (39 kDa) and the housekeeper protein vinculin (124 kDa).

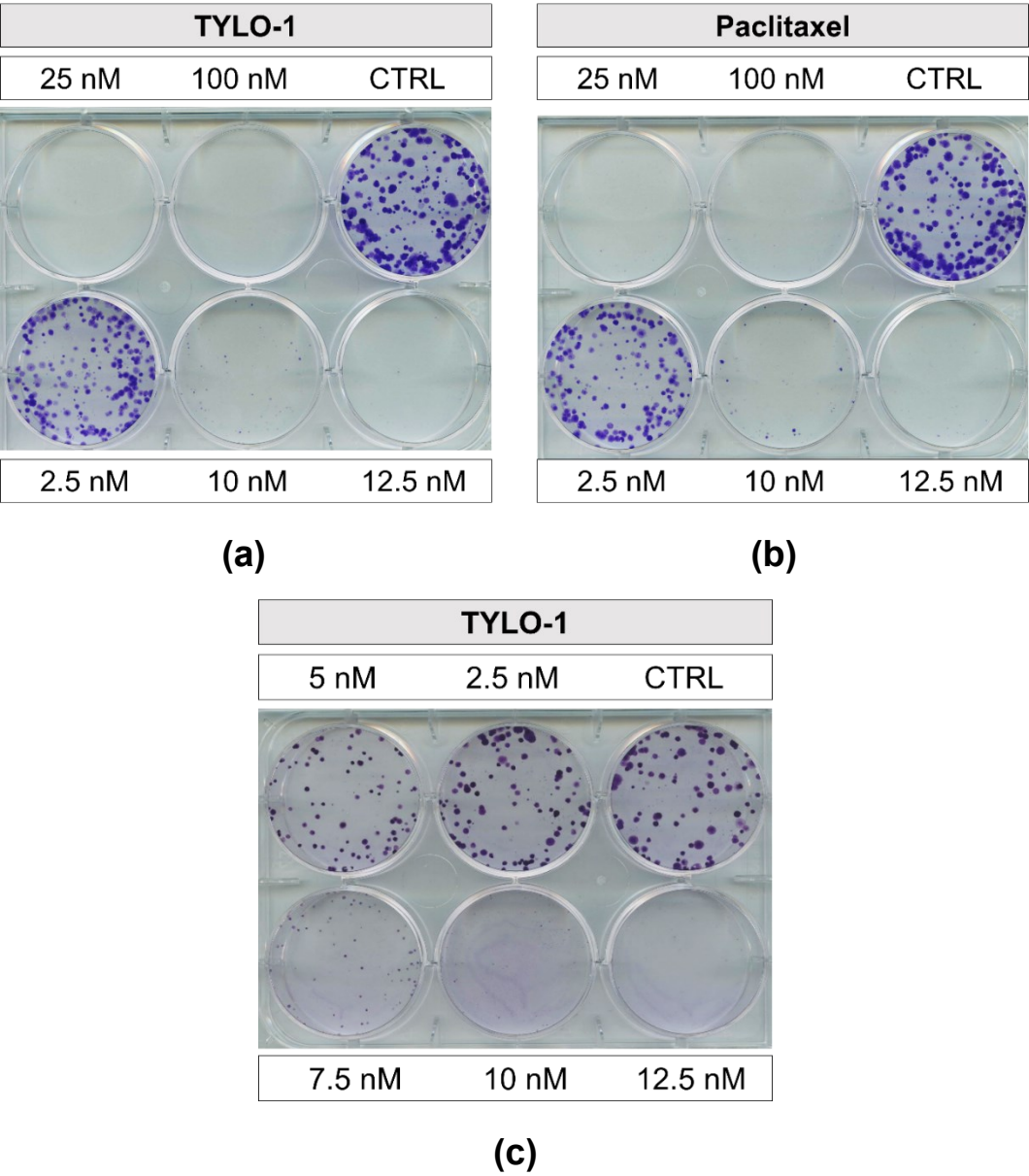


Figure S 4 TYLO-1 and paclitaxel suppressed colony formation of murine D2A1 cells. Cells were treated for 10 days with **(a, c)** TYLO-1 or **(b)** paclitaxel at the indicated concentration. The area of cells was visualized by crystal violet staining according to the colony formation assay.

24 h

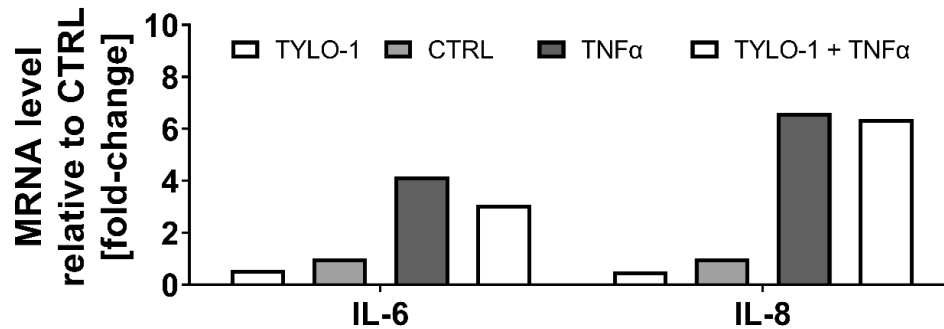
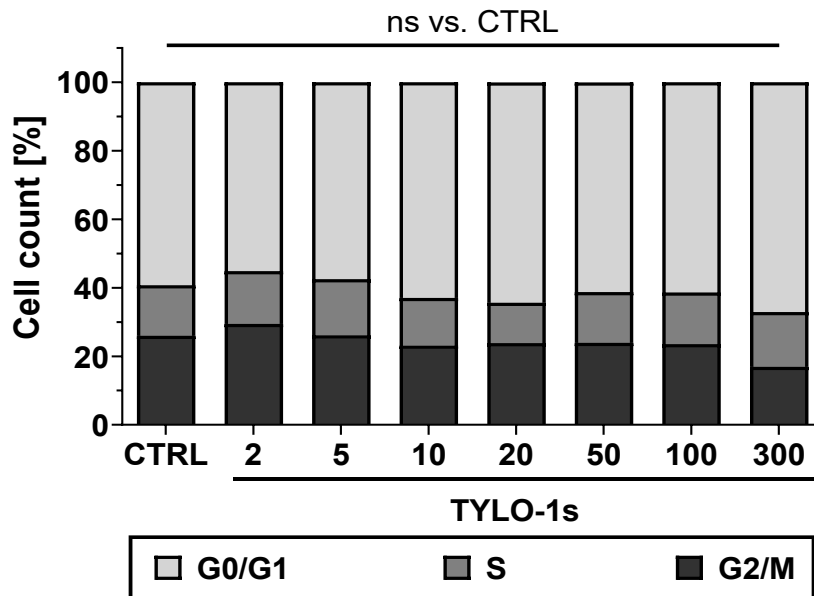


Figure S 5 TYLO-1 reduced TNFα-induced expression of IL-6 but not IL-8. Per well, 3×10^5 MB-231 cells were seeded. Before treatment, cells were allowed to attach for 72 h, which is equivalent to the treatment course of knockdown studies. Cells were pre-incubated for 20 min with 7 nM TYLO-1 before stimulated with 20 ng/ml TNFα. Untreated (CTRL) or TNFα stimulated cells (TNFα) served as control. Expression of IL-6 or IL-8 was quantified 24 h post-stimulation with RT-qPCR. Based on the 2- $\delta\delta$ CT method, fold-change in cytokine expression was calculated by initial normalization to the housekeeping gene GAPDH and following normalization to CTRL (which was set to 1).

24 h



(a)

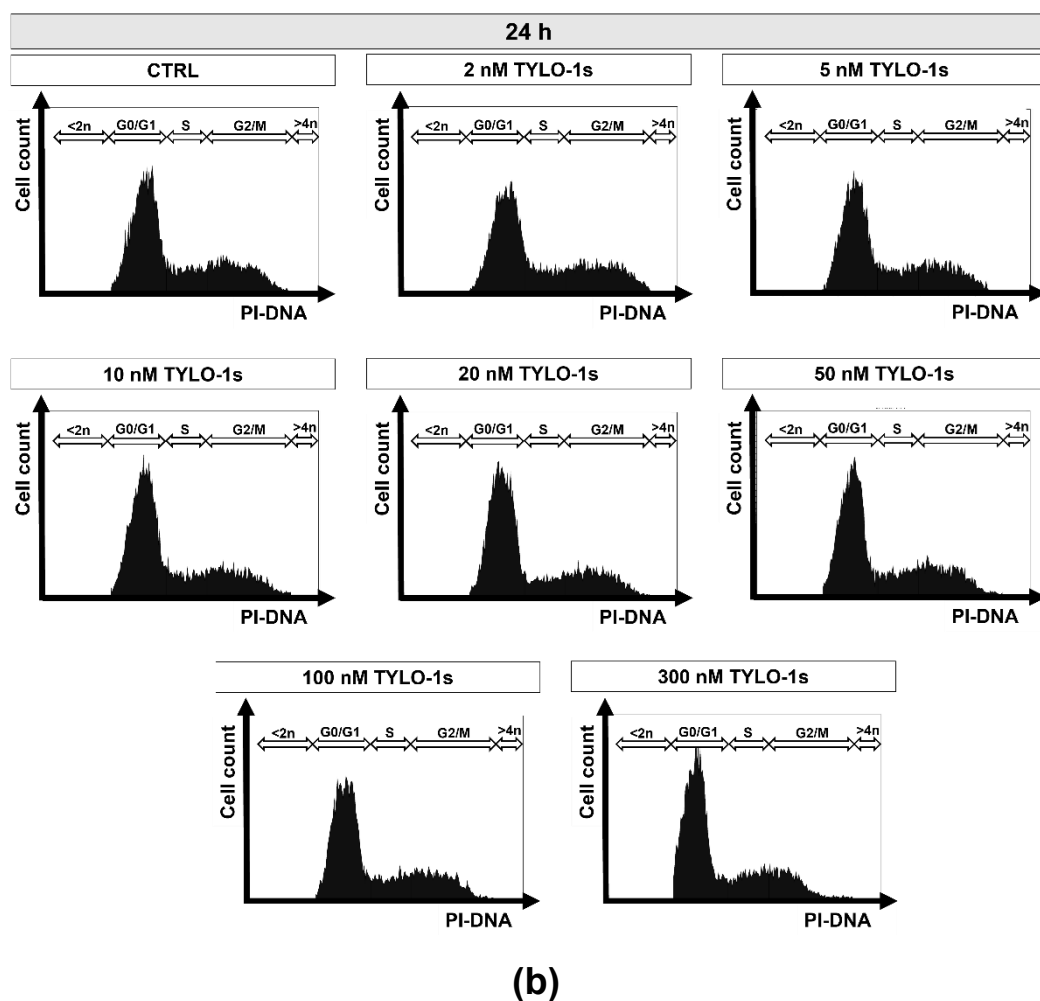
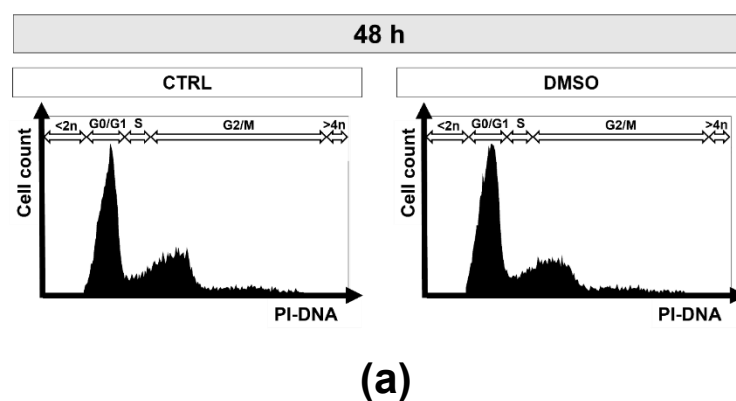
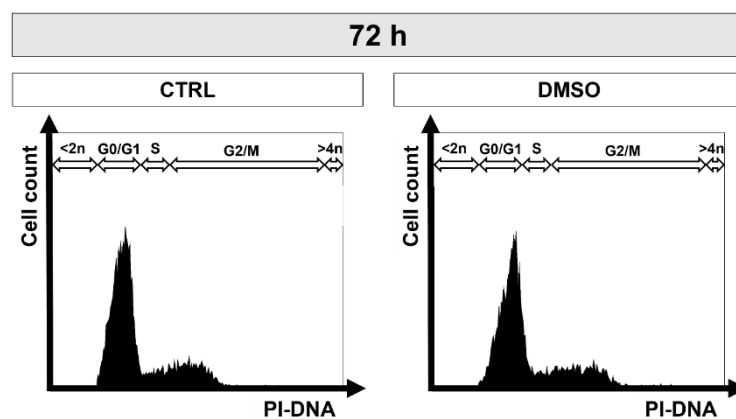


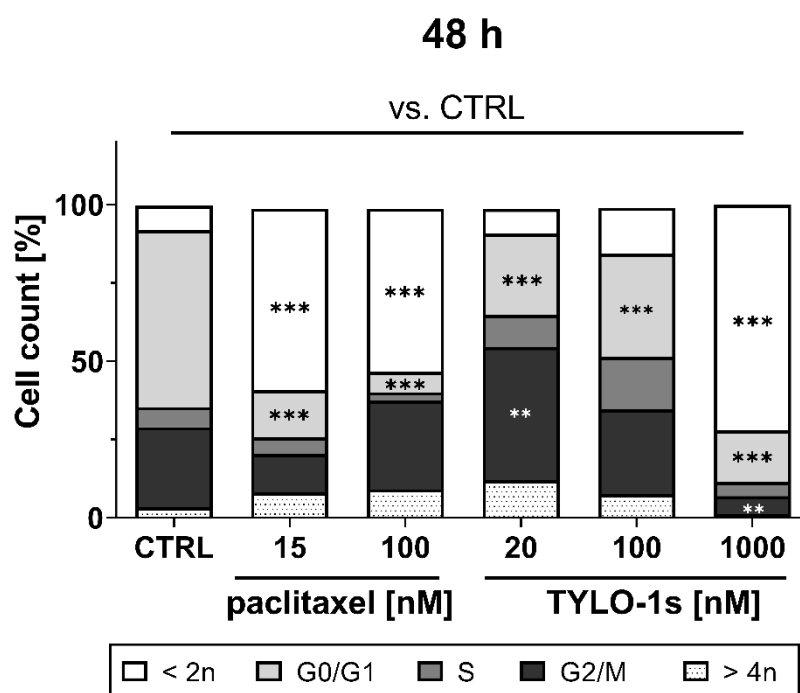
Figure S 6 TYLO-1s did not modulate the cell cycle state in MB-231 within 24 h. Cells were left untreated (CTRL) or treated for 24 h with TYLO-1s at the indicated concentration. Cell cycle phase population (G0/G1; S; G2/M) was determined based on the signal of the PI-DNA complex using CytExpert. **(a)** Stacked bars represent one independent experiment. **(b)** Histograms depicting the cell count within the PI-signal were illustrated with CytExpert.



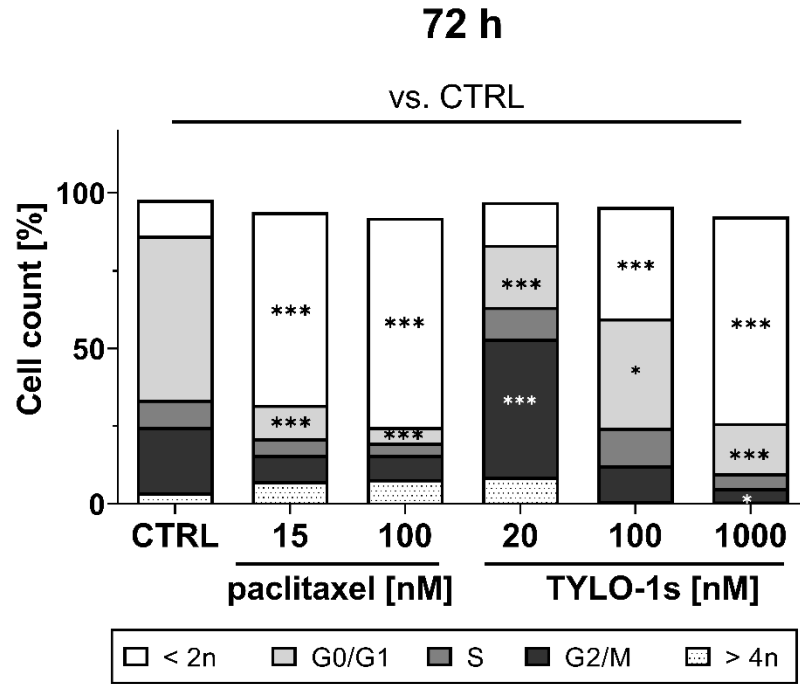


(b)

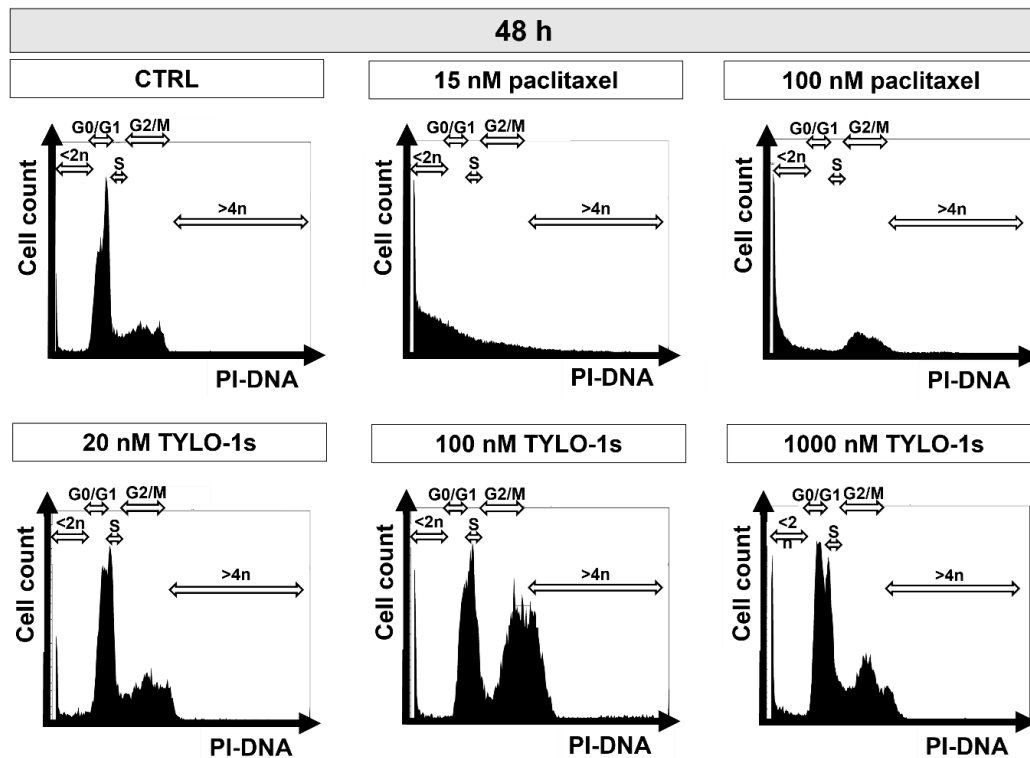
Figure S 7 DMSO did not modulate the cell cycle state. MB-231 cells were left untreated (CTRL) or treated for a maximum of 72 h with the highest DMSO applied in compound treatment (which is 0.01% DMSO). Cell cycle phase population (G0/G1; S; G2/M) was determined based on the signal of the PI-DNA complex using CytExpert. Histograms depicting the cell count within the PI-signal were illustrated with CytExpert.



(a)



(b)



(c)

Figure S 8 Paclitaxel and TYLO-1s increased DNA fragmentation in MB-468-UnaG. Cells were left untreated (CTRL) or treated for (a,c) 48 h or (b) 72 h with paclitaxel or TYLO-1s at the indicated concentration. Cell cycle phase population (sub-G0/G1; G0/G1; S; G2/M, hyperplaid cells) was determined in recorded single cells events based on the signal of the PI-DNA complex using CytExpert. (a, b) Stacked bars represent the mean ($n=3$).

Statistical difference vs. CTRL was calculated with two-way-ANOVA (* $p < 0.05$, ** $p < 0.01$, *** $p < 0.001$). (c) Representative histograms depicting the cell count within the PI-DNA signal were illustrated with CytExpert. Illustration from Reimche *et al.* 2022 [187].

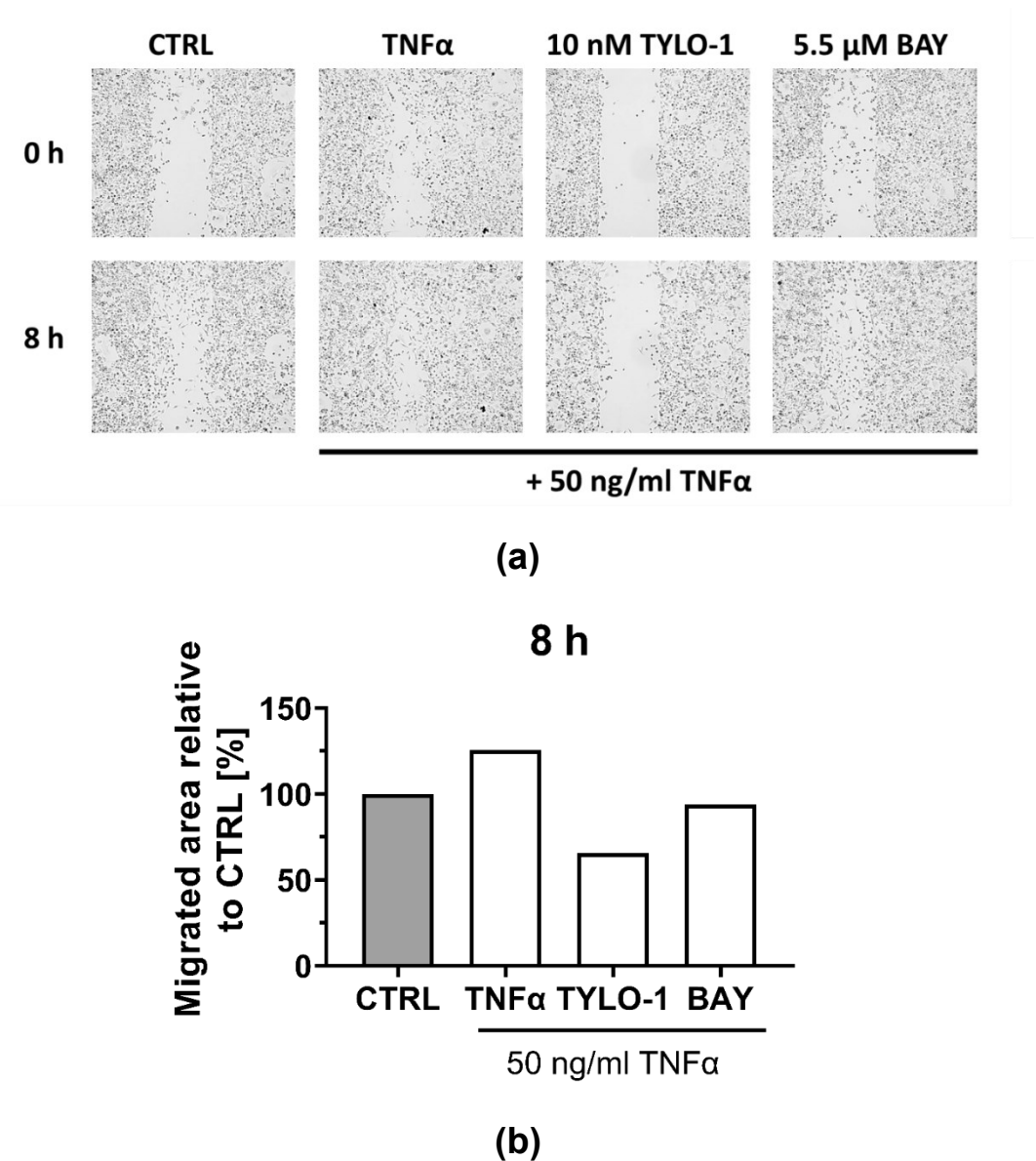
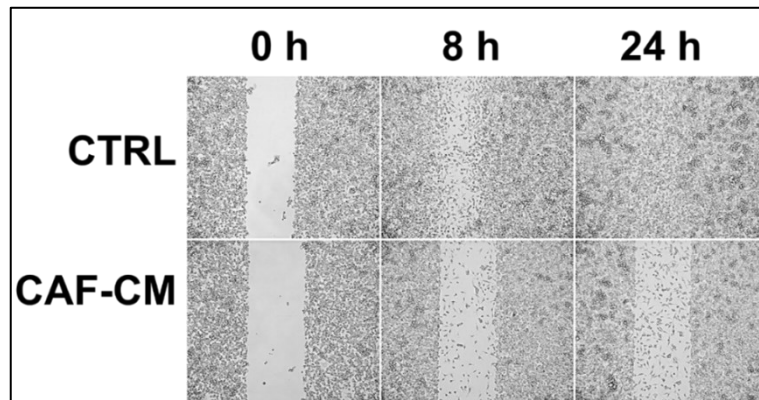
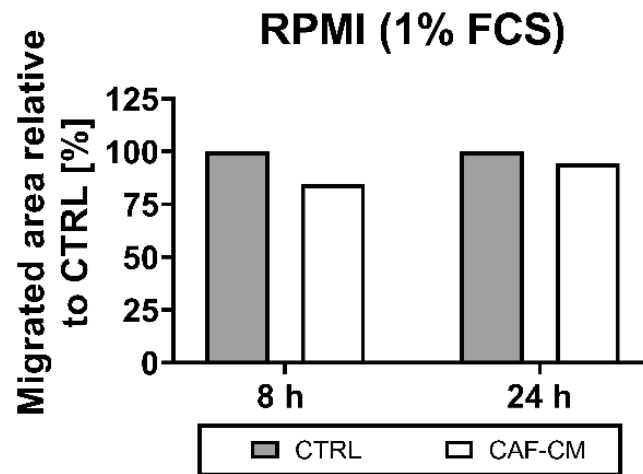


Figure S 9 TYLO-1 blocked TNFα-induced migration of MB-231. Two monolayer cells were generated by physical exclusion. Cells were pre-treated for 20 min in serum-reduced medium (1% FCS) containing 10 nM TYLO-1 or 5.5 μM BAY 11-7085 (BAY). Subsequently, cells were stimulated with 50 ng/ml TNFα for 8 h. Untreated (CTRL) or TNFα stimulated cells (TNFα) served as control. (a) Brightfield images of the migration gap before and post-treatment. Magnification: 100×. (b) The area of migrated cells was quantified based on the reduction of the cell free area within the migration gap. The cell free area was determined in microscopic images using CellPathfinder and normalized to the CTRL group post-treatment (CTRL; which was set to 100%). Bars represents the mean of one independent experiments.



(a)



(b)

Figure S 10 CAF-conditioned medium decreases TNBC migration. CAF-CM was collected from CAFs grown for 24 h in serum-reduced RPMI medium (1% FCS). Two MB-231 monolayer cells were incubated with (CAF-CM) or without (CTRL) CAF-CM. **(a)** The migration gap was imaged before and post-stimulation. Magnification: 100×. **(b)** The area of migrated cells was quantified based on the reduction of the cell free area within the migration gap. The cell free area was determined in microscopic images using CellPathfinder and normalized to the untreated group post-treatment (CTRL, 100%). Each column represents the mean of one independent experiment.

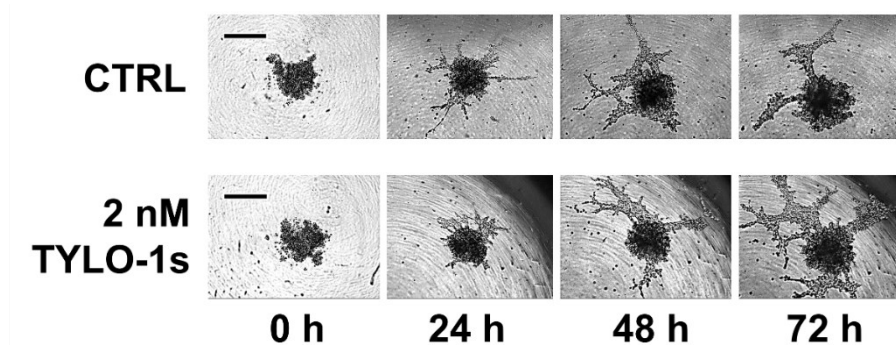


Figure S 11 Low concentration of TYLO-1s did not impact TNBC monoculture spheroid invasion. Monoculture spheroids of MB-231 were formed for 72 h before matrigel® was applied for ECM formation. Spheroids were treated for further 72 h without (CTRL) or with 2 nM TYLO-1s. Representative brightfield images. Scale bar: 500 μ m.

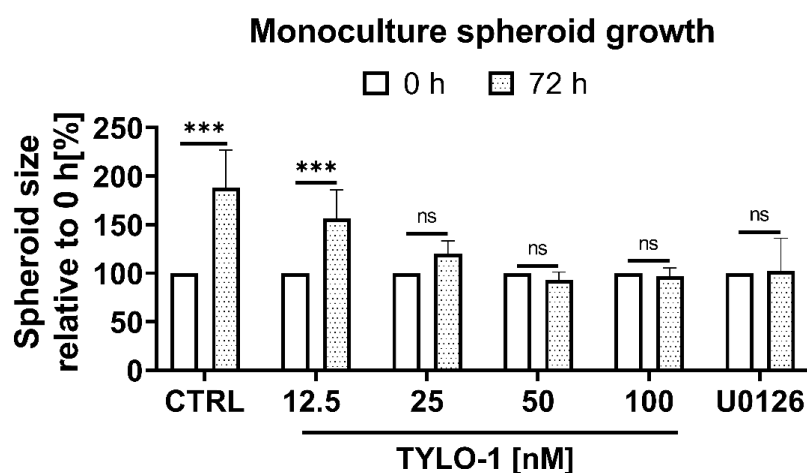


Figure S 12 Dose-dependent monoculture spheroid growth blockade by TYLO-1. Monoculture spheroids composed of MB-231 cells were formed for 72 h in 2.5% matrigel®. Spheroids were left untreated (CTRL), treated for 72 h with 10 μ M U0126 or TYLO-1 at 12.5 nM, 25 nM, 50 nM and 100 nM. Spheroid size was determined pre-treatment (0 h) and post-treatment (72 h) based on the spheroid area that was measured in the brightfield images. In each independent experiment, the spheroid size was normalized to the spheroid area at 0 h (which was set to 100%). Bars represent the mean of at least three independent experiments \pm SD. Statistical difference vs. 0 h was calculated with one-way ANOVA using Šidák's multiple comparison test (ns = not significant, *** $p < 0.001$).

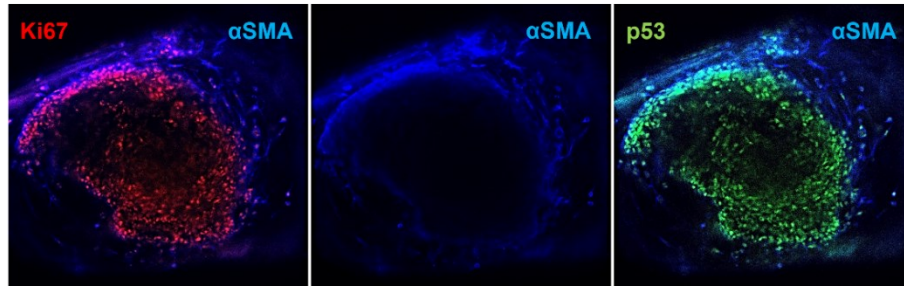


Figure S 13 Cell type identification in TNBC co-culture spheroids. Co-culture spheroids were formed for 144 h with seeding 3000 cells (MB-231:CAF, 1:2) in a total of 0.05 mg/ml collagen type I. Fluorescence was recorded after immunologically staining for Ki67 (red, MB-231), p53 (green, MB-231) and αSMA (blue, CAFs). Representative digital cross section of the spheroids. Magnification: 200×.

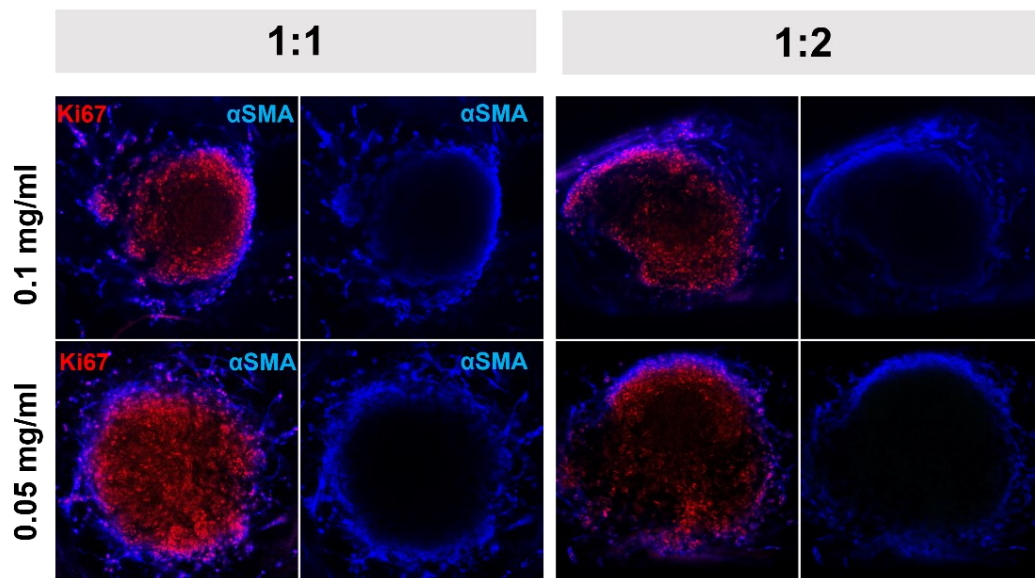


Figure S 14 CAFs encompass the core of tumour cells within the spheroids. Co-culture spheroids were formed for 144 h with seeding 3000 cells (MB-231:CAF, 1:1 or 1:2) in a total of 0.05 mg/ml or 0.1 mg/ml collagen type I. Fluorescence was recorded after immunologically staining for Ki67 (red, MB-231) and αSMA (blue, CAFs). Representative digital cross section of the spheroids. Magnification: 200×.

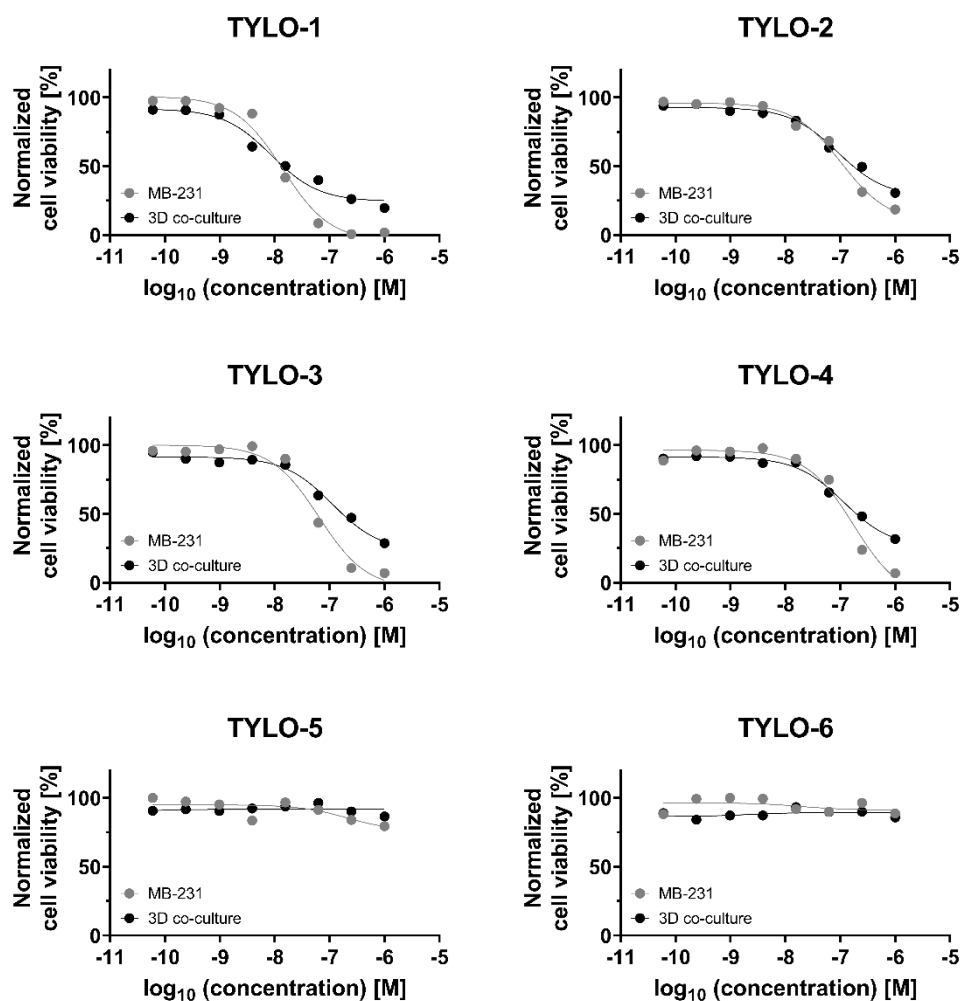
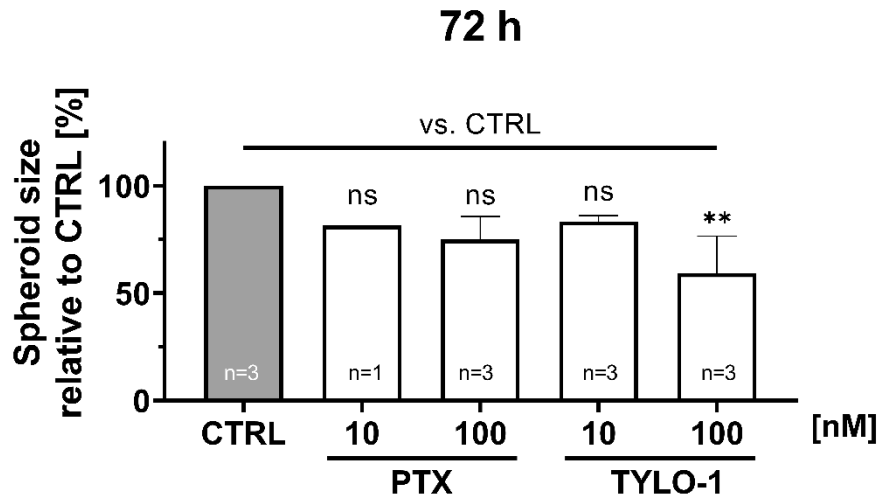
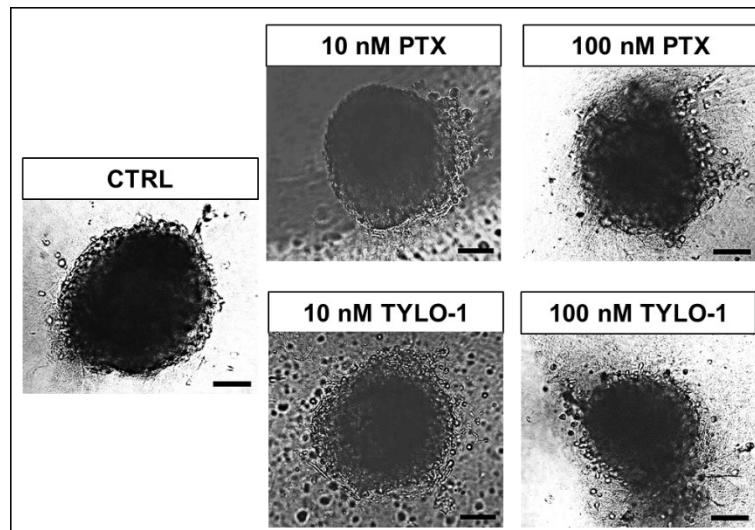


Figure S 15 Decreased cell viability of co-culture spheroids by TYLO-1 treatment correlates with bioactivity in MB-231. MB-231 cells were seeded at a high cell density and cell viability-dependent fluorescence [RFU] was determined 24 h post-treatment according to the 2D PrestoBlue (grey data points). Co-culture spheroids were formed for 72 h and treated for 72 h. Cell viability-dependent luminescence [RLU] was determined and 72 h post-treatment according to the 3D CellTiterGlo (black data points). P-alkaloids were applied at a four-fold serial dilution in the concentration from 1000 nM to 0.06 nM. Untreated cells and spheroids or treatment with 20 μ M of cytotoxic staurosporine served as control. In each independent experiment, fluorescence or luminescence was normalized to the smallest value (which was set to 0%) and to the highest value (which was set to 100%) (normalized cell viability). Data points represent the mean ($n=3$). Data points for TYLO-5 and TYLO-6 in MB-231 monolayer represent one individual experiment.



(a)



(b)

Figure S 16 Dose-dependent co-culture spheroid growth blockade by TYLO-1. Co-culture spheroids of a total of 3000 cells (MB-231:CAFs, 1:2) were formed for 72 h in 0.05 mg/ml collagen type I. Spheroids were treated for further 72 h TYLO-1 or paclitaxel (PTX) at a concentration of 10 nM and 100 nM. Co-culture medium served as untreated control (CTRL). **(a)** Spheroid size was determined 72 h-post-treatment based on the spheroid area that was measured in the brightfield images of at least three spheroids per treatment group. In each independent experiment, average spheroid size of the treatment group was compared to the average spheroid size of the CTRL group (which was set to 100%). Bars represent the mean of at least one independent experiment \pm SD. Statistical difference vs. CTRL was calculated with one-way-ANOVA (ns = not significant, ** $p < 0.01$). **(b)** Representative brightfield images 72 h post-treatment. Scale bar: 200 μ m.

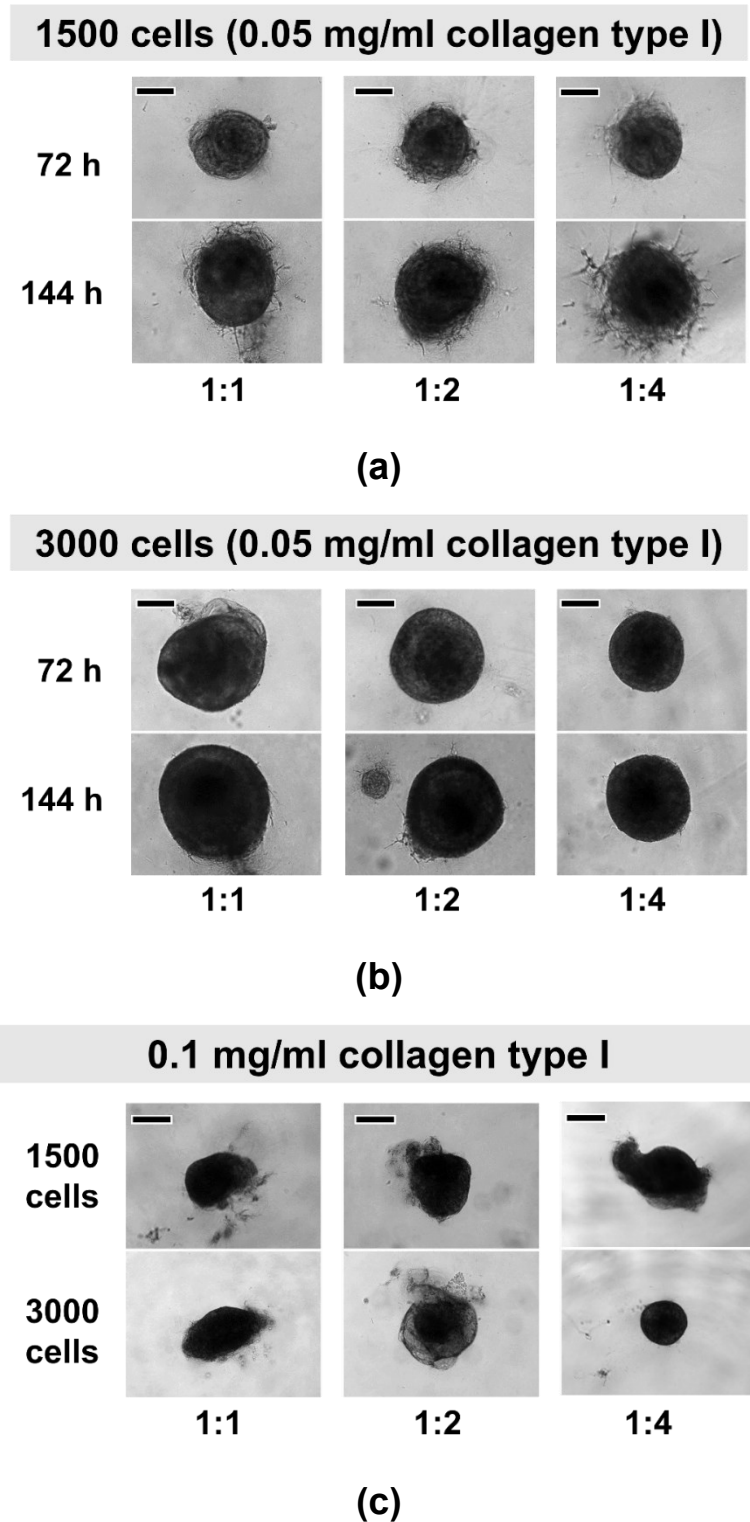


Figure S 17 Co-culture spheroids (MB-468-UnaG:CAF) at various culture conditions. Co-culture spheroids were composed at different cell type ratios of MB-468-UnaG:CAFs (1:1, 1:2 and 1:4) with a seeding cell number of a total of **(a)** 1500 or **(b)** 3000 cells. Spheroids were formed for 144 h in **(a,b)** 0.05 mg/ml or **(c)** 0.1 mg/ml collagen type I. Representative brightfield images. Scale bar: 200 μ m.

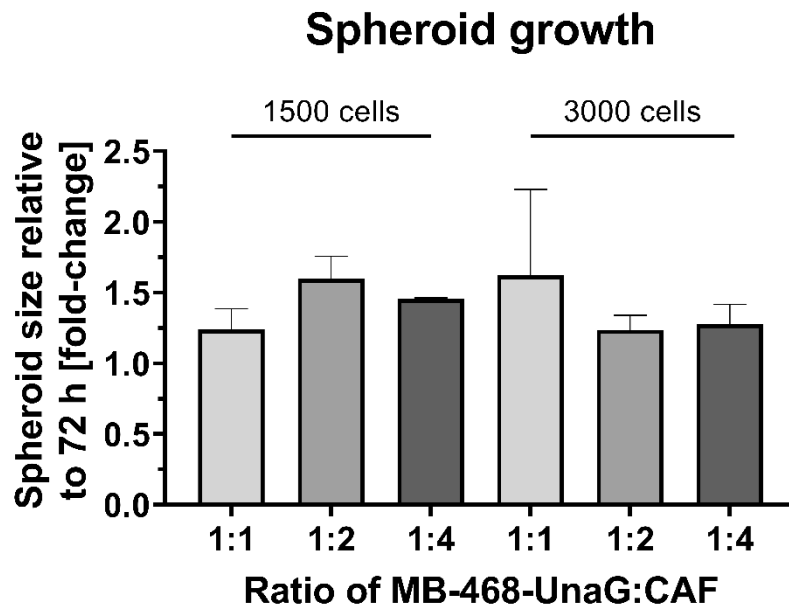
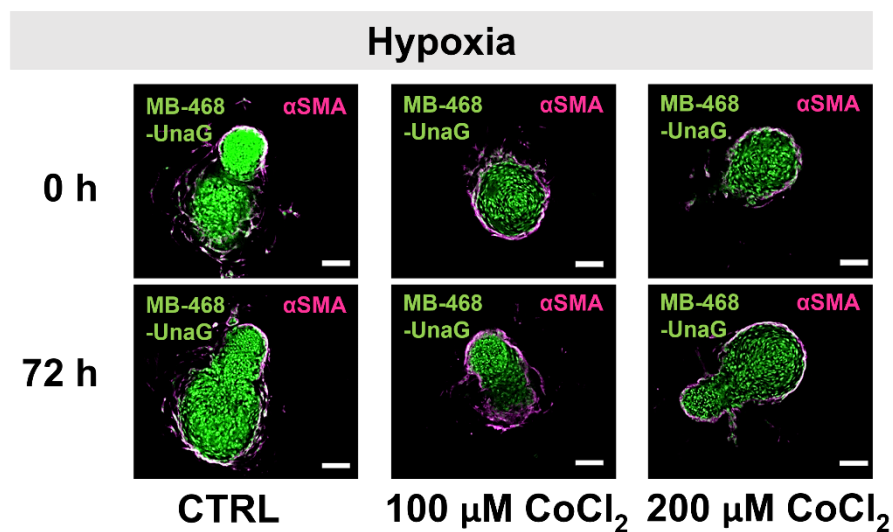


Figure S 18 Co-culture spheroid growth (MB-468-UnaG:CAF) in 0.05 mg/ml collagen type I. Co-culture spheroids were composed at different cell type ratios of MB-468-UnaG:CAFs (1:1, 1:2 and 1:4) with a seeding cell number of a total of 1500 or 3000 cells. Spheroids were formed for a total of 144 h in 0.05 mg/ml collagen type I. The spheroid size, equivalent to the start-point of treatment (72 h post-seeding) and equivalent to the end-point of treatment (144 h post-seeding), was determined by the spheroid area that was measured in brightfield images. In each seeding condition, average spheroid size at 144 h was normalized to the average spheroid size at 72 h (which was set to 1; fold-change). Bars represent the mean \pm SD of one independent experiment with analysing three spheroids per seeding condition.



(a)

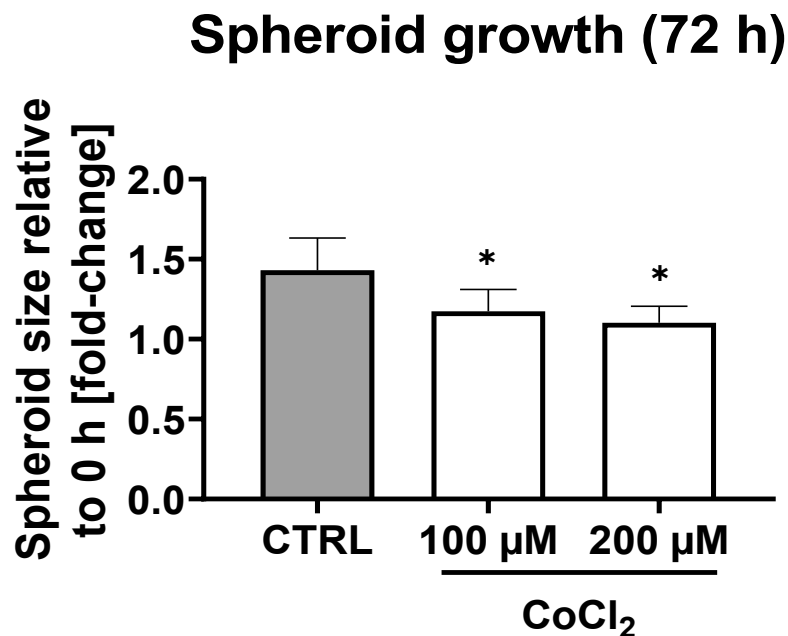
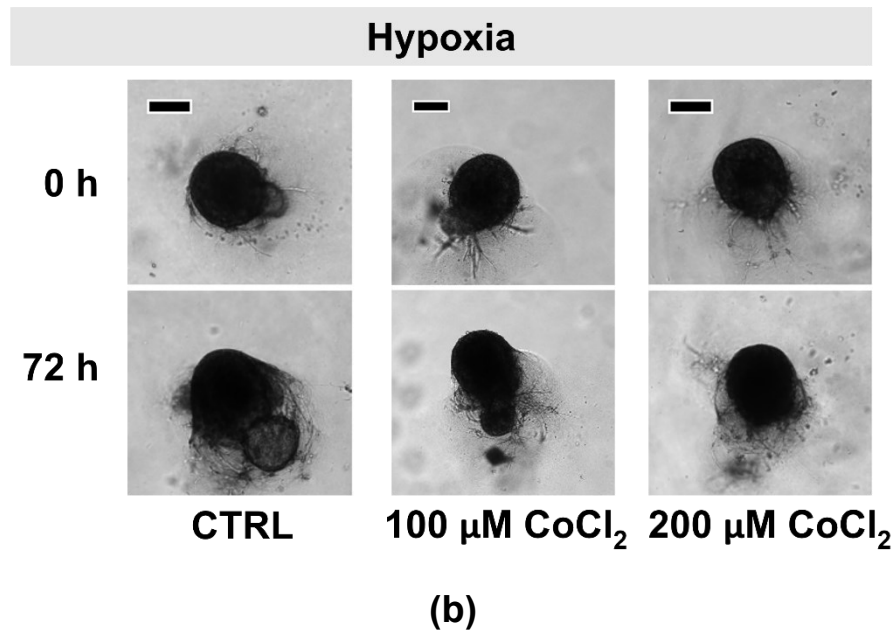


Figure S 19 Co-culture spheroid growth (MB-468-UnaG:CAF) was attenuated under CoCl_2 -simulated hypoxia. Co-culture spheroids (MB-468:CAF, 1:2) were formed for 72 h in 0.05 mg/ml collagen type I. After formation, spheroids were stimulated for further 72 h with 100 μM or 200 μM CoCl_2 to induce hypoxia. Co-culture medium served as control (CTRL). **(a)** Spheroids were immunologically stained for αSMA (CAF, magenta). MB-468-UnaG express UnaG (green) under regulation of a hypoxia responsive promotor. Scale bar: 100 μm . **(b)** Representative brightfield images. Scale bar: 200 μm . **(c)** Spheroid size pre-treatment (0 h) and post-treatment (72 h) was determined by the spheroid area that was measured in brightfield images. In each treatment group, average spheroid size post-treatment was normalized to the average spheroid size pre-treatment (which was set to 1;

fold-change). Statistical difference vs. CTRL was calculated with one-way ANOVA (* $p < 0.05$). Bars represent the mean \pm SD of one independent experiment with analysing five spheroids per treatment group.

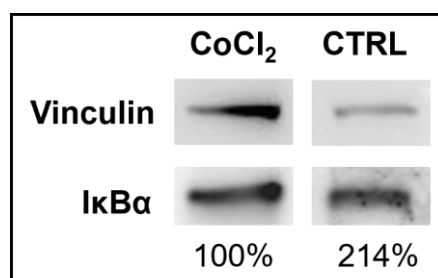


Figure S 20 CoCl₂ induced NFκB via degradation of IκBα. For hypoxia induction, MB-468-UnaG cells were exposed to 100 μ M CoCl₂ for 24 h. Culture medium served as control (CTRL). Representative western blot with protein lysates that are immunologically stained for IκBα (39 kDa) and the housekeeper protein vinculin (124 kDa). IκBα protein level was normalized to the CoCl₂ stimulated cells (which was set to 100%).

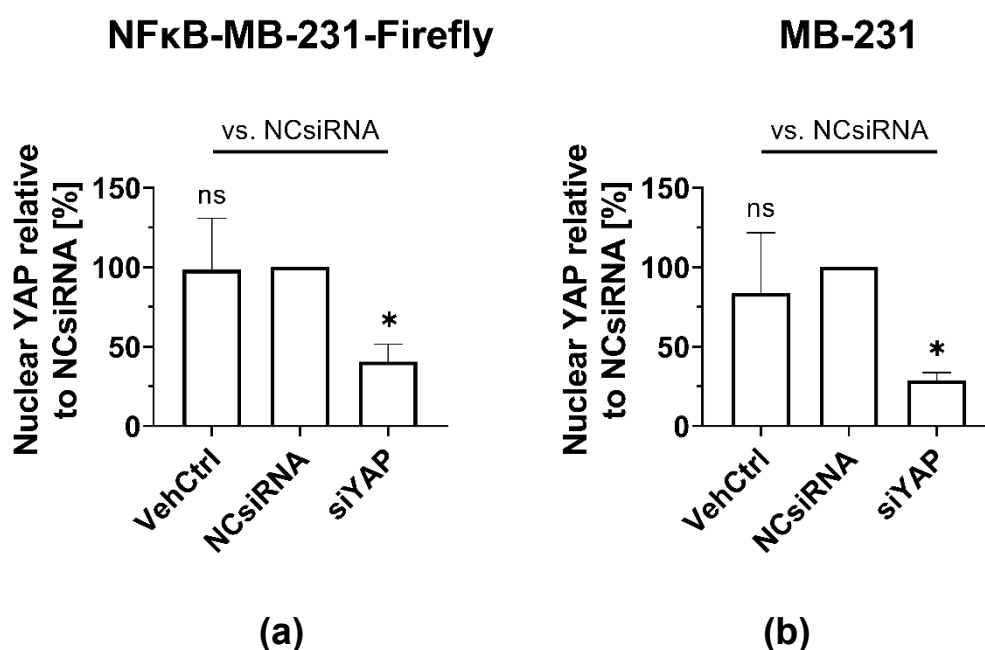


Figure S 21 Lipofectamine™-based siRNA transfection does not affect YAP activity. Transfection to **(a)** NFκB-MB-231-Firefly and **(b)** MB-231 was performed using the vehicle control (VehCtrl), non-targeting siRNA (NCsiRNA) or YAP-targeting siRNA (siYAP). Cells were stained for the nucleus (DAPI) and for YAP, 72 h-post transfection. Nuclear YAP protein level was determined as integrated density (IntDens) of the fluorescence intensity. Bars represent the mean \pm SD ($n=3$). Statistical difference vs. NCsiRNA was calculated with one-way-ANOVA (ns = not significant, * $p < 0.05$).

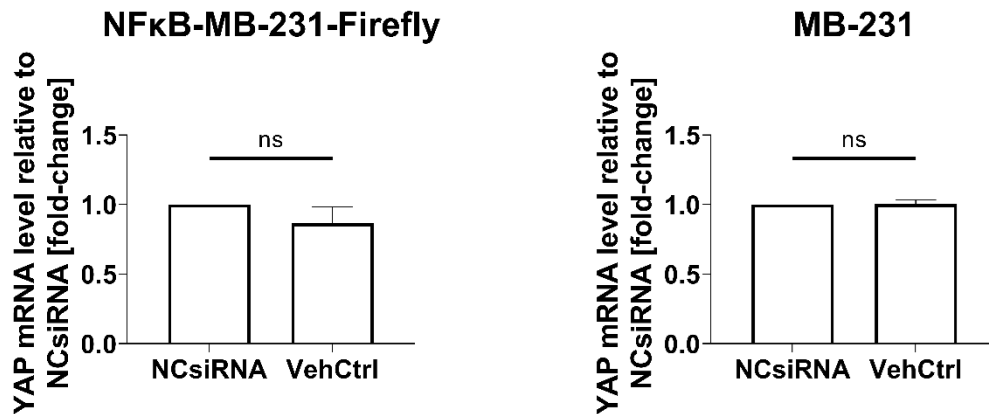


Figure S 22 Lipofectamine™-based siRNA transfection does not affect YAP expression. Transfection to (a) NFkB-MB-231-Firefly and (b) MB-231 was performed using the vehicle control (VehCtrl) and non-targeting siRNA (NCsiRNA). YAP expression was quantified 72 h post-transfection according to the RT-qPCR. Based on the $2^{-\Delta\Delta CT}$ method, the YAP mRNA level was normalized to GAPDH, followed by normalization of all groups to the untreated NCsiRNA group. Bars represent the mean \pm SEM ($n=3$). Statistical difference was calculated with the unpaired two-tailed t -test (ns = not significant).

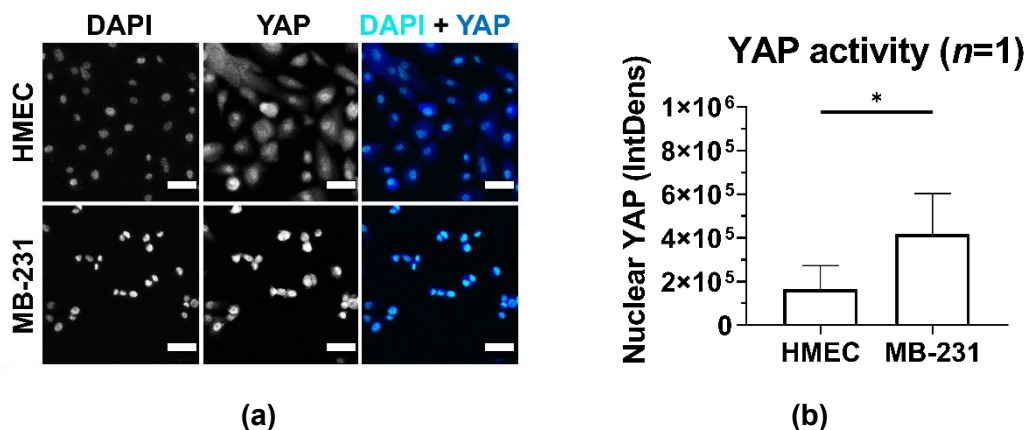


Figure S 23 Nuclear YAP is upregulated in tumour cells. Non-cancerous HMEC and cancerous MB-231 cells were stained for the nucleus (DAPI) and for YAP. (a) Representative fluorescence images for DAPI (turquoise) and YAP (blue). Scale bar: 50 μ m. (b) Nuclear YAP protein level was determined as integrated density (IntDens) of the fluorescence intensity. Bars represent the mean \pm SD of one independent experiment with at least three different images analysed per cell type. Statistical difference was calculated with an unpaired two-tailed t -test (* $p < 0.05$).

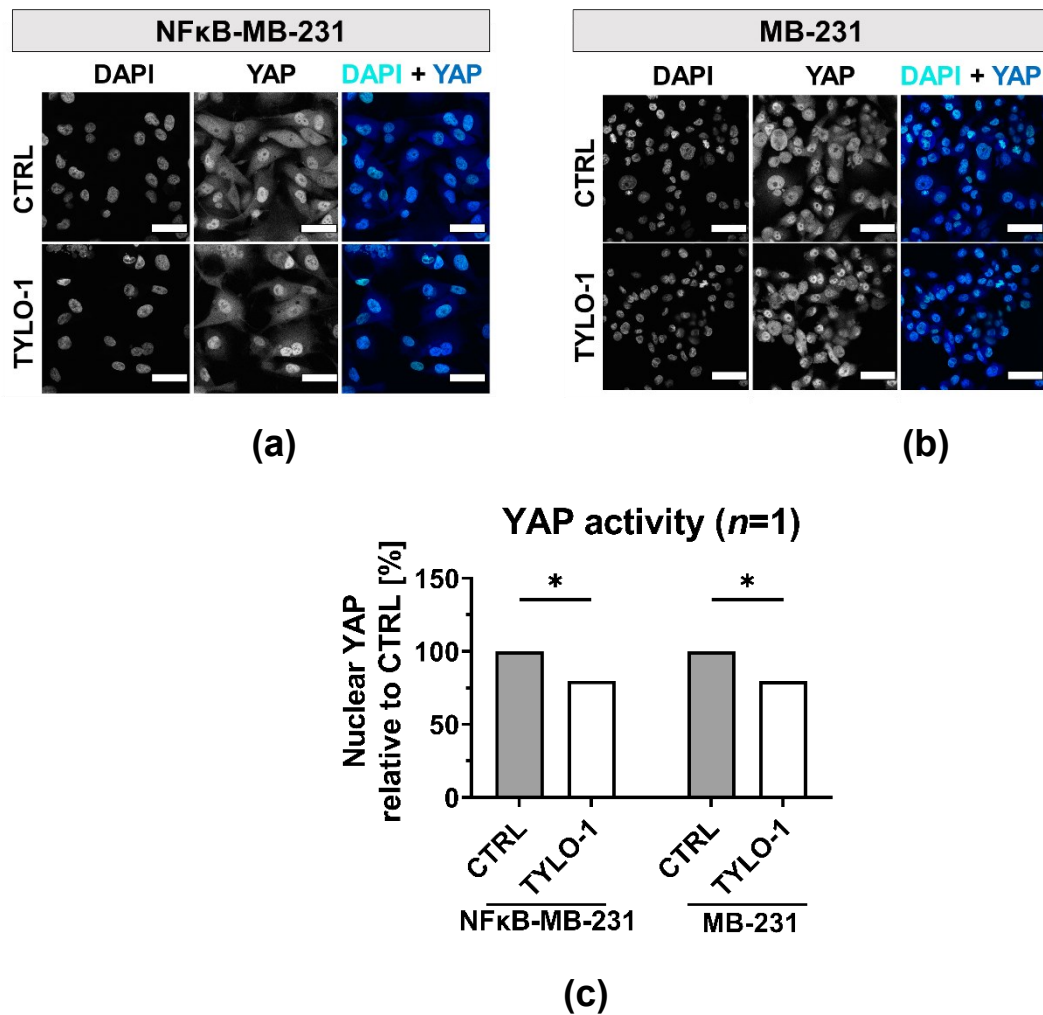


Figure S 24 TYLO-1 decreases YAP activity in TNBC. (a,c) NFκB-MB-231-Firefly (NFκB-MB-231) and (b,c) MB-231 were left untreated (CTRL) or treated with 100 nM TYLO-1 for 24 h. Cells were stained for the nucleus (DAPI) and for YAP. (a) Representative fluorescence images for DAPI (turquoise) and YAP (blue). Scale bar: 50 μm. (b) Nuclear YAP protein level was determined as integrated density (IntDens) of the fluorescence intensity. Bars represent the mean ± SD of one independent experiment with at least three different images analysed per treatment group. Statistical difference within all groups was calculated with two-way-ANOVA (* $p < 0.05$).

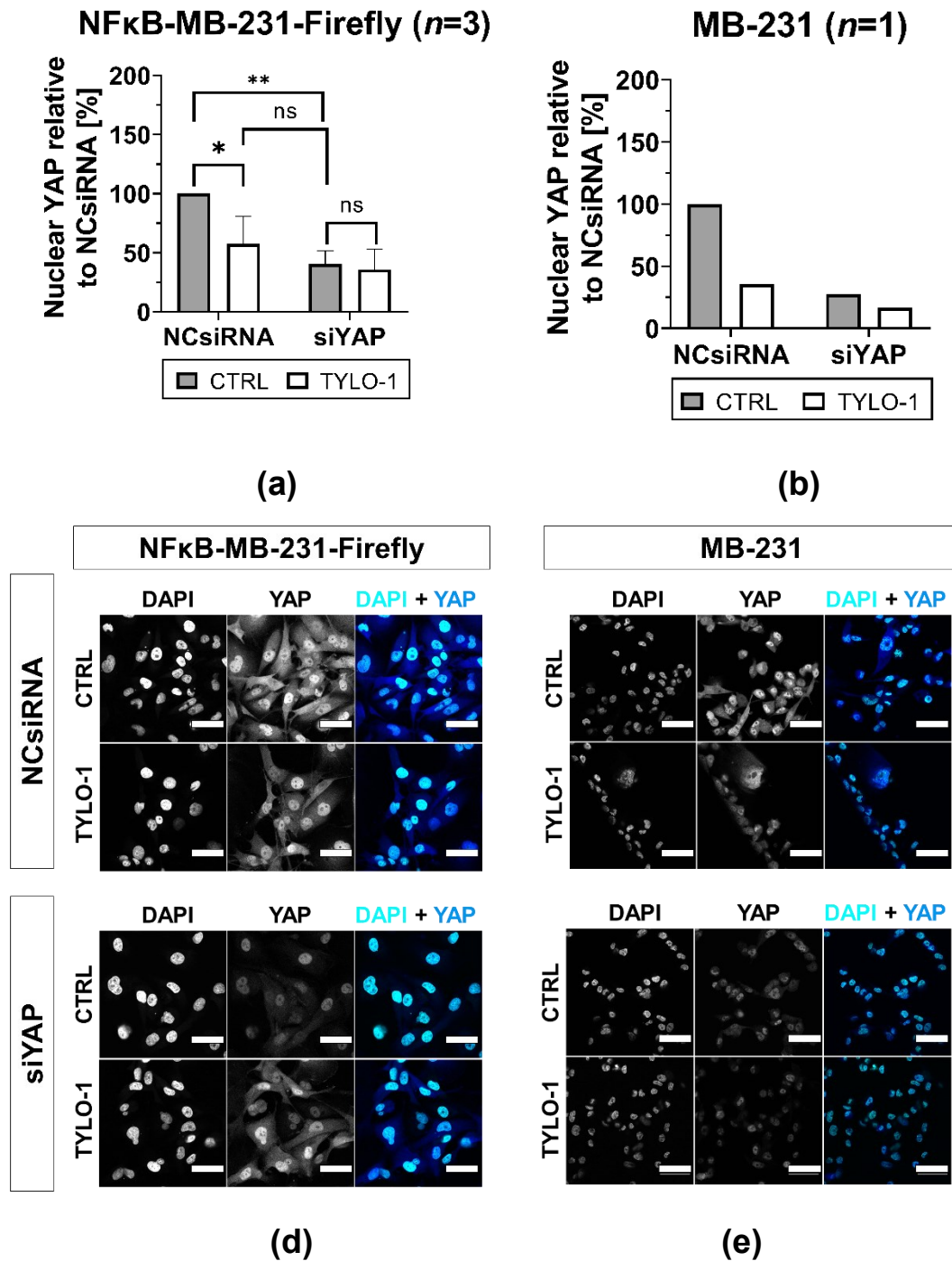


Figure S 25 TYLO-1 does not reduce YAP activity additionally to YAP knockdown. Transfection to **(a,c)** NFκB-MB-231-Firefly and **(b,d)** MB-231 was performed using the non-targeting siRNA (NCsiRNA) or YAP-targeting siRNA (siYAP). **(a-d)** 48 h post-transfection, cells were left untreated (CTRL) or treated for 24 h with 100 nM TYLO-1. After treatment, cells were stained for the nucleus (DAPI) and for YAP. **(a,b)** Nuclear YAP protein level was determined as integrated density (IntDens) of the fluorescence intensity. Bars represent the mean \pm SD ($n=3$). Statistical difference within all groups was calculated with two-way-ANOVA (ns = not significant, * $p < 0.05$). **(b)** Bars represent the mean \pm SD of one independent experiment with at least two images analysed per treatment group. **(d,e)**

Representative fluorescence images for DAPI (turquoise) and YAP (blue). Scale bar: 50 μ m.

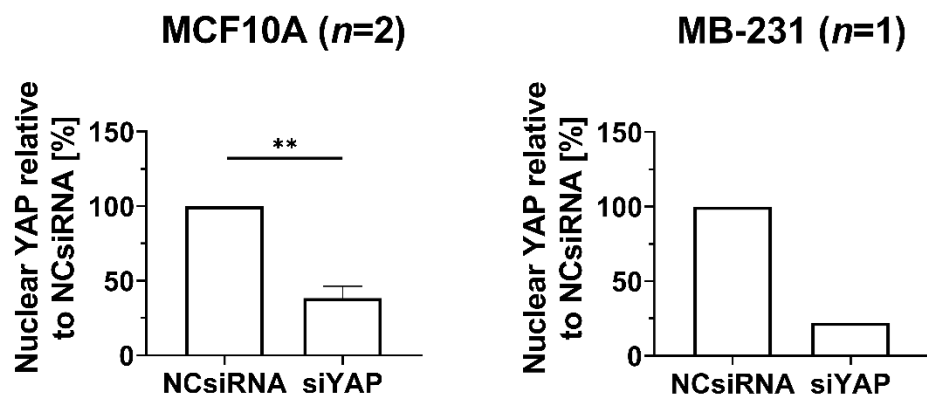
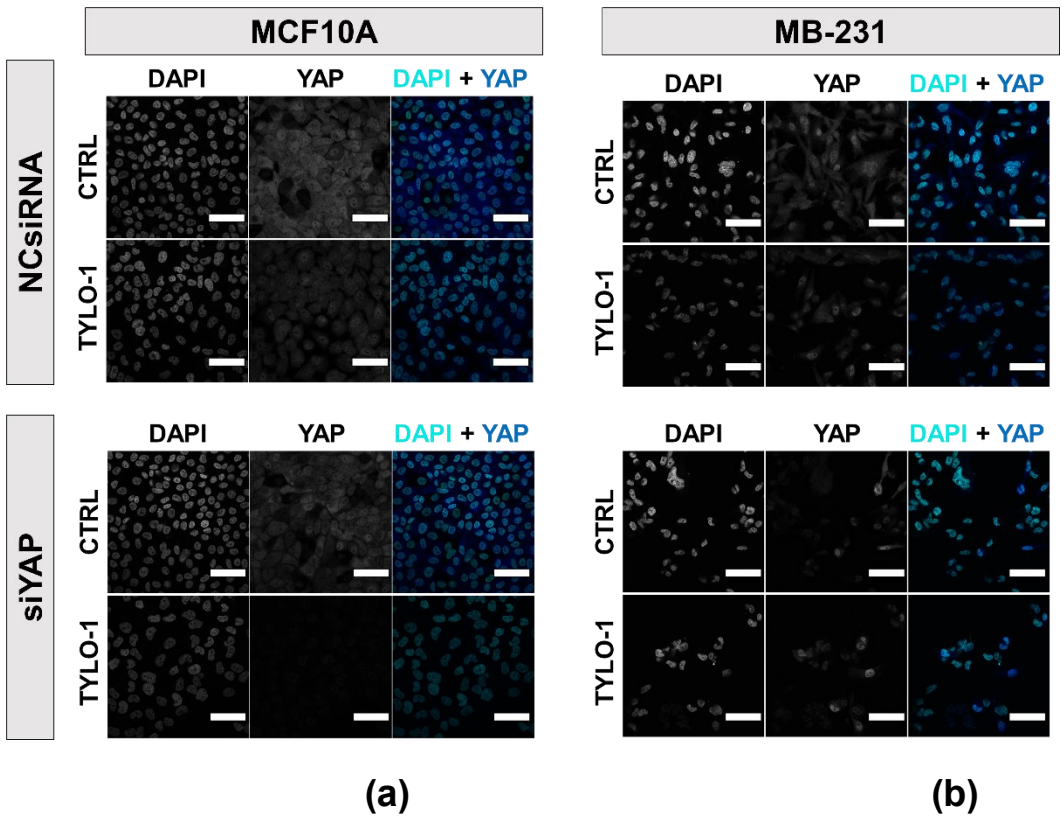


Figure S 26 YAP knockdown reduces YAP activity in MB-231 and MCF10A. Transfection to (a) MCF10A (b) MB-231 was performed using the non-targeting siRNA (NCsiRNA) or YAP-targeting siRNA (siYAP). (a,b) Cells were stained for the nucleus (DAPI) and YAP, 72 h-post transfection. Nuclear YAP protein level was determined as integrated density (IntDens) of the fluorescence intensity. (a) Bars represent the mean \pm SD (n=2). Statistical difference was calculated with the unpaired two-tailed *t*-test (** *p* < 0.01). (b) Bars represent the mean of one independent experiment with at least two images analysed per treatment group.



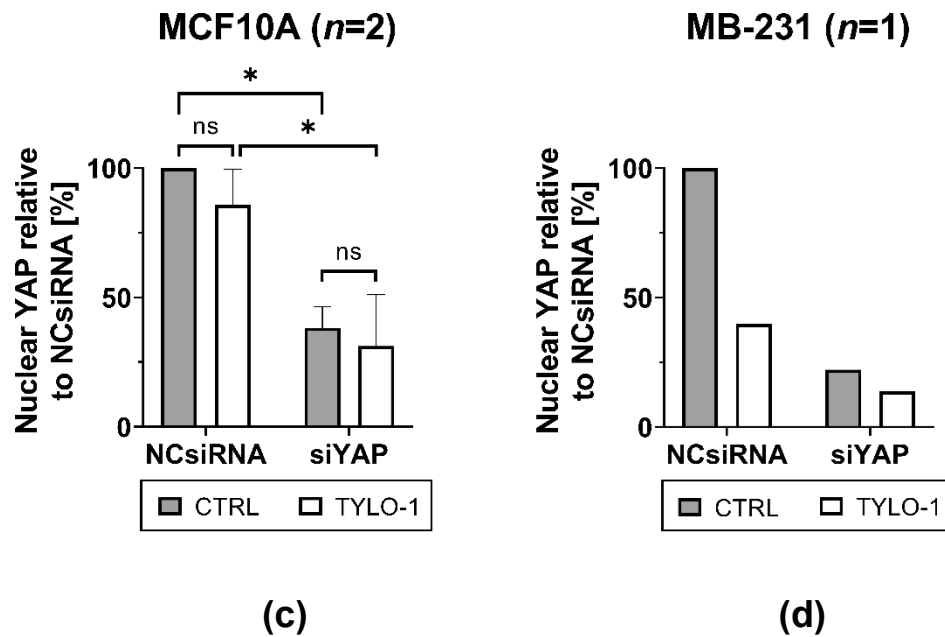


Figure S 27 TYLO-1 decreases YAP activity in MB-231 but not in MCF10A. Transfection to **(a)** MB-231 and **(b)** MCF10A was performed using the non-targeting siRNA (NCsiRNA) or YAP-targeting siRNA (siYAP). 48 h post-transfection, cells were left untreated (CTRL) or treated for 24 h with 100 nM TYLO-1. After treatment, cells were stained for the nucleus (DAPI) and for YAP. **(a,b)** Representative fluorescence images for DAPI (turquoise) and YAP (blue). Scale bar: 50 μ m. **(c,d)** Nuclear YAP protein level was determined as integrated density (IntDens) of the fluorescence intensity. YAP protein level was normalized to untreated NCsiRNA group. **(c)** Bars represent the mean of one independent experiment with at least two images analysed per treatment group. Statistical difference within all groups was calculated with two-way-ANOVA (ns = not significant, * $p < 0.05$). **(d)** Bars represent the mean of one independent experiment ($n=1$).

6.2 Supplementary tables

Table S 1 Molecular subtypes of TNBC

Authors	TNBC subtype ¹	Molecular characteristics
	BL	Increased CK5/6, EGFR expression
	LAR	Increased AR expression
Ma <i>et al.</i>	„Claudin- low”	CD44+/CD24- immunophenotype
		Decreased claudin 3, 4, 7 expression
Lehmann <i>et al.</i>	BL1	Increased Ki-67 expression
	BL2	Increased CD10, p63 expression
	LAR	Increased AR expression
	M	Aberrant regulation of Wnt, ALK, TGF- β
	MSL	Aberrant regulation of Rho, ALK, TGF- β , Wnt/ β -catenin, ERK1/2, EGFR, PDGF, PI3K
	IM	Aberrant regulation of NF κ B, TNF, JAK/STAT
Burstein <i>et al.</i>	LAR	Increased AR, MUC1 expression
		Aberrant PIK3CA, AKT1, CDH1 gene activation
	M	Increased PDGF-A, c-Kit expression
	BLIA	Aberrant regulation of S0TAT
		Presence of B /T/NK immune cells
	BLIS	Aberrant regulation of VTCN1
Jézéquel <i>et al.</i>	BL	Immune cells –, TAM – like cells
	LAR	Increased AR expression
		Aberrant <i>FOXA1</i> , <i>KRT18</i> , <i>XBP1</i> gene activation
	“BL-enriched”	Immune cells +, TAM – like cells
Ahn <i>et al.</i>	BL	Aberrant <i>ATR</i> , <i>BRCA1/2</i> , etc. gene activation
		<i>PIK3CA</i> gene mutation, <i>PTEN</i> gene inactivation
	M	Aberrant regulation of PI3K / AKT
	IM	Aberrant regulation of NF κ B, TNF, JAK/STAT, VTCN1, presence
		of B/T/NK immune cells
	LAR	Increased AR expression
		Aberrant <i>FOXA1</i> , <i>KRT18</i> , <i>XBP1</i> gene activation

Authors	TNBC subtype ¹	Molecular characteristics
Zeng <i>et al.</i>	BL	Increased CK5/6, EGFR expression
	NBL	Absence of CK5/6, EGFR expression

Table was adapted with minor modifications from Kolečková, Vomacková and Kolar (2021) [17]. ¹ BL = basal-like; BL1/2; LAR = luminal androgen receptor; M = mesenchymal; MSL = mesenchymal stem – like; IM = immunomodulatory; BLIA = BL immune-activated; BLIS = BL immune-suppressed; NBL = normal breast – like.

Table S 2 Natural sources of P-alkaloids

Kingdom	Plant family ¹	Latin name of the species ¹
Plants	Apocynaceae [314] ¹	<i>Cynchananchum komarovii</i>
		<i>Cynchananchum vincetoxicum</i>
		<i>Pergularia Pallida</i> [231]
		<i>Tylophora atrafolliculata</i> [150]
		<i>Tylophora hirsute</i> [315]
		<i>Tylophora indica</i> [316]
		<i>Tylophora liu</i> ³ [140]
		<i>Tylophora ovata</i> [161]
		<i>Tylophora tanakae</i> [213]
		<i>Vincetoxicum pumilum</i> [317]
Animals	Moraceae ¹	<i>Ficus fistulosa</i> ca. <i>tengerensis</i>
		<i>Ficus fistulosa</i>
		<i>Ficus hispida</i> [204]
		<i>Ficus septica</i> [206,318]
	Lauraceae ¹	<i>Cryptocarya chinensis</i>
		<i>Cryptocarya densiflora</i>
		<i>Cryptocarya laevigata</i>
	Nymphalidae [319]	<i>Ideopsis similis</i> [320], a <i>Tylophora tanakae</i> feeding butterfly [142].
		Alkaloids may be found in its pupae and imagines.

¹ Adapted from [142] and [314]. ² Plants were also reported in the subfamily Asclepiadaceae [142]. ³ New species discovered in Taiwan in 2011 [140].

Table S 3 Bioactivities of P-alkaloids and their analogues

Bioactivity	Compound and targeted cell type
Agrochemicals	<ul style="list-style-type: none"> Anti-feedant: Tylophorine, septicine and O-methyltylophorinidine reduced leaf consumption of the insect <i>Spodoptera litura</i> [321]. Anti-parasitic: Crude methanolic extract of <i>tylophora hirsute</i> reduced growth of <i>Leishmania major</i> [315]. Insecticidal: Crude methanolic extract of <i>tylophora hirsute</i> increased mortality in e.g. the bug <i>Stiphilus oryzae</i> [315]. (<i>R</i>)-Tylophorine and (<i>R</i>)-antofine are cytotoxic against e.g. the moth <i>Spodoptera litura</i> [322].
Anti-adipogenic	<ul style="list-style-type: none"> Antofine suppresses pre-adipocyte cell (3T3-L1) proliferation and differentiation [323].
Anti-asthmatic	<ul style="list-style-type: none"> Tylophorine stimulates β-receptor activity in peripheral leukocytes from asthmatic children [324].
Anti-bacterial	<ul style="list-style-type: none"> Tylophorine and O-methyltylophorinidine ¹ inhibit growth of bacteria, including <i>Staphylococcus aureus</i> but not <i>Escherichia coli</i> [321].

	<ul style="list-style-type: none"> Pergularinine (Tylophorinine) and tylophorinidine block thymidylate synthase [210] and dihydrofolate reductase in <i>Lactobacillus leichmannii</i> [231].
Anti-fungal	<ul style="list-style-type: none"> Tylophorine and O-methyltylophorinidine inhibit growth of the fungus e.g. <i>Aspergillus niger</i> [321]. Hydrochloride salts of tylophorinine and tylophorinidine inhibit growth of diverse fungi including <i>Aspergillus</i> spp. and <i>Candida</i> spp. [325]
Anti-malarial	<ul style="list-style-type: none"> Tylophoridicine D reduces cell viability in plasmodium falciparum (3D7) [318].
Anti-viral	<ul style="list-style-type: none"> Tylophorine suppresses viral RNA replication in a corona virus [326]. Tylophorine intermediates, 5-Oxo-1-[(2,3,6,7-tetramethoxy-9-phenanthrenyl) methyl]-L-proline blocked hepatitis C virus attachment [327].
Oviposition stimulation in insects	<ul style="list-style-type: none"> Phenanthroindolizidine alkaloids, including 7-demethyltylophorine, enhance the number of eggs laid by <i>Ideopsis similis</i> [328], that is a <i>Tylophora</i> spp. feeding butterfly.

Table S 4 Mode of action of P-alkaloids and their analogues *in silico*, *in vitro* and *in vivo*

Mode of action	Compound and targeted cell type (cell line)
Anti-inflammatory	<ul style="list-style-type: none"> Tylophorine suppressed LPS-induced expression of pro-inflammatory cytokines (e.g. COX1, iNOS and TNFα) in murine macrophages (RAW264.7) [329]. Tylophorine blocks upstream regulator of NFκB and AP-1 (MEKK1) in murine macrophages (RAW264.7) [329] Tylophorine analogue, e.g. DCB-3503, tylophorinine, tylophorinidine and the isomer of 2-demethoxytylophorine, namely (<i>R</i>)-demethoxytylophorinidine, block NFκB-mediated transcription in in hepatocellular cancer (HepG2) [150]. Tylophorine analogue, DCB-3503 blocks phosphorylation of NFκB/p65 in pancreatic cancer (PANC-1) [151].
Anti-angiogenic	<ul style="list-style-type: none"> Tylophorine inhibited <i>in vitro</i> and <i>in vivo</i> vessel formation of human umbilical vascular endothelial cells through blocking VEGF signalling [152]. Tylophorine blocked proliferation of human umbilical vascular endothelial cells by downregulation of cell cycle related factors. Anti-angiogenic effects were species independent, as proliferation blockade was observed in vascular smooth muscle cells derived from rats and human umbilical vascular endothelial cells [262]. Antofine blocks tube formation of human umbilical vascular endothelial cells [330].

Anti-hypoxic	<ul style="list-style-type: none"> Targeting the key regulator of angiogenesis, the hypoxia-induced HIF pathway, in T47D by tylophorinine, O-methyltylophorinidine, tylophorinidine, deoxytylophorinine but not tylophoridicine D [157].
Anti-migration	<ul style="list-style-type: none"> Antofine inhibits VEGF-induced migration of human umbilical vascular endothelial cell [330]. Synthetic, phenanthrene-based YS206 blocks colon cancer (HCT-116) migration and YS306 blocks hepatocellular cancer migration (HepG2) [270] Sulfonamide analogue of (<i>R</i>)-cryptopleurine blocks migration of renal cancer (Cak1) [295]. Tylophorine blocks migration of human umbilical vascular endothelial cells [152] and vascular smooth muscle cells [262]. Tylophorine analogue, NK007, blocks migration of (paclitaxel resistant) ovarian cancer (A2780) [149]. Ethanol extract of <i>Ficus septica</i>, presumably tylophorine, blocks migration of murine TNBC (4T1) [206].
Anti-proliferative	<p><u><i>In vitro</i>, human cell lines:</u></p> <ul style="list-style-type: none"> Tylophorine blocks proliferation of vascular smooth muscle cells [262]. <p><u><i>In vitro</i>, human cancer cell lines:</u></p> <ul style="list-style-type: none"> Tylophorine inhibits proliferation in MCF-7, T47D, MDA-MB-231 [148,155,156]. The synthetic analogue YPC-10157 inhibits proliferation in colon cancer (HCT-116), leukaemia (HL-60) and breast cancer (MCF-7, MDA-MB-231, MDA-MB-468) [203]. Antofine inhibits proliferation in MDA-MB-231 [153]. Tylophorine inhibits proliferation in MCF-7 and MDA-MB-231 [204]. Tylophorine analogue, NK007, inhibits proliferation of (paclitaxel resistant) ovarian cancer (A2780) [149]. Tylophorinidine prevents DNA synthesis in leukaemia (primary leukocytes) through inhibition of the thymidylate synthase [166]. <p><u><i>In vitro</i>, 3D tumour spheroids:</u></p> <ul style="list-style-type: none"> O-Methyltylophorinidine suppresses growth of microtumours that comprise pancreatic carcinoma cells (Capan-2 and PANC-1) and primary hepatic or pancreatic stellate cells. Spheroids were formed in a collagen-based matrix [161]. <p><u><i>In vivo</i>:</u></p> <ul style="list-style-type: none"> Tumour growth blockade of hepatocellular carcinoma (HepG2, xenograft model) by DCB-3503 [331], tylophorinidine and the isomer of (<i>R</i>)-(+)-deoxytylophorinidine [150].

	<ul style="list-style-type: none"> • Tumour growth blockade of murine sarcoma (Meth A) by tylophorinine and tylophoridicine E [163]. • Tumour growth blockade of colon cancer (HCT-116) [153] by antofine. • Tumour growth blockade of colon cancer (HCT-116) by the dehydrated derivative of tylophoridicine E [164]. • Tumour growth blockade of Murine Ehrlich Ascites tumour by tylophorine [152]
	<u>G0/G1 arrest:</u> <ul style="list-style-type: none"> • G0/G1 arrest by antofine in colon cancer (HCT-116) [153]. • G1-arrest by tylophorine in breast cancer (T47D) [154]. • G1/S arrest by NK007 in (paclitaxel resistant) ovarian cancer [149].
	<u>S-phase arrest:</u> <ul style="list-style-type: none"> • S-phase arrest by tylophorine analogues, DCB-3503 and DCB-3500, in nasopharyngeal carcinoma (KB) [331].
Modulation of cell cycle transition	<u>Decreased expression of proteins involved in cell cycle transition:</u> <ul style="list-style-type: none"> • Cyclin D1 decreased by tylophorine in vascular smooth muscle cells [262], antofine in colon cancer (HCT-116) [153], by DCB-3503 in HepG2 [223]. • Cyclin E decreased by antofine in colon cancer (HCT-116) [153]. • CDK4 decreased by antofine in colon cancer (HCT-116) [153]. • Cyclin A2 decreased by tylophorine in hepatocellular carcinoma (HepG2), HONE-1 and NUGC-3 [226]. • p21 and p27 decreased by tylophorine [262]. • Rb-phosphorylation decreased by tylophorine [262].
Cell cytotoxicity	<ul style="list-style-type: none"> • Hispiloscine (tylophorinine acetate) in breast cancer MCF, MDA-MB-231 (IC₅₀ is about 1 µM) [204]. • Tengerensine in breast cancer (MCF7, MDA-MB-231 and MDA-MB-468) at a nanomolar concentration [205]. • Tylophorine analogue, DCB-3503, in hepatocellular (HepG2) and pancreatic cancer (PANC-1) [150]. • Tylophorinine in nasopharyngeal carcinoma (KB), lung cancer (A549), colorectal cancer (HT-29) [163] and rectum adenocarcinoma (HCT-8) [162]. • O-Methyltylophorinidine in prostate cancer [160], in hepatocellular cancer (HepG2) [150] and pancreatic cancer (PANC-1) [150,161]. • Tylophorinidine in hepatocellular cancer (HepG2) and pancreatic cancer (PANC-1) [150], nasopharyngeal carcinoma (KB) and rectum adenocarcinoma (HCT-8) [162]. • Hydrochloride salt derivative of tylophorinidine, namely 3-O-demethyl tylophorinidine, in e.g. pancreatic (PANC-1) [279]

	<ul style="list-style-type: none"> • (Synthetically prepared) tylophoridicine E in rectal (HCT-8) [162], nasopharyngeal (KB), lung (A549), colorectal (HT-29) [163], colon (HCT-116) [164], but not hepatocellular (HepG2) nor pancreatic (PANC-1) [150] carcinoma. • (Synthetically prepared) 2-demethoxytylophorine in colon cancer (HCT-116) [164], in nasopharyngeal carcinoma (KB) and rectum adenocarcinoma (HCT-8) [162]. • Tylophoridicine D was tested, but showed no cytotoxicity in nasopharyngeal carcinoma (KB) and rectum adenocarcinoma (HCT-8) [162].
Pro-apoptotic	<ul style="list-style-type: none"> • Synthetic YPC-10157 enhances caspase 3 and 7 activity in leukaemia (HL-60) [203]. • Tylophorine enhances caspase 3 and 9 activity in breast cancer (T47D) [154]. • Antofine enhances caspase 8 activity and PARP-cleavage in colon cancer (HCT-116) [153]. • Ethanolic extract of <i>Ficus septica</i>, presumably tylophorine, reduces expression of anti-apoptotic Bcl-2 in breast cancer (MCF7) [206].
	<p><u><i>In vitro</i>:</u></p> <ul style="list-style-type: none"> • Tylophorine analogue, DCB-3503, decreases IκBα and NFκB phosphorylation via blocking IKK-mediated phosphorylation in pancreatic cancer (PANC-1) [151].
Phosphorylation blockade	<p><u><i>In silico</i>, molecular docking studies:</u></p> <ul style="list-style-type: none"> • Isomer of O-methyltylophorinidine with the short name HTBP1 binds to the ATP-binding site in AKT [222]. • Tylophorinine, tylophorinidine and tylophorinidine-N-oxide bind to the ATP-binding site in Aurora A and Aurora B receptors [224]. • Tylophorine binds to the ATP-binding site of VEGFR [152].
DNA and RNA synthesis blockade	<ul style="list-style-type: none"> • Antofine in colon cancer (HCT-116) [153]. • Thymidylate synthase blockade in leukaemia (primary human leukocytes) by pergularinine and tylophorinidine reduces DNA synthesis [166]. • Tylocrebrine reversibly blocks <i>de novo</i> RNA synthesis [208]. • Tylocrebrine irreversibly blocks DNA synthesis [208]. • The stereoisomer of 2-demethoxytylophorine, namely (+)-(13aS)-deoxytylophorinine, intercalates at AT-rich sequences, which is mainly found upstream of the transcription start site [158].
Protein synthesis blockade	<ul style="list-style-type: none"> • Tylophorine, tylocrebrine, cryptopleurine block protein synthesis [208]. <p><u>Blockade of transcription:</u></p> <ul style="list-style-type: none"> • Allosteric regulation of HSC70 in hepatocellular carcinoma (HepG2): DCB-3503 binds to HSC70 and stimulates ATP hydrolysis when bound to

its target genes at the specific RNA motifs “AUUUA” in the 3'UTR of e.g. cyclin D1 [223].

Blockade of translation:

- Protein translation blockade by the synthetic analogue YPC-10157 in a cell-free translation assay [203].
- Tylocrebrine irreversibly inhibits peptide-chain elongation by targeting 40S ribosome [208].
- Tylophorine binds to caprin-1, thereby recruiting and sequestering mRNA of e.g., c-Myc and cyclin D2. Formation of the ribonucleoprotein complex results in blockade of protein translation [332].
- Tylocrebrine inhibits translocation of the peptidyl tRNA in ribosomes [332].

Reverse drug-resistance	<ul style="list-style-type: none"> • Tylophorine enhanced sensitivity to doxorubicin in breast cancer (T47D) [154].
Telomerase inhibition	<ul style="list-style-type: none"> • Tylophoridine D and anhydrodehydrotylophorinidine block the telomerase activity by forming a G-quadruplex at guanine-rich telomeric DNA [165].

¹ Studies including P-alkaloids, that were investigated in this study, or studies that included BC cells were highlighted in bold font.

Table S 5 IC₅₀-values determined for P-alkaloids in reduction of cell viability in MB-231

Compound	2D CellTiterGlo ¹	2D PrestoBlue ²
	MB-231	MB-231
	24 h	24 h
	IC ₅₀ [nM] ¹	IC ₅₀ [nM] ¹
TYLO-1	10.2 ± 3	n.t.
TYLO-2	88.5 ± 24	30.8 ± 2.9
TYLO-3	50.2 ± 10.3	21.5 ± 3.6
TYLO-4	227.1 ± 61.4	59.1 ± 9.1
TYLO-5	>1000	15400 ⁵
TYLO-6	>1000	n.t.
Paclitaxel	>1000	37.4 ± 8.6

¹ Tested in MB-231 using the 2D CellTiterGlo (384-well format). ² Tested in MB-231 using the 2D PrestoBlue assay with a low cell seeding density. ³ Tested in 3D TNBC co-culture spheroids comprising MB-231 and CAFs (1:2) using the 3D CellTiterGlo assay. Mean ± SD (n=3). ⁴ Mean ± SD (n=2). ⁵ (n=1). Not tested (n.t.).

Table S 6 Dose-response inhibition for BAY-117085 in MB-231

Compound	NFkB Inhibition		Reduction of Cell Viability	
	2 h ¹ IC ₅₀ [nM]	24 h ² IC ₅₀ [nM]	24 h ³ IC ₅₀ [nM]	24 h ⁴ IC ₅₀ [nM]
BAY 11-7085	5,500 ± 2,000 ⁴	12,623 ± 1,542 ⁴	5,800 ± 1,208 ⁴	12,765 ± 1,435 ⁵

NFkB-inhibition was tested after ¹ 2 h or ² 24 h treatment with the NFkB-inhibition assay. ³ Reduction of cell viability was determined 24 h post-treatment with the ³ 2D PrestoBlue or ⁴ 2D CellTiterGlo. Compound was applied in triplicates in a two-fold or three-fold serial dilution starting at ^{1,3} 100 µM or ² 50 µM. ⁴ Mean ± SD (*n* = 3). ⁵ Mean ± SD (*n* = 2). ⁶ Mean ± SD (*n* = 1).

Table S 7 Dose-response of TYLO-1 and paclitaxel in CAFs

CAFs	
Compound	24 h IC ₅₀ [nM]
TYLO-1	12.3 ± 8.9 ¹
Paclitaxel	35.1 ± 5.4 ²

Cell viability was measured in CAFs at a low seeding density (2.5 × 10⁴ cells/ml) using the 2D CellTiterGlo assay (96-well format). Compound concentration was applied in triplicates in a four-fold serial dilution starting at 1000 nM for TYLO-1 and in a three-fold serial dilution starting at 100 µM for paclitaxel. Mean ± SD of ¹ (*n*=3), ² (*n*=2).

Table S 8 Dose-response in different cell lines for different treatment duration

Compound	PBMC ¹ 24 h ² IC ₅₀ [nM]	MCF10A ¹ 24 h ² IC ₅₀ [nM]	MB-231 ¹ 48 h ² IC ₅₀ [nM]	D2A1 (<i>n</i> =1) ¹ 72 h ² IC ₅₀ [nM]
TYLO-1	12.6 ± 0.1 nM ^{3,8}	9.0 ± 2.4 nM ^{4,7} <i>n</i> =3	10.8 ± 1.8 nM ^{5,7}	10.6 nM ^{6,9}
Paclitaxel	n.t.	56.6 ± 18.4 ^{4,8}	18.3 ± 9.8 nM ^{5,8}	3.2 nM ^{6,9}

¹ Cell type. ² Duration of treatment. ³ Cell viability was measured in ³ PBMC monolayer cells at density of 3.5 × 10⁵ cells/ml using the 2D CellTiterGlo assay (96-well format). Mean ± SD (*n*=2). Cell viability was measured in ⁴ MCF10A at a density of 1 × 10⁵ cells/ml ⁵ MB-231 at a density of 6 × 10⁴ cells/ml using the 2D PrestoBlue assay. Cell viability was measured in ⁶ D2A1 monolayer cells at density of 1 × 10⁴ cells/ml using the 2D CellTiterGlo assay (96-well format). ⁷ Mean ± SD (*n*=3). ⁸ Mean ± SD (*n*=2). ⁹ Mean (*n*=1). Not tested (n.t.).

Table S 9 Drug-dose response in MB-468-UnaG

Compound	MB-468-UnaG
	24 h ¹
	IC ₅₀ [nM]
TYLO-1	4.4
BAY 11-7085	4200 ± 800
Paclitaxel	3.7

Cell viability was measured in MB-468-UnaG at a density of ¹ 1.0×10^5 cells/ml or ² 1.5×10^5 using the 2D PrestoBlue assay.³ Cells were treated for 24 h in triplicates with a compound concentration in a two-fold or three-fold serial dilution starting at 50 μ M for Bay 11-7085 ($n=2$) and in a three-fold serial dilution starting at 100 nM for TYLO-1s ($n=1$) and at 1 μ M for paclitaxel ($n=1$). ¹ Duration of treatment.

Table S 10 Drug-dose reduction in reduction of cell viability of 3D co-culture spheroids

Compound (concentration; serial dilution)	3D Co-culture IC ₅₀ [nM]
TYLO-1 (1 μ M; 1:4)	9.9 ± 2.1 nM
Paclitaxel (1 μ M; 1:3)	> 1,000
Paclitaxel (100 μ M; 1:3)	> 100,000

Reduction of cell viability was determined 72 h post-treatment in a 3D TNBC co-culture according to the 3D CellTiterGlo assay.

Table S 11 Drug-dose response for TYLO-1 and paclitaxel in 3D co-culture spheroids

Compound	MB-468-UnaG	MB-468-UnaG
	Normoxia IC ₅₀ [nM]	Hypoxia ¹ IC ₅₀ [nM]
TYLO-1s ²	6.5	6.7
Paclitaxel ²	6.7	> 1000

Cell viability was measured in MB-468-UnaG at a density of 1.5×10^5 cells/ml using the 2D PrestoBlue assay. ¹ To induce hypoxia, cells were pre-treated for 24 h using 100 μ M CoCl₂. ² Cells were treated for 24 h. Compound concentration was applied in triplicates in a three- -fold serial dilution starting at 100 nM for TYLO-1s and at 1 μ M with paclitaxel. IC₅₀ represents one independent experiment.

6.3 Plasmid sequences for reporter gene assays

Stable cell lines were created with a vector that contains an artificial promoter construct to regulate NFκB-dependent luciferase expression (6.3.1. 6.3.2) or HIF-dependent UnaG expression (6.3.3).

6.3.1 MDA-MB-231-NanoLuc

The MB-231-NanoLuc cell line contains a plasmid with a NFκB-response element to study inflammation-associated NFκB signalling. Stable cell line generation is described [116]. The compartments of the plasmid vector “pNL3.2.NF-κB-RE[NlucP/NF-κB-RE/Hygro]” is provided by Promega are shown in **Figure S 28**.

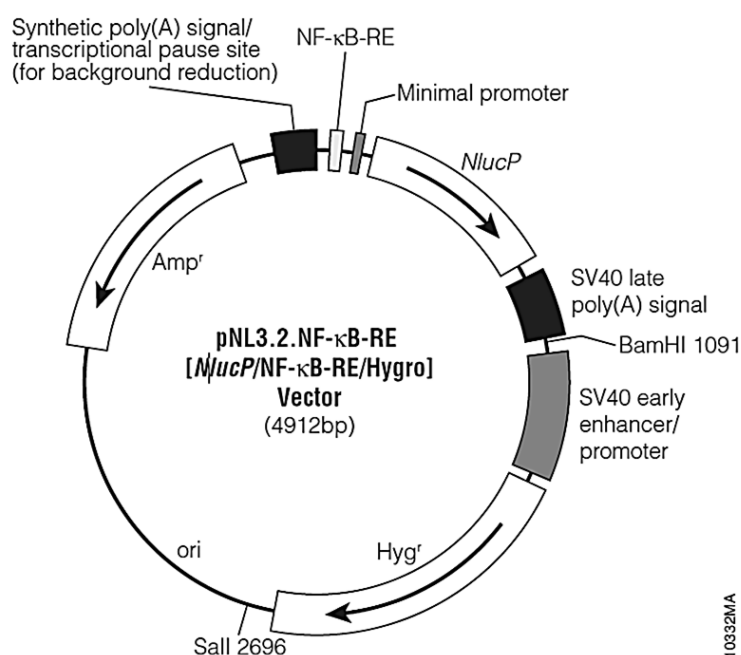


Figure S 28 Plasmid compartments for NFκB NanoLuc-luciferase reporter. The plasmid DNA sequence contains the following compartments (with depicting its specific position in the direction from the 5'-phosphate to the 3'-hydroxyl group): NFκB response elements (33–84), minimal promoter (117–147), nlucP (NanoLuc®-PEST) reporter gene (180–818), SV40 late poly(A) signal (858–1079); SV40 early enhancer/promoter (1127–1545), synthetic hygromycin (Hyg coding region (1570–2607), synthetic poly(A) signal (2631–2679), Reporter Vector primer 4 (RVprimer4) binding region (2746–2765), Col E1-derived plasmid replication origin (3003), synthetic β-lactamase coding region for resistance to ampicillin (Amp^r) (3794–4654), synthetic poly(A) signal/transcriptional pause site (4759–4912), Reporter Vector primer 3 (RVprimer3) binding region (4861–4880). Illustration was extracted from the vector product information sheet (Promega, #N1111).

6.3.2 MDA-MB-231-Firefly

The MB-231-Firefly cell line contains a plasmid with a NFκB-response element to study inflammation-associated NFκB signalling. The stable cell line was provided by Promega and regulation of the firefly luciferase reporter gene is depicted in **Figure S 29**. Plasmid vector of the stable cell line (pTA-NFκB-luciferase reporter vector) was not provided.

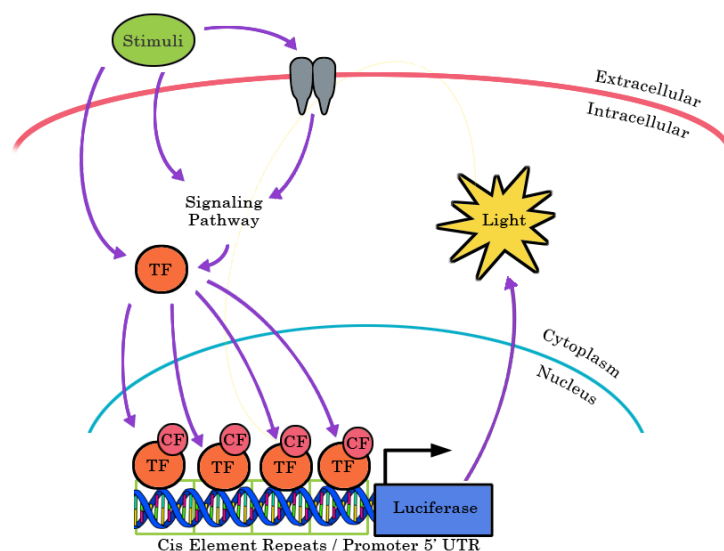


Figure S 29 Plasmid composition for NFκB Firefly-luciferase reporter. Abstract of the reporter gene mechanism for the transcription factor (TF) NFκB was extracted from the cell line product information sheet (Signosis, #SL-0043-FP). The plasmid DNA sequence contains four cis-element repeats of the NFκB binding site and a minimal promoter upstream of the firefly luciferase coding region. along with hygromycin expression vector followed by hygromycin selection. The hygromycin coding region is not depicted. CF: co-factor.

6.3.3 MDA-MB-468-UnaG

The MB-468-UnaG cell line contains a plasmid with a hypoxia response element (HRE) to study hypoxia-associated HIF-1α signalling. To overcome limitations of GFP or RFP due to oxygen-dependent maturation, it was incorporated the fluorescent protein UnaG that is naturally found in an Japanese freshwater eel [82]. The plasmid and its compartments are depicted in (**Figure S 30**). The DNA sequence within the plasmid is shown below in the direction from the 5'-phosphate to the 3'-hydroxyl group. Gene sequences are shown in colour for the five HRE in tandem with the CMV minimal promotor (mCMV; red), UnaG (green), PEST (orange), gene for resistance against neomycin and kanamycin (NeoR/KanR; blue), gene for resistance against ampicillin (AmpR; violet) or non-functional sequences (grey).

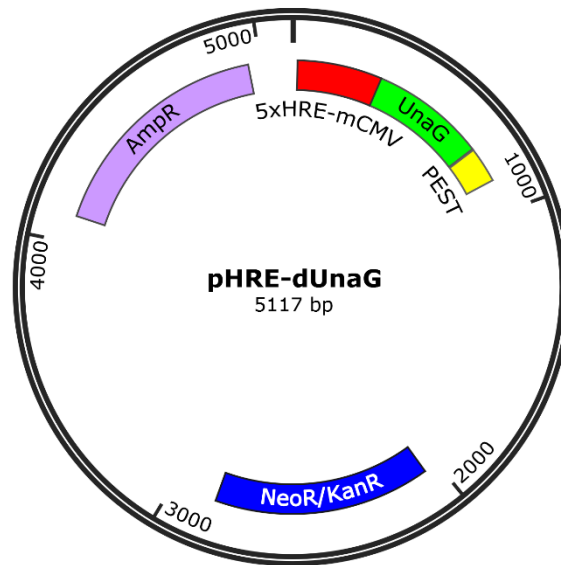


Figure S 30 Plasmid compartments for HIF-reporter gene studies. The plasmid pHRE-dUnaG contains five repeats of the HIF binding site (HRE) in tandem with the mCMV promoter (red), sequence encoding for UnaG (green), PEST (yellow) and resistance against neomycin and kanamycin (blue), as well as against ampicillin (violet). Plasmid was constructed with SnapGene.

5'-

gtaccgagctttctcgagccacagtgcatacgtgggtccaacaggtcctctgtcgagccacagtgcatacgtgggtcca
acaggtcctctgtcgagccacagtgcatacgtgggtccaacaggtcctctgtcgagccacagtgcatacgtgggtcca
caggtcctctgtcgagccacagtgcatacgtgggtccaacaggtcctctgtcgagatctggtaggcgtgtacggtgggag
gtctatataagcagagctcggttagtgaaccgtcagatcactagaagcttggcattccggtactgttgtaaagccaccatggtc
gagaaattgttgccacctggaagatcgagacagccataatttggtaatacctgaaagctatcggagcccaaaggaat
taagcgatggtgggatgccacgacgccgacattgtacatctccagaaggacggagacaaaatgacagtgaataataga
gaatggacctctacgttcttgacactcaagtaaagtcaaataggaggaggtcgacgaatttctctgatcgaagaaa
aggcgtaaaatctgtcgtgaacttggtgggagagaagctggtgtacgtacaaaagtgggacggcaaggagacgacgtatg
tccgagagataaaggacggtaaactggtcgtgacacttacgatgggagacgtcgtggctgtgcgcagctaccggaggggcg
acggaaaacggtaagaagcttagccacggcttccgcccggagggtggaggagcaggatgatggcacgctgcccatgtcttg
tgcccaggagagcgggatggaccgtcacctgcagcctgtgcttctgctaggatcaatgtggtcgacccgcggggatccac
gcgtgcggccgcagaacaaaaactcatctcagaagaggatctgaatggggccgcatagtctagaagctcgtgatcagcc
tcgactgtgccttctagttgccagccatctgtgtttgccctccccgtgccttcttgaccctggaagggtgccactcccactgtcc
tttctaataaaatgaggaaattgcatcgcatgtctgagtaggtgtcattctattctgggggtgggtggggcaggacagcaa
gggggaggattgggaagacaatagcaggcatgctggggatggccgggctctatggctctgaggcggaagaaccagc
tggggctctaggggtatcccacgcgcctgtagcggcgattaagcgcgcggtgtggtggttacgcgcagcgtgacc
gctacacttgccagcgccctagcggcgtccttctgcttctcccttcttctcgccacgttcgcccgttccccgtcaagctct
aaatcggggcatcccttagggttccgatttagtgccttacggcacctcgaccccaaaaaacttgattaggggtgatggtcacgt
agtgggcatcgccctgatagacgggttttcgcccttgacgttgaggtccacgttcttaatagtggaactctgttccaaactgga

acaacactcaaccctatctcggtctattcttttgattataagggattttggggatttcggcctattggttaaaaaatgagctgattta
acaaaaatttaacgcgaattaattctgtggaatgtgtgtcagttagggtgtggaagtccccagggtccccaggcaggcaga
agtatgcaaagcatgcatctcaattagtcagcaaccagggtgtggaagtccccagggtccccaggcaggcagaagtatgca
aagcatgcatctcaattagtcagcaaccatagtcggccccctaactccgccccatccccggcctaactccgcccagttccgccc
attctccgccccagggtgactaattttttattatgagaggccgaggccgcctctgcctctgagctattcagaagtagtgag
gaggctttttggaggcctaggcttttgcataaagctccggggagggtccacaatgattgaacaagatggattgcacgcagggttc
tccggccgcttgggtggagaggctattcggctatgactgggcacaacagacaatcggctgctctgatccgcccgtgttccggc
gtcagcgcagggggcgccgggttcttttgcagaccgacctgtccgggtccctgaatgaactccaggacgaggcagcgcg
gctatcgtaggtggccacgacggggcggttccctgagcagctgtgctcgacgtgtcactgaagcggaagggaaggactggctgctatt
gggcaagtgcgggggaggatctcctgtcatctcacctgtcctgcccagaaaagtatccatcatggctgatcaatgcggc
ggctgcatacgcttgatccggctacctgccattcgaccaccaagcgaaacatcgcatcgagcgagcacgtactcggatgg
aagccgggtctgtcgatcaggatgatctggacgaagagcatcaggggctcgcgccagccgaactgttcgccagggtcaagg
cgctatgcccgacggcgaggatctcgctgtgactcatggcgatcctgcttgcgaatatcatggtggaaaatggccgctttt
ctggattcatcgactgtggccggctgggtgtggcgaccgctatcaggacatagcgttggctacccgtgatattgctgaagag
cttggcggaatgggctgaccgcttccctgtgctttacggtatcgccgctcccgattcgagcgcatcgcccttctatcgcccttct
gacgagttctctgagcgggactctgggggtcgaaatgaccgaccaagcgacgcccacactgccatcacgagatttcgattc
caccgccccttctatgaaagggtgggcttcggaatcgtttccgggacgcccggctggatgatcctccagcgcggggatctcat
gctggagttctcgccaccccaactgtttattgcagctataatggttacaataaagcaatagcatcacaatttcacaata
aagcattttttcactgcattctagttgtggtttgtccaaactcatcaatgtatcttatcatgtctgtataccggatcttccgcttctcgc
tactgactcgctcgctcggtcgttcggctcgggcgagcggatcagctcactcaaaggcggaataacggttatccacagaa
tcaggggataacgcaggaaagaacatgtgagcaaaaggccagcaaaaggccaggaaccgtaaaaaggccggtgct
ggcgttttccataggctccgccccctgacgagcatcaaaaatcgacgtcaagtacagagggtggcgaaacccgacag
gactataaagataaccagggtttccccctggaagctccctcgctcgctctcctgttccgaccctgccgttaccggatacctgtc
cgcttctccctcgggaagcgtggcgcttctcaatgtcacgctgtaggatctcagttcgggtgtaggtcgctccaagct
gggctgtgtgcacgaacccccgttcagcccagcgtgcgcttatccggtaactatcgctttagtccaacccggtaagac
acgacttatcgccactggcagcagccactggaacaggattagcagagcgaggatgttaggcgggtgtacagagttctgaa
gtggtggcctaactacggctacactagaaggacagtatttggtatctcgctctgtgaagccagttaccttcggaaaaagagt
tggtagctcttgatccggcaaaacacaccgctggtagcgggtggttttttggcaagcagcagattacgcgcagaaaaaa
aggatctcaagaagatcctttgatctttctacgggtctgacgtcagtggaacgaaaactcacgttaagggattttggtcatg
agattatcaaaaaggatcttcacctagatccttttaataaaaaatgaagtttaaatcaatctaaagtatatagtaaactgg
tctgacagttaccaatgcttaacagtgaggcacctatctcagcgatctgtctatttcgttcatccatagttgcctgactccccgtcg
ttagataactacgatacgggagggttaccatctggccccagtgctgcaatgataccgcgagacccacgtcaccgggtcc
agatttatcagcaataaaccagccagccggaaggccgagcgagaagtggctcctgcaactttatccgctccatccagctc
attaattgttccgggaagctagagtaagtagttcccgagtaataagtttgcgaacggtgttgccattgtacaggcatcggtg
gtcacgctcgctggttggtatggcttcaatcagctccggtcccaacgatcaaggcgagttacatgatccccatgttgtcaaaa
aagcggtagctccttcggtcctccgatcgtgtcagaagtaagttggccgagtggtatcactcatggttatggcagcactgc
aattcttactgtcatgccatccgtaagatgctttctgtgactggtgagtactcaaccaagtcattctgagaatagtgatgcggc

gaccgagttgctcttgcggcggtcaatacgggataataccgcgccacatagcagaactttaaagtgtcatcattgaaa
acgttcttcggggcgaaaactctcaaggatcttaccgctgttgagatccagttcgatgaaccactcgtgcacccaactgatct
tcagcatcttttactttcaccagcgtttctgggtgagcaaaaacaggaaggcaaaatgccgcaaaaaagggaataagggcg
acacggaaatgttgaatactcatactcttcttttcaatattatgaagcatttatcagggttattgtctcatgagcggatacatatt
gaatgtatttagaaaaataaacaataaggggtccgcgcacatttccccgaaaagtgccacctgacgtcagatcgacggatc
gggagatcgn-3'

6.4 Macro script for batch processing using Fiji

For nuclear YAP quantification, it was performed YAP measurement within the nucleus (6.4.1) For automatically saving images of each recorded channel (DAPI or YAP) in colour or greyscale, images were saved in a PNG format (6.4.26.4.2). Automated batch analysis of recorded fluorescence images was performed using the open-source software Fiji. It was used images with two (6.4.1.1, 6.4.2.1) or three (6.4.1.2, 6.4.2.2) different fluorescent dyes recorded at with the cLSM FluoView3000.

Batch analysis was set by selecting “process“, ”batch” and “macro” in Fiji. Following, it was selected the input folder containing all the images for processing and the output folder for saving the result. For each analysis, it was loaded the macro script of choice. For each batch analysis, there were new folder created within the output folder to save processed data.

6.4.1 Quantification of nuclear YAP in images with

For YAP quantification, the fluorescence signal for YAP was transformed to a grey value (8-bit) and fluorescence intensity of YAP was measured within the area of the nucleus (DAPI stained area). The background fluorescence signal (value of 2000) was subtracted from all data. The nuclear YAP protein level was determined as integrated density (IntDens).

6.4.1.1 YAP quantification in images with two separate fluorescence dyes

The macro script applied for batch analysis is shown below in grey letters. The protocol was created to analyse the recorded fluorescence signal for DAPI (channel 1) and YAP (channel 2).

```
//Get Image title
imageTitle=getTitle();//returns a string with the image title

//Get path for saving results in the same file folder
//Open image will be used as variable "image"
path = getDirectory("image");

//process original image (imageTitle)
```

```

        selectWindow(imageTitle);
        run("8-bit");
        run("Split Channels"); //concatenate "C1-" or whichever channel you want ("C1-
        ", "C2-"etc)

//Duplicate and rename duplicated window (channel 2 = YAP)
//Saving steps comparing to duplicate the whole image ahead
//saved steps are: splitting, converting
        selectWindow("C2-"+imageTitle);
        run("Duplicate...", "title=duplicate-"+ "C2-"+imageTitle);
        imageTitleDc2=getTitle(); //D = duplicated, c2 = channel 2
        //print (imageTitleDc2); //If it is necessary to check the name of the duplicated image

//Convert all channels to 8 bit
        selectWindow(imageTitleDc2);
        run("8-bit");
        selectWindow("C2-"+imageTitle);
        run("8-bit");
        selectWindow("C1-"+imageTitle);
        run("8-bit");

//Measure YAP in nucleus

//Determine nucleus area by DAPI staining
// run Threshold
selectWindow("C1-"+imageTitle);
setAutoThreshold("Mean dark");
setOption("BlackBackground", false);
run("Convert to Mask");
run("Analyze Particles...", "size=3-Infinity display add in_situ");
//Automatisch wird für jedes ROI die Intensität für DAPI als Result ausgegeben
//Hierbei sind Mean, Mn und Max jeweils "255"

// measure mean intensity in channel 2 = YAP staining
selectWindow("C2-"+imageTitle);
run("Select All");
roiManager("Combine");

```



```

run("Measure");

//measure beackground fluorescence signal
makeRectangle(808, 416, 120, 112);
run("Measure");
//String.copyResults();//can be left out. Results will be directly saved as an csv file
//check if name already exists ?
//save results before deleting the list
Result_name_DAPI = path+"/Results_DAPI"+imageTitle+".csv";
run("Input/Output...");
saveAs("Results", Result_name_DAPI);

//delete results
resultnr = getValue("results.count");
Table.deleteRows(0, resultnr-1);

//Delete saved ROI to make space for new ROIs
run("Select All");
roiManager("Deselect");
roiManager("Delete");

//Measure YAP in the whole cell body

//Determine cell area by YAP staining
// run Threshold
selectWindow(imageTitleDc2);
setAutoThreshold("Mean dark");
setOption("BlackBackground", false);
run("Convert to Mask");
run("Analyze Particles...", "size=3-Infinity display add in_situ");

// measure mean intensity in channel 2 = YAP staining
selectWindow("C2-"+imageTitle);
run("Select All");
roiManager("Combine");
run("Measure");

```

```

//measure beackground fluorescence signal
makeRectangle(808, 416, 120, 112);
run("Measure");

//String.copyResults();//can be left out. Results will be directly saved as an csv file
//save results before deleting the list
Result_name_cell = path+"/Results_cell"+imageTitle+".csv";
run("Input/Output...");
saveAs("Results", Result_name_cell);

//delete results
resultnr = getValue("results.count");
Table.deleteRows(0, resultnr-1);

//Delete saved ROI for separate ROIs in each image
run("Select All");
roiManager("Deselect");
roiManager("Delete");

//close all windows
close("C1-"+imageTitle);
close("C2-"+imageTitle);
close(imageTitleDc2);

```

6.4.1.2 YAP quantification in images with three separate fluorescence dyes

The macro script applied for batch analysis is shown below in grey letters. The protocol was created to analyze the recorded fluorescence signal for DAPI (channel 1) and YAP (channel 3).

```

//Get Image title
imageTitle=getTitle();//returns a string with the image title

//Get path for saving results in the same file folder
//Open image will be used as variable "image"
path = getDirectory("image");

//process original image (imageTitle)
selectWindow(imageTitle);

```

```

run("8-bit");
run("Split Channels"); //concatenate "C1-" or whichever channel you want ("C1-
", "C2-"etc)

//Duplicate and rename duplicated window (channel 3 = YAP ~cell body)
selectWindow("C3-"+imageTitle);
run("Duplicate...", "title=duplicate-"+ "C3-"+imageTitle);
imageTitleDc3=getTitle(); //D = duplicated, c3 = channel 3

//Convert all channels to 8 bit
selectWindow(imageTitleDc3);
run("8-bit");
selectWindow("C3-"+imageTitle);
run("8-bit");
selectWindow("C2-"+imageTitle);
run("8-bit");
selectWindow("C1-"+imageTitle);
run("8-bit");

//Measure fluorescence intensity in the nucleus (determined by DAPI=DNA staining)

//Determine nucleus area by DAPI staining
// run Threshold
selectWindow("C1-"+imageTitle);
setAutoThreshold("Mean dark");
setOption("BlackBackground", false);
run("Convert to Mask");
run("Analyze Particles...", "size=3-Infinity display add in_situ");
//Automatisch wird für jedes ROI die Intensität für DAPI als Result ausgegeben
//Hierbei sind Mean, Mn und Max jeweils "255"

// measure mean intensity in channel 2 = p65 staining
selectWindow("C2-"+imageTitle);
run("Select All");
roiManager("Combine");
run("Measure");

```

```

//measure beackground fluorescence signal
makeRectangle(808, 416, 120, 112);
run("Measure");
//String.copyResults();//can be left out. Results will be directly saved as an csv file
//check if name already exists ?
//save results before deleting the list
Result_name_DAPI_p65 = path+"/Results_p65nuc_"+imageTitle+".csv";
run("Input/Output...");
saveAs("Results", Result_name_DAPI_p65);

//delete results
resultnr = getValue("results.count");
Table.deleteRows(0, resultnr-1);

// measure mean intensity in channel 3 = yap staining
selectWindow("C3-"+imageTitle);
run("Select All");
roiManager("Combine");
run("Measure");

//measure beackground fluorescence signal
makeRectangle(808, 416, 120, 112);
run("Measure");
//String.copyResults();//can be left out. Results will be directly saved as an csv file
//check if name already exists ?
//save results before deleting the list
Result_name_DAPI_YAP = path+"/Results_YAPnuc_"+imageTitle+".csv";
run("Input/Output...");
saveAs("Results", Result_name_DAPI_YAP);

//delete results
resultnr = getValue("results.count");
Table.deleteRows(0, resultnr-1);

//Delete saved ROI to make space for new ROIs
run("Select All");

```

```

roiManager("Deselect");
roiManager("Delete");

//Measure fluorescence intensity in the whole cell body (determined by YAP expression)

//Determine cell area by YAP staining
// run Threshold
selectWindow(imageTitleDc3);
setAutoThreshold("Mean dark");
setOption("BlackBackground", false);
run("Convert to Mask");
run("Analyze Particles...", "size=3-Infinity display add in_situ");

// measure mean intensity in channel 2 = phospho p65 staining
selectWindow("C2-"+imageTitle);
run("Select All");
roiManager("Combine");
run("Measure");

//measure beackground fluorescence signal
makeRectangle(808, 416, 120, 112);
run("Measure");

//String.copyResults();//can be left out. Results will be directly saved as an csv file
//save results before deleting the list
Result_name_cell_p65 = path+"/Results_p65cell_"+imageTitle+".csv";
run("Input/Output...");
saveAs("Results", Result_name_cell_p65);

//delete results
resultnr = getValue("results.count");
Table.deleteRows(0, resultnr-1);

// measure mean intensity in channel 3 = YAP staining
selectWindow("C3-"+imageTitle);
run("Select All");

```

```

roiManager("Combine");
run("Measure");

//measure background fluorescence signal
makeRectangle(808, 416, 120, 112);
run("Measure");

//String.copyResults();//can be left out. Results will be directly saved as an csv file
//save results before deleting the list
Result_name_cell_YAP = path+"/Results_YAPcell_"+imageTitle+".csv";
run("Input/Output...");
saveAs("Results", Result_name_cell_YAP);

//delete results
resultnr = getValue("results.count");
Table.deleteRows(0, resultnr-1);

//Delete saved ROI for separate ROIs in each image
run("Select All");
roiManager("Deselect");
roiManager("Delete");

//close all windows
close("C1-"+imageTitle);
close("C2-"+imageTitle);
close("C3-"+imageTitle);
close(imageTitleDc3);

```

6.4.2 Image saving of separate recorded channels

The macro script applied for batch analysis is shown below in grey letters. The protocol was created to process and save images with the recorded fluorescence signal for DAPI (channel 1) and YAP (channel 2).

6.4.2.1 Automatic image saving for two recorded fluorescence dyes

The macro script applied for batch analysis is shown below in grey letters. The protocol was created to process and save images with the recorded fluorescence signal for DAPI (channel 1) and YAP (channel 2).

```

//create a new directory = output folder for processed images
path = getDirectory("image");
newDir= path + "/output/";
File.makeDirectory(newDir);

//get the image Title and set a scale bar
imageTitle=getTitle();//returns a string with the image title
run("Scale Bar...", "width=50 height=16 font=200 colour=White background=Black
location=[Lower Right] bold hide overlay");

run("Channels Tool...");

//saving coloured image, all channels
Stack.setDisplayMode("composite");
saveAs("PNG", newDir+imageTitle+"DAPI+YAP");

//saving coloured image, seperate channels
Stack.setActiveChannels("10");
saveAs("PNG", newDir+imageTitle+"DAPI-c");
Stack.setActiveChannels("01");
saveAs("PNG", newDir+imageTitle+"YAP-c");

//saving grey scale
Stack.setDisplayMode("grayscale");
Stack.setChannel(1);
saveAs("PNG", newDir+imageTitle+"DAPI-g");
Stack.setChannel(2);
saveAs("PNG", newDir+imageTitle+"YAP-g");

```

6.4.2.2 Automatic image saving for three recorded fluorescence dyes

The macro script applied for batch analysis is shown below in grey letters. The protocol was created to process and save images with the recorded fluorescence signal for DAPI (channel 1) and YAP (channel 3).

```

//create a new directory = output folder for processed images
path = getDirectory("image");
newDir= path + "/output/";
File.makeDirectory(newDir);

```

```

//get the image Title, set a scale bar and open tool for choosing separate channels
imageTitle=getTitle();//returns a string with the image title
run("Scale Bar...", "width=50 height=16 font=200 colour=White background=Black
location=[Lower Right] bold hide overlay");
run("Channels Tool...");
Stack.setChannel(2);
run("Magenta");

//saving coloured image, all channels
Stack.setDisplayMode("composite");
Stack.setActiveChannels("110");
saveAs("PNG", newDir+imageTitle+"DAPI+phospho-p65");
Stack.setActiveChannels("101");
saveAs("PNG", newDir+imageTitle+"DAPI+YAP");

//saving coloured image, seperate channels
Stack.setDisplayMode("colour");
Stack.setChannel(1);
saveAs("PNG", newDir+imageTitle+"DAPI-c");
Stack.setChannel(2);
saveAs("PNG", newDir+imageTitle+"p-p65-c");
Stack.setChannel(3);
saveAs("PNG", newDir+imageTitle+"YAP-c");

//saving grey scale
Stack.setDisplayMode("grayscale");
Stack.setChannel(1);
saveAs("PNG", newDir+imageTitle+"DAPI-g");
Stack.setChannel(2);
saveAs("PNG", newDir+imageTitle+"p-p65-g");
Stack.setChannel(3);
saveAs("PNG", newDir+imageTitle+"YAP-g");

```


List of publications

Phenanthroindolizidine Alkaloids Isolated from *Tylophora ovata* as Potent Inhibitors of Inflammation, Spheroid Growth, and Invasion of Triple-Negative Breast Cancer

Authors: **Irene Reimche**, Haiqian Yu, Ni Putu Ariantari, Zhen Liu, Kay Merkens, Stella Rotfuß, Karin Peter, Ute Jungwirth, Nadine Bauer, Friedemann Kiefer, Jörg-Martin Neudörfl, Hans-Günther Schmalz, Peter Proksch, Nicole Teusch

Journal: International Journal of Molecular Sciences (Impact factor: 6.208 (2022))

DOI: 10.3390/ijms231810319

Published: 7 September 2022

Contribution: Cell culture; NFκB-inhibition assay; 2D cell viability assay; 3D co-culture spheroid studies: establishment, generation, treatment, immunofluorescence staining; brightfield and fluorescence imaging; 3D cell viability assay; 3D invasion; hypoxia studies (including cell line); western blot; cell cycle studies (including establishment); experimental design, data acquisition and analysis; manuscript writing

Pseudopterosin and O-Methyltylophorinidine Suppress Cell Growth in a 3D Spheroid Co-Culture Model of Pancreatic Ductal Adenocarcinoma

Authors: Bailu Xie, Jan Hänsel, Vanessa Mundorf, Janina Betz, **Irene Reimche**, Mert Erkan, Ibrahim Büdeyri, Anne Gesell, Russell G. Kerr, Ni Putu Ariantari, Haiqian Yu, Peter Proksch, Nicole Teusch, Randall J. Mrsny

Journal: Bioengineering

DOI: 10.3390/bioengineering7020057

Published: 14 June 2020

Contribution: Cell culture; 3D co-culture spheroid generation; 3D co-culture spheroid treatment; 3D immunostaining; brightfield and fluorescence imaging; data acquisition and illustration

Azaphilones from the Red Sea Fungus *Aspergillus falconensis*

Authors: Dina H. El-Kashef , Fadia S. Youssef, Rudolf Hartmann, Tim-Oliver Knedel, Christoph Janiak , Wenhan Lin, **Irene Reimche**, Nicole Teusch, Zhen Liu; Peter Proksch

Journal: Marine drugs

DOI: 10.3390/md18040204

Published: 10 April 2020

Contribution: Cell culture; NFκB-inhibition assay; 2D cell viability assay; experimental design, data acquisition and analysis contribution to manuscript writing (results)

Polyketides from the marine-derived fungus *Aspergillus falconensis*: In silico and in vitro cytotoxicity studies

Authors: Dina H. El-Kashef, Fadia S. Youssef, **Irene Reimche**, Nicole Teusch, Werner E.G. Müller, Wenhan Lin, Marian Frank, Zhen Liu, Peter Proksch

Journal: Bioorganic & Medicinal Chemistry

DOI: <https://doi.org/10.1016/j.bmc.2020.115883>

Published: 16 November 2020

Contribution: Cell culture; 2D cell viability assay; Wound Healing assay (including experiment establishment); experimental design, data acquisition and analysis; contribution to manuscript writing (results)

Didymellanosine, a new decahydrofluorene analogue, and ascolactone C from *Didymella* sp. IEA-3B.1, an endophyte of *Terminalia catappa*

Authors: Ni P. Ariantari, Elena Ancheeva, Marian Frank, Fabian Stuhldreier, Dieter Meier, Yvonne Gröner, **Irene Reimche**, Nicole Teusch, Sebastian Wesselborg, Werner E. G. Müller, Rainer Kalscheuer, Zhen Liu, Peter Proksch

Journal: RSC Advances

DOI: 10.1039/c9ra10685e.

Published: 18 February 2020

Contribution: Cell culture; NFκB-inhibition assay; 2D cell viability assay; experimental design, data acquisition and analysis; contribution to manuscript writing (results)

Curriculum vitae

Irene Reimche, geboren in Druschba/Kaliningrad (Russische Föderation) am 02.07.1993.

Ausbildung

05/2022 – 08/2022	Heinrich-Heine-Universität Düsseldorf Promotion: Pharmazie Dissertation mit dem Titel " <i>Pharmacological Characterization of Phenanthroindolizidine Alkaloids and Fungal-Derived Metabolites as Novel Drug Candidates for the Treatment of Triple-Negative Breast Cancer</i> "
05/2019 – 04/2022	Universität Osnabrück Weiterführung der Promotion
11/2018 – 04/2019	Technische Hochschule Köln Beginn der Promotion
10/2016 – 10/2018	Philipps-Universität Marburg Master of Science, Humanbiologie Masterthesis mit dem Titel " <i>Activation of natural killer (NK) cells cytotoxicity towards EpCAM+ ovarian cancer cells using antibody-based recombinant proteins</i> "
10/2013 – 8/2013	Justus-Liebig-Universität Gießen Bachelor of Science, Biologie Bachelorthesis mit dem Titel: " <i>Synthesis of small circular RNAs</i> "
08/2004 – 06/2013	Wilhelm-von-Oranien Schule, Dillenburg Allgemeine Hochschulreife

Teilnahme an Konferenzen und Symposien

5/2021	3D Cell Culture 2021: Models, Applications & Translation Digitale Veranstaltung; Poster: " <i>3D co-culture model based for triple negative breast cancer (TNBC) encompassing cancer associated fibroblasts (CAFs)</i> "
10/2019	Integrated Research Group of the SFB 944 (IRTG) Retreat Langwedel, Deutschland; Poster: " <i>Targeting the Tumor Stroma of Triple Negative Breast Cancer</i> "

Betreute Abschlussarbeiten

11/2020

Laura Karrasch, Master of Science

Titel der Arbeit: *“Three-dimensional (3D) cell-based approaches to model the tumor microenvironment of breast cancer for drug discovery”*

04/2020

Stella Rotfuß, Bachelor of Science

Titel der Arbeit: *“Characterization of 3D Co-Culture Spheroids as a Molecular Model of the Tumor Microenvironment of Triple-Negative Breast Cancer”*

Danksagung

An erster Stelle möchte ich mich bei meiner Betreuerin, Frau Prof. Dr. Nicole Teusch, bedanken. Trotz Wechsel zu anderen Universitäten, hat sie mir die Möglichkeit zur Weiterzuführung und Finalisierung meines Forschungsprojekts gegeben. Ihre zielführende Leitung sowie Beratung während dieser Zeit waren enorm hilfreich. Bei der Anfertigung von Publikationen hat Frau Teusch mich maßgeblich unterstützt, vor allem durch die Teilhabe an erfolgreichen Kooperationen.

Obwohl ich nur eine kurze Zeit Teil der Arbeitsgruppe von Frau Prof. Dr. Teusch an der Heinrich-Heine-Universität war, bin ich sehr dankbar, für das Kennenlernen, die Unterstützung und die guten Gespräche mit folgenden Personen: Daria Janßen, Dr. Dina Hassouna El-Kashef, Dr. Rizwan Rehman Rehimi und ebenso Mohamed Said El-Naggar, Ph.D. Ein besonderer Dank gilt Katja Friedrich, Simone Miljanovic und Claudia Eckelskemper.

Für die Unterstützung bei den Experimenten, die ich an der Universität Osnabrück durchgeführt habe, bedanke ich mich herzlich bei Karin Peter und ebenso Johanna Hölken. Vor allem schätze ich die Zusammenarbeit mit Stella Rotfuß, die maßgeblich dazu beigetragen hat, das 3D Ko-Kultur Model zu etablieren. Darüber hinaus bedanke ich mich bei Dr. Gabriele Baron-Ruppert und Dr. Janina Krause für wertvolle Gespräche.

Meine Promotion hatte ich an der Technischen Hochschule Köln begonnen. Ich schätze es sehr, dass Dr. Julia Sperlich mich in das Thema Naturstoffforschung und Brustkrebs einarbeiten konnte. Ich bedanke mich auch für die Zusammenarbeit mit Jan Hänsel. Eine große Unterstützung waren ebenso Alessandra Großert und Katharina Toepler.

Ein besonderer Dank gilt meinen Kooperationspartnern, durch deren Beitrag meine Forschungsarbeit ermöglicht wurde.

Ein großer Dank geht an die damalige Arbeitsgruppe von Prof. Dr. Proksch, die Naturstoffe von Pflanzen und Pilzen zur Untersuchung zur Verfügung gestellt hat. Namentlich möchte ich mich bei folgenden Personen bedanken: Dr. Haiqian Yu, Dr. Ni Putu Ariantari, Zhen Liu und Dr. Dina Hassouna El-Kashef.

Ebenfalls bedanke ich mich bei der Arbeitsgruppe von Prof. Dr. Schmalz für die Bereitstellung von einem chemisch synthetisierten Naturstoff.

Im Zuge der Promotion konnte ich die Technik zur Generierung von 3D Modellen an der Universität Bath (Vereinigtes Königreich) erlernen. Ein großer Dank gilt dem Arbeitskreis von Prof. Dr. Randy Mrsny für die Aufnahme und Betreuung, insbesondere die Betreuung

von Bailu Xie. Ebenfalls danke ich Ass. Prof. Dr. Ute Jungwirth für die Betreuung zur initialen Generierung von einem 3D Brustkrebs Modell und zur Bereitstellung von Zellen.

Die Teilnahme an der 3D *Cell Culture* Konferenz von Dechema führte zu einer Kooperation und ich bin sehr dankbar, dass Nadia Bauer und Prof. Dr. Friedemann Kiefer meine Hypoxie Studien unterstützt haben, indem sie eine Hypoxie-Sensor Zelllinie zur Verfügung stellten.

Ein besonderer Dank geht an meine Familie und Freunde, die mir durchgängig zur Seite standen und mir in schwierigen Situationen Mut zugesprochen haben. Meine Familie, insbesondere mein Vater, haben mir eine riesige Last genommen, indem sie meine Umzüge während der Promotion mitorganisiert haben. Mein größter Dank geht an meine Mutter, die alles dafür gegeben hat, dass ich meine Ziele erreichen kann.

Im Laufe der Promotion habe ich besondere Menschen kennen gelernt und wissenschaftlich so wie auch persönlich viele neue Erfahrungen gewonnen. Ich schätze jeden Erfolg, sowie jede Hürde, die ich durchgestanden habe. Bei aller Motivation und allem Engagement wurde mir jedoch eines bewusst, nämlich, dass Durchhaltevermögen, Geduld und Gelassenheit eine große Stärke sind.

Eidesstaatliche Erklärung

Ich versichere an Eides Statt, dass die Dissertation von mir selbständig und ohne unzulässige fremde Hilfe unter Beachtung der „Grundsätze zur Sicherung guter wissenschaftlicher Praxis an der Heinrich-Heine-Universität Düsseldorf“ erstellt worden ist. Die Dissertation wurde in der vorgelegten oder in ähnlicher Form noch bei keiner anderen Fakultät eingereicht. Ich habe bisher keine erfolglosen und erfolgreichen Promotionsversuche unternommen.

Die Promotion wurde an folgenden Hochschulen durchgeführt:

Heinrich-Heine-Universität, Institut für Pharmazeutische Biologie und Biotechnologie
unter Anleitung von Prof. Dr. Nicole Teusch

Universität Osnabrück, Institut für Gesundheitsforschung und Bildung
in der Abteilung „Biomedizinische Grundlagen“
unter Anleitung von Prof. Dr. Nicole Teusch

Technische Hochschule Köln, Fakultät für Angewandte Naturwissenschaften
in der Arbeitsgruppe „Bio-Pharmazeutische Chemie & Molekulare Pharmakologie“
unter Anleitung von Prof. Dr. Nicole Teusch

Düsseldorf, 09.11.2022

Irene Reimche